# UNIVERSITY OF CALIFORNIA

## Santa Barbara

## Etchless Core-Definition Process for the Realization of Low Loss Glass Waveguides

A Dissertation submitted in partial satisfaction of

the requirements for the degree

Doctor of Philosophy in Electrical and Computer Engineering

by

Demis D. John

Committee in charge:

Professor Daniel J. Blumenthal, chair

Professor John E. Bowers

Professor Larry A. Coldren

Professor Nadir Dagli

Dr. Jonathon S. Barton

June 2012

UMI Number: 3540189

UMI

Dissertation Publishing

UMI 3540189

ProQuest®

ProQuest LLC.
789 East Eisenhower Parkway
P.O. Box 1346
Ann Arbor, MI 48106 - 1346

The dissertation of Demis D. John is approved.

_____

 Professor Daniel J. Blumenthal

_____

Professor John E. Bowers

_____

Professor Larry A. Coldren

_____

Professor Nadir Dagli

_____

Dr. Jonathon S. Barton

March 2012

# Etchless Core-Definition Process for the Realization of Low Loss Glass Waveguides

Demis D. John

typeset in LaTeX

# Acknowledgments

As is the case with most engineering projects, the results obtained during my time at UCSB were only made possible with the help of many brilliant and helpful scientists. The collaboration between students, research groups and local companies is an invaluable asset of the UCSB scientific community.

I would first like to thank my advisor, Dr. Daniel J. Blumenthal, for not only enabling the world-class research performed throughout his group, but for allowing me to be deeply involved in the development of the project we were eventually funded for. Professors Dan Blumenthal & John Bowers have provided brilliant and poignant advice and direction during my research.

Immediately upon beginning work within Dan's group, the patience and support of existing group members enabled me to quickly understand the very complex fabrication processes and devices being implemented in the LASOR project (LAbel Switched Optical Router).

In particular, Dr. Milan Mašanović & Dr. Henrik Poulsen have always exhibited tremendous patience in explaining and re-explaining complex devices and systems. Melissa Chun and Walt Donat taught my much of what I know about the fabrication of photonic integrated circuits (PICs) and electro-optic testing. Dr. John Mack, John Garcia, Erica Lively, Kim Nguyen and Biljana Stamenic have all contributed to my knowledge in important ways.

Later on, the IPhOD (Integrated Photonic Delay) team proved to be an impressive factory of novel ideas. Dr. Jonathon S. Barton, in particular, has worked with me on building up the project with Dan from the beginning, resulting in many fantastic brainstorming sessions. Jon has developed an impressive number of novel ideas that have turned out to be key in some of the major advances we achieved.

My close collaboration with Jared F. Bauters & Dr. Martijn J. R. Heck,

*This dissertation is dedicated to my family,*
*Azita & Jacob "JooJoo" John*

# Vita of Demis D. John

*PERSONAL*

Full Name: Demis David John

Date of Birth: April 24, 1982, in Dewsbury, United Kingdom

Nationality: United States of America & United Kingdom of Great Britain

Marital Status: Married

Spouse: Azita Rafique John

Children: Jacob Jezreel John

Email: demis@engineering.ucsb.edu (mail-forwarding address)

*EDUCATION*

Master of Science in Electronics and Photonics, Electrical & Computer Engineering Department, University of California Santa Barbara, Santa Barbara, California, U.S.A., March 2007

Bachelor of Science in Electrical Engineering, Electrical & Computer Engineering Department, University of Massachusetts Lowell, Lowell, MA, U.S.A., December 2005 (Cum Laude)

High School Diploma, Concord-Carlisle High School, Concord, Massachusetts, U.S.A., June 1999

*OTHER ACTIVITIES*

Mentor, Research Mentorship Program (RMP), May 2011 – August 2011. Intern: Alex Erstad (High school student from Arizona). Project Title: "Automated Loss Detection For Photonic Integrated Circuits Using A Top Down Infrared Camera."

Coordinator, Let's Explore Physical Science (LEAPS) after-school science clubs (NSF funded), Oct. 2009 – Aug. 2010. Hired & managed 5 UCSB undergraduates in designing and teaching after-school science clubs at five Santa Barbara Elementary and Middle schools.

Mentor, Research Experience for Teachers (NNIN-RET), May – Aug. 2009. Intern: Marilyn Garza (8th grade Teacher at Santa Barbara Junior High). Project Title: "Glass Deposition & Etching for Glass Waveguides", Curriculum Developed: "Lesson 1: Small Scale Stenciling: Mask Lab" & "Lesson 2: Small Scale Sculpting: Etch Lab."

Mentor, Research Experience for Teachers (NNIN-RET), May – Aug. 2008. Intern: Marilyn Garza (8th grade Teacher at Santa Barbara Junior High). Project Title: "Optical fibers fabricated on a microchip level", Curriculum Developed: "Lesson 1: Refraction Tank", "Lesson 2: Waveguides (Gelatin)" & "Lesson 3: Optical Fiber Limbo."

Mentor, Research Experience for Teachers (NNIN-RET), May – Aug. 2007. Intern: Richard Moore (High school Teacher from San Fernando Valley). Project Title: "Fabrication of Chip-Scale Optical Waveguides for High-Speed Communications", Curriculum Developed: "Jell-O$^{\circledR}$ Waveguides and Power Loss."

Mentor, 8th Grade Science Fair, Dec. 2006 – March 2007. Student: Connor Lynch. Project: "Energy and Cleanliness Comparison between a Motor Running on Gasoline versus Hydrogen."

DJ, KCSB 91.9 FM Santa Barbara, 2006-2010. Program Title: "Reelin' & Rockin' with D & Z."

*AWARDS*

Fellowship from the National Science Foundation (NSF): LEAPS ("Let's Explore Applied Physical Science"), 2009–2010

*PUBLICATIONS*

Jared F. Bauters, Martijn J. R. Heck, Daoxin Dai, Demis D. John, Jonathon S. Barton, Daniel J. Blumenthal, and John E. Bowers, "High Extinction, Broadband, and Low Loss Planar Waveguide Polarizers," to be presented at *Integrated Photonics Research 2012*, Colorado Springs, Colorado, United States, Jun. 2012.

D. D. John, R. Moreira, J. S. Barton, J. F. Bauters, M. J. R. Heck, J. E. Bowers, and D. J. Blumenthal, "Demonstration of Etch-less Core Definition Process for Low-Loss Glass Waveguide Fabrication," in *European Conference on Integrated Optics*, Sitges, Barcelona, Spain, paper 129, Apr. 2012.

J. F. Bauters, M. J. R. Heck, D. D. John, J. S. Barton, D. J. Blumenthal, J. E. Bowers, C. M. Bruinink, A. Leinse, and R. G. Heideman, "A Comparison of Approaches for Ultra-Low-Loss Waveguides," to be

published in *Proc. of OFC/NFOEC 2012*, Los Angeles, CA, Paper OTu1I.3, Mar. 2012.

D. D. John, M. J. R. Heck, J. F. Bauters, R. Moreira, J. S. Barton, J. E. Bowers, and D. J. Blumenthal, "Multi-Layer Platform for Ultra Low Loss Waveguide Applications," *IEEE Photonics Technology Letters*, vol. 24, no. 11, pp. 676-678, Apr. 2012.

J. F. Bauters, M. J. R. Heck, D. D. John, J. S. Barton, C. M. Bruinink, A. Leinse, R. G. Heideman, D. J. Blumenthal, and J. E. Bowers, "Planar waveguides with less than 0.1 dB/m propagation loss fabricated with wafer bonding," *Optics Express*, vol. 19, no. 24, pp. 2409024101, Nov. 2011.

J. F. Bauters, M. J. R. Heck, D. D. John, J. S. Barton, D. J. Blumenthal, J. E. Bowers, C. M. Bruinink, A. Leinse, and R. G. Heideman, "Ultra-Low-Loss (< 0.1 dB/m) Planar Silica Waveguide Technology," in *IEEE Photonics Conference 2011*, Arlington, Virginia, USA, 2011.

J. F. Bauters, M. J. R. Heck, D. D. John, M.-C. Tien, W. Li, J. S. Barton, D. J. Blumenthal, J. E. Bowers, A. Leinse, and R. G. Heideman, "Ultra-low-loss Single-mode Silicon Nitride Waveguides with 0.7 dB/m Propagation Loss," *European Conference on Optical Communication (ECOC) 2011 Technical Digest*, paper Th.12.LeSaleve.3, Jul. 2011.

D. D. John, J. F. Bauters, J. Nedy, W. Li, R. Moreira, J. S. Barton, J. E. Bowers, and D. J. Blumenthal, "Fabrication and Demonstration of a Pure Silica-Core Waveguide Utilizing a Density-Based Index Contrast," *Proc. of OFC/NFOEC 2011*, Los Angeles, California, U.S.A., paper

OWS3, Mar. 2011.

J. F. Bauters, M. J. R. Heck, D. D. John, D. Dai, M. C. Tien, J. S. Barton, A. Leinse, R. G. Heideman, D. J. Blumenthal, and J. E. Bowers, "Ultra-low-loss high-aspect-ratio Si3N4 wavequides," *Optics Express*, vol. 19, no. 4, pp. 31633174, Feb. 2011.

J. F. Bauters, M. J. R. Heck, D. D. John, M. Tien, A. Leinse, R. G. Heideman, D. J. Blumenthal, and J. E. Bowers, "Ultra-low loss silica-based waveguides with millimeter bend radius," *Proceedings of European Conference on Optical Communication (ECOC) 2010*, Torino Italy, p. Paper We.8.E.6, Sep. 2010.

# Abstract

Etchless Core-Definition Process for the

Realization of Low Loss Glass Waveguides

by

Demis D. John

Optical waveguides integrated onto microchips form some of the major components that enable the optical communication system we now use for our Internet, television and communication systems around the world, and are soon to be replacing some of the electrical components in high-speed computers. Deployed optical fibers form a web that spans the globe due to the very low loss of light - less than a decibel per kilometer. Chip-scale waveguides, on the other hand, typically exhibit losses 3-5 orders of magnitude higher - a few decibels per centimeter!

In an attempt to unleash the potential of photonics in the numerous applications rendered unfeasible by these high losses, we have taken a systematic approach to understanding, modeling and improving the loss mechanisms in optical waveguides. We follow the path of optical fibers by focusing on glass-based designs, in particular the silicon dioxide/silicon oxynitride ($SiO_2/SiO_xN_y$) material platform. In addition to a materials study of a number of deposited glasses, and the development of simulation tools for the major loss mechanisms, we have developed a process to tackle the largest loss contributor - sidewall roughness of waveguide cores.

We demonstrate for the first time a process for the selective oxidation of silicon oxynitride, which converts high index core $SiO_xN_y$ into cladding $SiO_2$ via a thermal oxidation. We thoroughly characterize the wet oxidation process, and apply this to the fabrication of optical waveguides. We discuss the underlying chemistry behind the oxidation process, which affects the shape and index of the resulting materials. We propose a model for the smoothing of waveguide sidewalls by oxidant diffusion, and present the most recent results obtained with this novel process.

Additionally, we present an iterative process for optimizing the waveguide structure for propagation loss, using a non-destructive loss measurement scheme based on Optical Frequency Domain Reflectometry and subsequent re-oxidations. This trimming technique, enabled by the oxidation process, is applicable to all glass waveguide foundries that use $SiO_xN_y$ or $Si_3N_4$ materials for waveguide cores.

# Contents

# List of Figures

# List of Tables

# Chapter 1

# Introduction

Optical waveguides integrated onto microchips form some of the major components that enable the communication system we now use for our Internet, television and communication systems around the world, and are soon to be replacing some of the electrical components in high-speed computers and datacenters [1, 2, 3]. Deployed optical fibers form a web that spans the globe due to the very low loss of light - less than a decibel per kilometer - in layman's terms, about half of the optical is lost after 3 kilometers of travel.

Chip-scale waveguides, the microchip analogue to optical fibers, are used to route and manipulate light on optical microchips (also known as a photonic integrated circuits, or PICs). Optical microchips not only enable many of the inter-fiber links used in our sophisticated communications networks, but find use in many other optical technologies, such as medical imaging, solid-state gyroscopes and biological sensing, to name just a few [4, 5, 6, 7].

The benefits of using an integrated waveguide over a coil of optical fiber are similar to the use of electrical microchips over wire connectors and discrete components - smaller package sizes, improved robustness and finer control over certain properties of the devices due to the microfabrication tech-

niques applicable to integrated devices. One particular optical property that is considerably easier to predict in a chip-scale waveguide than in an optical fiber is the polarization of light, where optical fibers are notorious for exhibiting random polarization rotations throughout the optical travel due to bend-induced strains.

Many of the aforementioned applications benefit greatly from the ability to create long optical time-delays, where looped waveguides store or delay the light over a fixed distance of waveguide, an example of which is shown in Figure 1.1. PIC-based optical routing as in [8] & [9], optical gyroscopes [10] and beam-steering for phased array antennas [11] all require long waveguide-based optical delay lines, and the optical loss of these delays directly impacts the performance of the device in each application. Coiled optical fiber is the most common way these delay lines are created. In the case of optical routing for communications, in which very significant progress has been made in the large-scale integration of functionality onto PICs, the power consumption of these chips due to light amplification and the required cooling could be dramatically reduced if the waveguide technology itself were to be reduced to the sub-dB/meter loss range.

**Figure 1.1:** *An example of a 1 meter-long waveguide fabricated out of the glasses $Si_3N_4$ & $SiO_2$, illuminated with a red laser from an optical fiber (top-left). The time-delay corresponds to about 5 ns.[12]*

## 1.1 Glass Waveguide Technology

Low loss optical fibers to date exhibit losses of less than 0.15 dB/km [13, 14], 4 to 6 orders of magnitude lower than typical planar waveguide losses, which today are on the order of a few dB/meter for silica-based waveguides and a few dB/cm for semiconductor waveguide platforms [15, 16, 17, 18]. The operating principle for any waveguide, be it optical fiber or otherwise, is that of total internal reflection, requiring a "core" glass with higher refractive index ($n$) than the "cladding" glass (Figure 1.2). The core thus forms the central waveguide region in which light is trapped due to the outer cladding region having a faster velocity of light than the core region (since the velocity of light in a material, $v$, is defined by $v = c/n$, where $c$ is the speed of light).

Optical fibers, drawn from a boule of molten glass rather than etched into
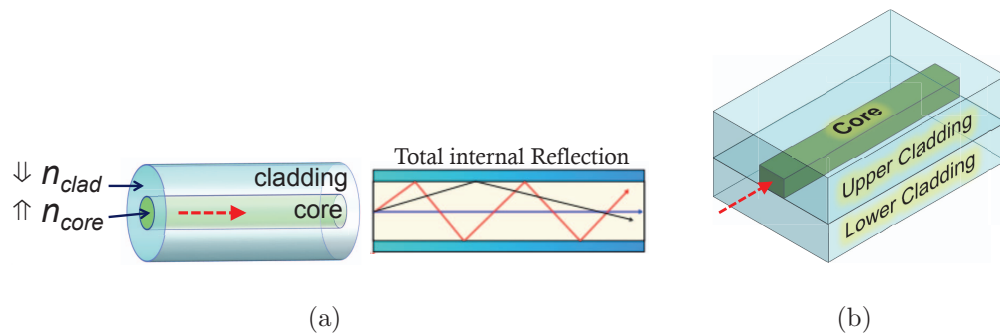
**Figure 1.2:** *(a) Optical fibers, drawn from a rod of molten glass, have a cylindrical shape. n is the refractive index of the glass, which must be higher in the core region. (b) Planar waveguides, fabricated on flat, polished wafers, typically have a rectangular shape, defined by the top-down nature of wafer processing.*

a thin-film, are typically not limited by the roughness of the core/cladding interface, while the losses of integrated (planar) waveguides have been shown to be dominated by waveguide roughness [15, 19].

This roughness originates from the planar nature of microchip fabrication, in which the waveguide core must be etched in a vertical direction, from the top, to remove the core in unwanted areas.

## 1.2 Losses in Optical Waveguides

A survey of the history of optical fiber loss reduction (Figure 1.3) reveals that as silica waveguide roughness losses are reduced the next major loss contributions will be due to OH- concentration and impurities/dopants. In particular, we observe that the lowest loss fibers currently utilize Pure-Silica Core Fiber (PSCF) designs [13, 14], which maximizes the amount of optical power overlapped with pure $SiO_2$, minimizing the impact of dopants and
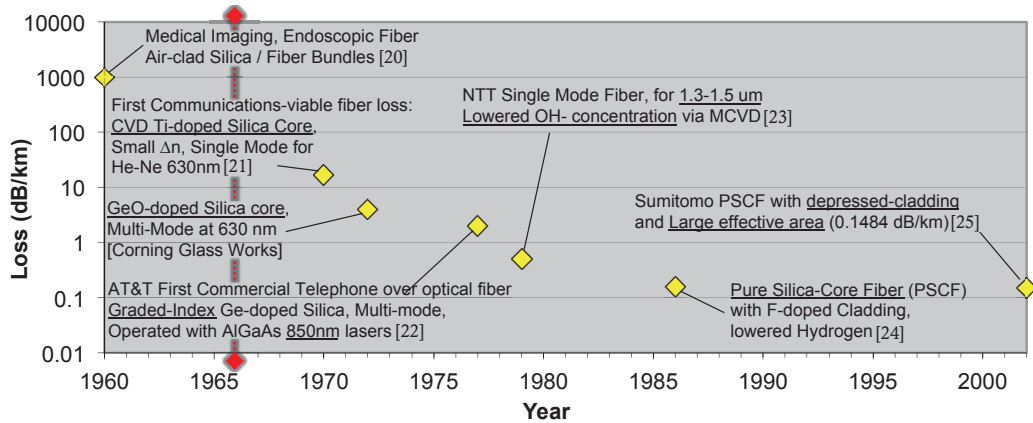
**Figure 1.3:** *History of fiber loss reduction. The publication of Kao & Hockham's key investigation is indicated by the red dashed line [26].*

other impurities.

Thus we have decided to focus entirely on the relatively mature silica-based platform, often referred to as Planar Lightwave Circuits, or PLCs. This consists of a $SiO_2$ upper and lower claddings as base materials [27]. A particularly versatile and relatively common core material of Silicon Oxynitride, or $SiO_xN_y$ was chosen, as the refractive index of this material can be continuously varied from that of pure $SiO_2$ ($n \approx 1.44$) to $Si_3N_4$ ($n \approx 2.00$) by varying of the O/N ratio. A plot of this variable refractive index is shown in Figure 1.4, where the gas flow ratio in a glass deposition tool can easily be varied to attain any desired refractive index between the two stoichiometric materials.

Optical fibers first became considered as viable as a communication medium when C. K. Kao & G. A. Hockham published their Nobel-prize winning paper in 1966 [26]. One of the primary contributions of their seminal work was the separation of each mechanism that could cause an optical loss in fibers. Their analysis led to a distinction between the types of loss into separate

"waveguide" and "material" losses, in which waveguide losses deal with the materials as if they are macroscopic, uniform materials, while material losses deal with molecular-level issues specific to the materials used.

Understanding each optical loss contribution with respect to planar waveguides is key to performing a similar loss reduction on a PIC platform. A literature study of the estimated order of magnitude of each known loss mechanism along with some modeling detailed in Chapter 2 was used to produce the plot shown in Figure 1.5 [28, 29, 30, 31, 32, 33, 34]. The figure
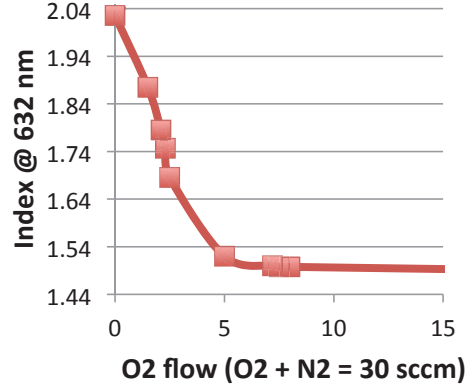


**Figure 1.4:** $SiO_xN_y$ glass deposited with ion-beam sputtering.

shows the approximate percentage contribution of each loss mechanism for an $Si_3N_4$-based waveguide, illustrating that as sidewall roughness losses are reduced, N-H bond resonances would become the next loss-limiting factor.

It should be noted that these order-of-magnitude loss contributions come from different types of waveguides with various geometries, so the chart serves primarily as a guide for which mechanisms should be given highest priority - ie. Roughness and Hydrogen losses dominate, with impurities and sub-wavelength scattering contributing only once the roughness and hydrogen-based losses are significantly reduced.

6
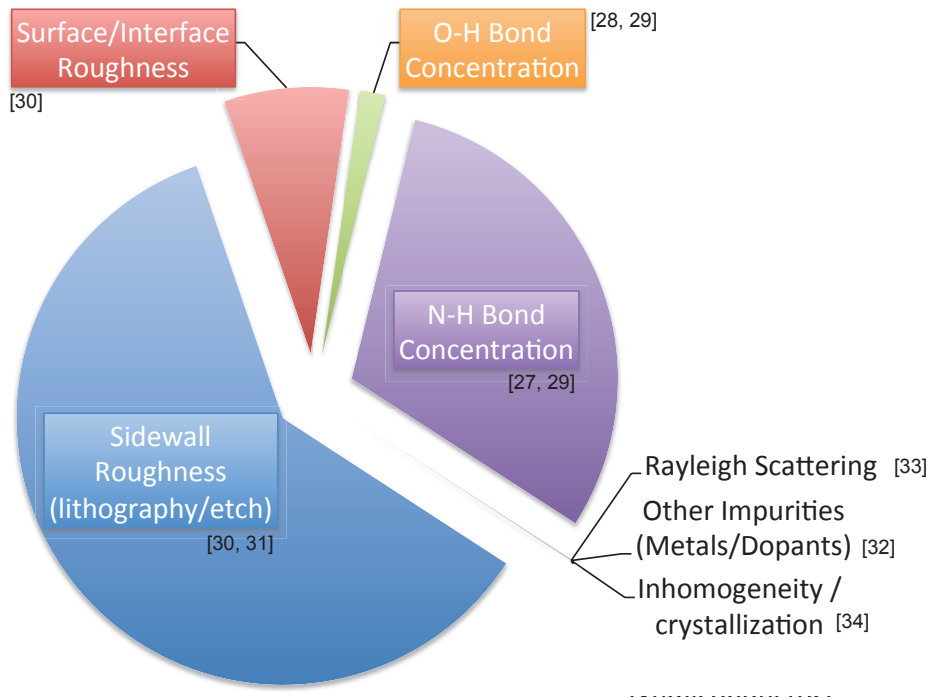
**Figure 1.5:** *Order-of-magnitude loss contributions in SiON waveguides.*

## 1.3 State-of-the-art Waveguide Losses

When designing a long optical delay on the order of meters or nanoseconds of delay, as is needed for the aforementioned applications, it is irrational to discuss the losses of straight waveguides as one would then be envisioning a meter long substrate. A particularly spacially-efficient way to lay out a long delay waveguide without reflecting mirrors or waveguide crossings is with an Archimedean spiral, as shown in Figure 1.6. The Archimedean spiral is mathematically defined as a spiral in which the radius increases constantly with angle - which translates into a constant separation between waveguides. The figure technically only shows the Archimedean characteristic for all spiral points larger than the "s-bend" - the s-bend requires a sudden reduction in bend radius by half to change propagation direction.

7
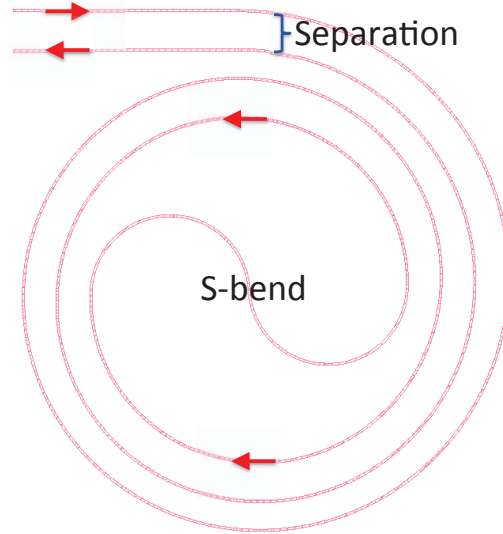
**Figure 1.6:** *Optical delay line layout in Archimedean spiral configuration.*

With the long optical delay in mind, losses for ultra low-loss waveguides should always be discussed in terms of the bend radius at which those losses were measured. This is extremely important when comparing waveguide technologies and their application.

For example, Adar *et al.* at Bell Labs demonstrated planar waveguide losses in 1994 of 0.85 dB/meter [35]. This record low number has caused their paper to be repeatedly referenced as the lowest loss waveguides to date, for more than a decade. These losses were measured on a ring resonator of 30 mm bend radius, and Table 1.1 shows how dramatically the losses for the same waveguide design increased at smaller bend radii.

More recently, commercial companies have made available planar waveguides with what appear to be higher losses at first glance. However if one compares the waveguide losses at *similar* bend radii, we see that the Bell Labs devices perform similarly or worse when compared with ANDevices or Enablence waveguides at similar bend radii.

8

**Table 1.1:** *Commercially available PLC losses and the associated bend radii.*

| Company | Loss (dB/m) | Bend Radius (mm) | Technology |
|---|---|---|---|
| Bell Labs [35] | 0.85 | 30 | 5 x 5 µm, P-doped $SiO_2$, $\Delta n$=0.70, Rectangular Channel |
| | 1.22 | 20 | |
| | 4.72 | 10 | |
| | 173 | 5 | |
| ANDevices [36] | 4 | 6 | 5 x 5 µm, $SiO_xN_y$, $\Delta n$=0.75, Rectangular Channel |
| Enablence [37] | 21.22 | 3 | 4.3 x 4.3 µm, $\Delta n$=1.50, Rectangular Channel |
| LioniX BV [38] | 12 | 0.400 | 2 x ˜0.100 µm, Non-symmetric $Si_3N_4$ co-planar rib |
| | 10 | 0.750 | 1-2 µm x ˜1 µm, A-shaped $Si_3N_4$, Silica core |
| | 6 | 0.500 | ˜1 µm x ˜1 µm, Box-shaped $Si_3N_4$, Silica core |

The Dutch company LioniX BV shows similar propagation losses, although at considerably smaller sub-millimeter bend radii, which indicates that these technologies are rather promising for very long delays, as the losses at larger bend radii may in fact be quite low. For a customer to really predict if the waveguide technology is applicable to their size constraints, the Loss vs. Bend Radius would need to be specified explicitly, enabling a designer to predict the waveguide losses at any chosen bend radius.

In fact, I would go as far as to say that any waveguide technology designed for low propagation losses should always be specified with the loss versus bend radius explicitly defined, as that ultimately limits the applicability and performance of a delay or ring resonator. Some commercial companies will quote "loss per 90° bend", and this metric should be accompanied with the radius of this bend.

A more thorough description would be to provide three parameters allowing a waveguide designer to calculate the loss at any bend radius. Bend losses (in dB) increases exponentially with reduced bending radius (see Section 2.2), so a simple metric for loss vs. bend radius would be the coefficients
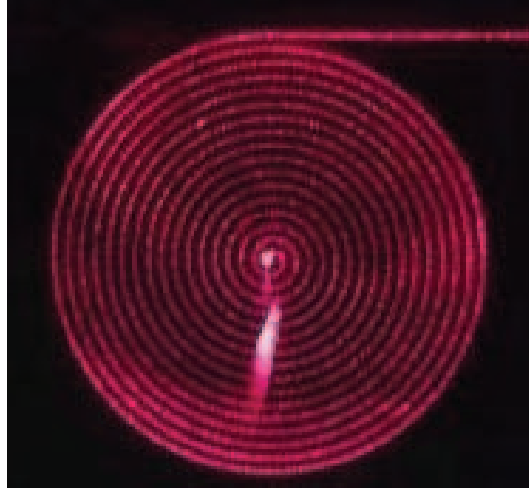
**Figure 1.7:** *A "Spiral-In" test structure, illuminated with a red laser. (Photo courtesy LioniX B. V.)*

of the Loss vs. Bend Radius curve, which can be simply given as

$$\alpha(dB/m) = a_1 \ e^{-a_2 \cdot R} + a_3 \tag{1.1}$$

where $\alpha$ is the loss in dB/m and $R$ is the bend radius. $a_1$ is the exponential prefactor, $a_2$ is the exponential coefficient that indicates the change in loss with bend radius, and $a_3$ is the loss of a straight waveguide. Specification of $a_1$, $a_2$ and $a_3$ would completely describe the bending potential of a particular waveguide type/design.

In [12] we presented a waveguide test structure that is well suited to the determination of these three parameters. The "Spiral-In" test structure, shown in Figure 1.7, was measured with a commercial OFDR tool (see Section 4.2 on page 111 for background on this technique), and the resulting curve was fit to obtain the three bending parameters.

The availability of a high quality commercial OFDR measurement tool and simple curve-fitting enabled with this test structure makes it possible for any commercial waveguide foundry to determine these bending parameters

with relative ease.

## 1.4   Thesis Outline

In light of the above considerations, we realized the necessity of understanding the interplay between each of the loss contributions prior to the choice of a final waveguide design.

This thesis focuses on first outlining the theory behind each of the largest loss contributions and then understanding the design tradeoffs inherent in minimizing the total optical loss. The bending capability of the waveguide design should be kept in mind throughout these discussions.

Numerous simulations are discussed, tackling the macroscopic "waveguide" losses, which treat all materials as homogenous regions of constant refractive index, $n$ (Chapter 2 on page 20).

First, simulations of the loss due to roughness are used to inform on the effect of core geometry (shape) on scattering losses. This is followed my techniques developed to measure the roughness of etched waveguide sidewalls.

Secondly, simulations of the loss due to bending are performed, again developing an intuition for the effect of waveguide design on bending capability. Substrate leakage is also simulated, to determine what cladding thicknesses are required for a given loss target.

Lastly, the tradeoff between low scattering and low bend loss is investigated, with the intention of determining an optimal geometry given a required bend radius. Finally, the layout of a long optical delay is described given the constraints of wafer size and fabrication area.

Moving to the sub-wavelength nano-scale, we then investigate the material properties of the various glasses available in the UCSB NanoFabrication

Facility, with the intention of identifying the optimal materials with which to fabricate a waveguide (Chapter 3 on page 64).

We measure the surface roughness of a number of deposition methods, which informs on each deposition technqiue's effect on the aforementioned scattering losses.

We then investigate the next-largest material contribution of hydrogen-based absorption, and rank each deposited film with respect to hydrogen content. Lastly, we measure low-level impurities via two different spectroscopic techniques.

In order to measure waveguides fabricated with the geometries, layout and materials identified in the prior chapters, we discuss the measurement of low-loss waveguides, settling on a particular technique that suits our needs for rapid prototype testing with high accuracy (Chapter 4 on page 106). The measurement technique is explained, and then used to measure the losses and group indices ($n_g$) of glass waveguides fabricated with a direct-etching process in the UCSB NanoFab.

Determination of the limiting loss contributions of these devices leads us to pursue novel fabrication processes for lowered scattering loss, which I will show also enables smaller bend radii & device footprints.

A novel process for glass waveguide fabrication without direct-etching of the core is then proposed, utilizing the first selective thermal oxidation of Silicon Oxynitride (Chapter 5 on page 147). Additionally, a technique to optimize loss or group index after fabrication & testing is proposed, enabled by the non-destructive measurement technique and an unmasked reoxidation of the waveguides after measurement.

We show a simulation of the roughness reduction performed by this diffusion–controlled process, and thoroughly characterize the thermal oxi-

dation of $SiO_xN_y$, elucidating the chemical processes involved, and finally applying these findings to the optimal process for waveguide fabrication via the Local Oxidation of Silicon-Oxynitride.

Waveguides fabricated with the LOO Process are analyzed for the resulting core geometry, propagation loss and group index ($n_g$), using the aforementioned measurement techniques. The major loss contributions are then determined, followed by unmasked reoxidation to progressively lower losses.

As a final note, we describe an experiment that elucidates the important effect of thick glasses on the waveguide characteristics (Chapter 6 on page 190). The thick deposited upper claddings often utilized in glass waveguide fabrication cause a significant stress-optic effect, which, although difficult to describe completely for the various glasses we use, is clearly shown to reduce the refractive indices of embedded core materials.

Following these results, I describe the future applications and potential continuations of the work developed in this theses (Chapter 7 on page 209).

The appendices contain detailed fabrication processes for both the direct-etched and locally-oxidized core processes, along with other measurement procedures developed to obtain the results presented in this thesis.

# References

[1] A. Alduino, L. Liao, R. Jones, M. Morse, B. Kim, W.-Z. Lo, J. Basak, B. Koch, H.-F. Liu, H. Rong, M. Sysak, C. Krause, R. Saba, D. Lazar, L. Horwitz, R. Bar, S. Litski, A. Liu, K. Sullivan, O. Dosunmu, N. Na, T. Yin, F. Haubensack, I.-W. Hsieh, J. Heck, R. Beatty, H. Park, J. Bovington, S. Lee, H. Nguyen, H. Au, K. Nguyen, P. Merani, M. Hakami, and M. Paniccia, "Demonstration of a high speed 4-channel integrated silicon photonics WDM link with hybrid silicon lasers," in *Integrated Photonics Research, Silicon and Nanophotonics*, p. PDIWI5, 2010.

[2] D. Vantrease, R. Schreiber, M. Monchiero, M. McLaren, N. Jouppi, M. Fiorentino, A. Davis, N. Binkert, R. Beausoleil, and J. Ahn, "Corona: System Implications of Emerging Nanophotonic Technology," in *35th International Symposium on Computer Architecture*, Beijing, China, pp. 153164, June 2008

[3] C. L. Schow, F. E. Doany, C. Chen, A. V. Rylyakov, C. W. Baks, D. M. Kuchta, R. A. John, and J. A. Kash, "Low-Power 16 x 10 Gb/s Bi-Directional Single Chip CMOS Optical Transceivers Operating at $\ll$ 5 mW/Gb/s/link," *Solid-State Circuits, IEEE Journal of*, vol. 44, no. 1, pp. 301313, 2009.

[4] M. L. Masanovic, E. Burmeister, M. M. Dummer, B. Koch, S. C. Nicholes, B. Jevremovic, K. Nguyen, V. Lal, J. E. Bowers, L. A. Coldren, and D. J. Blumenthal, "Advanced photonic integrated technologies for optical routing and switching," in *Proc. of SPIE*, vol. 7219, pp. 72190I1 72190I10, 2009.

[5] L. Babaud, F. Groen, X. Leijtens, M. Bertogna, J. den Besten, Y. Barbarin, Y. Oei, F. Karouta, J. Binsma, and M. Smit, "First integrated continuously tunable AWG-based laser using electro-optical phase shifters," *Proc. 12th Eur. Conf. on Int. Opt. (ECIO05)*, pp. 156159, 2005.

[6] C. Ciminelli, F. DellOlio, C. E. Campanella, and M. N. Armenise, "Photonic technologies for angular velocity sensing," *Advances in Optics and Photonics*, vol. 2, pp. 370404, Jun. 2010.

[7] R. Osellame, V. Maselli, R. M. Vazquez, R. Ramponi, and G. Cerullo, "Integration of optical waveguides and microfluidic channels both fabricated by femtosecond laser irradiation," *Applied Physics Letters*, vol. 90, no. 23, pp. 231118231118, 2007.

[8] E. F. Burmeister and J. E. Bowers, "Integrated gate matrix switch for optical packet buffering," *IEEE Photonics Technology Letters*, vol. 18, no. 1, pp. 103105, 2006.

[9] G. Kurczveil, M. J. R. Heck, J. D. Peters, J. M. Garcia, D. Spencer, and J. E. Bowers, "An Integrated Hybrid Silicon Multiwavelength AWG Laser," *IEEE J. Select. Topics Quantum Electron.*, vol. 17, no. 6, pp. 15211527, Nov. 2011.

[10] P. Mottier and P. Pouteau, "Solid state optical gyrometer integrated on silicon," *Electronics Letters*, vol. 33, no. 23, pp. 19751977, 1997.

[11] S. Yegnanarayanan, P. D. Trinh, F. Coppinger, and B. Jalali, "Compact silicon-based integrated optic time delays," *IEEE Photonics Technology Letters*, vol. 9, no. 5, pp. 634635, May 1997.

[12] J. F. Bauters, M. J. R. Heck, D. D. John, J. S. Barton, C. M. Bruinink, A. Leinse, R. G. Heideman, D. J. Blumenthal, and J. E. Bowers, "Planar waveguides with less than 0.1 dB/m propagation loss fabricated with wafer bonding," *Optics Express*, vol. 19, no. 24, pp. 2409024101, Nov. 2011.

[13] G Tanaka, M Watanabe, K Yano, "Characteristics of pure silica core single-mode fiber," *Fiber and Integrated Optics*, vol. 7, no. 1, p. 47, 1988

[14] K Nagayama, M Matsui, I Saitoh, Y Chigusa, "Ultra-low-loss (0.1484 dB-km) pure silica core fibre and extension of transmission distance," *Elect. Lett.*, vol. 38, no. 20, p.1168, Sept. 2002

[15] J. F. Bauters, M. J. R. Heck, D. John, M. Tien, A. Leinse, R. G. Heideman, D. J. Blumenthal, J. E. Bowers, "Ultra-low Loss Silica-based Waveguides with Millimeter Bend Radius," *Proceedings of the 36th European Conference on Optical Communication 2010*, Torino, Italy, paper We.8.E.6, 2010

[16] R. Adar, M. R. Serbin, V. Mizrahi, "Less than 1 dB per meter propagation loss of silica waveguides measured using a ring resonator," *IEEE Journal of Lightwave Technology*, vol. 12, no. 8, 1994

[17] K. K. Lee, D. R. Lim, H. Luan, A. Agarwal, J. Foresi, L. C. Kimerling, "Effect of size and roughness on light transmission in a Si:SiO2 waveguide: Experiments and model", *Appl. Phys. Lett.*, vol. 77, no. 11, pp. 1617-1619, 2000

[18] R. J. Deri, E. Kapon, "Low-Loss III-V Semiconductor Optical Waveguides," *IEEE Jnl. Quant. Elect.*, vol. 27, no. 3, 1991

[19] C. Ciminelli, F. Dellolio, V. M. N. Passaro, and M. N. Armenise, "Fully three-dimensional accurate modeling of scattering loss in optical waveguides," *Opt Quant Electron*, vol. 41, no. 4, pp. 285298, Mar. 2009.

[20] L. E. Curtiss, B. Hirshowitz, C. Peters, "A Long Fiberscope for Internal Medical Examinations," in *41st Meeting of the Optical Society of America* in *Journal of the Optical Society of America*, Vol. 47 of , Jan. 1957

[21] Vivek Alwayn, *Optical network Design and Implementation*, Cisco Press, Indianapolis, IN, 2004

[22] Jeff Hecht, *City of Light: The Story of Fiber Optics*, Oxford University Press, New York, NY, 1999

[23] M. Horiguchi, H. Takata, "Transmission-Loss Characteristics of Low-OH- Content Optical Fibers," *Rev. Electr. Commun. Lab (Tokyo)*, 27(3-4), p.226-235, 1979.

[24] G Tanaka, M Watanabe, K Yano, "Characteristics of pure silica core single-mode fiber," *Fiber and Integrated Optics*, Vol. 7, No. 1, p. 47, 1988.

[25] K Nagayama, M Matsui, I Saitoh, Y Chigusa, "Ultra-low-loss (0.1484 dB-km) pure silica core fibre and extension of transmission distance", *Elect. Lett.*, Vol. 38, No. 20, p.1168, Sept. 2002

[26] C.K. Kao and Hockham G.A., "Dielectric-Fibre Surface Waveguide for Optical Frequencies," *Proceedings of the Institute of Electrical Engineers*, Vol. 113, No. 7, p.1151-1158, July 1966

[27] C H Henry, R F Kazarinov, H J Lee, K J Orlowsky, L E Katz, "Low loss Si3N4-SiO2 optical waveguides on Si". *Applied Optics*, vol. 26, no. 13, pp. 2621-2624, 1987

[28] A Iino, M. Kuwabara, K. Kokura, "Mechanisms of hydrogen-induced losses in silica- based optical fibers," *IEEE Journal Lightwave Technology*, vol. 8, no. 11, pp. 1675  1679, 1990

[29] F. Ay, A. Aydinli, "Comparative investigation of hydrogen bonding in silicon based PECVD grown dielectrics for optical waveguides," *Optical Materials*, vol. 26, no. 1, pp. 33-46, 2004

[30] F. P. Payne, J. P. R. Lacey, "A theoretical analysis of scattering loss from planar optical waveguides", *Opt. and Quant. Elect.*, vol.26 pp. 977-986, 1994

[31] J. H. Jang, W. Zhao and J. W. Bae, "Direct measurement of nanoscale sidewall roughness of optical waveguides using an atomic force microscope", *Journal App. Phys.*, vol. 83, no. 20, pp.4116-4118, Nov 2003

[32] M. Kuwazuru, K. Mochizuki, Y. Namihira, Y. Iwamoto, "Dopant Effect On Transmission Loss Increase Due To Hydrogen Permeation," *Electronics Letters*, vol. 20, no. 3, p116, February, 1984

[33] G. P. Agrawal, *Fiber-Optic Communication Systems*, Wiley & Sons Inc., NY, 2002

[34] R. Maurer, "Crystal nucleation in glass containing titanium," *Journal App. Physics*, v.33 n.6, June, 1962

[35] R Adar, M.R Serbin, V Mizrahi, "Less than 1 dB per meter propagation loss of silica waveguides measured using a ring resonator," *Journal of Lightwave Technology*, Vol. 12, No. 8, pp. 1369-1372, 1994

[36] ANDevices (7/31/2006). *Product Quotation # US073106-W001*, ANDevices, Fremont, California, U.S.A.

[37] Enablence Product Specifications, Prepared by W.L. (12/30/2005). *1.5% Index Delta Waveguide Design Rule and Process Conditions, Rev: 1.2*, Enablence, Toronto, ON, Canada

[38] R. Heideman, A. Leinse, W. Hoving, R. Dekker, D. Geuzebroek, E. Klein, R. Stoffer, C. Roeloffzen, L. Zhuang, and A. Meijerink, "Large-scale integrated optics using TriPleX waveguide technology: from UV to IR," *Proceedings of SPIE*, Vol. 7221, p. 72210R, 2009.

# Chapter 2

# Structural Waveguide Losses

Traditionally, fiber losses have been separated into *waveguide* losses and *material* losses, where the former concerns structurally-based loss mechanisms and the latter refers to loss mechanisms due to the interactions of light on the molecular level. For example, light can escape the guiding core material when a waveguide (or fiber) is bent such that light encounters the core/cladding wall at greater than the critical angle. Agrawal considers this a waveguide loss, as we're dealing with the structure macroscopically, as if they were bulk uniform materials with only some large-scale structural imperfection [1].

This does not mean that the size-scale of features we are studying must be much larger than the wavelength of light used - we can still calculate the effect of nano-scale roughness, for example, by using statistical mathematics. On the other hand, the interaction of a single molecule with some incident light, say, via the absorption of some energy into a vibration of the molecule, is considered a material loss mechanism. These molecular-level interactions will be discussed in Section 3 (page 64). Also, since the surface roughness of a deposited film is highly dependent on the deposition method used, surface roughness measurements of various materials can be found in Section

3.2.1:*Atomic Force Microscopy of Surface Roughness* on page 77.

In this chapter I will review the structural (*waveguide*) loss mechanisms that we must take into account to lower waveguide losses to the fiber-like loss regime.

In isolating structural waveguide losses from material losses, we are inherently assuming that the materials used are uniform and homogeneous, and that the point at which two materials meet (the *interface* between them) is perfectly abrupt. We will mostly be envisioning how an allowed optical mode varies with waveguide structure and how the resulting field overlaps with various structural features.

In this chapter I will discuss the following structural loss mechanisms:

1. Scattering loss at the core/cladding interface, which results from deviations from the ideally smooth core sidewall.

2. Bend loss, in which some light is radiated as it propagates through a curved waveguide.

3. Substrate Leakage loss, which accounts for any light that couples into a high-index substrate such as Silicon.

Additionally, I discuss how all of these effects should be combined to direct the design of a waveguide (page 52).

## 2.1   Sidewall/Surface Scattering Loss

In bulk materials, we consider propagating light to have experienced a reflection or otherwise *scattered* when it encounters a change in refractive index. In the case of a buried channel glass waveguide, only the refractive index of the core and cladding materials are intended to interact with the guided light

21
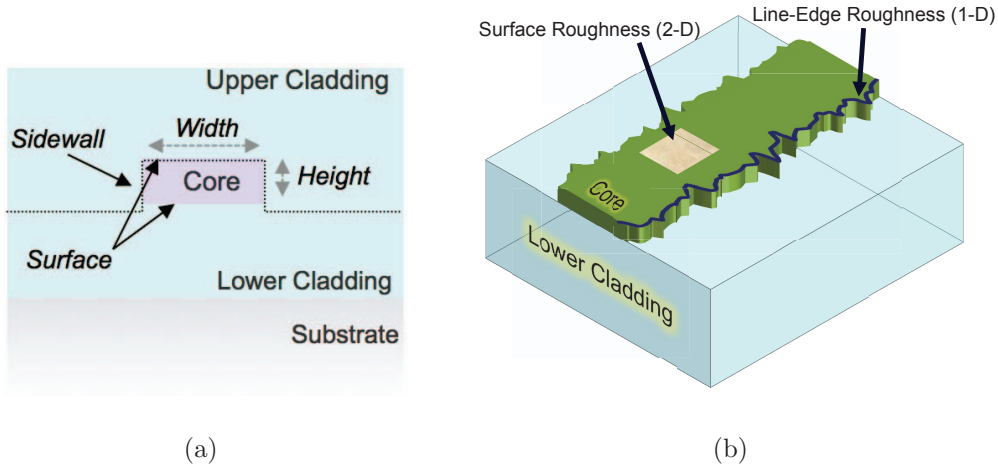
**Figure 2.1:** *(a) Slice-through view of a typical channel waveguide, showing the definition of* surface *&* sidewall *interfaces and corresponding roughness location. (b) Traditional surface roughness indicated as height data mapped onto a 2 dimensional square (beige), and line-edge roughness (LER) as deviations mapped along a 1 dimensional line (black).*

(although in reality the substrate below the lower cladding and air above the upper cladding also have some effect, as will be discussed in Section 2.3 on page 47).

The refractive index profile depicted in Figure 2.1a indicates that there are four core/cladding interfaces that represent abrupt refractive index changes, which we will refer to as the horizontal *surface* interfaces and the vertical *sidewall* interfaces. Any aberration in this ideally smooth boundary between core & cladding can scatter light out of the waveguide, resulting in optical loss due to roughness.

According to the popular models for slab waveguide scattering loss developed by Marcuse [3] and later refined by Payne and Lacey [4], two primary parameters may be measured to quantify the roughness of a surface. The standard deviation, $\sigma$, is standard statistical quantity indicating the devia-

(a)             (b)
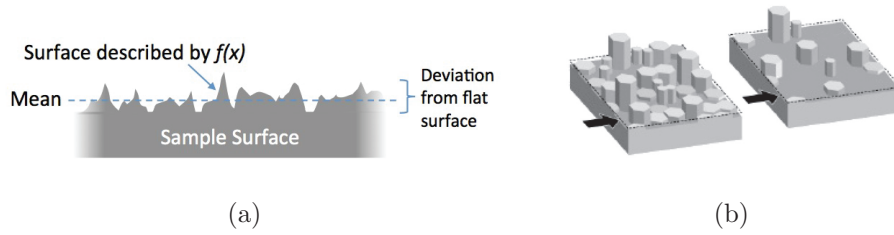
**Figure 2.2:** *(a) For a surface described by a function $f(x)$, $\sigma$ is the root-mean-square deviation from a flat surface, which is the mean, $\overline{f(x)}$, of the surface (b) These two scans would have identical RMS roughness [11].*

tion from a flat surface. The root-mean square (RMS) deviation from a perfectly smooth surface, $\sigma^2$, is often used to describe describes the height/width variation, identical to the use of RMS voltage to describe AC electrical signals without the DC component. This parameter alone does not completely describe the surface because there is no lateral spatial information - ie. how much distance lies between roughness features. This spatial parameter is necessary because two surfaces can have identical $\sigma$ values even if the the spatial separation between bumps/gouges is completely different, as illustrated in Figure 2.2. Researchers will often use a plot of the roughness power spectral density - essentially a plot of how many features occur at each spatial frequency - to get a qualitative idea of the spatial period of the surface. For random roughness this may not yield useful data, and is not easily quantifiable if one desires to compare the roughness between samples.

For this reason the correlation length, $L_c$, has been defined as the spatial parameter of the roughness, important in determining how much a particular wavelength will interact with the roughness [5, 7, 4]. If $L_c$ represents a period of the roughness that is much smaller or much larger than the wavelength of light, it will scatter less power and vice versa [7].

Ogilvy *et. al* simulated roughnesses that correspond to exponential and

gaussian autocorrelation functions in [15]. They found that small-scale rough-ness is best described by exponential ACFs, while a gaussian ACF either describes an interface with fewer small-scale features, or an exponentially-varying ACF that is undersampled (and thus obscures the small-scale features).

For this reason, we will use an exponential autocorrelation fit to model the correlation length, as the worst-case form of a rough interface. Additionally, Ladouceur *et al.* showed that this form provides a better fit for etched sidewall roughness [5]. We also confirmed that small-scale roughness is better-described by the exponential function in Section 2.1.1.2.

It should be noted that although $L_c$ provides a spatial parameter of the roughness, it is not as simple as a spatial period or frequency, and should not be treated as such. The correlation length is a fitting parameter used to an-alytically describe the autocorrelation of the surface roughness. If the rough surface in only the $x$ dimension is described by $f(x)$, it's autocorrelation, $R(x)$ can be mathematically expressed as so:

$$R(u) = \int_{-\infty}^{\infty} f^*(x) \ f(x+u)dx \qquad (2.1)$$

where $f^*$ is the complex conjugate, and the dependent variable, $u$, is essen-tially a spatial offset applied to the original roughness function. Since height data is not a complex number, we are effectively taking an overlap integral of the roughness, $f(x)$, with a shifted copy of itself, $f(x+u)$, over the whole range of $x$ at varying shifts, $u$. At zero shift ($u = 0$), this yields the $\sigma$ value, or standard deviation.

As the shifted copy of the roughness, $f(x+u)$, is shifted further away from zero, the overlap of the two functions decreases and the corresponding autocorrelation value drops, so our autocorrelation function (ACF) should

decrease from an initial value.

We can attempt to fit an analytical curve to this monotonically decreasing function. It has been found that exponential and gaussian functions describe surface roughness well [15]. Equations (2.2) and (2.3) show the functional form of gaussian and exponential autocorrelation functions, respectively.

$$R(u) = \sigma^2 \; exp\left(-\left(\frac{u}{L_c}\right)^2\right) \tag{2.2}$$

$$R(u) = \sigma^2 \; exp\left(-\frac{|u|}{L_c}\right) \tag{2.3}$$

The exponential prefactor, $\sigma^2$, and exponent factor, $L_c$, are fitting parameters, in that we would vary both of these values until the ACF best matches the autocorrelation of the measured data. This mathematically defines the value of $R(u)|_{u=0}$ as $\sigma^2$, the RMS roughness, as stated above.

Both of these equations define the physical meaning of the correlation length, $L_c$, in the same way. $u$ is the amount of spatial shift applied to a copy of the roughness before the overlap integral is taken, and when $u$ equals $L_c$, $R(u) = \sigma^2 \; exp(-1) = \sigma^2 \frac{1}{e}$. Therefore, $L_c$ is the the amount of spatial shift required for the overlap integral between the roughness and a shifted copy of itself to drop by $1/e$.

According to [15], the ACF will tend to fit to an exponential when more high-frequency components are included, and will tend towards a gaussian shape as the roughness is smoothed out - either because the roughness is physically less sharp, or because it is being undersampled/averaged by the measurement method.

As aforementioned, for a buried channel waveguide there are two distinct roughness sources:

- Interfacial *surface* roughness, due to depositions and substrate polishing, manifested as roughness in the lateral plane.

25

- *Sidewall* roughness due to etching or liftoff after lithography, creating roughness in the vertical direction.

Each of these sources of scattering loss contributes different portions towards the total loss, due to the vastly different values of $\sigma$ and $L_c$ found in each case. Figure 2.1b illustrates the physical difference between sidewall and surface roughness, and it should be noted that the latter is created via deposition and/or wafer polishing, while the former results from an etch or lift-off. Typical parameters for these contributions are given in Table 2.1. Surface and sidewall roughness can both be measured directly using atomic force microscope (AFM), as shown by [6], although sidewall roughness measurements can be quite difficult to obtain with this method.

The surface roughness of a film is highly dependent on the deposition method, so these measurements can be found in Section 3.2.1:*Atomic Force Microscopy of Surface Roughness* on page 77.

**Table 2.1:** *Typical roughness quantification parameters*

|  | $\sigma^2$ Range | $L_C$ Range |
|---|---|---|
| Sidewall Roughness | 3 nm – 10 nm | 50 nm – 60 nm [7] |
| Surface Roughness | 0.1 nm – 0.7 nm | 20 nm – 50 nm |

If our waveguide core were perfectly square, the fundamental mode would have equal field along the horizontal and vertical surfaces and only the actual roughnesses of these interfaces would cause a difference in the amount of power lost to either interface, which would lead to the sidewall scattering loss contribution being considerably higher than the surface roughness loss. In this case it is clearly advantageous to reduce the height of the sidewall, as that should reduce the amount of loss incurred by the larger roughness. If we

define the aspect ratio of the waveguide as *width* : *height*, then we can say that a high aspect ratio waveguide will reduce the significant losses incurred by sidewall roughness.

This intuitively leads us to the conclusion that, due to the realities of roughness creation in fabrication, a planar waveguide should be much wider than it is tall to lower the losses due to sidewall roughness. We can confirm this by simulating various core geometries and core confinements (index contrasts).

Payne & Lacey derive an analytical expression for the loss due to roughness, using the method of equivalent currents that that allows the guided mode overlap at a rough interface to coupled to radiation modes[4]. The method is reduced to a two dimensional system for sidewall scattering only, and derived for both exponential and gaussian ACFs. Ovilgy *et al.* showed that an exponential ACF is most accurate for describing small-scale roughness, while the gaussian ACF likely represents undersampling of the real surface roughness [15]. The result of Payne & Lacey's derivation for an exponential autocorrelation fit is as follows:

$$\alpha(cm^{-1}) = \frac{\sigma^2}{\sqrt{2}k_0 d^4 n_1} g(V) f(x,y) \qquad (2.4)$$

Where $\sigma$ is the roughness standard deviation and $g$ & $f$ are parameters of the waveguide design that describe the modal field at the interface and the modal interaction with the roughness length-scale via $L_c$, respectively. $g(V)$ and $f(x,y)$ are given by:

$$g(V) = \frac{U^2 V^2}{(1+W)} \quad and \quad f(x,y) = \frac{x\sqrt{\sqrt{(1+x^2)^2 + 2x^2\gamma^2} + 1 - x^2}}{\sqrt{(1+x^2)^2 + 2x^2\gamma^2}} \qquad (2.5)$$

Where

$$x = W\frac{L_c}{d} \ , \quad \gamma = \frac{n_2 V}{n_1 W \sqrt{\Delta}} \ , \quad \Delta = \frac{n_1^2 - n_2^2}{2n_1^2} \qquad (2.6)$$

And the normalized waveguide parameters are given by:

$$U = d\sqrt{n_1^2 k_0 - \beta^2} \ , \quad V = k_0 d\sqrt{n_1^2 - n_2^2} \ , \quad W = d\sqrt{\beta^2 - n_2^2 k_0} \qquad (2.7)$$

As aforementioned, these equations only allow for a 2-dimensional waveguide to be defined (defined in the lateral and propagation directions only). We can reduce our real, 3-D waveguide (with a 2-D cut-through index profile) into the necessary lateral 1-D index profile by utilizing the effective index model, which is well described by Coldren & Corzine [9] (although originally developed much earlier). We can deconstruct the 2-dimensional buried-channel cut-through profile into two cases of slab waveguide propagation and model each type of roughness scattering separately. In one case we assume the waveguide is of infinite height, and is thus a slab waveguide (on it's side), with a simple analytical expression for the modal index of the resultant mode, $n_{eff}$. This value can be used as the refractive index of the 1-D core, the edges of which represent the sidewalls.

Since the claddings to the left and right of the core are all uniformly SiO$_2$, the lateral 1-D claddings will simply have the refractive index of $n_{clad} = n_{SiO2}$ (since we can't solve for a slab waveguide in these homogeneous regions). These refractive indices are readily plugged into the Payne and Lacey model, above, to yield an approximate sidewall roughness scattering loss.

Then to calculate the surface scattering loss, we can make use of the previous intuition that a high aspect ratio ($width >> height$) is desirable. If the waveguide is much wider than it is tall, we can assume that the surface roughness loss can be estimated if we simply extend the width to infinity and use the resultant two dimensional system to describe our horizontal surfaces, with the original $n_{core}$ describing the high-index slab.

This allows us to de-couple these two scattering loss contributions, surface

roughness scattering and sidewall roughness scattering. Figure 2.3 shows that for a rectangular core geometry of 500 nm x 3000 nm with varying $n_{core}$ embedded in silica claddings ($n_{clad}$=1.46), sidewall scattering dominates the losses. Typical roughness parameters were chosen for each interface. Reduced modal confinement with decreasing $n_{core}$, and the resulting reduction in mode field overlap with the roughness interfaces, results in lower scattering losses.
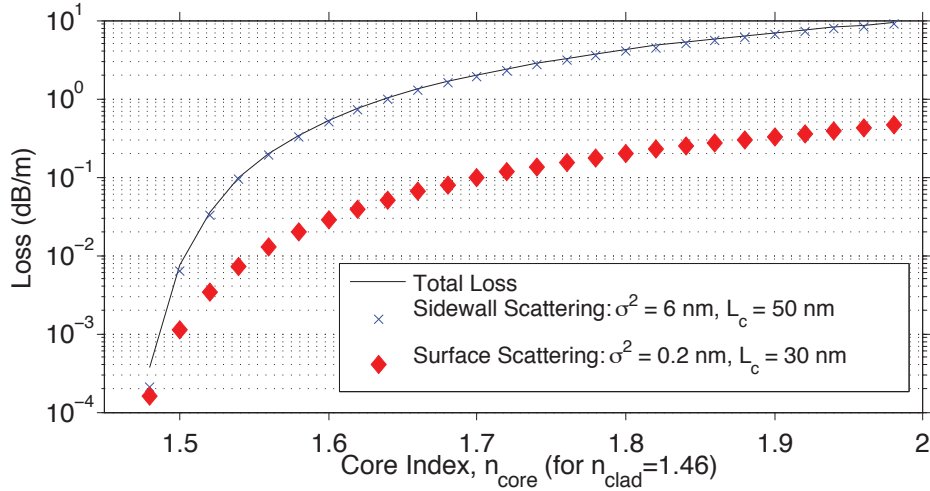


**Figure 2.3:** *1-D simulations showing that sidewall roughness contributes an order of magnitude more to total waveguide loss at most optical confinement levels for a rectangular core of 500 nm x 3000 nm. The core indices plotted reflect the typical range of refractive index for $SiO_xN_y$, from $n_{clad}$ at n=1.46, up to $n_=1.997$.*

To verify the concept of high aspect ratio for reduced sidewall scattering, simulations for a high-index contrast ($n_{core}/n_{clad}$=1.99/1.46), 100 nm core with varying width are shown in Figure 2.4, with the same roughness parameters. This shows that the fundamental mode experiences lower scattering for increasing widths. The surface scattering simulation is less accurate for narrow widths in this case, as the 2-D method extends the width to infinity

29

in that case. The fact that surface scatter appears constant with width is a result of this inaccuracy with the 2-D technique.
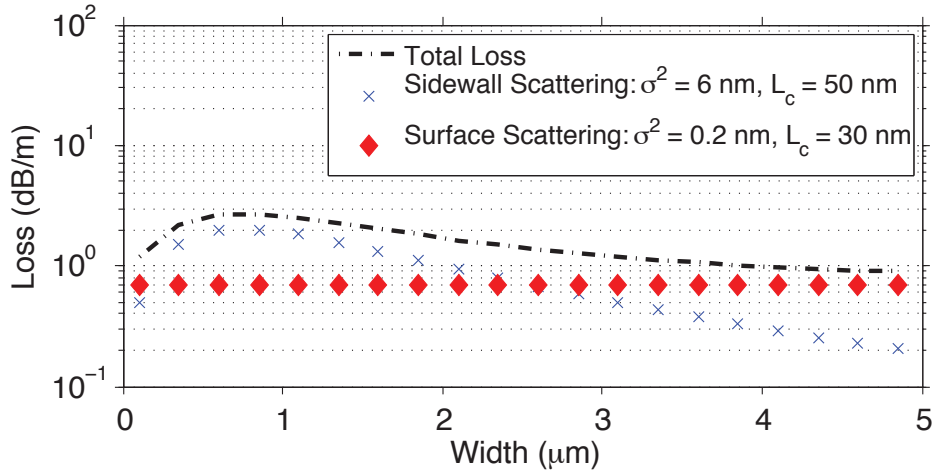


**Figure 2.4:** *1-D simulations of scattering loss versus core width for the fundamental mode of a high aspect-ratio, high index contrast geometry. Simulations used 100 nm thick $Si_3N_4$-cores waveguide, with $n_{core}/n_{clad} = 1.99/1.46$.*

More recently, Barwicz & Haus developed a 3-dimensional scattering loss model in [10], that models the sidewall roughness as radiating antennas (equivalent current sources) that enable guided modes to couple to radiation modes. The primary benefit of their technique over that of Payne & Lacey is that one can utilize a 2-D guided mode, as opposed to requiring approximation of a 1-D mode profile. Thus field values at each point along the rough surfaces will be much more accurate.

Simulations performed with the 3-D model confirm that sidewall roughness contributes much more to the total scattering loss at most index contrasts, as shown in Figure 2.5.

The 3-D technique vastly improves the accuracy for variations in core width as it obviates the need to assume an infinite slab for surface scattering
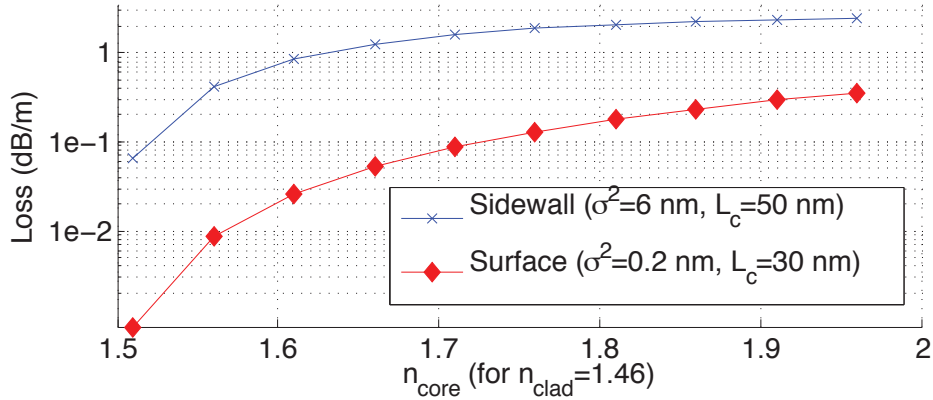
**Figure 2.5:** *3-D scattering model, showing a similar trend as the Payne & Lacey model. The same geometry as Figure 2.3 was used.*

loss calculation. Figure 2.6 shows that, as expected, very small waveguide cores show small scattering losses due to the "squeezed-out" mode – ie. low core confinement (mode profiles are shown in Figure 2.7). As the width is increased, the modal overlap with roughness increases up to a point, with maximum power confinement and highest loss for a 1 µm x 100 nm core, similar to the previous simulations. As the core width is further increased, the power is distributed over a larger area and sidewall scattering drops, but surface roughness increases as that length is increased - which was not accounted for in the previous analytical method.

A high *width* : *height* aspect-ratio is advantageous, and low confinement can be used to reduce both contributions by using even thinner cores than simulated here.

Calculation of the 2-D mode using an eigenmode solver does take considerably longer than the analytical expressions of Payne & Lacey with the effective index technique – the index sweep of Figure 2.3 took only a few seconds, while the same with eigenmode calculations in Figure 2.5 took about an hour. Large parameter sweeps, although possible with the 3-D method,
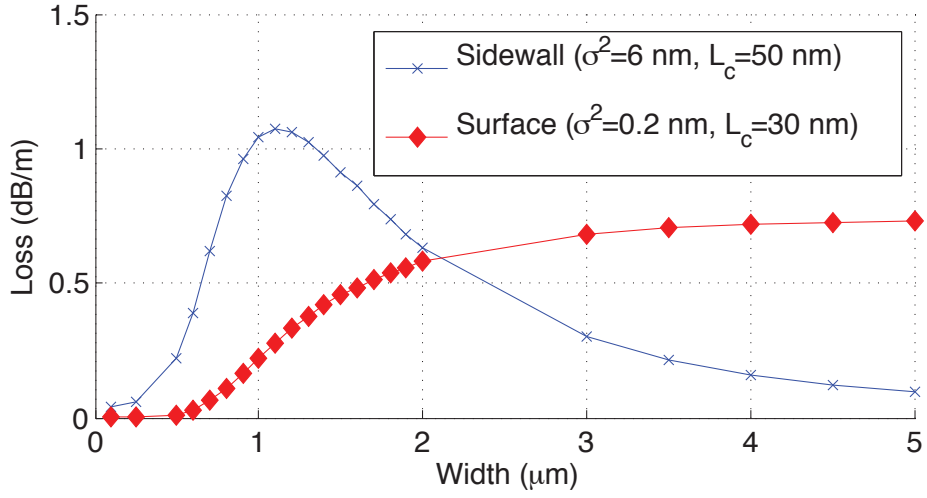
**Figure 2.6:** *3-D scattering model vs. width, for same parameters as Figure 2.4, with greater accuracy due to calculation of a 2-D mode profile.*



(a)                    (b)                    (c)
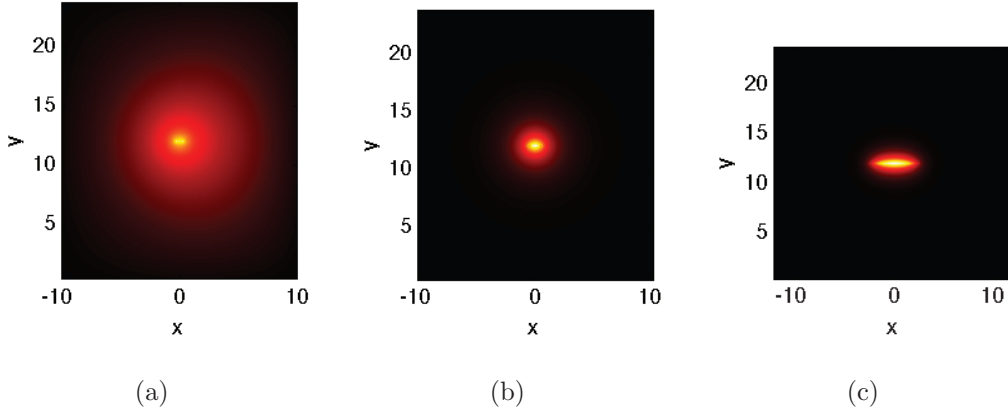
**Figure 2.7:** *(a) Fundamental Mode Profile for $n_{core}/n_{clad}$=1.99/1.46, thickness = 1.0 µm and widths of 0.50 µm, (b) 1 µm and (c) 5 µm. All axes are in microns.*

thus require large amounts of time and many computers to cover the whole design space. The analytical method is thus very helpful for rapid generation of qualitative plots.

This 3-D technique also allows one to predict the difference in scattering of
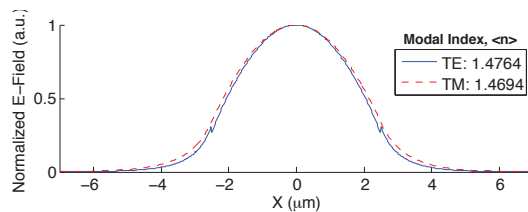
**Figure 2.8:** *Vertical slice-through of mode profiles simulated with finite-difference show that the TM mode is slightly larger than the TE mode, leading to lower effective modal index (from higher overlap with the low-index cladding). The geometry simulated here is 5µm x 0.40 µm, with core/cladding indices of 1.596/1.448.*

the TE & TM modes with greater accuracy, and investigate the polarization dependence of scattering loss.

To apply the definition used by Barwicz & Haus, the TE mode is that with the electric field oriented horizontally (perpendicular to the sidewall), and the TM mode is that with the electric field oriented vertically (parallel to the sidewall).

With this model, they show that the TM mode will interact more strongly with the rough sidewall, as the $\overrightarrow{E}$ field in this case oscillates in parallel with the vertical, columnar sidewall roughness (given an identical size for each mode).

However, even though the TM electric field interacts more strongly with sidewall roughness, the TM mode is also less tightly confined than the TE mode for high-aspect ratio geometries (Figure 2.8), and this lower confinement can actually reduce the scattering loss by reducing the field at the rough sidewall.

### 2.1.1 Measurement of Sidewall Roughness

RMS roughness, $\sigma^2$, is an extremely common measurement of surface roughness, and is automatically calculated by most Atomic Force Microscope software packages. This is always for a 2 dimensional flat surface area, not for the edge of photoresist or a sidewall, as shown in Figure 2.1. In this section I describe methods used to extract the roughness of the sidewall only, which, if viewed from the top of the device, is a one dimensional line. The roughness of an edge in one dimension is typically referred to as the *Line Edge Roughness*, although this usually assumes that the entire feature varies in this way. (*Line Width Roughness* on the other hand is a 2-D indicator of the random width variation of a line.) We will define Line Edge Roughness, or LER, as the standard deviation of height data along a single 1-D edge with respect to a straight line.

In this section I describe methods to measure the $\sigma$ & $L_c$ of a sidewall during the fabrication process.

Obtaining physical values of sidewall $\sigma$ & $L_c$ is extremely helpful for two reasons: 1) for quantifying lithography and etch quality of a particular fabrication process, and 2) for obtaining the parameters necessary to simulate the losses for that process. Ideally we could verify the scattering loss model & simulations by correlating physical loss measurements to roughness measurements. Additionally we could simulate what level of roughness is necessary to obtain some target loss, and proceed to optimize the fabrication process until it meets that quality.

In the following sections I will describe the methods we have used to obtain the roughness parameters of our lithography and etched sidewalls. I investigated top-down Atomic Force Microscopy (AFM) and Scanning Electron Microscope (SEM) techniques for acquiring images that can be analyzed

to extract the 1-D line-edge. Measurement of 2-D surface roughness parameters is detailed in Chapter 3 on page 64.

It is necessary to specify some requirements for the acquired images. The nature of optical delay waveguides is such that long-range variations (on the order of or greater than the optical wavelength) and nano-scale roughness (much smaller than the optical wavelength) are both important. Thus it is important that the pixel-to-pixel resolution of the acquired image be sufficiently small to a sample the nano-scale roughness.

At the same time, accurate calculation of correlation length requires a very long dataset. Since $L_c$ is generated via an overlap integral between the line-edge and a shifted copy of itself, the longer the dataset, the more the physical roughness will be averaged out of the resulting curve. A short dataset will show oscillations away from zero shift due to the actual bumps in the line-edge strongly influencing the overlap integral, while a very large dataset of random roughness will average out the random roughness fluctuations, resulting in a smoother autocorrelation (AC) curve. Consequently, the shorter the dataset, the closer to $u = 0$ the oscillations will begin, causing the analytical autocorrelation function (ACF) to deviate from the measurement more quickly.

To illustrate this effect, we took a 2-D AFM surface scan and unravelled it into a single, long line of height data, producing a very long dataset of 262,143 points over ~1.23 mm. Figure 2.9a shows the ACF calculated for this huge scan length, exhibiting a relatively smooth, monotonically decreasing curve that can then be fit to the analytical expressions.

However, the figure shows that as the data set is truncated to smaller datasets, the ACF begins to become less smooth, which would make curve-fitting less accurate. This is because the overlap integral of (2.1) is beginning

35
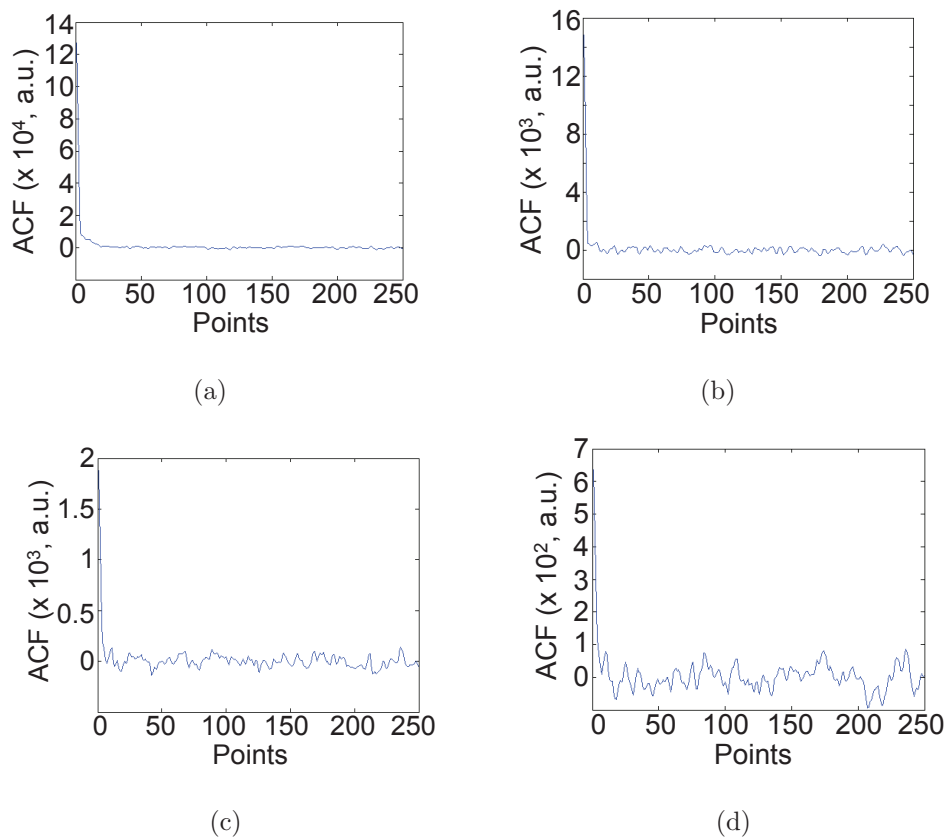
**Figure 2.9:** *(a) ACF as calculated for a large, unravelled, AFM surface scan dataset with 262,143 points, and (b) with the data set truncated to 32,767 points, (c) truncated to 4,095 points and (d) 1,023 points. As the dataset size is reduced, the overlap integral shows more of the actual measured roughness in the resulting ACF. Courtesy Wenzao Li.*

to show the actual roughness of the surface, $f(x)$, while a very large dataset allows the random roughness fluctuations to cancel each other out, smoothing the resulting ACF curve.

Since a reduced scan size causes the bumps in the CF curve to encroach closer to zero, where we are trying to fit our analytical ACF, we can assume that a scan size smaller than this will reduce the accuracy of the $L_c$ curve-fitting, although quantified uncertainty is unknown. With this in mind, it is important to acquire images over a long enough length-scale to obtain accurate ACF fits.

Ogilvy & Foster performed a thorough numerical investigation into the effect of dataset size and sampling interval on ACF calculation [15]. They show that for a scan size about 60 times larger than the correlation length, the analytical ACF deviates from the measured AC curve after about one correlation length, concluding that the dataset length must be at least $60 \times L_c$ for reasonable estimates of the correlation length. They are specific in stating that these are only estimates of $L_c$, because exact $L_c$ calculation would require extremely large dataset lengths.

They also show that exponential ACFs will exhibit neither exponential or gaussian shapes if small-scale roughness is undersampled (or high-frequency roughness is smoothed out). In order to ensure that the exponential ACF component is accurately sampled, it is stated that the sample size (distance between datapoints) should be $\frac{1}{10}^{th}$ of $L_c$.

Both of the above requirements indicate that some prior knowledge of $L_c$ is necessary. From Ciminelli *et al.*'s comparative investigation in [7] we can see that typical $L_c$'s range from tens of nanometers up to ˜50-70 nm for etched waveguides.

Combining the aforementioned requirements, we arrive at the following

requirements: a line-edge measurement length of 3-5 µm or greater, and a data spacing/resolution of 2-5 nm or smaller. These requirements happen to be right at the limits of typical nano-scale metrology methods. For both of the utilized methods, SEM & AFM, the tools perform raster scans, with quick scans along a single line that are repeated in a much slower perpendicular direction. To achieve a long line-edge scan, many of these lines must be concatenated, and the measurement time increases as more of these lines are requested. Both the AFM and SEM can experience image drift over long imaging scans - for the AFM this is due to thermal reasons, while for the SEM it is due to sample charging. This results in skewed images, so both methods will require stabilization of these effects, usually by simply repeating scans until drift is minimal.

#### 2.1.1.1 SEM of Sidewall Roughness

Top-down imaging has been widely used for the characterization of LER, LWR and similar roughness parameters of photolithography and etched side-walls [16, 18, 17]. For photolithography characterization, scanning electron microscopes (SEM) are widely used, with some commercial SEMs even providing edge roughness analysis for this purpose. The imaged edge is analyzed with edge detection algorithms, such that RMS roughness ($\sigma^2$), correlation length ($L_c$) or roughness power spectrum can then be calculated.

At the UCSB Nanofabrication Facility we used an FEI XL-30 and a JEOL 7600F FESEM to acquire top-down SEMs of photoresist and etched sidewalls. In either case the sample being imaged is a dielectric and can acquire a significant electric charge, which causes image drift and distortion when imaging with electron beams.

In an effort to enable the measurement of "live" samples that will be

made into waveguides after roughness measurement, a technique was used that reduces sample charging called the "gentle beam" mode on the JEOL 7600F FESEM. This mode applies a negative bias to the sample, such that a low imaging beam acceleration can be used to reduce charging, while the bias maintains a high signal-to-noise ratio by causing higher electron reflection off of the sample. In addition to preventing the damage of live samples (via Au/Pd coating), even metal coated photoresist still exhibits some drift due to charging, so this technique is applicable also to sample that can be destroyed for inspection.

Figure 2.10 shows the top-down sidewall roughness of a chromium hardmask, which will mask an ensuing silica etch. The scan was obtained with no conductive coating via the use of "gentle beam" mode. Sample charging is reduced via the use of a low accelerating voltage of 1kV, which results in a very poor signal to noise ratio. To compensate, the reflection of electrons off the sample is increased by applying a 2 V bias to the sample stage (this is the function of gentle beam mode). To further reduce any charging artifacts, a low-angle backscatter detector may be used, although in this case the standard secondary electron detector was adequate. Lastly, the fast scanning axis (usually left-right on the software) should be perpendicular to the line-edge, such that charging effects are minimized and will stabilize over the course of the scan - although the top and bottom of the image must typically be removed prior to analysis to remove the curvature form charging.

To reiterate, the fact that a gaussian best describes the ACF indicates that roughness much smaller than the correlation length is not being captured, either because the edge does not contain small-scale roughness, or more likely because the SEM is undersampling, smoothing out, or otherwise unable to image smaller scale roughness. However, the long-scale informa-
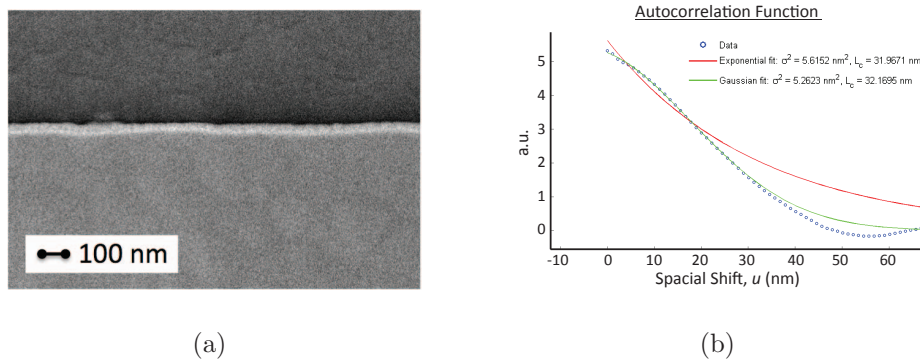
Figure 2.10: *(a) SEM of the etched sidewall of a chromium hard mask for an SiO$_2$ deep-etch, with 1.88 nm pixel and 2.41 µm scan sizes. (b) Corresponding ACF (circles) and analytical curve fits (lines). Courtesy of Wenzao Li.*

tion obtained via SEM does allow for a reasonably accurate correlation length determination, while the RMS value could be inaccurate due to this effect.

### 2.1.1.2  AFM of Sidewall Roughness

To obtain the small-scale roughness data, atomic force microscopy can be utilized, also from a top-down measurement. Jang et. al and others have landed AFM tips on the etched sidewalls of waveguides by tilting the samples or using custom probes, but these are typically destructive techniques that require dicing or cleaving the sample [19].

The standard tapping-mode AFM parameters on the Nanofabrication Facility's Digital Instruments Dimension D3100 provide a tip oscillation of a few microns, so a 1µm thick resist or 100 nm etched core is relatively easy to measure without damaging the sample or AFM probe tip. The drawback is that AFM can not acquire high-resolution (sub nanometer) scans over areas larger than a few microns on a side without excessively long scan times (which then suffer from drift). So we can obtain $\sigma$ values, but not $L_c$ due to

the requirement that the scan length being about 50 times larger than one correlation length.

Similar to the SEM scan, the line-edge must be parallel to the slow-scan axis (ie. oriented top-to-bottom on the scanning software) to ensure that parachuting does not blur out the nano-scale roughness. Figure 2.11 shows the line-edge as measured by AFM, of a 0.8 µm thick photoresist. This profile shows the results of a photolithography process as optimized for sidewall roughness, feature sharpness and resolution on a Karl Suss MA-6 contact aligner, in which these line-edge measurements were used as one of the primary feedback parameters for the optimization.
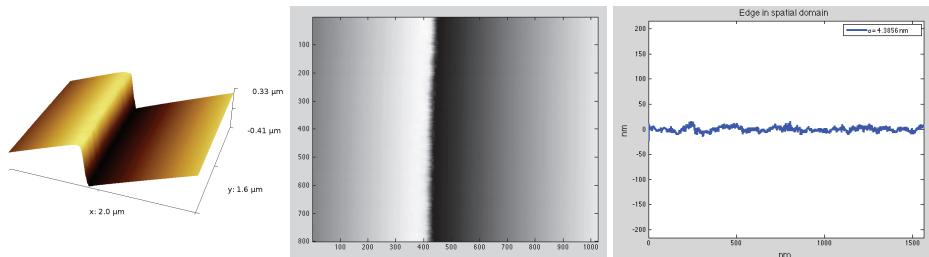


**Figure 2.11:** *Top-down AFM scans and corresponding line-edge of photoresist for contact lithography process after optimization for roughness (with no resist reflow), courtesy of Renan Moreira. The line-edge shows $\sigma = 4.4 nm$.*

Only 800 nm of line-edge was acquired in this scan, a fairly typical length, and even of that length the top 100 nm show some artificial skew. Thus we only have at best 700 nm to obtain an $L_c$ with, which in practice yields very little data to fit the ACF to - the roughness shape itself causes the ACF to deviate from the analytical equations at a fairly short a distance, as shown in Figure 2.12. Both the exponential and gaussian curves have similar fit quality, neither of which describes the ACF for more than about 150 nm, so the curve fitting was only performed from $u = 0$ to 150 nm (although the full
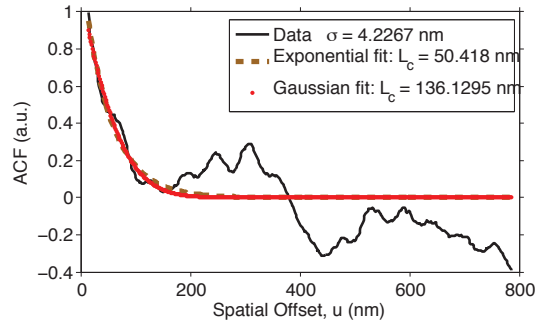
**Figure 2.12:** *Autocorrelation Function with Exponential fit for line-edge measured with AFM.*

length is plotted). If either of these values are to be used, the exponential value of 50.4 nm is expected to describe the roughness more accurately, due to the prevalence of small-scale roughness in the AFM scan, and matches well with literature values of $L_c$ for etched sidewalls[7].

As previously mentioned, the SEM method should be used for $L_c$ while the AFM method is best for $\sigma$ determination. However, since the AFM appears to more accurately sample small-scale roughness, the real $L_c$ value may be different (ie. smaller) than that determined by SEM - the actual correlation length must lie between these two values.

## 2.2 Bend Loss

In the previous section, Figure 2.3 shows that using a reduced core/cladding index contrast lowers the scattering loss. The tradeoff is that as confinement is reduced, an optical mode will experience higher bend losses for a given bend radius. If it weren't for this critical concern, one would simply reduce the optical mode confinement as much as possible, until a waveguide is barely discernible! I emphasized in Chapter 1 that consideration of bent waveguides

is of paramount importance when discussing any device that depends on waveguide losses for long delays or ring resonators.

The simple ray tracing approach to envisioning light guided in a bent waveguide illustrates this well, although the ray tracing method is not an accurate method with which to perform analysis of a system with sub-wavelength length-scales. This can be analyzed in two dimensions, eliminating the vertical direction, to elucidate understanding.

In the ray tracing method, we envision a ray of light originating from within the waveguide core that impinges upon the core/cladding interface. Snell's law predicts the refraction of light at this interface, which is given by $n_1 \, sin(\theta_i) = n_2 \, sin(\theta_T)$, where $n$ is the refractive index, $\theta$ is the ray angle with respect to the surface normal, and the subscripts indicate either of the two materials, as indicated in Figure 2.13(a). The reflection angle, $\theta_R$, is always equal to the incidence angle, $\theta_i$. The case in which the transmission angle is 90°indicates that the light be totally internally reflected and thus completely trapped within the core material. Given that the critical angle for total internal reflection is given by the case where the $\theta_T$ is 90 °, we can rearrange to give a condition of $\theta_i = sin^{-1}(n_2/n_1)$.

This shows that as the ratio of $n_2$ to $n_1$ is lowered (the index contrast is reduced), the required angle to achieve total internal reflection gets closer and closer to being tangential to the core/cladding interface, and thus a greater proportion of the impinging rays will not be totally reflected (but instead only partially reflected), and more light leaves the waveguide and is transmitted into the cladding. Thus a lower index contrast results in greater loss at a given bend radius. Conversely, to maintain a desired bend loss, the bend radius would have to get larger as index contrast is reduced. The tradeoff with bend radius is thus also a tradeoff with device footprint, as larger bend
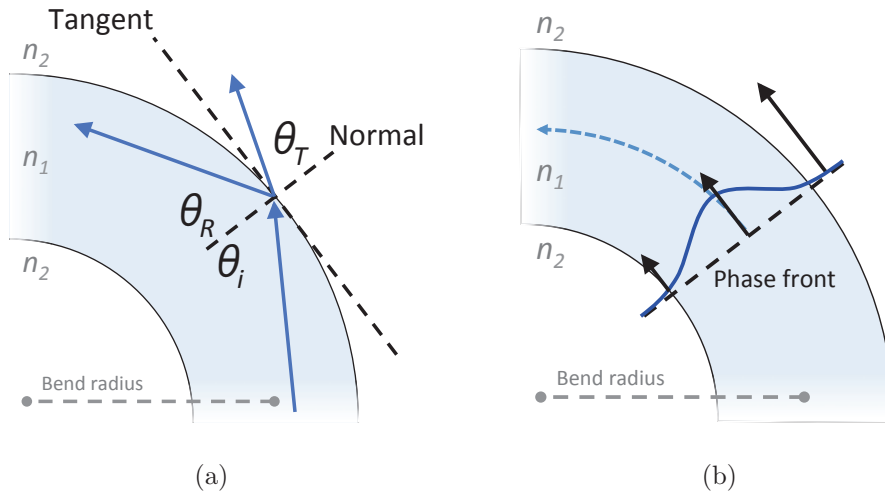
**Figure 2.13:** *(a) Ray tracing illustration of light propagating in a bent waveguide. (b) Fundamental eigenmode of a waveguide propagating through a bend, showing relative velocities of phasefront.*

radii would cause bent waveguides to take up more space. As stated earlier, the ray tracing analogy is inaccurate for waveguides of dimensions much smaller than the wavelength.

A more accurate analysis of this situation uses the characteristic modes of the waveguide as solutions to the Helmholtz wave equation. An intuitive understanding of this view can be gained by considering the phase front of a mode propagating through a bend, as shown in Figure 2.13(b). In order for the phase front remain intact, the mode front further towards the outside of the bend must travel a longer distance than those at the inside, and thus must travel faster. At some radius sufficiently far away from the center, $r_{critical}$, the front would have to travel faster than the speed of light in the cladding material, $v_p = c/n_{clad}$, which is not considered possible. We can consider any part of the mode field that is beyond $r_{critical}$ to break away from the mode front and radiate into the cladding [9].
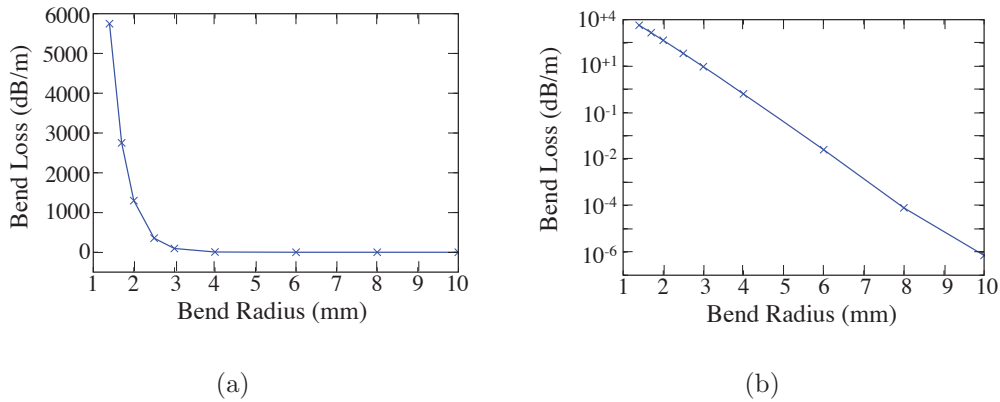
**Figure 2.14:** *(a) Propagation Loss vs. Bend Radius for conformal index transformation method and, (b) for Loss vs. Bend Radius on a log scale.*

Because the waveguide mode is composed of a continuously decreasing exponential tail in the cladding (extending to infinity), we can see that there will *always* be some amount of bend–induced loss. However, as the bend radius is reduced, $r_{critical}$ decreases, encompassing more of this exponential tail, and so the amount of power radiated increases with an exponential dependence. Thus a plot of loss (in dB) versus bend radius shows a dramatic increase in the bend loss at some critical bend radius, as shown in Figure 2.14.

Since there is theoretically always some loss associated with bend radiation, choice of an appropriate bend radius necessitates selection of a target loss value first. For example, in Figure 2.14, the bend loss appears to increase dramatically at about a 3000 µm radius, and a designer may be tempted to simply choose any bend radius larger than 3000 µm. However the log plot shows that there is still a radius-dependent loss in the large bend radius region. If a designer targets 0.01 dB/meter loss, then a radius of greater than 6000 µm would be required.

It should be noted that the method of Coldren & Corzine does not account for the observation that an optical mode in a bend will actually shift

towards the outside of the bend, unlike Figure 2.13 which shows the mode perfectly centered within the core. In reality the guided mode of a bent waveguide actually propagates laterally shifted from the waveguide core. A more accurate method with which to simulate bend losses is to perform a transformation of the lateral refractive index profile [12, 13]. This method, which we used to simulate our bending losses in Figure 2.14, states that the refractive index profile in the lateral direction can be skewed in order to accurately reflect the effect of the bend. This conformal index transformation was applied as described in the paper to the refractive indices in discrete slices, such that the skewed index is really described as a staircase index. The freely available 2-D simulation software CAMFR was used to solve for the guided optical mode of the resulting index profile, using the field mode matching method [14]. The loss of the mode due to bending was found by applying perfectly matched layers to the simulation boundaries, such that any optical power radiating away from the simulation space would result in an imaginary part of the mode's effective index, and this imaginary effective index was then used to calculate propagation loss.

This indicates that lower confinement designs will incur larger bend losses, as shown in Figure 2.15 where the simulated bend loss increases from effectively zero ($10^{-11}$ dB/m) to a few dB/m when the core index is lowered.

Heiblum & Harris state in [12] that another intuitive way to think about the loss incurred by the conformal index transformation is that the field in regions where $n_{clad} > n_{core}$ will be radiated, which is illustrated by the dashed lines in Figure 2.15.

It should be noted that the choice of bend radius is influenced greatly by the available fabrication area and required waveguide length, not solely propagation loss. These tradeoffs in design will be discussed in Section 2.4.

46
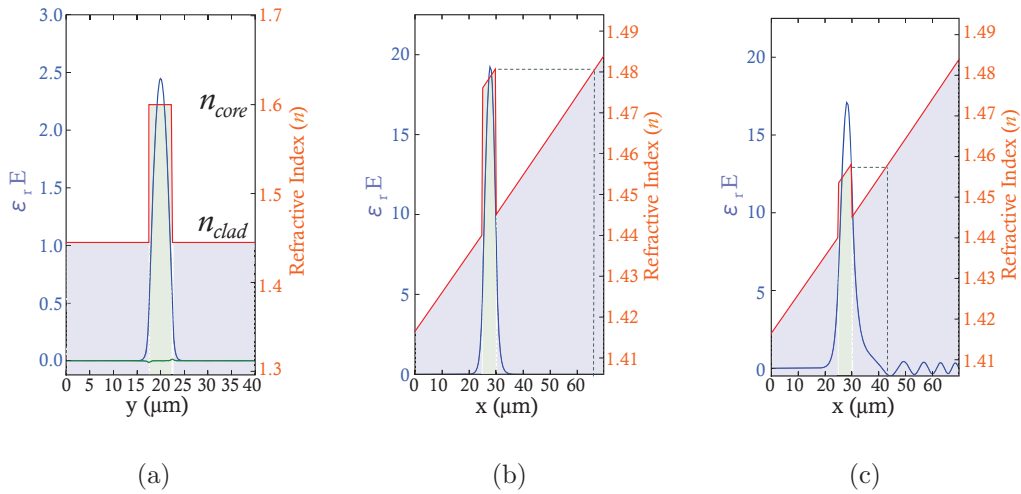
**Figure 2.15:** *(a) The initial step-index profile (red) of a channel waveguide, in the lateral direction, for a 5 µm x 0.400 µm core of $n_{core}$ = 1.600. The E-field of the guided TE mode is shown in blue. (b) The same structure at a bend radius of 1.5 mm, with very low simulated losses due to bending (effectively zero). (c) For lower confinement, with $n_{core}$ = 1.535, the bend loss increases to 8.67 dB/m.*

## 2.3   Substrate Leakage Loss

The part of our waveguide structure that has so far been unaccounted for is the substrate on which the various glasses will be deposited, and the air above the core. The lower cladding separates the substrate from the core, and the upper cladding separates the core from atmospheric air. Due to the high purity of commercially available silicon, the use of thermally oxidized silicon as cladding oxide is preferred over, say, glass substrates. The quality of these substrates will be investigated in Chapter 3.

The drawback to using silicon as a substrate is that it has a high refractive index of ~3.4. Thus any optical power that overlaps with this high index will preferentially couple into it, and into a substrate mode.

47

Since the modes of a channel waveguide always have power extending into the cladding (via the exponential tail of the mode profile), in theory infinitely (although decreasing exponentially), an appropriate lower cladding thickness is dependent on the desired losses, and of course the modal confinement. In other words, there is always some power extending beyond the claddings, and we must choose how much power loss is acceptable in order to design the correct cladding thickness.

Figure 2.16 (a) shows the vertical mode profile for a high aspect ratio waveguide with 10 µm upper and lower claddings. The plot shows the refractive index (red line) versus $x$, where smaller $x$ is up such that air (yellow) is at $x < 0$ µm; the silicon substrate (grey) is at $x > 25$ µm; the core is a very thin 50 nm at $x \approx 10$ µm and the blue regions are cladding oxide. The vertical electric field profile is overlaid in blue, clearly showing the exponential tails of the mode profile, and always interact with both the air and substrate interfaces at some magnitude. The waveguide core is 50 nm x 6.0 µm, with core/cladding indices of $n_{core} = 2.001$ & $n_{clad} = 1.447$, typical refractive indices for $Si_3N_4$ and $SiO_2$.

Figure 2.16 (b) shows the effect of a thinner lower cladding, in this case reduced to 5 µm. At $x > 15$ µm this clearly shows increased magnitude of the field that radiates into the substrate, although it should be noted that this effect is also present in (a) with magnitude too small to see on the plot.

The upper cladding serves to protect the guided mode from dust and other atmospheric variables, allowing for a robust structure. Since the refractive index of air is very low, at $n_{air} \approx 1$, the field that extends into this material will not leave the guided mode, as the air also acts like a cladding material. However, as shown in (b), the field can interact with dust particles or other contaminants that become introduced to the surface of the device through

48
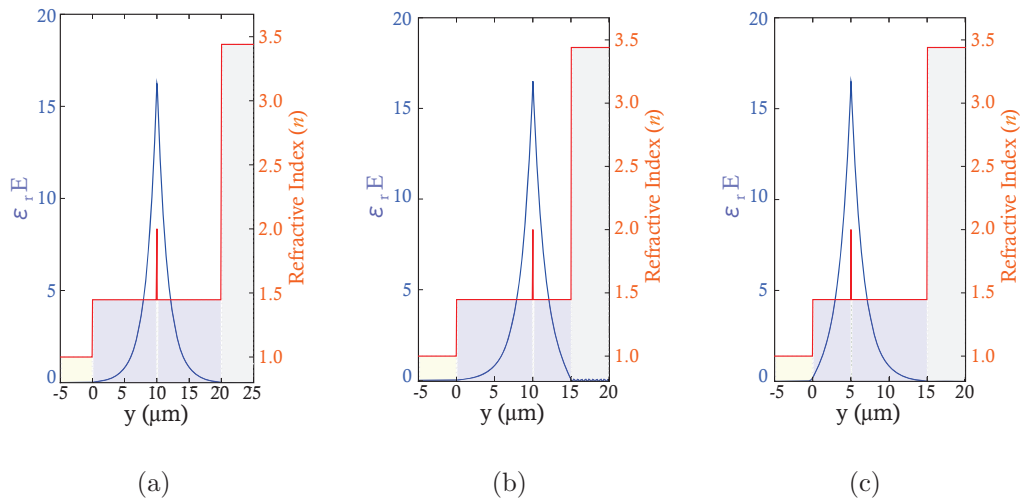
**Figure 2.16:** *(a) Vertical mode profile for 10 µm Upper & Lower Claddings; (b) for reduced Lower Cladding of 5 µm; (c) for reduced Upper Cladding of 5 µm.*

the evanescent tail extending beyond the upper cladding surface.

However, the upper cladding has a more subtle effect that can yield significant propagation losses when the target loss is very low. Since there is some small amount of exponential tail that "sees" this air/cladding interface, the low index of air serves to push the mode away, closer to the substrate. This subsequently increases the substrate leakage loss. In the case of the designs simulated in Figure 2.16, the effect of a thin 5 µm upper cladding increased the substrate leakage loss by about 0.026 dB/meter in (c), while the decreased lower cladding thickness in (b) increased the loss by 149 dB/meter.

The design simulated here has a relatively low-confinement mode, and shows sub-dB/meter substrate leakage loss for 10 µm. Thus, for flexibility of design, we chose to use the mode conservative 15 µm lower claddings. The Japanese company KST World Corp. stocks thermally oxidized silicon with $SiO_2$ thicknesses of 10 µm and 15 µm. Since oxidations to these thicknesses

take 30 days or more, purchasing these wafers from a supplier that stocks them readily is a huge advantage.

Lastly, since the upper cladding has a much smaller effect, with loss increases below 0.1 dB/m for a 10 µm lower cladding, we have chosen to deposit 10 µm of upper cladding silica. This, again, is overkill, but provides for lower confinement designs without the risk of loss limiting by substrate leakage.

## 2.4 Loss vs. Bend Radius

The inherent tradeoff that the majority of PIC designers face is that a reduced modal confinement (large mode size) is needed to lower scattering losses, while a high confinement (small mode) is needed for tight bend radius. Consequently, these loss mechanisms must be simulated simultaneously to really locate the optimal design.

Utilizing the simulation tools for surface and sidewall roughness, the conformal index transformation for bend loss, and the free Field-Mode-Matching method solver found in the CAMFR package, we simulated a large range of core geometries. The tradeoff between these two loss contributions can be seen in Figure 2.17, which is only for pure $Si_3N_4$-core designs. Additionally, only single-mode waveguide geometries are plotted. Each line represents a single waveguide core geometry, simulated for Loss vs. Bend Radius ($R$). The conglomeration of all simulated designs on top of each other shows that a design is either able to achieve low losses at large bend radii, or higher losses at lower bend radii (for a given roughness).

The figure shows that as the core is enlarged, the bend-loss "knee" – the minimum bend radius at which the loss increases rapidly – does in fact move
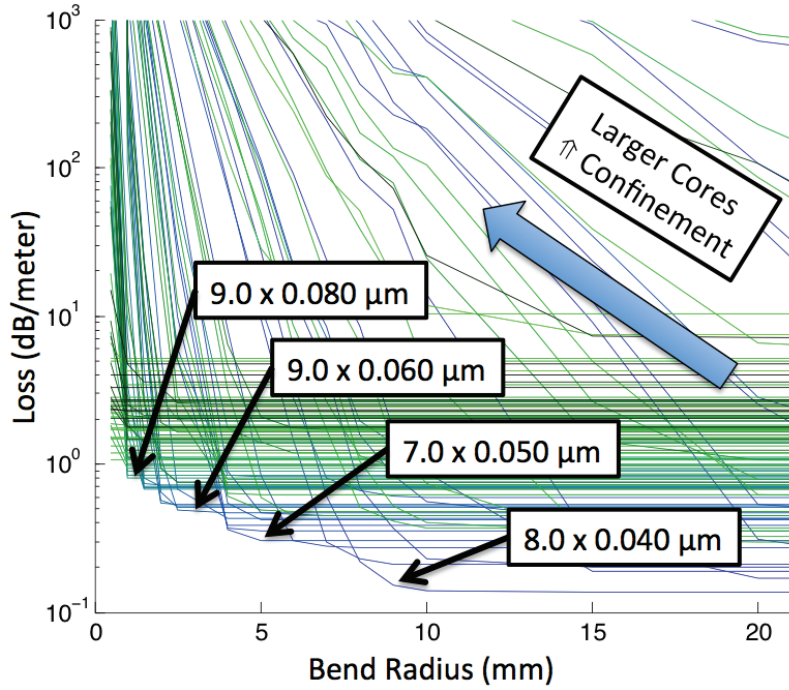
**Figure 2.17:** *Loss versus Bend Radius for a large sweep of core geometries, where each curve is a single geometry. $Si_3N_4$-core ($n = 1.9876$) and assumed surface roughness parameters of $\sigma$=0.213 nm, $L_c$=31 nm and sidewall roughness of $\sigma$=5.0 nm, $L_c$=200 nm.*

to smaller bend radii, but with a significant increase in the loss minimum, which is due to the increased scattering loss. In fact, the asymptote for every design (at $R = \infty$) is effectively the loss in the scattering-limited regime, while left of the bend-loss knee is the bend-loss limited regime.

However, simulating these effects at the same time enables the location of design optima, depending on the required bend radius (footprint) and propagation loss.

It should be noted that the minima on this plot illustrates a sort of "fundamental limit" of loss versus bend radius – but only for a single-mode, rectangular geometry with fixed roughness parameters. In reality, techniques

to improve roughness, or otherwise minimize it's effect (such as graded indices or tapered sidewalls) can overcome this Loss Vs. Bend Radius limit. Additionally, multimode geometries excited with only the fundamental mode have been show to break this limit [21, 22, 23].

In general, for a given roughness (ie. fabrication process), the lowest loss design is determined by the largest bend radius that can be used, and thus the minimum confinement necessary to achieve that bend radius.

Small-bend radii (and thus small devices) will have higher losses due to the required high confinement - the scattering-loss asymptote is higher for these small bends. A reduction in the roughness contribution will lower *all* the asymptotes on this plot, and would be the only way to achieve sub-dB/m losses at sub-mm bend radii.

## 2.5 Layout Design

The most efficient delay line configuration for a planar waveguide is an Archimedean spiral, in which the bend radius continually decreases and separation between waveguides is constant throughout the spiral, shown in Figure 2.18. About $\frac{1}{2}$ of the delay is composed of the inward spiral, with the bend radius decreasing gradually at a constant rate in the typical fashion of an Archimedean spiral. The light then enters the *s-bend* with a sudden halving of the bend radius to $R_{min}$. This inner s-bend radius will be the highest-loss portion of the delay.

To target the lowest loss possible, the largest $R_{min}$ is desired, and the layout would be specified in the following order to maximize this value:

1. Footprint constraint (as large as possible)

2. Separation between waveguides (as small as possible)
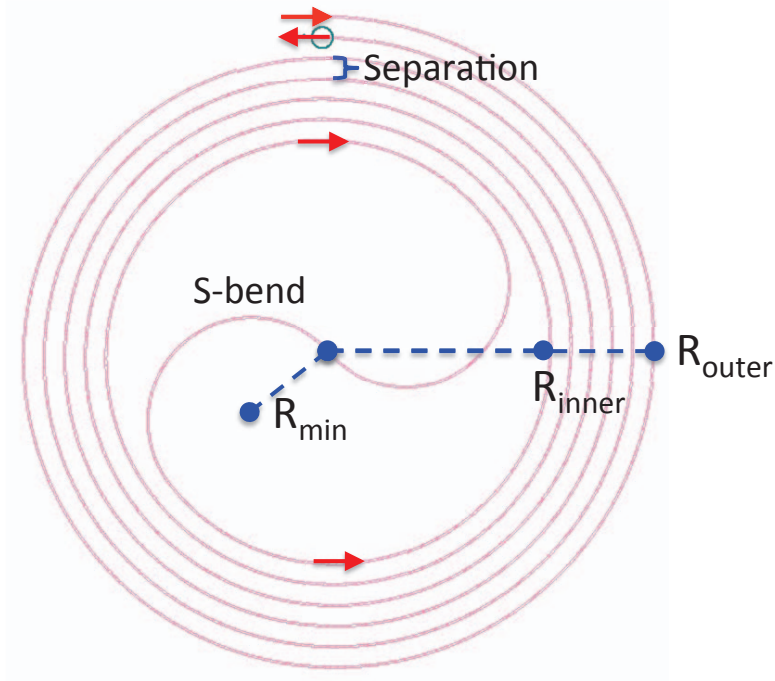
**Figure 2.18:** *Radius and Footprint restrictions on Archimedean spiral layout.*

3. Delay length

4. Minimum Bend Radius (as large as possible)

In other words, if one is most concerned with the per-unit loss of the waveguide, one should aim to layout the largest bend radii possible, especially in the central s-bend. The best way to achieve this is to build the spiral starting from the outer bends and progressing inward. Thus, one specifies the largest layout footprint, $F$, first. We chose 20 cm$^2$, which is about a centimeter smaller than the uniform fabrication area on a circular 4-inch wafer (10 cm).

The outer bend radius for this circular footprint is then given by

$$R_{outer} = \sqrt{\frac{F}{\pi}} \qquad (2.8)$$

which, for this example, is about 25 mm.

The next parameter, waveguide separation, $S$, dramatically impacts the s-bend radius. This is especially true for a long delay, as each spiral roundtrip reduces the s-bend radius by $S$, and once each for the inward and outward spirals. For $N$ spiral roundtrips, the inner bend radius is related to the aforementioned parameters as so:

$$R_{min} = (R_{max} - N \times (S \times 2)) / 2 \tag{2.9}$$

If we can choose the separation first, then our spiral layout program can simply be written to fit the largest inner bend radius possible.

The major effect of too small a separation between waveguides would be coupling between adjacent waveguides. This is especially a concern for very long delays, where a small amount of modal overlap can be maintained for as long as meters, possibly resulting in a significant amount of coupling. Additionally, the coupling would transfer power to a retrograde spiral (in the reverse direction), since adjacent waveguides are actually guiding light in opposite spiral directions. This would not only appear as transmission loss, but also as reflected power.

Treating adjacent waveguides as simple directional couplers, Coldren & Corzine [9] use a standard coupled-mode approach to show that the coupling coefficient is described by

$$\kappa_{2 \to 1} = \frac{\int_{A_1} \left( n_{core}^2 - n_{clad}^2 \right) U_1^* \, U_2 \, dA}{\int |U_1|^2 \, dA} \tag{2.10}$$

where the subscripts denote each of the two waveguides, $U_n$ is the mode profile of each waveguide (as perturbed by the adjacent guide), and $A$ indicates the lateral area that creates the mode overlap integral. For a symmetric channel waveguide, this integral could be reduced to one dimension, the lateral direction in which the waveguides are offset from each other, and the core indices replaced by 1-D effective indices. This shows that the coupling

between guides is determined by a mode overlap of the guided modes of adjacent waveguides.

One could additionally account for the bend mode profile, which is shifted towards the outside of the bend, but since directional coupling is simply dependent on optical mode overlap, one can assume that the bend modes in adjacent waveguides will be similarly shifted, and thus the mode overlap would not be significantly different from that of two adjacent straight waveguides. So $U_n$ can be the simple 2-D eigenmode of the waveguide cross-section.

The CAMFR simulation package was used once again to simulated this system. The 2-D waveguide index profile was converted into a 1-D index profile by computing the modal index of an infinitely wide slab waveguide, and this $n_{eff}$ was used as the 1-D core index. Two cores, of the actual waveguide width, were then simulated side-by-side as shown in Figure 2.19. This example simulation shows a 4 µm x 100 nm $Si_3N_4$-core waveguides separated by 4 µm of cladding, which exhibits a coupling length of about 22 mm to transfer 100 % of the power from one guide to the other.

A multitude of these simulations were performed with varying coupling gaps. Figure 2.20 shows the length required for 0.1 dB coupling between adjacent waveguides, for two high-aspect ratio geometries. The thinner, 50 nm geometry is much less confined than the 100 nm geometry, resulting in shorter lengths that produce 0.1 dB of coupling.

Intersection with the blue dotted line (marked at 1 meter) indicates the minimum separation required for a loss of 0.1 dB/meter. For the thinner, low confinement design, we can see that a separation of 20 µm or greater is required.

To ensure complete flexibility of the waveguide design (for example, perhaps fabricating thicknesses or indices with even lower confinement), a very
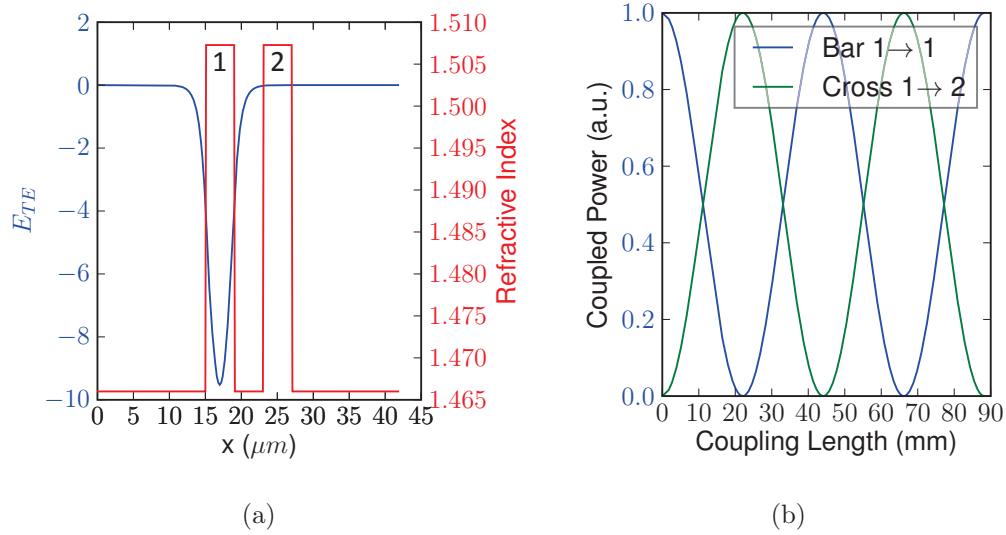
**Figure 2.19:** *(a) Index profile (red) & mode for waveguide #1 (blue) for two adjacent waveguides. (b) Power in waveguide #1 (blue) & #2 (red) versus length for a 4 µm separation.*
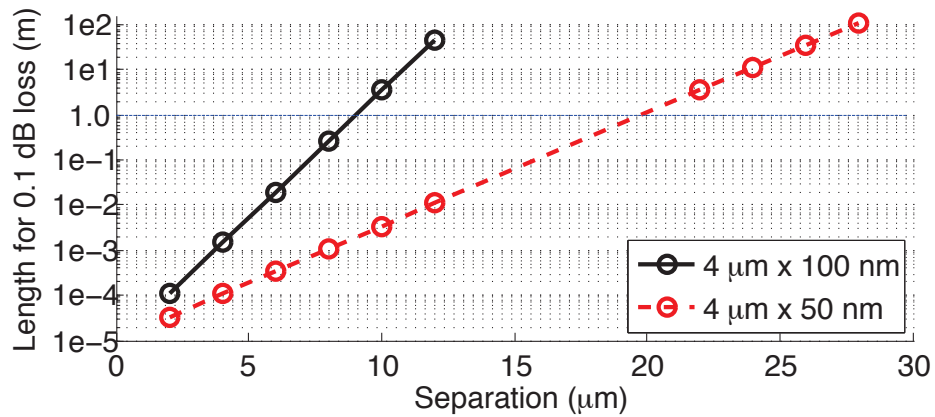


**Figure 2.20:** *Propagation length that reaches 0.1 dB of coupling between adjacent waveguides, plotted versus separation, for two high-aspect-ratio geometries ($Si_3N_4$-core).*

conservative waveguide separation of 50 um was chosen.

Choice of the total optical delay length effectively determines how many

spiral round trips are necessary, which reduces the s-bend radius due to the waveguide separation. Choice of this length mostly stems from minimizing the loss measurement error, as will be discussed in Chapter 4 (p. 106). To summarize briefly, the majority of loss measurement error stems from uncertainty in the group index, which is a result of error in the exact placement of the diced facets. As the waveguide is made longer, this facet position uncertainty becomes a smaller proportion of the total delay, and thus the length uncertainty is reduced. It is necessary to have some idea of what the loss will be to determine the desired uncertainty (and thus length), so this was done empirically with a few successive mask layouts.

Alternatively, this length may also be specified by the application of the waveguide - for example the length of a packet for an optical buffer. A reasonable packet length, including data and headers, is about 100 ns [20].

With the above three parameters specified, a layout program can now be written to generate a spiral with the maximum achievable $R_{min}$, building from the outside to the inner s-bend.

For a 20 cm² footprint, 50 µm separation and 100 ns time-delay (assuming fiber-like $n_{eff}$ of 1.5), our layout program generates a minimum s-bend radius of about 10 mm. For this bend radius, Figure 2.17 shows that, for a Si₃N₄-core, the theoretically lowest-loss, single-mode design is 8.0 µm x 40 nm. Such a geometry is very sensitive to small changes in thickness of index, which can reduce the confinement enough to dramatically increase bend loss. Additionally, the stress of deposited upper cladding oxide tends to decrease the core index via the stress-optic effect (see Section 6: *The Stress-optic Effect in Glass Waveguides* on page 190). In order to fabricate a design more tolerant to these variations, a 100 nm thick Si₃N₄-core is targeted, with a variety of widths interleaved into a 1-meter spiral. This produces about 26

meters of total waveguide with a similar 10 mm s-bend radius as a single, 26 meter spiral.

Special thanks is given to Dr. Xaveer Leijtens (of the Dutch university Technische Universiteit Eindhoven), whose turtle-graphics style C-libraries for waveguide layout made continuously varying, interleaved spirals possible.

## 2.6 Chapter Summary

Three structural waveguide losses were discussed in this chapter, namely scattering loss due to roughness, bend loss and substrate leakage loss. The optical theory behind each was shown, along with techniques upon which each loss contribution has be modeled. In doing so, one can see what design parameters have the greatest impact on each loss factor, often uncovering non-obvious effects and parameters.

Loss due to sidewall roughness originates from the random roughness produced by the waveguide core etch during fabrication. The actual roughness must be quantified by two parameters - RMS deviation from the ideal flat surface ($\sigma$), and Correlation Length ($L_c$) - the distance at which the rough edge must be shifted to reduce the overlap integral with itself by $1/e$.

We described techniques for non-destructively measuring the sidewall roughness of fabricated devices using SEM and AFM, and found that $\sigma$ is best obtained by AFM line-edge detection and that the $L_c$ likely lies somewhere in between the values obtained by the two measurements.

This loss contribution is not only dependent on the quality of the sidewall etch, but also on the optical mode strength at the rough interface. Simulations using 2-D analytical expressions for the method of equivalent currents show that it is beneficial to reduce the modal confinement, spreading out

the total transmitted power across a larger area so that a smaller proportion is scattered by the roughness. The fact that sidewall roughness is much larger, and hence a larger loss contribution, than surface roughness, naturally leads to the conclusion that designs with high *width:height* ratio will result in lower loss. 3-D versions of the simulation corroborated the benefit of the high aspect-ratio design while improving the physical accuracy.

Bend radiation loss is primarily dependent on lateral modal confinement, and increases rapidly as bend radius decreases (becomes tighter). Alternatively, the bend loss at a given radius would increase exponentially as the mode size increases. This provides the major tradeoff for reducing scattering losses, as low confinement for reduced scattering increases the bend loss dramatically. This is especially important when designing an optical delay for which the length cannot be laid out in a straight line, and is instead constrained by the dimensions of a substrate wafer. Maintaining a reasonable bend radius is also necessary for the practicality of a compact delay. In the case of long delays, the choice of bend radius involves many parameters, including the total footprint occupied, the total delay length, the separation between waveguides and maximum bend loss allowed. Simulations of the coupling between adjacent waveguides showed that waveguide separations of 20 µm or more were needed to achieve coupling below 0.1 dB/m, so we used a 50 µm separation.

For a 100 mm wafer size, laying out an Archimedean spiral with the largest bend radius within a 6 cm circle a 50 µm separation, we find that an s-bend radius of 10 mm is produced.

Substrate leakage loss was also shown to also be highly dependent on the mode field extent, although in the vertical direction only. However, this loss contribution can be mitigated without significantly affecting the others by

simply choosing an appropriate upper and lower cladding thickness. I showed that lower cladding thickness has a very strong effect on propagation loss, which is not surprising. A more subtle effect was exhibited by the upper cladding thickness, however, which served to push the mode further towards the substrate as it is reduced in thickness. The loss increase from this effect is relatively small, although not insignificant depending on the loss range targeted. An effect of these thick deposited glasses not discussed here is a change in $n$ due to the stress-optic effect. This effect will be elucidated with a novel multi-layer experiment in Chapter 6.

Simulations showed that 10 µm of lower cladding produces sub-dB/m losses, so we targeted a lower cladding thickness of 10 µm or greater.

The largest two loss contributions, scattering and bend loss, were simulated together, revealing a "fundamental limit" on the loss for a given roughness. The tradeoff between low confinement for reduced scattering and high confinement for reduced bend loss finds it's optimum at the "bend loss knee" - the design should be chosen such that the bend loss knee occurs just above the desired bend radius. Hence, the designer must specify the maximum allowed bend radius first, as this determines the lowest loss design. For our minimum bend radius of 10 mm, a high-aspect ratio design of 40 nm x 8.0 µm is simulated as optimal single-mode design for a high-index $Si_3N_4$-core. A more conservative design of 100 nm thick at many widths from 5.0 µm to 15 µm was chosen.

The asymptote of any design's Loss vs. Bend Radius curve is a result of roughness, and the "fundamental limit" can be lowered for all designs if roughness is reduced. This illustrates that the only way in which to achieve very low loss for very small bend radii (eg. sub-millimeter) is to dramatically lower sidewall roughness.

# References

[1] G. P. Agrawal, *Fiber-optic Communication Systems*, 3rd ed., John Wiley & Sons Inc., New York, NY, 2003.

[2] H. Kroemer, *Quantum Mechanics*, Prentice Hall, 1994.

[3] MARCUSE, D., "Mode conversion caused by surface imperfections of a dielectric slab waveguide", *Bell Syst. Tech. Jnl.*, Vol. 48, pp. 3187-321 5, 1969.

[4] F. P. Payne and J. P. R. Lacey, "A theoretical analysis of scattering loss from planar optical waveguides", *Opt and Quant Elect*, vol.26, pp. 977-986, 1994.

[5] F. Ladouceur, J. D. Love and T. J. Senden, "Effect of side wall roughness in buried channel waveguides." *IEE Proc.-Optoelectron.*, vol. 141, no. 4, pp. 242-248, August 1994.

[6] J. H. Jang, W. Zhao and J. W. Bae, "Direct measurement of nanoscale sidewall roughness of optical waveguides using an atomic force microscope," *J. App. Phys.*, Vol. 83, No. 20, pp. 4116-4118, Nov 2003.

[7] C. Ciminelli, F. Dellolio, V. M. N. Passaro, and M. N. Armenise, "Fully three-dimensional accurate modeling of scattering loss in optical waveguides," *Opt Quant Electron*, vol. 41, no. 4, pp. 285298, Nov. 2009.

[8] H. Park, *Silicon Evanescent Devices for Optical Networks and Buffers*, Ph.D. Dissertation, University of California Santa Barbara, 2008.

[9] L. A. Coldren and S. W. Corzine, *Diode Lasers and Photonic Integrated Circuits*, New York NY: Wiley & Sons, 1995

[10] T. Barwicz and H. A. Haus, "Three-dimensional analysis of scattering losses due to sidewall roughness in microphotonic waveguides," *Jnl. Lightwave Tech.*, vol. 23, no. 9, pp. 27192732, 2005.

[11] Bruker AXS (formerly Digital Instruments/Veeco), 2002. *NanoScope 6.13b28 [software]*, Santa Barbara, California.

[12] M. Heiblum and J. H. Harris, "Analysis of curved optical waveguides by conformal transformation," *Quantum Electronics*, vol. 11, no. 2, pp. 7583, 1975.

[13] D. Rowland, "Nonperturbative calculation of bend loss for a pulse in a bent planar waveguide," in *Optoelectronics, IEE Proceedings*, vol. 144, no. 2, pp. 9196, 1997.

[14] P. Bienstman, E. Six, A. Roelens, M. Vanwolleghem, and R. Baets, "Calculation of bending losses in dielectric waveguides using eigenmode expansion and perfectly matched layers," *IEEE Photon. Technol. Lett.*, vol. 14, no. 2, 164 166, 2002.

[15] Ogilvy and Foster, "Rough surfaces: gaussian or exponential statistics?." *J. Phys. D: Appl. Phys.*, vol. 22, pp. 1243-1251, 1989

[16] V K M Kuppuswamy *et al.*, "Contact edge roughness (CER) characterization and modeling: Effects of dose on CER and critical dimension (CD) variation." *Proc. of SPIE*, vol. 7971, pp. 79710Q-1 - 79710Q-10, 2011

[17] T. Barwicz and H. I. Smith, "Evolution of line-edge roughness during fabrication of high-index-contrast microphotonic devices," *J. Vac. Sci. Technol. B*, vol. 21, no. 6, pp. 28922896, Dec. 2003.

[18] K. K. Lee, D. R. Lim, H.-C. Luan, A. Agarwal, J. Foresi, and L. C. Kimerling, "Effect of size and roughness on light transmission in a Si/SiO2 waveguide: Experiments and model," *Applied Physics Letters*, vol. 77, no. 11, pp. 16171619, Sep. 2000.

[19] J. H. Jang, W. Zhao, J. W. Bae, D. Selvanathan, S. L. Rommel, I. Adesida, A. Lepore, M. Kwakernaak, and J. H. Abeles, Direct measurement of nanoscale sidewall roughness of optical waveguides using an atomic force microscope [J H Jang, W Zhao, J W Bae, App Phys Nov 2003], *Applied Physics Letters*, vol. 83, no. 20, pp. 41164118, Nov. 2003.

[20] J. P. Mack, *Asynchronous Optical Packet Routers*, Ph.D. Dissertation, Univ. of California Santa Barbara, 2009.

[21] J. F. Bauters, M. J. R. Heck, D. D. John, M.-C. Tien, W. Li, J. S. Barton, D. J. Blumenthal, J. E. Bowers, A. Leinse, and R. G. Heideman, "Ultra-low-loss Single-mode Silicon Nitride Waveguides with 0.7 dB/m Propagation Loss," *ECOC Technical Digest*, p. Th.12.LeSaleve.3, Jul. 2011.

[22] M. Kohtoku, T. Kominato, Y. Nasu, and T. Shibata, "New Waveguide Fabrication Techniques for Next-generation PLCs," *NTT Technical Review*, vol. 3, no. 7, pp. 3741, Jul. 2005.

[23] J. F. Bauters, M. Heck, D. John, and J. S. Barton, "Planar waveguides with less than 0.1 dB/m propagation loss fabricated with wafer bonding," *Optics Express*, vol. 19, no. 24, pp. 2409024101, Nov. 2011.

# Chapter 3

# Material Losses in Glass Waveguides

Numerous optical loss factors were discussed in Chapter 2, and some of these can be attributed to and manipulated during the production of the various glasses used in the construction of an optical waveguide. However there are additional loss mechanisms that are due to material properties at the molecular level, and in this chapter we will discuss these losses, which are commonly referred to as *material losses* in the fiber world (separated from the *waveguide losses* which stem from structural properties).

In the following sections I will discuss the relevant material loss contributors, the physics behind their effects and the associated material parameters that yield a metric of a film's quality in regards to that loss mechanism.

Surface roughness, although discussed in the previous section as it relates to scattering loss, is highly dependent on the deposition technique used. For that reason, surface roughness measurements are included in this chapter where we compare numerous deposition techniques.

### 3.0.1 Effect of Deposition Method

The roughness of a grown or deposited film is highly dependent on the specific technique used to create the desired film. The method in which deposited material is introduced to the substrate, resulting grain size and whether or not the film is conformal will play a role in the final roughness of the thin-film. One can envision the the initial particle size of a sputtered film versus the adsorption of material out of a chemical solution, as in chemical vapor deposition (CVD). The following are a few examples of deposition techniques and the way in which film roughness evolves during the process, each of which will be expounded upon in the following section.

A CVD-based deposition system is typically conformal due to the way that solid material is adsorbed out of a chemical solution (vapor) onto any surfaces in the deposition chamber. In this way, any grain or bump present on the deposition surface will then be layered upon - in this way the grain should get larger. In Section 3.2.1.1 I investigate how the deposition technique affects the measured RMS roughness by measuring roughness versus deposition thickness.

Conversely, silica on a thermally oxidized silicon wafer is produced as water or oxygen diffuses into the surface of a silicon substrate. This can be modeled as if the surface of the substrate were covered with infinitesimally small point sources of the oxidizing precursor, which then diffuse into the substrate in every direction - ie. radially. A bump on the surface of the silicon will contain radial point-sources across it's entire surface, and also on either side. Consequently the oxide/silicon interface below this bump will actually be smoothed out by the radii of point sources on either side of the bump - the oxide/silicon interface can actually be smoothed by this process. However, the air/oxide surface will still exhibit the original bump, albeit

perhaps slightly larger as dictated by the increased volume occupied by $SiO_2$ as compared with crystalline Silicon.

Yet another type of roughness evolution is seen in the sputter deposition technique. In a sputter system utilizing pure metal sputter sources, one utilizes ionized argon atoms to ballistically sputter a silicon target (for example), which creates very small particles of silicon, that also have high velocity and energy. Due to the high energy of the sputtered particles, these particles tend to travel around the surface of a substrate for a while before finally adhering and contributing to the deposited film.

## 3.1 Deposition Techniques

Knowledge of the physics behind a given deposition method can provide substantial insight into the expected impact on the various loss contributions. Thus I will discuss some specifics of each deposition tool at our disposal at the UCSB Nanofabrication facility and how each method impacts the various material loss contributions.

Table 3.1 lists some of the numerous glass deposition techniques at our disposal at the UCSB Nanofabrication Facility, each of which is discussed in the following sections.

Since predictability of refractive index, film roughness and defect density is absolutely critical for fabrication of optical waveguides, evaporation techniques have already been eliminated from our list of potential deposition techniques, although both thermal evaporators and electron beam evaporators are available at the Nanofabrication facility.

**Table 3.1:** *Deposition approaches and intended use of each film.*

| Film Type | Deposition Tool | Important Deposition Parameters | Film Use | Notes on Method/Film |
|---|---|---|---|---|
| **SiO2** | Capacitive PECVD | 250°C | Cladding | |
| | ICP-PECVD | 50°C, Ar | Cladding | Ar for cool-plasma ignition |
| | ICP-PECVD | 100°C, Ar | Cladding | Ar for cool-plasma ignition |
| | ICP-PECVD | 250°C, Ar | Cladding | Ar for cool-plasma ignition |
| | ICP-PECVD | 50°C, No Ar | Cladding | no Argon |
| | ICP-PECVD | 100°C, No Ar | Cladding | no Argon |
| | ICP-PECVD | 250°C, No Ar | Cladding | no Argon |
| | ICP-PECVD+Anneal | 50°C, Ar | Cladding | Densification Anneal - 30m @ 700°C |
| | ICP-PECVD+Anneal | 100°C, Ar | Cladding | Densification Anneal - 30m @ 700°C |
| | ICP-PECVD+Anneal | 250°C, Ar | Cladding | Densification Anneal - 30m @ 700°C |
| | Tystar WetOx | 1050°C, Wet | Lower Cladding | H2O based, but high temperature |
| | IBD - Ion-Beam Sputter | Ion-Beam Assist | Cladding | No H2 used in process, High repeatability & uniformity |
| | AJA Int'l Sputter | Biased Subtrate | Cladding | Similar to IBD, less repeatable |
| | TecPort IBD | | Cladding | external vendor |
| **Si3N4** | Capacitive PECVD | 250°C | Core | Silane – H2 content |
| | ICP-PECVD | 50°C | Core | No NH3 - Possibly lower H2 |
| | ICP-PECVD | 100°C | Core | No NH3 - Possibly lower H2 |
| | ICP-PECVD | 250°C | Core | No NH3 - Possibly lower H2 |
| | IBD - Ion-Beam Sputter | Ion-Beam Assist | Core | No H2, high stress, best uniformity & repeatability |
| | AJA Int'l Sputter | Nitrogen Atmosphere | Core | Similar to IBD, less repeatable |
| **SiOxNy** | Capacitive PECVD | 250°C | Core | Higher H2 |
| | ICP-PECVD | 250°C, No Ar | Core | Fewer particulates than Cap. PECVD |
| | IBD | | Core | Low H2 |
| **Ta2O5** | IBD | | Core | No N-H bond resonance |

### 3.1.1 PECVD

*PECVD* refers to Plasma Enhanced Chemical Vapor Deposition, which is similar to CVD in terms of the precursor gases used, but the energy to react the gasses originates from an ionizing RF source applied to the parallel plates of the deposition chamber. The RF source generates a plasma in the precursor gasses, increasing the chemical reaction rate dramatically, allowing for a high deposition rate as compared with other methods. In this work we used a PlasmaTherm 790 system with capacitively coupled plasma, which utilizes a platen heated to 250°C.

The applied RF power (at the standard 13.56 MHz for RF plasma sources [20]) is applied between the sample platen (cathode) and an upper electrode (anode), which are both 6 inches (150 mm) in diameter in this case. The platen is grounded, but still builds up some negative electric charge from

the released electrons that impact it, allowing it to charge up negatively as electrons build up on its surface (Figure 3.1a). The difference in electric potential between this charged lower electrode and the remaining positively charges ions is called the *sheath field* (Figure 3.1b), which is on the order of tens of volts in this case (much lower than a reactive ion etching system). The applied RF power creates both the reactive ion species (and resulting plasma density) and the DC bias (and resulting ion bombardment of the sample). The DC sheath field is a result of electrons being significantly lighter than the atomic nuclei, which allows them to impact and be collected by the metallic surfaces of the platen much more rapidly than the massy nuclei, which leaves a positively charged gas with respect to the platen. Even though the platen is grounded, a small sheath charge on the order of tens of volts will build up, creating some ion bombardment towards the sample platen.

The precursor gasses used are Silane ($SiH_4$) which is 98% diluted in Helium (for safety), $N_2O$, $N_2$ and $NH_4$. In terms of $SiO_2$ deposition, the gases used are silane and nitrous oxide ($N_2O$). The ionization dissociates the gaseous precursors allowing them to react into more energetically favorable configurations. The reaction takes place as so:

$$SiH_4 + 2\,N_2O \longrightarrow SiO_2 + 2\,N_2 + 2\,H_2O$$

although it has been shown that these films actually contain significant amounts of both nitrogen and hydrogen (in the form of $SiO_xN_y$ and $O-H/N-H$ bonds, respectively)[2]. This method of plasma generation is performed at relatively low RF powers (tens of Watts), which necessitates the use of these hydrogen-based precursors with low bond strengths (as compared to the double and triple bonds of $O_2$ and $N_2$, respectively).

The reaction to produce $Si_3N_4$, silicon nitride, with silane and ammonia precursors is

(a)                                    (b)
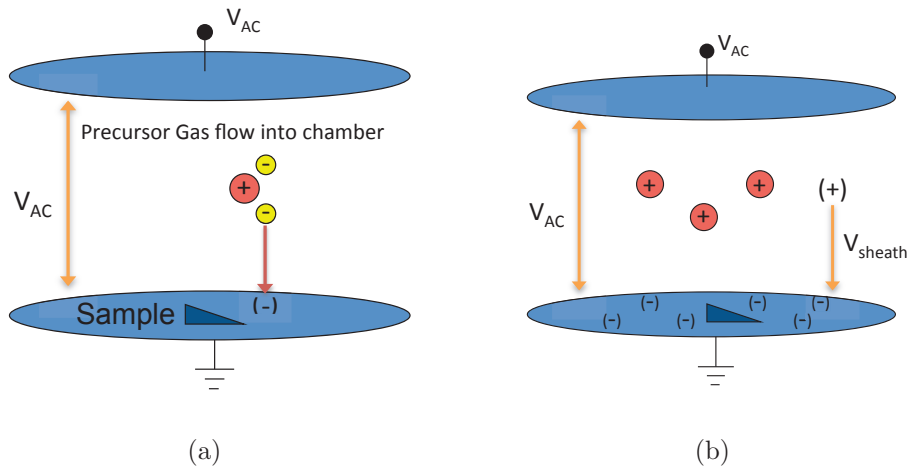
**Figure 3.1:** *(a) Precursor gasses are injected into the top electrode showerhead and ionized via an RF voltage applied to the same. Freely moving electrons are collected by the lower electrode (platen) and charge builds up. (b) The potential difference between the positively charged ionized gasses and the electrodes create the sheath field, which serves to attract the ions towards the sample platen.*

$$3\,\mathrm{SiH_4} + 4\,\mathrm{NH_3} \longrightarrow \mathrm{Si_3N_4} + 12\,\mathrm{H_2}$$

which also produces a hydrogen-rich film (often written as SiN−H). These findings were confirmed in our absorption studies, as detailed in Section 3.2.2. Both of these reactions take place on a sample platen heated to 250°C, as these higher temperatures have been shown to produce the highest quality nitrides [26].

## 3.1.2  ICP-PECVD

*ICP-PECVD* refers to a Unaxis VLR system with an inductively coupled plasma (ICP), which allows for lower pressure, higher plasma density, and independent control of plasma energy and ion acceleration towards a substrate. This results in better thickness uniformity across a wafer as compared with a capacitive PECVD. When a sample is placed directly on the capacitive plate (platen) of a PECVD system the sheath electric field strength is reduced near the center of the sample, lowering the deposition rate gradually from edge to center. In an ICP system, an RF coil outside the vacuum chamber ignites a "remote" plasma away from the platen with power $P_{ICP}$- in theory having little effect on the sample. Separately, a "bias" RF voltage ($P_{RF}$) is applied between the platen and the chamber, which serves to accelerate the ionized, reactive gasses towards the sample. The separation of ion energy and plasma density enables one to lower sample damage (roughening) while maintaining a high deposition rate, and also increases uniformity somewhat.

Compared with capacitive PECVD, an ICP-PECVD system usually couples about 10-40 times more RF power into the the plasma which makes it possible to use less complex precursor gasses. This additional power makes the dissociation of stronger bonds more probable, so even the triple bond of $N_2$ can be broken and used as a nitride precursor. So rather than using $N_2O$

70

and $NH_4$ as the oxide & nitride precursors, we used pure $O_2$ and $N_2$. Silane is still used as the silicon precursor, although it is 100% pure, and helium is added to temper the reaction (and partly just to mimic the earlier recipes used on the PlasmaTherm).

So we would expect the $SiO_2$ from the ICP-PECVD to contain no nitrogen (in contrast with the PlasmaTherm oxide), and perhaps have a lower hydrogen content (due to the lack of $NH_4$ precursor), but to still have some $H_2$ inclusions from the use of $SiH_4$. Please see Section 3.2.2 (page 87) for an investigation of the hydrogen content of these films and comparisons between the two PECVD methods.

This system is set up to deposit pinhole-free oxides using substrate temperatures of 50°C, 100°Cand 250°C.

### 3.1.3   IBD

Ion-Beam Deposition, or *IBD*, refers to a Veeco Nexus IBD-O ion beam assisted sputter deposition system.        This system is a sputter system, as shown in Figure 3.2, that utilizes two ion beams. An ion beam of xenon, referred to as the *depo* ion beam, is focussed on a 15.5" sputter target, which sputters the metallic precursor of the desired dielectric film. Simultaneously, an ion beam (the *assist* source) of oxygen or nitrogen (corresponding to oxide and nitride films) is focussed directly on the sample, which provides the second precursor for the deposited film. A silicon target is used for $SiO_2$ and $Si_3N_4$ films, although tantalum, aluminum, titanium and indium-tin-oxide targets are also available.

Sputter deposition is characterized by low deposition rates as compared with PECVD methods, and the use of the assist ion beam serves to somewhat alleviates this limitation. In fact, it is uncommon to have an ion beam impact
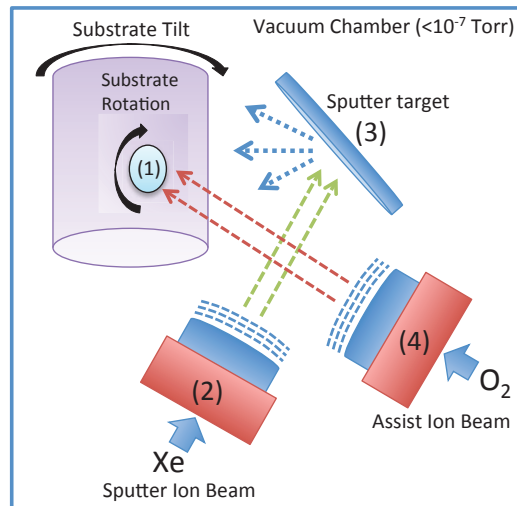
**Figure 3.2:** *Schematic of the the Ion Beam Deposition system - top-down view of vacuum chamber. The Sample (1) is tilted at 40 relative to the view-plane, and rotating at 20rpm. The Depo ion beam source (2) is focused on the Sputter target (3), sputtering Silicon particles using a Xe ion-beam. The Assist ion beam source (4) oxidizes the film with an Oxygen ion-beam.*

the sample directly in a sputter system - more commonly the metallic target is sputtered and the vacuum chamber is filled with an atmosphere of $O_2$ or $N_2$ to provide the oxide or nitride element of the film, as in the AJA sputter tool (Section 3.1.4). This single-beam method is also possible on the IBD system, but the use of the assist ion beam source increases the deposition rates by about a factor of 10 and also serves to compact the film (increasing the physical density).

The physical density of sputtered films is often claimed to be higher than other methods (such as evaporation or CVD). The theoretical reason that an IBD film has the potential to exhibit higher physical density is due to the ionization of sputtered silicon particles with ion energies greater than that of electrons on the sample surface [21].

A major benefit to the use of an IBD system in regards to optical waveguides is the simplicity of the film precursors - Ultra-High Purity (UHP) oxygen is used for the oxide precursor, and the only other gasses in the chamber are the inert gasses Xe and Ar (although these do incorporate into the film in small quanities). Consequently, in Section 3.2.2 it is shown that IBD films have an inherently low hydrogen content, especially when compared with the PECVD and ICP-PECVD methods. This low $H_2$ content is also enabled by the fact that the vacuum chamber, evacuated with both a turbopump and cryogenic molecular sieve, is pumped to a base pressure below 1E-8 Torr, often maintaining pressures below 1E-10 Torr after the chamber has been running processes for a few weeks.

Additionally, the IBD offers independent control over ion energy and ion flux via the use of acellerating grid sets to launch ions towards the sputter target and sample. The voltages applied to the grids control the acceleration of particles, while the measured current from those same grids yields infor-

mation on the number of ions passing through them. The RF power applied to the plasma can is controlled by a feedback loop which maintains the programmed current readback, such that ion flux is constant from run to run, even though the RF power may vary. However since the RF power is applied to only one gas in each ion source, and thus does not enable any chemical reaction of that gas, the RF power does not affect the film properties at all.

This separation of ion count and ion acceleration from the applied RF power is key to yielding consistent refractive indices and deposition rates for a dielectric film, as this separation is not achievable in most other plasma-based deposition methods. For example, in PECVD and magnetron sputtering, the applied RF power induces a DC bias on the platten and sputter target, respectively. The RF power controls the number of reactive ion, and thus coarsely the number of ions that form the final dielectric compound. However the DC bias provides the acceleration of ions, and is entirely determined by the number of electrons trapped on the platten or sputter target and can not be independently controlled. Thus for PECVD and magnetron sputtering, the deposition rate and refractive indices of the deposited films vary from run to run, or over time, due to the variation in this acceleration.

The contaminants that are more prevalent in IBD films are metals, which originate from the accelerating grids that produce the ion beams. As energetic ions leave the ion-beam source hardware, some amount of material is sputtered off of the metal hardware. This can be most clearly seen in the SIMS findings detailed in Section 3.2.3. Of note is the fact that when sidewall roughness scattering is not the primary loss contribution, metal impurities can contribute significantly to optical loss (as shown in [19]). However, in this early work we expected metal impurity contribution to be dwarfed by roughness scattering and phonon absorption losses.

74

### 3.1.4  AJA Sputter

*AJA Sputter* refers to a load-locked magnetron sputtering system fabricated by AJA International. This is a considerably simpler sputter tool than the IBD. Metallic targets are inserted into the magnetron sputter guns, and RF power (in the case of dielectric deposition) is applied to ignite plasma at the target. The vacuum chamber is filled with an atmosphere of Argon which performs the sputtering of the target. Small amounts of oxygen or nitrogen are added to the Argon gas flow to oxidize or nitridize the sputtered particles. This oxidation or nitridation reaction occurs primarily in the plasma at the sputter target.

The sputter target accumulates a negative DC bias as leave escape the plasma, similar to the PECVD platten, which attracts the positively charged ionized gasses towards the target, causing the target material to be sputtered. A metal turret directs this beam of sputtered material toward the sample holder, which is about 20 cm away from the sputter target, oriented at an angle with respect to the arriving material and rotating at 100 rpm.

The operation method is similar to IBD, although the main drawback is the coupling between applied RF power and target DC bias. The DC bias of the target, which determines particle acceleration, varies with target thickness as the amount of target material determines the number of electrons the target can hold. Consequently, as the sputter target thins during usage, the DC bias drops, which lowers the ion acceleration and flux, finally causing a reduction in deposition rate. Unfortunately, for $Si_3N_4$ films, this drop in bias also appears to reduce the refractive index, which indicates that some amount of the nitridation reaction may occur at or on the way to the sample surface, in that a lower acceleration/flux of sputtered silicon particles allows more nitrogen atoms to bond during the creation of each monolayer. However

this drop in both rate and index is fairly predictable and can be accounted for. It should be noted that the $SiO_2$ films exhibit constant refractive index, down to three decimal points, as Silicon favors the stoichiometric $SiO_2$ state naturally, and so simply maintaing a larger concentration of oxygen atoms than silicon atoms will typically ensure oxidation of every participating silicon particle, and will not incorporate more oxygen than is needed to produce stoichiometric $SiO_2$. $Si_3N_4$, on the other hand, can be either silicon-rich or nitrogen-rich (yielding higher or lower indices, respectively), so the rate of silicon particle arrival is rather important in terms of maintaining a particular refractive index or stoichiometry.

### 3.1.5  Thermal Oxide

*WetOx* refers to thermal oxidation of silicon using water vapor to accelerate the oxidation rate. When used with bare silicon substrates this process can only create $SiO_2$, and thus is only applicable to the upper and lower cladding materials of our waveguides, although dopants could be introduced to the substrate or later implanted to modify the refractive index of the grown oxide.

Thermal oxidation is performed at high temperatures, typically above 600°C, as the process is based on the diffusion of precursors (in this case $H_2O$ or pure $O_2$) into a substrate. This type of thermal diffusion follows the standard temperature-dependence on an Arrhenius equation, so higher temperatures yield faster oxidation rates as the diffusion of oxidant is accelerated. The rate-limiting factor is the diffusion of oxidant through the generated $SiO_2$, as this oxidant must reach the Si interface in order to react.

This particular system is a Tystar Tytan system with quartz hardware able to accommodate up to 400 8" wafers within the thermally uniform area

of the furnace tubes. During a wet oxidation, 200 sccm of $O_2$ is bubbled through heated water at 250°C, which flows water vapor into the tube. In general the temperature of the tube is variable between 650°C and 1050°C, although standard processes are run at 1050°C for the highest oxidation rate of silicon. The system ramps up to temperature over 2 hours, and performs a 15m anneal in an inert nitrogen atmosphere at completion of the oxidation.

The dependence on diffusion can can also smooth initially rough surfaces, as the oxidant diffuses isotropically and can blur out sharp features present in the original surface. A second effect that must be accounted for is the size difference between pure silicon and $SiO_2$. As the silicon incorporates more oxygen, the volume occupied increases. The ratio between the volume of Si and $SiO_2$ is called the volume expansion ratio, and this parameter plays a crucial role when oxidizing patterned features.

## 3.2 Material Losses & Measurements

A variety of material measurement tools are available at UCSB's Material Research Laboratory, and there exist numerous methods for measuring similar properties of a film. I chose the most common methods utilized in literature for measuring the appropriate material parameters discussed int he previous section. In some cases multiple methods were used in an attempt to make up for the limitations of tools used, to provide an aggregate measurement.

### 3.2.1 Atomic Force Microscopy of Surface Roughness

The roughness of a deposited film will create optical loss based on the mode field overlap at the roughness interface if the film surface forms an interface between two different refractive indices. Deposited film roughness tends to

be much lower than the roughness created by etched sidewalls or lithography, so allowing more mode power to overlap the surface roughness and reduce the sidewall overlap will decrease optical loss. Utilizing a high aspect ratio waveguide core decreases loss significantly by reducing sidewall roughness overlap, but also increases the modal overlap with surface roughness, resulting in surface roughness becoming a significant factor. For detailed analysis of this loss mechanism, please see Section 2.1 (page 21).

Roughness values tend to be highly dependent on the deposition technique used, and so the measurement of surface roughnesses are included in this chapter, where we analyze a number of different deposition techniques.

The Atomic Force Microscope (or AFM) is perhaps the most widely used tool for measuring the nanoscale texture of a surface. As discussed in Section 2.1, the roughness parameters we need to extract are $\sigma^2$, ie. root-mean-square deviation of the surface from an ideal flat plane (aka. "RMS roughness"), and $L_c$, the spatial parameter known as correlation length.

The AFM is a type of scanning probe microscope (SPM), first introduced in 1986 [31]. A fine probe tip makes physical contact with the surface of a sample, and height deviations are recorded as the tip is scanned over the surface. Atomic force microscopy is able to measure minute height deviations while applying very little force, without any special sample preparation. The probe we used in this work, Olympus model AC240TS, is manufactured out of single crystal silicon, such that the fine tip can be sculpted using a combination of etching and oxide sharpening processes, producing a tip radius of 9 $\pm 2$ nm with height of 14 $\pm 4$ µm[29, 30] (Figure 3.3). In addition, the top side of the probe is coated with a 100 nm layer of aluminum to enhance the reflection of the deflection-detecting laser.

At our disposal we have a Veeco Dimension D3100 and an Asylum MFP-
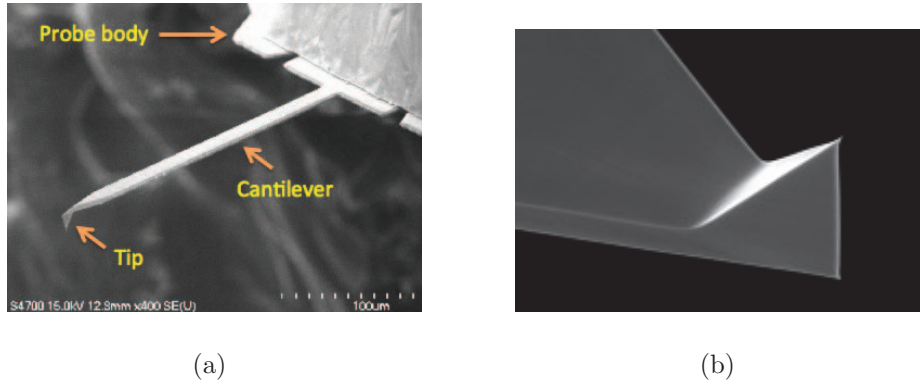
**Figure 3.3:** *(a) SEM image of the AFM probe used for roughness measurements (Model: Olympus AC240TS) [29]. (b) Close-up of the tip (facing upwards) that makes contact with the sample surface. [30]*

3D, both of which operate in a similar way. For nano-scale roughness measurements we use *AC* or *tapping mode* operation, which reduces damage to the surface and tip as compared with simpler contact mode. Figure 3.4 shows a schematic of this mode of operation, which shows the general technique of using a reflected laser signal to detect deflections in the cantilever position. The beam is reflected off the top of the cantilever and detected by a two-part photodetector, each of which detect part of the laser beam spot. The difference between each of the two photodetectors is used to create the deflection signal, where no difference indicates a beam exactly centered between the two photodetectors.

The probe is held by a head containing a piezoelectric *"shake" piezo* that provides movement of the probe in the Z direction. The drive signal for this Z-direction shaking, $\widetilde{V}_D$, is a kHz AC signal, causing the cantilever to vibrate up and down.

As the cantilever angle and position changes during this oscillation, the laser beam is deflected and moves the beam spot on the photodetectors,
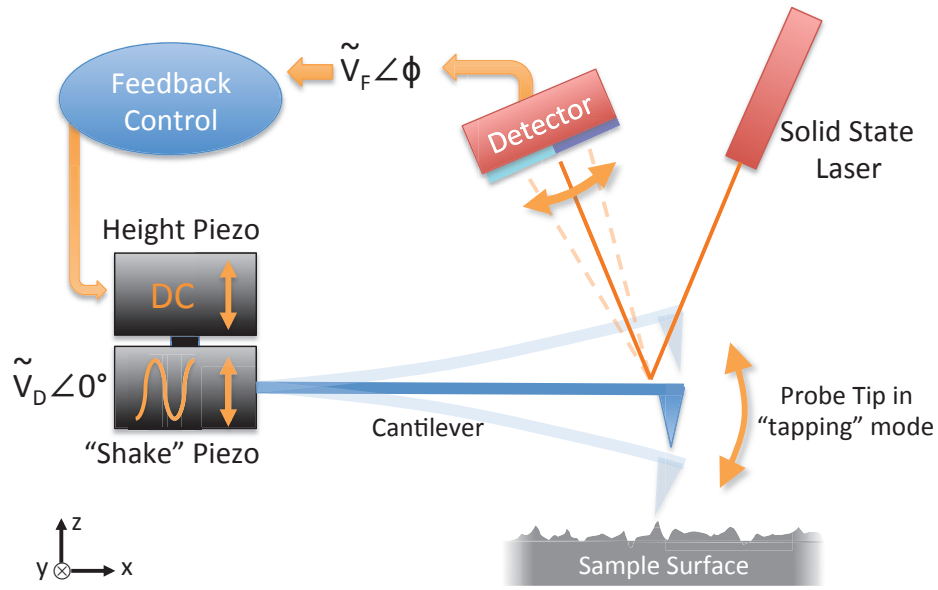
**Figure 3.4:** *The feedback loop of an AFM operated in tapping mode. $\widetilde{V}_D$ is an AC drive voltage, typically operating at or close to the cantilever's resonance frequency. It provides the reference phase, and the drive amplitude sets the swing height of the tip. The measured deflection of the laser reflected off the cantilever is used to produce a feed back AC voltage, $\widetilde{V}_F$. The feedback controller controls the height of the probe to try and maintain a given setpoint for $\widetilde{V}_F$, and this signal is recorded as the height measurement. The feedback phase, $\phi$, indicates operation in either attraction or repulsion mode.*

creating an imbalance in the two photodiodes. $\widetilde{V}_F$ is generated from the oscillating reflected signal. The amplitude of this signal is correlated with the height deviation of the tip, but this height deviation is not precisely known, as $|\widetilde{V}_F|$ depends on the cantilever length, mass and drive amplitude. Rather than accounting for all these variables we will simply use the signal for comparison. The phase of $\widetilde{V}_D$, $\phi$, is compared with the drive phase and yields information about any forces slowing down or speeding up the cantilever

oscillation.

With the probe vibrating away from any surfaces, $\widetilde{V}_F$ gives us the free-space amplitude and phase for a given $\widetilde{V}_D$.

The AC240TS probes we use have a resonance frequency of about 70 kHz for the cantilever vibration. The precise frequency of this resonance is dependent on the exact cantilever & tip geometry and mass, which varies slightly between probes, such that each probe may have slightly different resonance frequency. For this reason an *in-situ* "tuning" of the probe is performed every time a new probe is installed into the tool, in which the drive frequency, $f_D$ is varied across a large range and $|\widetilde{V}_F|$ is observed to detect a large spike in the feedback amplitude versus drive frequency. This spike in amplitude indicates the resonant frequency of the cantilever. It should also be accompanied by $\phi$ vs. $f_D$ showing a 90°phase offset from the drive signal at resonance, very similar to the universal resonance curve of an electrical resonator. During a probe tuning we choose a drive amplitude to achieve a desired tapping-height range, and note the free-space amplitude for the loaded tip.

The user chooses a setpoint for the feedback amplitude, $\widetilde{V}_{F,set}$, and the feedback controller will try to continually maintain the tip oscillation at that readback amplitude. At this point the user begins to lower the entire probe fixture towards the surface to be measured. The feedback controller adjusts the Z, or height piezo, to retract or extend the tip to maintain the amplitude setpoint for $\widetilde{V}_F$. The only reason the tip would not be able to reach the setpoint for the readback amplitude is if the tip oscillation were interrupted during it's swing, say by hitting a surface on the bottom of it's swing. If the setpoint is less than the readback, $\widetilde{V}_{F,set} < \widetilde{V}_F$, the system will extend the tip further downwards in an attempt to reduce the oscillation amplitude by

causing the tip to contact the surface. Conversely, if $\widetilde{V}_F < \widetilde{V}_{F,set}$, the tip must be impinging upon the sample surface sooner than desired, and the system will retract the tip via the Z piezo. This feedback signal to the height piezo is the $\Delta height$ reading recorded by the system. In this way, as long as $\widetilde{V}_D$ is constant, the tip always impacts the surface at approximately the same point in it's swing cycle, and thus always at the same force.

Height deviation measurements are taken continuously as the tip is scanned laterally (in the $x$ and $y$ directions) across the sample surface. In the case of the D3100, the probe is scanned using two additional piezotubes in the scan head, while for the MFP-3D the sample stage is scanned via piezoelectic elements.

There are two modes of surface interaction that one can take surface topography measurements with. *Repulsive* mode occurs when the tip is impacting the surface with enough force such that the strongest interaction between the tip and surface is due to coulombic repulsion - the electron clouds of the tip & surface atoms repelling each other. This is like normal contact between typical macro-scale solid objects. This method damages both the tip and surface fairly quickly, in that only a few scans of ˜4µm$^2$ can be performed before significant image degradation occurs. The Veeco systems operate only in repulsive tapping mode.

An alternate mode known as *attractive mode* enables measurement of the surface without physical contact. In this mode one sets the tip vibration amplitude much lower, to reduce the maximum speed & force attained during each swing, and measures the Van der Walls force between the tip and surface molecules. The Van der Walls force is an attractive force between molecules (the opposite of coulombic replulsion), and when a vibrating AFM tip is

brought very close to but not touching a surface, a sudden increase in the phase, $\phi$, is observed from it's resonance value of 90°. This increase in phase offset indicates that the tip is travelling slightly further in it's free-space response, and it can be surmised that it is being pulled towards the sample at the low point of it's oscillation. As this mode of imaging is measuring a force that occurs further away from the molecules of the surface, it is like measuring an envelope over the surface, rather than the surface itself.

Attractive mode imaging not only allows the tip to remain undamaged for a larger amount of scanning, but was also found to measure larger roughness values as compared with repulsive mode imaging on the same surfaces. If the "envelope" created by measuring Van der Waals forces had an adverse effect on the roughness measurement, one would expect an *underestimation* of the roughness ($\sigma^2$) in attractive mode. However, as attractive mode experimentally yields *larger* roughness values, we must conclude that attractive mode imaging is actually more accurate. Repulsive mode tapping must either damage and smooth the surface, or damage and round off the AFM tip during scans, resulting in measurements that show a smoother surface than existed prior to measurement.

### 3.2.1.1 Comparison of Deposited Glasses

The aforementioned glass films were deposited onto polished silicon and the surface roughness was measured with AFM. Figure 3.5 shows a number of ˜1 μm thick $SiO_2$ films analyzed in this way. The simplest and most common glass deposition method, Capacitive PECVD (or just "PECVD") yielded the largest roughness. Additionally, ICP-PECVD ("Unaxis") silica films were measured before and after a "densification" anneal, in which the samples were heated to 700°C for 30 minutes in an oxygen ambient.
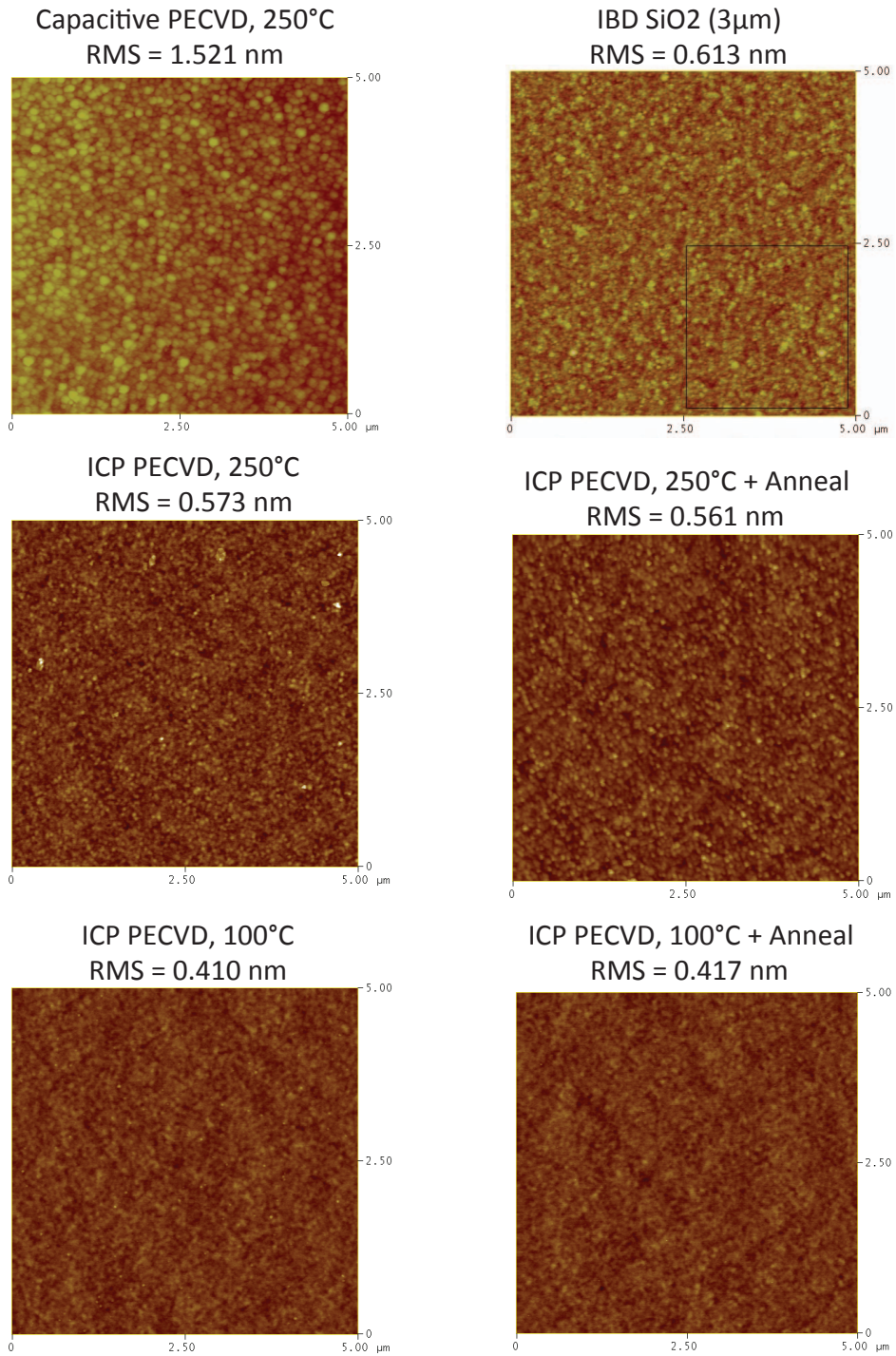
**Figure 3.5:** *AFM scans of various deposited SiO₂ films (Courtesy G. Sad-dik).*

Although we tend to see densification in that the thickness decreases and refractive index increases, any change in the surface roughness is obscured by measurement error, which is on the order of 0.050 nm RMS (see [32] for densification and polishing experiments on these films).

Figure 3.6 shows a comparison of the RMS roughness for a variety of thin-films, some of which are potential core materials (with high refractive index) and others of which are cladding materials (generally $SiO_2$). The high-index films produced by IBD sputter may in fact be the smoothest cores, but for low-index $SiO_2$ claddings, which tend to be much thicker (5–10 µm), it is necessary to investigate the evolution of roughness with film thickness.
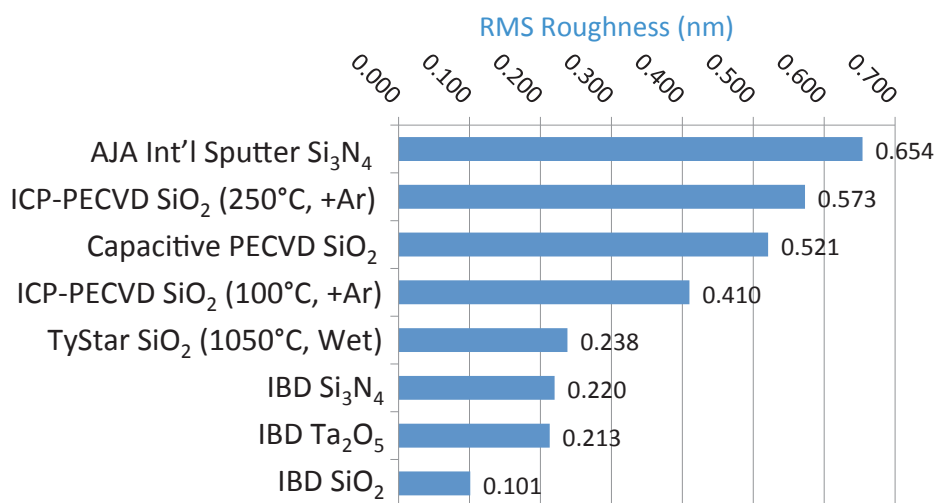


**Figure 3.6:** *RMS roughness for various deposited glasses (300–500 nm thick).*

The way in which film roughness varies with thickness depends on the film generation method. As mentioned before in Section 3.1, conformal deposition methods such as PECVD can be expected to show increased roughness with thickness, while thermal oxidation will behave differently due to the dependence on diffusion processes.

85
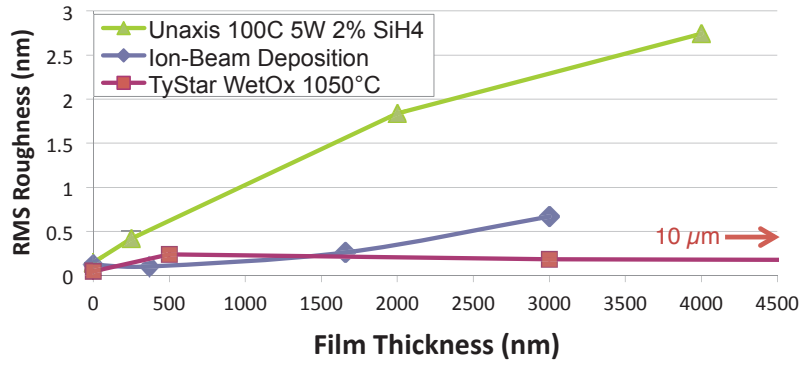
**Figure 3.7:** *RMS Roughness versus film thickness for SiO₂ produced via IBD, Unaxis ICP-PECVD and Wet Oxidation.*

Figure 3.7 shows the RMS roughness versus thickness for oxides produced via IBD Sputtering, ICP-PECVD and Wet Thermal Oxidation, which broadly encompasses the three main thin-film production methods utilized in this study. The points at zero-thickness indicate the roughness of the initial substrates.

The figure shows that the conformal PECVD deposition increases in RMS roughness rapidly, which is expected as bumps get coated and thus become larger. IBD sputter deposition exhibits a similar trend, although with generally lower roughness. Sputtered particles more energy, causing them to migrate around a surface before bonding, and will consequently fill small cracks and trenches. The thermal oxide, created by a diffusion-controlled process, show slightly more roughness than the initial substrate, but maintain a low roughness all the way to 10 µm of film, clearly making this the best choice for the lower cladding based on roughness. The diffusion process is expected to lower roughness due to the isotropic nature of diffusion, which is thought to smooth out small-scale roughness at the surface of initial surface. This smoothing effect is actually simulated in Section 5.2:*Roughness*

*Reduction* on page . Although the exact process parameters may play a role in these studies, the general trend is expected to be consistent across films produced by these various methods.

### 3.2.2 Fourier Transform IR Spectroscopy for measuring Bond Resonances

Vibrational states of the atoms in a material have been well-known as an optical loss mechanism in fibers since they were revealed in Kao & Hockman's pivotal 1966 paper [19] and directly attributed to loss in the C-band by Beales *et al.* [28]. As shown in Figure 1.3 (page 5), the reduction of hydrogen concentration and the resulting OH- bond resonances yielded a significant drop in optical propagation losses for single mode fibers. Reducing or otherwise circumventing absorption of light by these hydroxyl vibrations is often considered to have enabled dB/km losses over the communications band [23, 24], making optical fiber truly viable for long-haul data transmission. As discussed in Chapter 1, we targeted the use of Silicon Oxynitride ($SiO_xN_y$) and Silicon Nitride ($Si_3N_4$) as core materials for use in our integrated waveguides, which produces an additional loss contribution - the absorption exhibited by N-H bond resonances [27].

Humbach *et al.* show the locations of the numerous O-H and $SiO_2$ vibrational modes for optical fibers, and show that the 1st overtone of the O-H bond resonance contributes most strongly at about 1380 nm. They also show that this aggregate peak should be composed of four gaussian and lorentzian curves, corresponding to various O-H and $SiO_2$ tetrahedra combination vibrations [25].

As shown in [6], the N-H bond exhibits a primary stretching vibrational

mode at ˜2994–3015 nm (3317–3340 cm$^{-}$1), which results in a first overtone of $\lambda_{1/2}$ at ˜1495–1510 nm. This 1st overtone produces a very strong C-band loss peak, first shown by Albers et. al and repeated more recently by Wörhoff et. al [5, 34], due to the coupling between adjacent Hydrogen atoms, often represented as N-H...H. Yin & Smith suggested that this N-H...H tail extends all the way to 2900 cm$^{-}$1, which corresponds to $\lambda_{1/2}$=1724 nm - a 200 nm absorption range. From the research done by F. Ay et. al [2] we see that the N-H peak can be decomposed into 3 gaussians, representing various Hydrogen-based molecular bond resonances. The combination of these N-H bond resonances appears to dominate the optical loss for $Si_3N_4$-based waveguides, although the O-H (in particular, SiO-H) bond also plays a role.

Chemical-based deposition methods such as chemical vapor deposition (CVD), usually use hydrogen-based precursor compounds, which always results in some hydrogen incorporation into the deposited film. Silane, $SiH_4$, is the typical silicon precursor, while Ammonia ($NH_3$) and Nitrous Oxide ($N_2O$) as most often used as the nitrogen and oxygen precursors, respectively. Although deposition parameters can be varied to produce lowered hydrogen content (and thus high density) films, there will invariably be some residual hydrogen, which will be detectable as a wavelength-dependent optical loss.

High temperature annealing has been utilized to dramatically reduce the hydrogen content of deposited films after the fact. In fact, the Modified Chemical Vapor Deposition (MVD) method used to coat fiber preforms was specifically attributed to a major reduction in the hydrogen content of silica optical fibers, partly due to the use of very high temperatures (almost 2000°C). Similarly, deposition methods that utilize high temperatures tend to have lower hydrogen content to begin with.

Fourier Transform Infrared Spectroscopy, or FTIR, is an optical technique that probes the fundamental molecular vibrational resonances of a material, which typically occur in the mid-IR ranges. These vibrational states are dependent on the atomic masses and bond strengths between atoms in the material, where each bond will exhibit a spectrum of resonance frequencies, corresponding to different vibrational directions (eg. stretching, twisting etc.). Electromagnetic waves can be absorbed by the various bonds if the motion results in a change in dipole moment - thus the optical energy is converted into vibrations, or heat, through these resonances, and this optical absorption can be measured to determine the frequencies of light that the material responds to [33]. In this way the absorption spectrum of a material can be used to identify the atomic bonds present. The transmitted light intensity is directly related to the concentration of bonds via the Beer-Labert law, which states that

$$log_{10}\left(\frac{1}{T}\right) = \alpha \, t \, c \qquad (3.1)$$

where $T$ is the ratio of transmitted to incident optical intensity, $c$ is the bond concentration ($mol./m^3$), $t$ is the thickness of the thin-film ($m$) and $\alpha$ is the molar absorptivity ($m^2/mol.$). The absorptivity is the primary material parameter that enables quantification of the bond concentration, and is dependent on the specific bond type and overtone[33]. $\alpha$ is actually a wavelength-dependent value, which presents a problem when associating long-wavelength absorption (as is obtained with FTIR) to C-band loss, as the C-band wavelength-dependence is not well-described for the bonds investigated here.

For our purposes, to compare the various films at our disposal, an integration over an entire absorption band would capture all the various vibration types for a particular resonance, providing a comparative parameter for a

particular molecular bond provided that the film thicknesses are the same. A smaller integrated area would simply indicate fewer hydrogen bonds in that region.

A Nicolet Magna 850 FT-IR spectrometer was used to obtain the optical transmission versus wavenumber, $k$ (where $k = 1/\lambda$) for a number of the thin-films specified above. For deposited films, the technique requires that the substrate be pre-measured, allowing for correction of the transmitted spectrum to probe the deposited thin-film alone. P-type Boron-doped Silicon substrates with roughened backside were used to obviate the fabry-perot cavity created by double-side polished substrates.

The infrared beam, originating from a calibrated blackbody source, is directed through the sample chamber, which is purged with nitrogen to remove atmospheric water and carbon, and then passes through the wafer at normal incidence to the film and substrate surface, and is subsequently detected with a deuterium tryglycine sulfate (DTGS) detector.

The O-H absorption bands of three of the PECVD-based silica deposition methods are shown in Figure 3.9. Wet oxidized and IBD silica showed no detectable band in this region - the O-H bond concentration was below the noise floor of the FTIR.

Of these four, the film with the highest hydrogen content, namely the capacitive PECVD film, was annealed at 1000°C in an inert nitrogen environment. Although the anneal time was programmed as 30 seconds, the system takes two hours to ramp up to the anneal temperature. As shwon in Figure 3.10 this treatment reduced the hydrogen content to below detectable levels, and thus explains why the Wet-Oxidized films show no detectable hydrogen even though $H_2O$ is used as a process gas.

Similar analysis was performed for $Si_3N_4$ films prepared by PECVD and
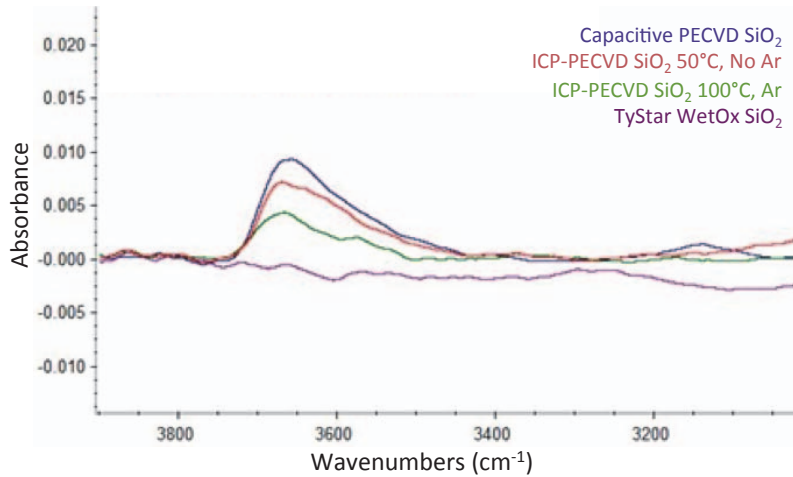
**Figure 3.8:** *The FTIR absorbance spectra of four silica films overlaid.*
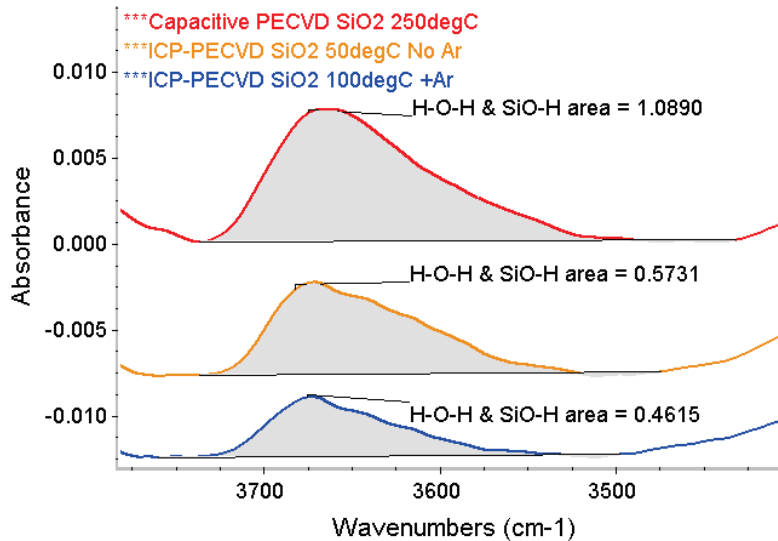


**Figure 3.9:** *Integrated area for the fundamental SiO-H resonance of various silica films on a comparative absorbance scale.*

IBD (ICP-PECVD was not analyzed in light of the pinhole issue). The N-H & N-H-...N stretching vibrations occur around 3300 cm⁻1, as shown in Figure 3.11. As expected, the IBD film shows an integrated area so low as to be considered at the noise floor of the instrument, while the PECVD film
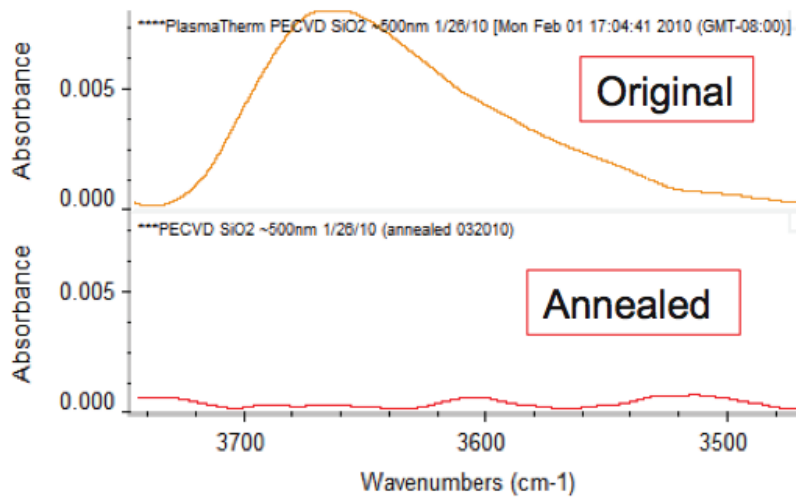
**Figure 3.10:** *PECVD Silica before and after a $1000°C$ Anneal. (Courtesy Renan Moreira)*
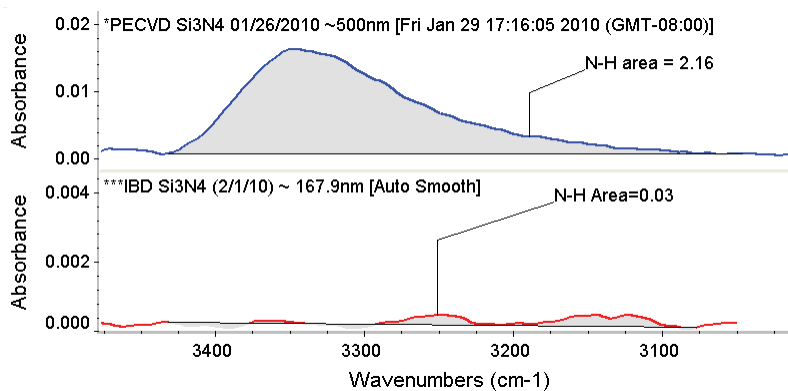


**Figure 3.11:** *Integrated area for the fundamental N-H bond resonances, comparing as-deposited PECVD and IBD $Si_3N_4$ films.*

shows a very strong resonance.

This study shows that, on the basis of hydrogen concentration, high temperature anneals effectively reduce the hydrogen concentration of silica films, and that ion-beam sputtered films do show undetectable hydrogen for both $SiO_2$ & $Si_3N_4$, as expected. Although both the wet oxidized and PECVD

silica films show no detectable O-H resonances after high temperature processing, it is expected that some hydrogen remains below the detection limit of thin-film FTIR. Light propagation through 500 nm films can only experience so much absorption - while light propagation through a 1 meter long waveguide may reveal more information on the trace impurities present in the film. Additionally, more sensitive techniques like Secondary Ion-Mass Spectroscopy may aid in confirming these results.

### 3.2.3 X-Ray Photoelectron Spectroscopy & Secondary Ion-Mass Spectroscopy for determining impurity concentration

In the previous section we found that IBD core films exhibit much lower hydrogen concentration than PECVD and ICP-PECVD films, although the hydrogen can be removed to below the FTIR detection limit with a high temperature anneal. Thus there may be little inherent advantage in utilizing ICP-PECVD films provided that high temperature annealing is allowed. However, the detection limit of FTIR may simply be too high, especially considering that we analyze the optical absorption on ~500 nm films, and eventually will be propagating light through 1 meter films - even small concentrations can become large loss contributions at such length scales.

We utilized two spectroscopy techniques with high sensitivity to impurities to investigate the presence of other unexpected impurities apart from hydrogen. Of particular concern was the metal impurity of sputtered dielectrics, since the physical sputtering of target material is expected to also sputter other metals within the vacuum chamber. However, a simulation of the expected loss that these impurities incur has not been developed at this

time due to the complexity of the problem, which depends on particle size, conductivity and the bonding states within the host material.

First, X-Ray Photoelectron Spectroscopy was used to obtain survey spectra of ion-beam sputtered $Si_3N_4$. This technique directs an x-ray beam at the sample, which causes inner-shell electrons to be ejected. The number of these electrons versus energy required to eject the particle is detected, providing the spectrum that allows for elemental identification.
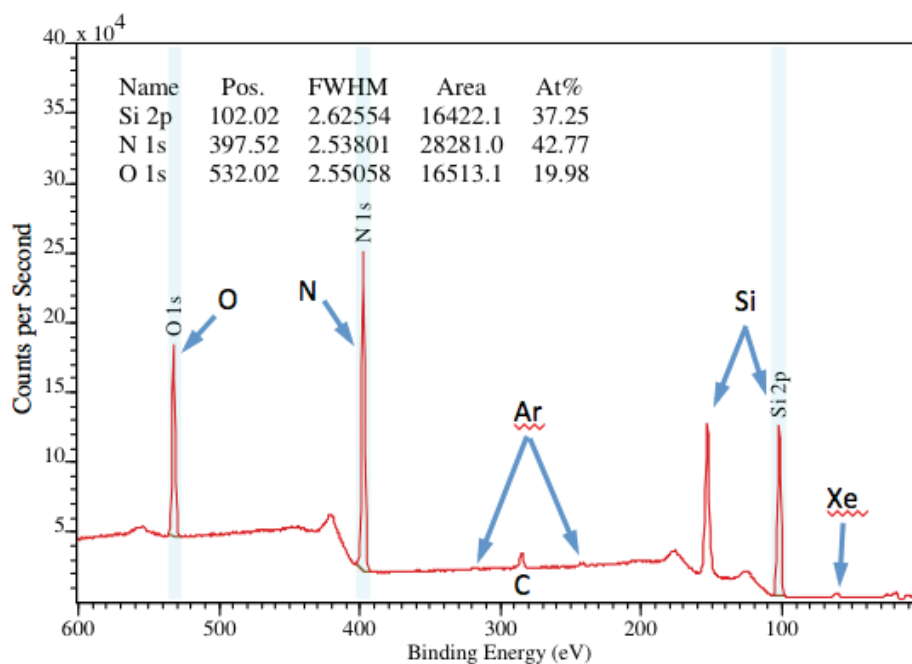


**Figure 3.12:** *XPS spectrum of IBD $Si_3N_4$, with detected impurities indicated.*

Figure 3.12 shows an example spectra of IBD $Si_3N_4$, in which only Xe and Ar impurities have been detected. The area under each peak with respect to the total elemental area shows that both nobel gas impurities show less than 0.5 atomic % concentration.

Since none of the expected metal impurities were detected, a more sensi-

tive detection technique was pursued.

A Physical Electronics 6650 Dynamic Secondary Ion Mass Spectrometry (SIMS) system available at the UCSB Materials Research Laboratory enables very sensitive detection of impurities in a material. The SIMS system sputters material from the sample in a high vacuum chamber, and detects the $mass \div charge$ of ejected particulates with a quadrupole detector. Due to the coupling of mass and charge of detected ions, it is difficult to unambiguously identify and quantify elements, as the ionization of an element can vary upon sputtering. However, the system is extremely sensitive to small impurity quantities, so we used this system to provide initial identification of potential elemental contaminants, and subsequently had Evans Analytical Group (EAG) perform quantified TOF-SIMS (time-of flight SIMS) to determine actual concentrations.

Results of the initial mass survey scans to simply identify potential contaminants are shown in Table 3.2. Although accurate quantification is not possible, we still compared the elemental counts between samples, using the TyStar $SiO_2$ as a baseline for comparison, as shown in the *SIMS (comparative)* column. Additionally, EAG performed a similar survey scan on the IBD and ICP-PECVD $SiO_2$ films to confirm some of the in-house survey scans.

Interestingly, the TyStar $SiO_2$ appeared to have an easily detectable hydrogen content, while $H_2$ in the IBD Sputtered $Si_3N_4$ was barely detectable. As suggested in the FTIR study, the detection limit of FTIR is higher than SIMS, and this difference in hydrogen content may in fact make an impact on an ultra-low loss waveguide. As expected, both PECVD silica films showed higher $H_2$ than the Tystar and IBD, with the capacitive PECVD exhibiting a much larger content - due to the use of $NH_3$ as a precursor, whereas the ICP-PECVD used $N_2$. Additionally, a host of metals were detected in the

sputtered films that were not present with other techniques. Although Fluorine was detected in some films, this is also a known contaminant present in the SIMS system at UCSB, so a background of F was expected to be present. However, large changes in F from sample to sample do indicate that the PECVD systems do contain some amount of Fluorine.

These surveys were then used to direct the quantified TOF-SIMS analysis of IBD and ICP-PECVD $SiO_xN_y$ films by Evans Analytical Group, the results of which are shown in Figure 3.13. We chose only $SiO_xN_y$ films of $n = 1.60$ as these appear to be the core materials of choice. The chart shows that as-deposited IBD films contain Mo, Cr and Cu metal impurities not found in ICP-PECVD films, along with much higher Boron concentrations. In general, Na, K and C are typically present in most films due to atmospheric contamination. The ion-beam acceleration grids are in fact constructed of Molybdenum, and the Silicon sputter target is Boron doped, which likely explains the high levels of these impurities.

The ICP-PECVD films shows relatively large levels of Fluorine, which originates from the plasma cleaning of the vacuum chamber, performed with as $SF_6$ plasma. The high Helium and Hydrogen content originates from the deposition process gasses, in which Helium is used to dilute the Silane $(SiH_4)$ gas flow.

**Table 3.2:** *Results from the SIMS mass surveys, yielding only comparative data for identification of elements present in deposited film.*

| Film Type | Deposition Tool | Important Deposition Parameters | SIMS (comparative) | TOF-SIMS (unquantified) |
|---|---|---|---|---|
| SiO2 | Capacitive PECVD | 250°C | H & H2 (7x > TyStar SiO2)<br>O-H (9x > TyStar)<br>F (9.5E5 > TyStar!)<br>Na<br>K<br>Ca | |
| SiO2 | ICP-PECVD | 100°C, Ar | H & H2 (2x TyStar)<br>He<br>B (0.2x TyStar)<br>F (1E3 > TyStar)<br>N (Si2-N)<br>Mo ?<br>Na<br>K | B=58.8<br>Na=0.816<br>K=0.308<br>Ca=24.2<br>Mo=1.31 |
| SiO2 | Tystar WetOx | 1050°C, Wet | H & O-H<br>B<br>F<br>Na<br>C ?<br>K<br>Ca ?<br>N (Si2-N) | |
| SiO2 | IBD - Ion-Beam Sputter | Ion-Beam Assist | | B=67.7<br>Na=7.72<br>K=18.5<br>Ca=1.67<br>Cr=15.4<br>Mn=2.06<br>Mo=55.8 |
| Si3N4 | Capacitive PECVD | 250°C | O (less than IBD)<br>O-H (> IBD)<br>C<br>Na<br>H (5x > IBD)<br>K (>IBD) | |
| Si3N4 | IBD - Ion-Beam Sputter | Ion-Beam Assist | B<br>Cr<br>Mo<br>Na<br>O<br>H (little) | |
| Ta2O5 | IBD | Ion-Beam Assist | Cu<br>In<br>Cr<br>Al<br>Fe | |
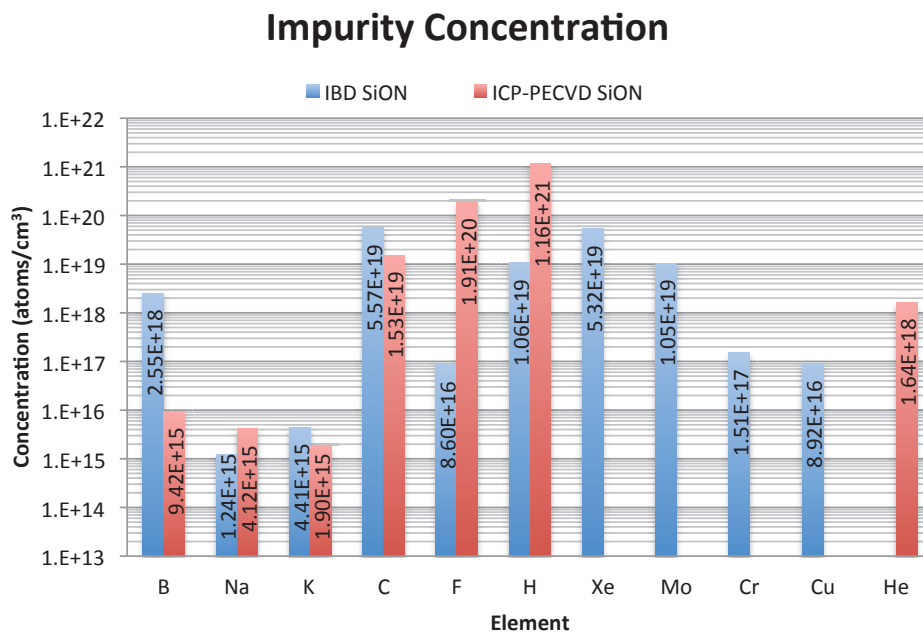
**Figure 3.13:** *Impurity concentrations in IBD and ICP-PECVD $SiO_xN_y$ films via TOF-SIMS.*

## 3.3  Chapter Summary

The conclusion of this study is that the IBD sputter deposited films show the lowest roughness and hydrogen content for high-index thin-films (¡ 1µm), but contain a number of metal impurities partly from the acceleration grids. Thermal oxide showed the lowest roughness for very thick oxide films (ie. claddings), with slightly higher hydrogen than IBD. Boron was found in wet oxidized and IBD films, which originates in the boron doping of the initial substrate and the sputter target, respectively. PECVD $SiO_2$ films have a a large hydrogen content, as expected, along with a contaminant of Fluorine, which is used to clean the chambers between depositions. Additionally, high temperature annealing was able to drive out hydrogen from PECVD $SiO_2$ films as measured with FTIR.

Thermally oxidized float-zone silicon contained no unexpected impurities apart from Hydrogen. All samples contained trace amounts of sodium (Na), carbon (C) and Potassium (K) embedded in the film. These impurities are generally considered to be due to atmospheric contamination from being situated next to an ocean, although the presence of these elements even inside a high-vacuum chamber is a little surprising.

The very high Hydrogen concentration of PECVD films was confirmed with the SIMS depth profiles, showing about 7-10x greater concentrations than in Tystar thermally grown films, although surprisingly, the Wet Oxidized films appear to contain more hydrogen than IBD sputter deposited films - confirming the detection limit of FTIR as inadequate for waveguide materials analysis, except as an initial starting point. This indicates that even annealed films must contain some amount of hydrogen, since the wet oxidation process occurs at 1050°C. Further TOF-SIMS studies of annealed

films would shed light on this issue.

Thus we conclude that Wet Oxidized films provide the highest quality oxide cladding, although the residual hydrogen will likely become a factor once waveguide losses reach low levels. Sputter deposited films appear to be very promising as core materials in terms of low hydrogen content and roughness, although numerous metals were found in appreciable concentrations. However, we do not have a good theoretical model for how much loss these metal impurities would incur, so their impact on waveguide losses is uncertain. Due to this uncertainty, and the unknown actual concentration reduction of hydrogen in annealed films, we must conclude that ICP-PECVD films may also be a viable alternative, albeit with slightly higher surface roughness.

# References

[1] Colligon, J. S., "Applications of ion-beam-assisted deposition," *Materials Science and Engineering*, vol. A139, p. 199-206, 1991.

[2] Ay and Aydinli, "Comparative investigation of hydrogen bonding in silicon based PECVD grown dielectrics for optical waveguides," *Optical Materials*, vol. 26, no. 1, pp. 33-46, 2004.

[3] F. Ladoceur, J. D. Love, and T. J. Senden, "Effect of side wall roughness in buried channel," *IEEE Proc. Optoelectron.*, vol. 141, no. 4, pp. 242248, Aug. 1994.

[4] T. Feuchter and C. Thirstrup, "High precision planar waveguide propagation loss measurement technique using a Fabry-Perot cavity," *IEEE Photonics Technology Letters*, vol. 6, no. 10, pp. 12441247, 1994.

[5] [1] H. Albers, L. Hilderink, E. Szilagyi, F. Paszti, P. Lambeck, and T. Popma, "Reduction of hydrogen induced losses in PECVD-SiOxNy optical waveguides in the near infrared," *IEEE Lasers and Electro-Optics Society Annual Meeting, 1995. 8th Annual Meeting Conference Proceedings*, vol. 2, Paper OFPW3.4, 1995.

[6] Z. Yin, F. W. Smith, "Optical dielectric function and infrared absorption of hydrogenated amorphous silicon nitride films: Experimental results

and effective-medium-approximation analysis," *Phys. Rev. B*, 42, 3666, 1990.

[7] K L Beales, D. M., "Increased Attenuation in Optical Fibres caused by the Diffusion of Molecular Hydrogen at Rooom Temperature," *Electronics Letters*, vol. 19, no.22, 917-919, 1983.

[8] K. Nagayama, M. Kakui, M. Matsui, I. Saitoh, and Y. Chigusa, "Ultra-low-loss (0.1484 dB-km) pure silica core fibre and extension of transmission distance," *Electronics Letters*, vol. 38, no. 20, 1168-1169, 2002.

[9] [1] K. B. Koller, W. A. Schmidt, and J. E. Butler, "In situ infrared reflection absorption spectroscopic characterization of plasma enhanced chemical vapor deposited SiO2 films," *Journal of Applied Physics*, vol. 64, no. 9, pp. 47044710, 1988.

[10] Kittel, C, *Introduction to Solid State Physics*, 8th ed., Wiley, New York, NY, 2005.

[11] F. Payne and J. Lacey, "A theoretical analysis of scattering loss from planar optical waveguides," *Opt Quant Electron*, vol. 26, no. 10, pp. 977986, 1994.

[12] R. Adar, M. Serbin, and V. Mizrahi, "Less than 1 dB per meter propagation loss of silica waveguides measured using a ring resonator," *Jnl. Lightwave Tech.*, vol. 12, no. 8, pp. 13691372, 1994.

[13] S. Mao, S. Tao, Y. Xu, X. Sun, M. Yu, G. Lo, and D. Kwong, "Low propagation loss SiN optical waveguide prepared by optimal low-hydrogen module," *Optics Express*, vol. 16, no. 25, pp. 2080920816, 2008.

[14] T. Matsutani, T. Asanuma, C. Liu, M. Kiuchi, and T. Takeuchi, "Comparison of surface morphologies of SiO2 films prepared by ion-beam induced chemical vapor deposition and ion-beam assisted deposition," *Nuclear Instruments and Methods in Physics Research Section B: Beam Interactions with Materials and Atoms*, vol. 206, pp. 343347, 2003.

[15] W. Lanford and M. Rand, "The hydrogen content of plasma?deposited silicon nitride," *Journal of Applied Physics*, vol. 49, no. 4, pp. 24732477, 2009.

[16] Y. Cheng and W. D. Westwood, "Losses in tantalum pentoxide waveguides," *Journal of Electronic Materials*, vol. 3, no. 1, 1974.

[17] Y. Nagasawa, I. Yoshii, K. Naruke, K. Yamamoto, H. Ishida, and A. Ishitani, "The study of the thermal oxide films on silicon wafers by Fourier transform infrared attenuated total reflection spectroscopy," *Journal of Applied Physics*, vol. 68, no. 4, pp. 14291434, 2009.

[18] Z. Yin and F. Smith, "Optical dielectric function and infrared absorption of hydrogenated amorphous silicon nitride films: Experimental results and effective-medium-approximation analysis," *Physical Review B*, vol. 42, no. 6, pp. 36663675, Aug. 1990.

[19] C.K. Kao, G.A. Hockham, "Dielectric-Fibre Surface Waveguide for Optical Frequencies", *Proceedings of the Institute of Electrical Engineers*, vol. 113, no. 7, pp. 1151-1158, July 1966.

[20] H. Conrads and M. Schmidt, "Plasma generation and plasma sources," *Plasma Sources Science and Technology*, vol. 9, p. 441, 2000.

[21] O. Lyngnes, N. Traggis, K. Li Dessau, C. Myatt, "Coating Technologies for High-Damage-Threshold Optics," *Optics and Photonics News*, vol. 17, no. 6, pp. 28-33, 2006.

[22] D. John, J. F. Bauters, J. Nedy, W. Li, R. Moreira, J. S. Barton, J. E. Bowers, D. J. Blumenthal, "Fabrication and Demonstration of a Pure Silica-Core Waveguide Utilizing a Density-Based Index Contrast," *Proc. OFC/NFOEC 2011*, Paper OWS3, Los Angeles, USA, 2011.

[23] Miya *et al.*, "Ultimate low-loss single-mode fibre at 1.55 m," *Electronics Letters*, vol. 15, no. 4, pp. 106-108, 1979.

[24] G P Agrawal, *Fiber-optic Communication Systems*, 3rd ed., John Wiley & Sons Inc., New York,2003.

[25] Humbach *et al.*, "Analysis of OH absorption bands in synthetic silica. Journal of Non-Crystalline Solids", vol. 203, pp. 19-26, 1996.

[26] T. Lauinger., A. G. Aberle and R. Hezel, "Comparison of Direct and Remote PECVD Silicon Nitride Films for Low-Temperature Surface Passivation", *Proc. of 14th EPSEC (Barcelona)*, p 853, 1997.

[27] Del Prado *et al.* "Composition and optical properties of silicon oxynitride films deposited by electron cyclotron resonance." *Vacuum*, vol. 67, pp. 507-512, 2002.

[28] Beales and Cooper, "Increased attenuation in optical fibres caused by diffusion of molecular hydrogen at room temperature." *Electronics Letters*, vol. 19, no.22, pp. 917-919, 1983.

[29] Olympus Corporation, "Olympus Microcantilevers: Medium-soft Silicon Cantilever Classic", `http://probe.olympus-global.com/en/product/omcl_ac240ts_w2/`, retrieved on Aug 30 2011.

[30] Asylum Research Inc., "Probe Store - AC240TS", `http://www.asylumresearch.com/Probe/AC240TS,Olympus`, retrieved on Aug 30 2011.

[31] G. Binnig, C.F. Quate, C. Gerber,"Atomic Force Microscope", *Phys. Rev. Lett.*, vol. 56, p. 930, 1986.

[32] G. N. Saddik, *Switchable and Tunable Ferroelectric Bulk Acoustic Wave Resonators and Filters*, Ph.D. Thesis, University of California Santa Barbara, Sept. 2011

[33] F. Ay, *Silicon Oxynitride Layers for Applications in Optical Waveguides*, Masters in Science Thesis, Bilkent University, 2000.

[34] K. Wörhoff, L. Hilderink, and A. Driessen, "Silicon oxynitride: A Versatile Material for Integrated Optics Applications," *Journal of The Electrochemical Society*, vol. 149, no. 8, pp. F85F91, 2002.

# Chapter 4

# Measurement of Ultra Low Losses

In order to choose an appropriate method to measure propagation losses, some prior knowledge of the range of expected losses is necessary. Many common loss measurement techniques are only well suited to the dB/cm range, or are only applicable to certain types of devices. For example, loss measurements of optical fiber are achieved by determining the power throughput for varying lengths of fiber, on the order of meters and kilometers. This is simple to do as fibers are drawn onto a spool, so producing kilometer-long lengths is common to the fabrication method. If the fiber loss is high on the order of dB/m, no throughput power will be detected for a kilometer-long spool, while if the loss is very low at dB/km levels, very little reduction in power will be detected for a short meter-long fiber, possibly below the noise floor of the detector used.

A quick review of common measurement methods and the loss ranges or other applicable regimes of each method will show us which tool best suits the measurement of very low waveguide losses.

## 4.1 Overview of common techniques

The most common method to measure the loss of an integrated waveguide is the *cutback method*. This simply involves measuring the power throughput of a waveguide, often with fibers butt-coupled to the flat facets of the waveguide, and then cleaving or cutting the waveguide into shorter lengths and taking power throughput measurements of each length. A plot of the power versus waveguide lengths yields a slope and y-intercept which correspond to the waveguide loss in dB/meter and the total fiber/chip coupling loss, respectively.

Power loss at the fiber-to-chip coupling interface is the largest uncertainty in this measurement, and this coupling loss is closely linked to the facet quality on the chip. Consequently, the cutback method requires the assumption that cutting back the waveguide yields facets (and fiber coupling losses) identical to the previous facets. This may in fact be a reasonable assumption for crystalline waveguides (such as III-V devices), as the cutback is performed via crystal cleaving. Even so, the measurement uncertainty created by variations in fiber coupling produces a limit on the minimum losses that can be measured with this technique.

For example, our first design for a 5-inch contact lithography mask plate was primarily for "cutback" measurements, as shown in Figure 4.1. The sets of waveguides, labelled "S", "M" and "L", have progressively increasing bend radii. Each set contains three different lengths of waveguides, and each serpentine length is formed with 5 different waveguide widths from 1 µm to 5 µm, a pair of each width.

Although the lengths of these cutbacks were chosen to enable loss measurement from the 0.5 dB/cm to 10 dB/cm range by accounting for the min-
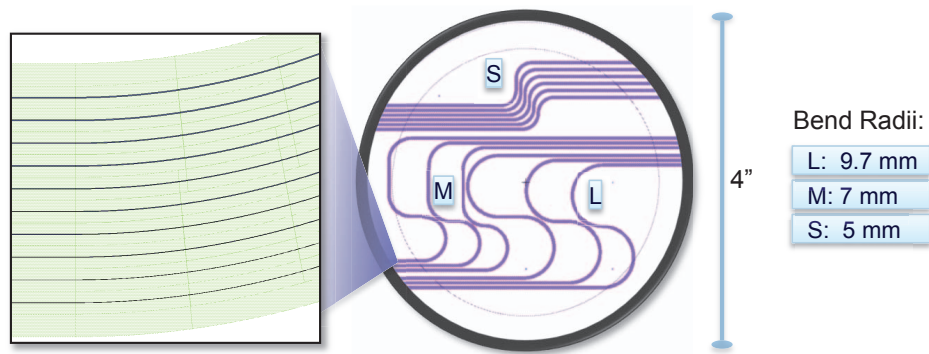
**Figure 4.1:** *First mask plate for contact lithography, with cutback loss measurement test structures for 3 different bend radii. Each bend radius has at least 3 lengths of waveguide, and each waveguide bus contains 5 different widths, a pair of each.*

imum measurable difference between two insertion losses, the fiber-to-chip coupling variation completely swamped these measurements in noise due to the glass facet quality. Figure 4.2 shows the dramaitc variation in mode excitation with simple movement of the launch fiber, which subsequently altered the throughput power (with the setup shown in Figure 4.3). Due to this change in transmitted power, these measurements had an insertion loss error of about 10 dB, which imparts an error of 0.5 dB/cm (50 dB/m) for the 20 cm long waveguides being measured, which is clearly not adequate for our target of dB/meter and lower losses.

Alternatively, the Fabry-Perot cavity method has also been used for calculating losses in small devices[3]. The measurement principal relies on the creation of an optical cavity when the waveguide is diced or cleaved out, such that the wavelength spectrum of the cavity can be used to obtain the cavity loss. The quality factor (Q) of a cavity is directly related to the cavity loss, as that determines the strength of interference between trapped waves.
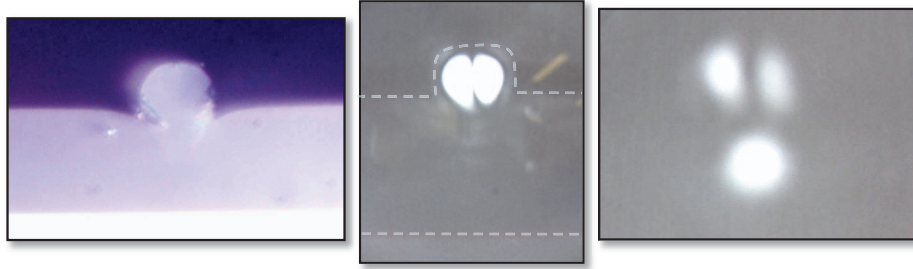
**Figure 4.2:** *Microscope image of the facet and mode profiles as imaged with IR camera at the output of the "S" chip.*
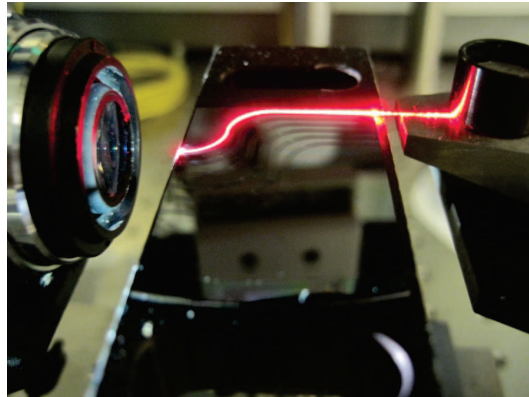


**Figure 4.3:** *Testing setup, in which the launch fiber is on the right and a microscope objective on the left couples the output mode to an IR camera through collimating optics (out of image). A red laser is shown here for alignment purposes.*

However this method also turned out to have numerous drawbacks.

Firstly, these cavity calculations also require the assumption of a facet loss (and reflection) that is identical (or indistinguishable) for either facet, which is generally not a good assumption for diced facets (but may be perfectly reasonable for cleaved crystalline facets), especially considering the previously shown facet quality issues. Secondly, accurate measurement generally requires a single-mode (lateral) cavity, which may not necessarily be
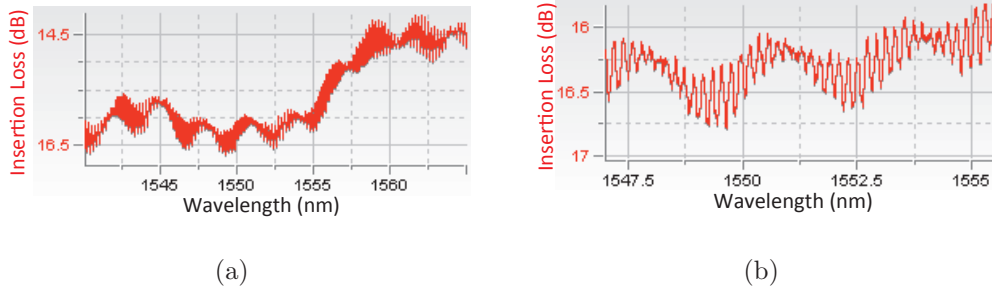
**Figure 4.4:** *(a) Spectrum of a multi-mode, cleaved-facet $Si_3N_4/SiO_2$ waveguide, showing the combined effects of mode-dependent group index, and wavelength-dependent coupling loss, material loss and bend loss. (b) Zoom in of (a), showing the complex waveform that must be analyzed to determine waveguide loss.*

the optimal design for low-loss propagation. A waveguide that support multiple guided modes typically exhibits disparate modal indices for each mode, which causes the spectrum to be a superposition of each mode's cavity resonance spectrum. Although this is able to be fit and is not generally an insurmountable problem, when added to the unknown facet losses (which are also wavelength-dependent), uncertainty in modal index simulations and wavelength-dependent losses, this adds too many variables for unambiguous determination of the waveguide loss.

Additionally, in a quest to continually improve and reduce propagation losses, this method does not allow for the designer to easily vary the waveguide geometry and indices while maintaining the ability to measure the resulting losses, due to the numerous variables that can yield an inconclusive spectrum.

Lastly, ring resonators have become a popular of measuring low waveguide losses [1, 2]. Although this technique does in fact obviate the fiber coupling uncertainy, it also requires single-mode waveguide design. In addition to

that, large bend radii devices would be fairly difficult to layout in more than one or two variations per wafer, due to the fact that a singe ring resonator with a 10mm bend radius would occupy a large portion of a 4-inch wafer.

We did in fact lay out and fabricate a number of ring resonator loss-test structures, but choice of core thickness and index parameters were highly constrained by multi-moding on one side and bend loss on the other, proving that a single mask plate would not suffice for the large range of geometries we desired to invesitgate.

In light of the fact that the accepted methods of waveguide loss measurement yield too high error for ultra-low propagation loss measurement, an alternative technique was needed that was not dependent on fiber-to-chip coupling losses or facet quality, provide a relatively rapid fabrication/test cycle with large design space, allow for multi-mode waveguides, and enable loss measurement with error below 1 dB/meter, preferably in a non-destructive manner.

## 4.2    Optical Frequency Domain Reflectometry

The Luna OBR 4400 (optical backscatter reflectometer) is a commercial tool that performs polarization-sensitive swept-wavelength Optical Frequency Domain Reflectometry (OFDR)[4]. The technique is a modern version of the original pulse-based OTDR (optical time-domain reflectometry) which has been used to probe reflections and losses in optical fibers since the late 1970's [5, 6].

In the OTDR technique, a short optical pulse is launched into a fiber at one end, and reflected pulses are collected at the launch site. The time delay

between reception of the pulses and amplitude of the reflection yields information on the distance and magnitude of the reflection event, respectively. The conversion of time delay into physical distance necessitates knowledge of the group index of light in the fiber, and the assumption that this is constant throughout the transmission, using the following expression

$$v_g = \frac{c}{n_g} = \frac{d}{t} \tag{4.1}$$

which states that the group velocity $(v_g)$ is defined as the speed of light $(c)$ divided by the group index $(n_g)$, and also equals the known propagation distance between reflections $(d)$ divided by the measured time delay between those reflections $(t)$.

The backscattered power is proportional to the launched power, and will decrease with increased distance into the fiber due to the attenuation of the optical fiber. In fact, Barnoski & Jensen first used this technique to probe the optical attenuation in a spool of fiber, showing a plot of continuously decreasing reflection versus time delay which could be fit to an exponential reduction in power versus length [6]. The oscillogram they published also reveals the reflection at the end of the spool of fiber.

Now this technique is more commonly used to probe portions of a fiber optic network, looking for anomalous reflection events to find bad connectors, splices or fiber damage. Loss events can also be located, as indicated by a sudden decrease in the backscattered power (typically after a reflection event).

### 4.2.1 Theory of operation

OFDR, in a simple sense, can be thought of in a similar way to OTDR, in that the result of an OFDR scan is reflected power versus time delay.

However, the method in which this is achieved does not actually use pulses, which would be limited in spacial resolution by the pulse width, and are rather expensive to generate and detect coherently [7].

Figure 4.5 shows a simple way to envision the theory of operation (courtesy of Jared F. Bauters). A laser source is swept over frequency, which corresponds to a wavelength sweep via $c = f/\lambda$, and is launched into a Mach-Zehnder interferometer (MZI). If this interferometer has an unequal time delay on one arm, then the frequency sweep will result in a sinusoidal frequency response, simply due to the varying phase difference between the two coherent waves interfering at the output of the MZI.

The Fourier Transform (FT) of this Amplitude vs. Frequency data yields time-domain data that shows a single sinusoidal component. The time-domain position of the peak is proportional to the time delay difference between the two MZI arms.
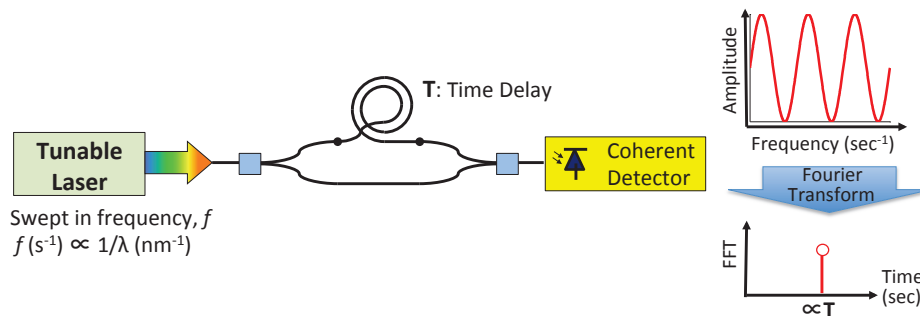


**Figure 4.5:** *A simple Mach-Zehnder interferometer with a delay on one arm will yield a sinusoidal spectrum when the source wavelength is swept. The fourier transform consequently shows a single sinusoidal component.*

In Figure 4.6, the same concept is extended to the capture of reflection data, via an optical circulator on one MZI arm. Two reflectors, with power
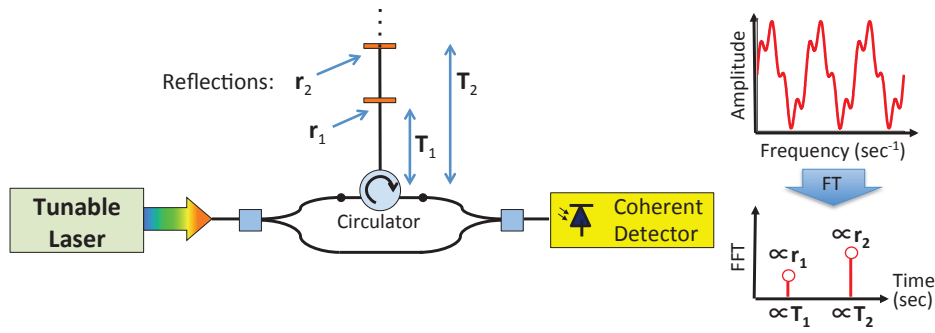
**Figure 4.6:** *For multiple delays, now caused by reflection events and captured via an optical circulator, a superposition of each sinusoid is detected. The F.T. thus shows multiple sinusoidal components, with amplitudes specific to each reflection event.*

reflectivity $r_1$ and $r_2$, are schematically shown at different positions, creating two different time delays, $T_1$ and $T_2$, on that MZI arm. The same frequency sweep will now result in the superposition of two sinusoidal responses. The Fourier Transform (or digital Fast Fourier Transform, FFT) will now reveal the two distinct frequency components and their locations in the time domain. The time delay to each reflector is proportional to the locations of the FFT peaks, and the amplitude of each peak is proportional to the magnitude of power reflected. In this way, the reflection versus time delay is obtained from the frequency sweep of a continuous–wave laser.

As is typical to the Fourier transform, more frequencies used will result in more time-domain datapoints, and the frequency range determines the time resolution.

Similar to an OTDR pulse, the "reflection events" actually occur at every point in the fiber/device, such that a continuous detection of reflected power at every point along an optical path is actually plotted, versus the time delay incurred to reach each of those points. This is provided that a high-sensitivity

114

detection scheme is used. These continuous reflections, or backscatter, are primarily a result of Rayleigh backscattering, resulting from the subatomic variations in optical density found in every material. This is the primary backscatter source for collimated beams traveling in air, but for guided waves, such as in optical fibers or waveguides, additional backscatter is incurred from rough waveguides walls, or local point-scatterers. One must keep in mind that only a certain amount of backscattered power *is actually detected* - that is, most backscattered power does not couple into the backwards-propagating waveguide mode, which necessitates modal overlap and velocity matching with the characteristic modes of the waveguide.

We use this continuously decaying reflected power to measure the propagation loss in a waveguide. The slope of the power versus distance plot yields twice the propagation loss of the waveguide - it must be halved due to the double-pass of reflected light.

The coherent detection scheme utilized in the Luna OBR 4400 enables a very high sensitivity of -130 dB, specifically to enable the detection of Rayleigh scattering, which results in very little power being returned to the OBR detector[8]. A dynamic range of 70 dB allows for the detection of this low-level backscatter at the same time as large reflection events. The full-range frequency scan from 186.15 THz to 196.59 THz (about 1525 nm to 1610 nm) results in a spacing between datapoints of about 9 μm. Fiber connectors, splices, and transitions between propagation methods are thus very easy to identify with this tool, and this is in fact it's primary application.

Figure 4.7 shows a screenshot of a fiber setup measured with the Luna OBR 4400, taken directly from the software and annotated with the physical features represented by each reflection spike. The OBR output connector is labelled at 0 meters, followed by the backscatter level of power propagating

in a fiber patch cord.
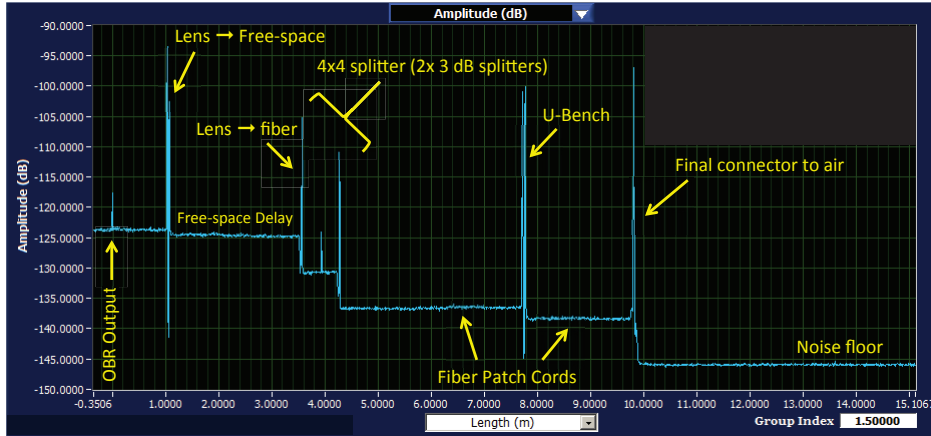


**Figure 4.7:** *Example OBR trace of a fiber setup. (Courtesy of Kimani K. Williams.)*

The screenshot shows that an assumed group index of $n_g = 1.500$ has been used to convert the time-domain data into a length-scale axis, in meters. Also, one can see that each reflection is often accompanied by a drop in power after that event.

Of note is the slightly lower backscatter level of collimated light propagating through air, as compared with the SMF-28 fiber patch cords. Additionally, the $4x4$ splitter, housed within a commercial package, is shown to be composed of two 3-dB ($2x2$) splitters, with a splice between them at 4m.

It should be noted that each 3-dB splitter shows a drop in the backscattered power levels in the fibers on either side. Since the backscattered power is directly proportional to the power level in the fiber, and the backscatter of each SMF-28 fiber can be assumed to be the same, this indicates a 6 dB drop in detected power due to each 3-dB splitter - twice the expected splitter value! This is because backscattered light must travel twice through the splitter - once in transmission and again in reflection towards the OBR

116

detector, so the loss of the splitter is actually $6\ dB \div 2 = 3\ dB$.

This halving of the loss value is also necessary for calculation of propagation losses, again, due to the double-pass of backscattered light.

## 4.2.2   Testing method

It should be noted that the sensitivity of OFDR to facet reflections must be addressed, as the dynamic range of the OBR detectors is constant, such that the noise floor changes with the maximum amount of reflected power returned. For a cleaved (or even lensed) fiber coupled to a glass waveguide, the backscattered power can be so high that the noise floor of the detectors is raised enough to interfere with the device measurement. To mitigate this effect, index matching gel or oil must be used, to eliminate the air gap between the fiber and chip (Cargille and FIS both supply these, with $n \approx 1.45 - 1.5$).

For the initial fiber-to-chip alignment, a visible red laser (a fiber-coupled "fault locator") can be used, as a significant amount of scattered light will be visible when the light is guided within the waveguide (see Figure 4.3). Without moving the fiber facet position, the fiber connector can then be attached to the Polarization Controller (PC) and IR output of the OBR. To ensure measurement of guided modes in the waveguide device, an infra-red camera is used to observe the power throughput, as shown in Figure 4.8. This requires that a microscope objective (typically 20x - 80x) is focused onto the output facet of the device.

To ease this alignment and focusing, an illuminator is coupled with an optical beamsplitter such that the light is reflected through the camera optics towards the device, and into the microscope objective. The polarizing beam splitter is not needed at this point and can be removed. Coarse alignment of the camera optics to the objective can be performed, such that the objective

117
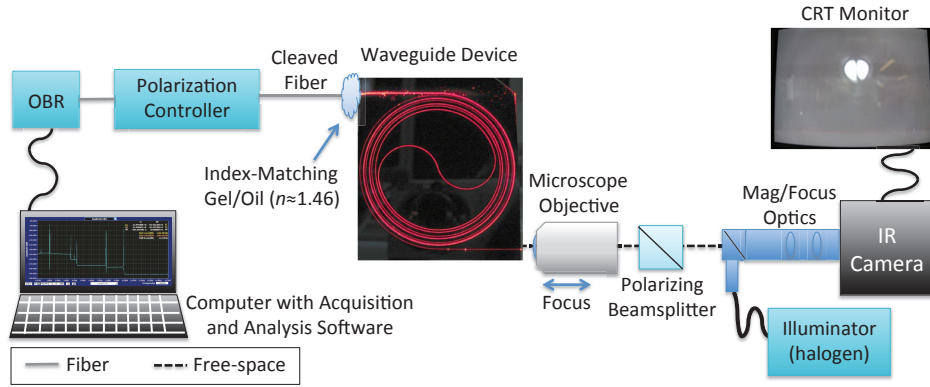
**Figure 4.8:** *Schematic of the testing setup for OBR measurements, with throughput mode observation. IR camera output can also be captured at the Computer.*

lens can be seen on the CRT monitor. The focal point can then be visually aligned to the device by observing the shape of light exiting the objective and impinging upon the device. This alignment can be refined by imaging the diced facets of the device with the IR camera, using the x/y/z micropositioners under the objective to bring the facet into focus, while maintaining the illuminator on the desired output waveguide via the top-down microscope.

Once the output facet is in focus on the IR camera, IR launch from the OBR light source through the device may proceed, which should produce a mode image on the CRT monitor. Alignment of the input fiber can be performed to ensure that substrate modes are avoided and maximum throughput power is achieved via visual observation of the CRT monitor (this usually corresponds very closely to the same optimization done with an optical power meter in lieu of the IR camera).

At this point the polarizing beam splitter can be used to select the polarization mode of propagation, inserted as shown in Figure 4.9. With the beamsplitter oriented for horizontally-oscillating electric fields to pass through

unreflected, only the TE mode will be imaged on the IR camera. The polarization controller should be manipulated to image maximum TE power, and also minimum TM throughput (with the beamsplitter oriented for vertical E-field on the through-port). We have found that minimizing TM is typically the most effective way to maximize TE propagation and vice versa.
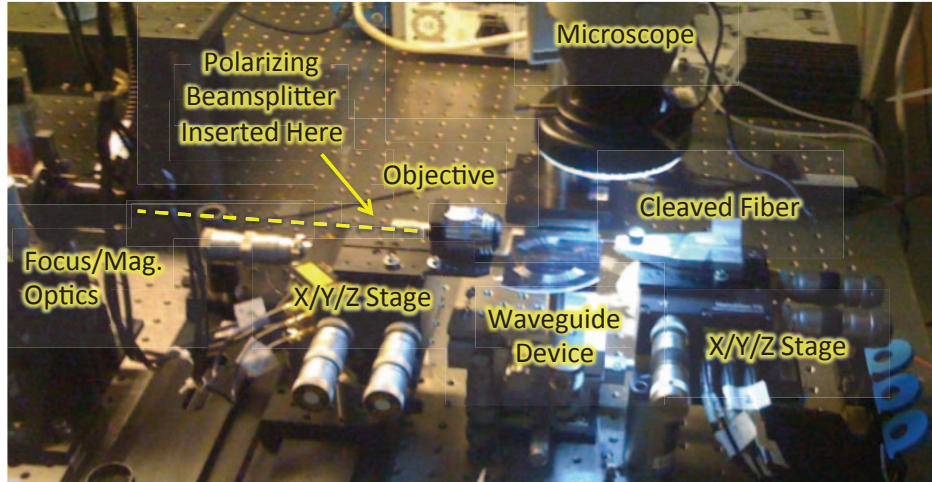


**Figure 4.9:** *Photograph of the OBR testing setup.*

Once the launch polarization has been set to maximize the propagation of a particular polarization, The OBR scan can commence. The IR camera illuminator should be turned off to minimize noise on the OFDR trace. Once the trace has been acquired, the polarization be be optimized for the orthogonal polarization and the trace re-taken.

This technique does in fact require that the waveguide has low enough loss such that IR light can be observed at the output waveguides. If this is not the case, if the loss is too high for a full 1-meter of spiral propagation, an alternative is to optimize polarization on shorter, spiral bypass waveguides, and then move the chip (via x/y/z stage) such that the fiber is aligned to the spiral waveguide, in theory without altering the launch polarization. Obvi-

ously this is not optimal, as the launch position can affect mode excitation.

The method in general assumes that the polarization is constant through-out the waveguide and that TE and TM modes do not exchange power during propagation. This does not appear to be entirely the case, although evidence will be shown that the two modes of excitation are in fact distinctly different, yielding disparate losses, modal indices and OFDR plots.

### 4.2.3   Analysis method

After coming to an understanding of the the OFDR method, we developed our own analysis tools to work with raw OBR data files. Although the soft-ware performs a reasonable number of coarse calculations that are adequate for general-use, detailed propagation loss analysis required more low-level manipulation of the acquired OFDR data.

The OBR software exports binary files that have already been converted into the time-domain (see the "OBR Binary File Definition" supplied by Luna Technologies for the positions and data types of each value). The system employs a polarizing beam-splitter directly before the detector, such that complex data arrays for the real and imaginary parts of each orthogonal polarization are acquired, $\tilde{P} = P_{real} + jP_{imaginary}$ and $\tilde{S} = S_{real} + jS_{imaginary}$. Conversion of this polarization data to total reflection amplitude is a matter of simply taking the magnitude of the two orthogonal vectors, like so: $R = \sqrt{|\tilde{P}|^2 + |\tilde{S}|^2}$. The time axis, $T$, can be constructed using the *start time*, *time increment* and *number of points*, as specified by the OBR data file. These two arrays, $[R]$ and $[T]$, enable one to recreate the plot produced by the OBR software in a programming language of our choice - we used Mathworks Matlab 2010a.

As aforementioned, conversion into a Length array, $[L]$ is performed via

the group index, $n_g$, as manually set in the OBR software, as so: $[L] = [T] \cdot c/n_g$, where $c$ is the speed of light in meters/nanosecond. During acquisition, user simply guesses at an expected $n_g$ - the default, chosen to describe optical fiber, is 1.500.

Since we are intending to obtain waveguide loss from the slope of the power vs. distance plot, the accuracy of the length scale is crucial, so correction of this assumed group index is necessary.

### 4.2.3.1 Group Index Correction

The first correction that must be performed on the data is accurate determination of $n_g$, since the user-defined value is only a guess. This correction can be performed via knowledge of the lithographically-defined length of the device. Due to the technique's sensitivity to reflections, the input and output facets of a waveguide device are easy to locate on an OFDR plot, which allows us to correlate the OFDR time-domain data to the known physical length of the device, as shown in Figure 4.10.

The user selects the highest reflection point on both facets, and this is used to scale the group index, time-scale and length scale of the data.

This correction also necessitates that the waveguide loss is low enough for IR light to propagate the entire spiral length. If this is not the case, then spiral bypass waveguides can be used to correct the modal index, and that modal index subsequently applied to correct spiral OFDR traces. This correction is fairly accurate, as the modal index should not change significantly, if at all, for identical waveguide geometries on the same chip.

It should be noted that some amount of loss measurement error stems from uncertainty in the group index, which is a result of error in the exact placement of the diced facets. As the actual waveguide is made longer, this

121
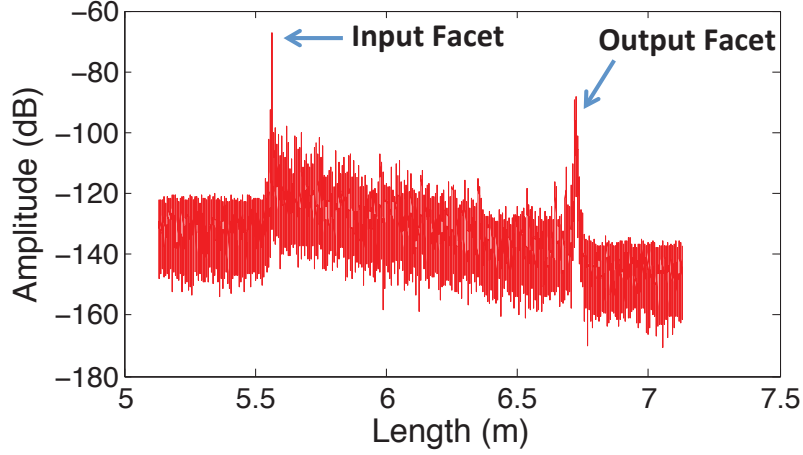
**Figure 4.10:** *Uncorrected OFDR plot for a fiber-coupled waveguide device with index-matching gel.*

facet position uncertainty becomes a smaller proportion of the total delay, and thus the length uncertainty is reduced. The major part of this error can be attributed to the dicing error, which we can place an upper bound on by assuming a length error of twice the width of the dicing kerf, which is 200 µm for the standard resnoid blades stocked by the UCSB nanofab. Jared Bauters showed in [9] that the group index error, $\delta n_g$ can be calculated with the following expression:

$$\Delta n_g \cong \left( \frac{1}{L^{actual}} \right) \left( \frac{\pm c}{2|f_{start} - f_{end}|} - n_g \delta L^{actual} \right) \tag{4.2}$$

where $L^{actual}$ is the lithographically defined device length, $n_g$ is the corrected group index. $f_{start}$ and $f_{end}$ are the start and end frequency sweep values which are 196.59 THz and 186.15 THz, respectively (about 1525 nm to 1610 nm).

### 4.2.3.2 Loss Measurement

With the length scale corrected, loss analysis can commence via determination of the slope of the OFDR power vs. length plot.

The large amount of random Rayleigh backscatter as in Figure 4.10 can obscure localized features, like point-scatterers caused by lithography errors or particulate defects. A moving-window averaging filter can make the trends and local features of the plot more apparent by removing the large noise band, and increasing the apparent length of each feature.

Figure 4.11 shows a typical workflow in the analysis of a 17.0 µm x 0.80 µm, $SiO_xN_y^{1.60}$-core waveguide.The smoothing performed in Figure 4.11(b) utilized a 50-point moving-window averaging filter, which corresponds to about 450 µm.

The smoothing reveals some point scatterers, likely due to lithographic errors and particulates present during the fabrication process. The user then chooses the region over which to perform a linear curve fit (c), and (d) shows the resulting linear curve fit performed with a least-squares fitting method. The choice of fitting region provides the user an opportunity to avoid point-scatterers if possible, as shown in Figure 4.12(a).

These point scatterers can significantly affect the resulting loss measurement, and in fact this illustrates the difficulty in achieving defect-free fabrication across an entire 100 mm wafer, where even micron-scale defects cause large optical scatter.

At worst, the scatterer can incur such high optical loss that the propagating power after that point is so low that the reflected backscatter is below the OBR sensitivity, as indicated in Figure 4.12(b). This figure also shows the noise floor of the measurement (determined by a fixed dynamic range), which makes the last segment of the waveguide appear to have a very low
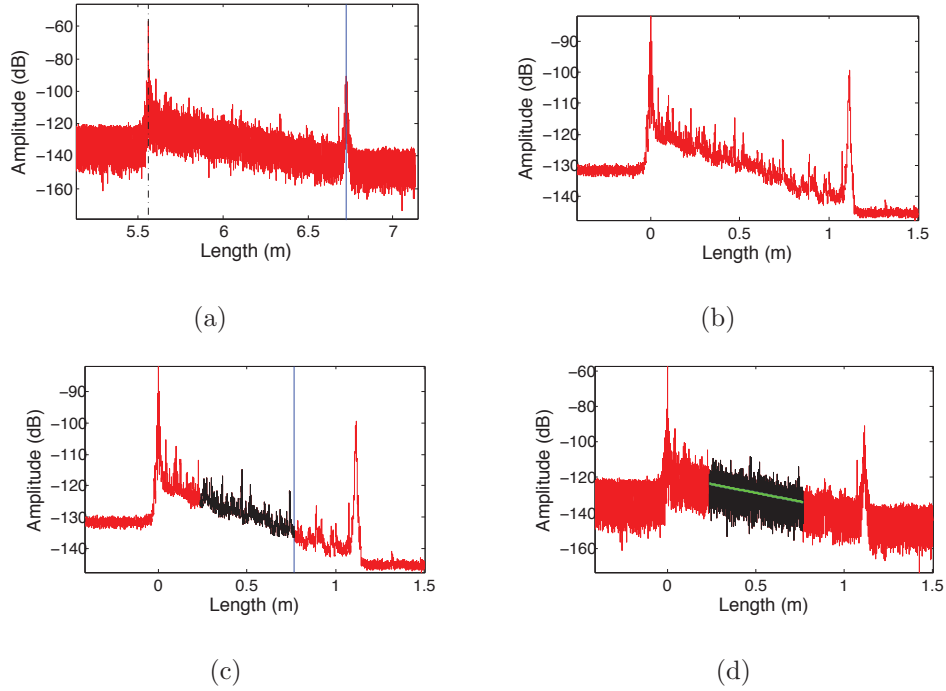
**Figure 4.11:** *(a) 17.0 µm x 0.80 µm SiO$_x$N$_y$$^{1.60}$-core waveguide, with group index corrected to n = 1.5668. (b) Smoothed with a 50-point (˜450 µm) moving-window averaging filter. (c) Curve fitting region selected, with some scatterers included. (d) Linear fit overlaid on unfiltered trace, measuring 9.7129 ± 0.023 dB/m.*
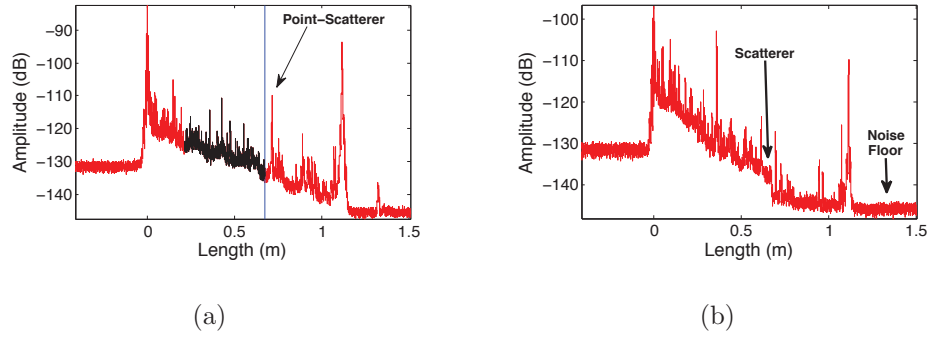
**Figure 4.12:** *(a) 16.0 µm x 0.80 µm waveguide, fitting around a scatterer.
(b) 10.0 µm x 0.80 µm waveguide, showing a high-loss scatterer.*

slope. For measurements close to the noise floor, such as this one, the fitting
region should be chosen far from the noise floor to avoid underestimating
propagation loss.

An additional source of error is the increased backscatter from localized
sidewall roughness. We have found that as a maskplate for contact lithog-
raphy is repeatedly used, some level of scum buildup occurs on the chrome
features, perhaps from repeated lateral sliding during the contact procedure.
This often manifests in an "oscillation" in the OFDR plots.

For a previous mask plate, after about 5 to 10 contact exposures (with
solvent cleaning between shots), each device began to exhibit these oscilla-
tions in the OFDR plot. Since each waveguide width in the bus is only 50
µm apart, plotting the reflectometry curves for each waveguide width on the
same axis would show any correlation between the physical location of these
oscillations.

Figure 4.13 shows that the locations line up perfectly for adjacent waveg-
uide widths, indicating the oscillations are clearly due a lithographically de-
fined roughness increase at certain areas around the spiral.        Optical
inspection of the MaskPlate confirmed this, with the reflectometry curves
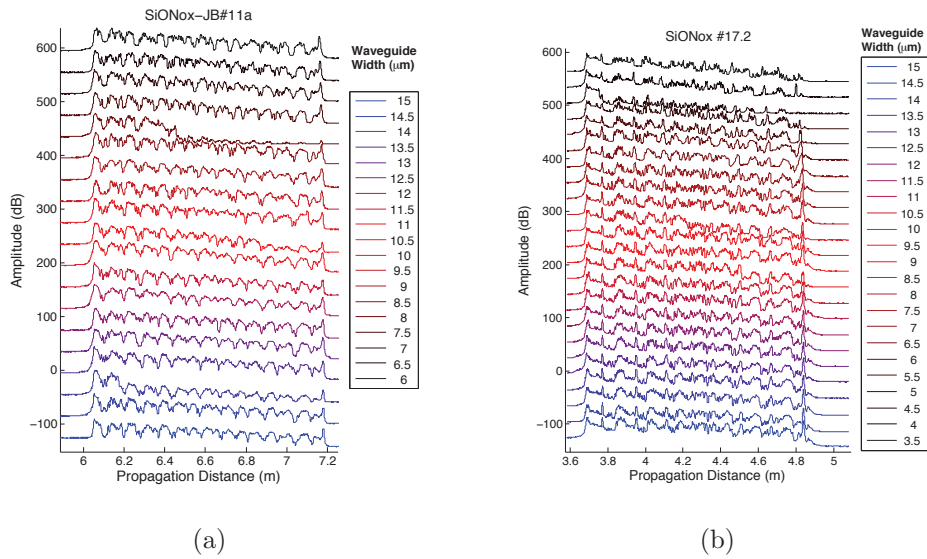
**Figure 4.13:** *(a) "Oscillations" in the reflectometry curve, which are shown to line up for adjacent waveguides. (b) Another device exposed with the same mask plate, showing similar oscillations and period despite different core geometry.*

effectively mapping out lithographic roughness over the 20 cm$^2$ area covered by the spiral. The rough photoresist shown in Figure 4.14 was located via the above reflectometry curves, and the corresponding areas on the mask plate were found to have photoresist scum built up on the chrome sidewalls, as shown in Figure 4.15.
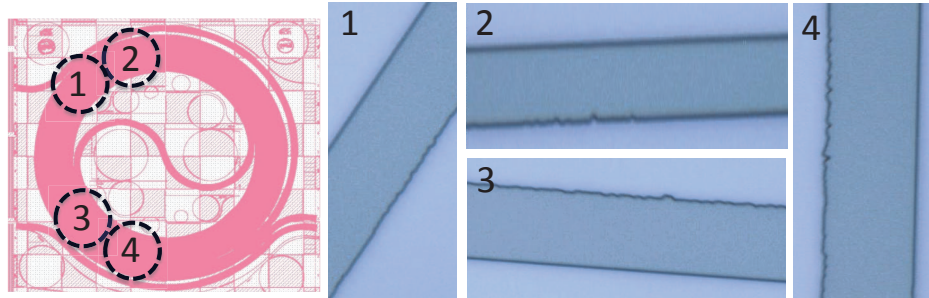


**Figure 4.14:** *A previous-generation mask plate (prior to non-stick coating) created rough photoresist on exposed wafers, located via the oscillations on reflectometry plots. Similar roughness was found on the mask plate itself. (Courtesy Renan Moreira)*

Since these humps do represent areas of higher scattering, they will increase the overall propagation loss. The problem of scum buildup on the contact mask plate was significantly alleviated through the use of a non-stick coating applied to the chrome side of the plate prior to first use. This coating also solved an issue with photoresist sticking to the plate and tearing off of the wafer, of causing the wafer to lose backside vacuum and adhere to the plate after contact. Once the scum has accumulated it must be removed via physical scrubbing, which we had done in a mask plate cleaning machine by the coating vendor, mostly recently by SÜSS MicroTec who provides the spin-on "MPT" coating after physical cleaning. However, even coated plates exhibit some amount of "oscillation" after many exposures, around 15 to 20
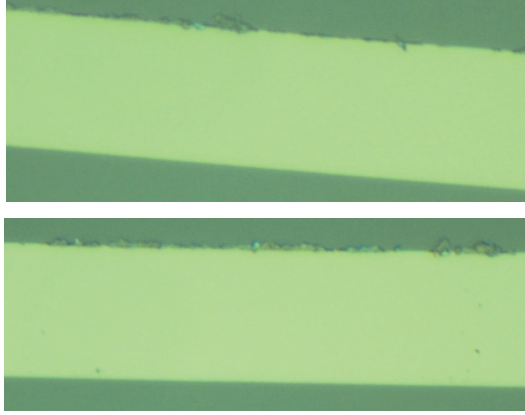
**Figure 4.15:** *Scum on the contact mask plate corresponding to the top and bottom regions of lithographic roughness.*

shots. This appears to be inevitable, and can be somewhat alleviated by sending out the plate for physical cleaning and re-coating every 10 shots or so (at a cost of about $500).

In the presence of these oscillations, even when they are mild (as is the case for MPT-coated plates after about 20 exposures), the curve-fitting can be greatly affected by the choice of fitting region. Care should be taken to choose regions that both avoid large scattering sites and also encompass enough oscillations to average over them.

## 4.3 Measurements of Directly-Etched Glass Waveguides

### 4.3.1 Fabricated Devices

Utilizing the previous simulations and materials measurements, we fabricated waveguides with Sputtered $Si_3N_4$-cores on thermally oxidized $SiO_2$ lower cladding, encapsulated in ICP-PECVD $SiO_2$ upper cladding. The Loss

vs. Bend Radius plot in Figure 2.17 (p. 51) shows that, for our maximum s-bend radius of 10 mm, the *width* : *thickness* aspect ratio should be between 150–200.

A 1.115 meter spiral test structure of 26 interleaved waveguides was fabricated, with guides for dicing included on the mask plate, as shown in Figure 4.16. The waveguide array consisted of evenly spaced waveguides with lithographically defined widths varying from 5.0 µm to 17.5 µm, in an Archimedean spiral configuration with bend-radii ranging from 18.55 mm – 29.1 mm and a central s-bend at a 9.756 mm bend radius. Due to the variations in core index caused by the stress of deposited upper claddings (described in Section 6), a conservative core thickness of 100 nm was targeted. A commercial company, KST World Corp., that stocked 15 µm thermally oxidized wafers was located and so these were purchased and utilized for all lower claddings even though thinner claddings may have been adequate. 10 µm of oxide requires wet oxidation at 1050°C for about 30 days, so it was helpful to locate a supplier that stocks these batch-oxidized wafers in large quantities. Their stocked 4-inch wafers are wet-oxidized from silicon substrates that are boron-doped to a resistivity of 5-10 $\Omega$-cm, which corresponds to a pre-oxidation concentration of 1.3E13 to 6.6E14 cm$^{-3}$ [10].

Due to the intermittent problem of particulate deposition on the IBD system (flaking due to the large number of depositions performed between chamber maintenance periods), the backup sputter tool, the AJA Int'l magnetron sputter system, was used to deposit 100 nm of $Si_3N_4$ directly onto the 4" thermal oxide substrate. 1 µm thick photoresist was spun and cured, and vacuum contact lithography was performed with the non-stick coated mask plate (to enable hard contact without the wafer adhering to the plate). After curing the photoresist at 95°C for 20 min., ICP-RIE etching with $CF_{4/}O_2$
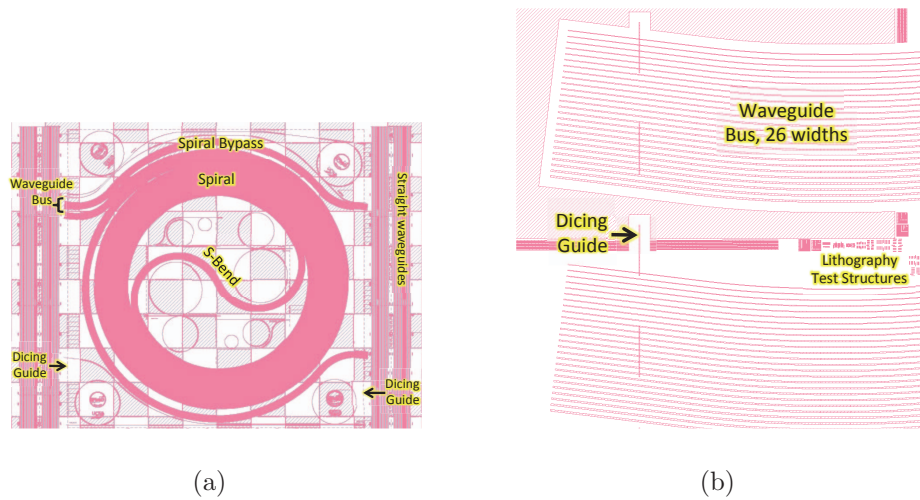
**Figure 4.16:** *(a) Mask plate layout for the fabrication of waveguides with the LOO Process. (b) Zoom of the waveguide facets and dicing guides.*

was used to remove the AJA Si$_3$N$_4$ in the lateral cladding regions, after which the photoresist was O$_2$ ashed, stripped with solvent and ashed again. With the defined waveguide core exposed, a 1 µm partial upper cladding of AJA SiO$_2$ was deposited and annealed at 1050°C, as annealed sputtered oxides were found to eliminate the growth "seams" at the top corners of the etched cores, as shown in Figure **??**. The upper cladding was completed by depositing ICP-PECVD SiO$_2$ in batches of 4 µm, with 1050°C, 3 hr. anneals in between each dep, until a cladding thickness of 11 µm was reached. In between each upper cladding deposition, backside SiO$_2$ was deposited with standard PECVD to alleviate some of the extreme wafer bow, as measured with a Tencor Flexus 2320 laser curvature measurement.

This fabrication process is described in detail in Appendix C.1 on page 238.

## 4.3.2 Group Index & Loss Measurements

As mentioned in the previous sections, it is necessary to choose fitting regions that avoided the many point-scatterers and, if possible, lithographic roughness oscillations. An example of the chosen fit region for one of the highest quality waveguides, the 10.5 µm with TM transmission, is shown in Figure 4.17. Some major defects are present near the output facet. Additionally, the exact location of the output facet is made difficult by the rounded facet reflection (at 1.1 m), possibly due to a damaged facet or the multi-mode nature of the guide (which causes numerous modes with different velocities to create many closely spaced time-domain reflections).
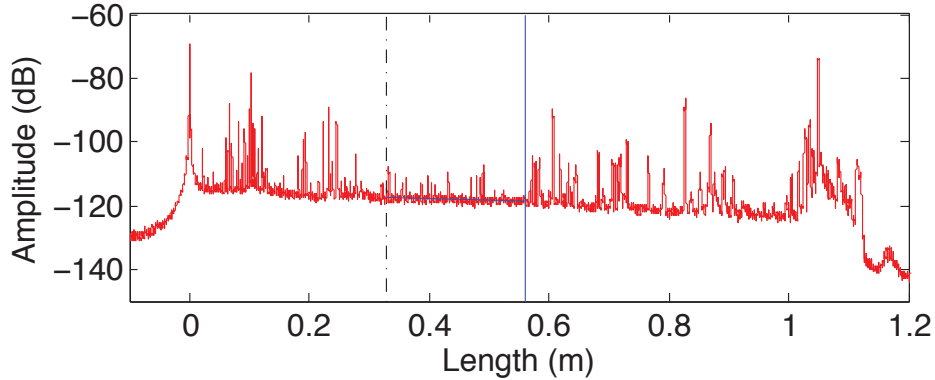


**Figure 4.17:** *Fitting region for the highest quality waveguide, the 10.5 µm wide core for TM transmission. The curve has been smoothed with a large 100-point window average.*

The aforementioned OFDR methods for length-scale correction were applied to obtain the group index of all 26 waveguide widths, for the output mode maximized for each polarization. The average error for these measurements, using equation (4.2) for each waveguide width, was 3.07E-4 and 3.06E-4 for the TE and TM polarizations, respectively.

Figure 4.18 shows an average group index of 1.6042 for the TE and 1.6031 for the TM modes. This confirms, that, as expected, the TM mode is less confined to the high-index core, with higher power overlap with the cladding oxide. The fact that the group index doesn't show a trend of increasing index with thickness indicates that the 5.0 µm width is still above the "squeeze-out" point – ie. all widths have relatively high modal confinement, and this confinement does not change significantly with increasing core width. If narrower widths were fabricated, we would expect to see $n_g$ decrease at smaller widths, as the mode is squeezed out of the high-index core.
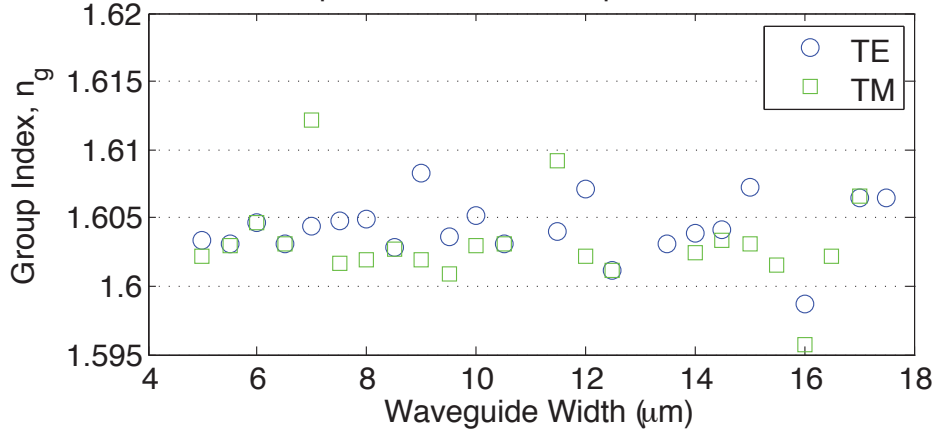


**Figure 4.18:** *Corrected group indices of direct-etched Si$_3$N$_4$-core waveguides for TE & TM polarizations.*

Simulations of these core geometries show that about 5 modes exist up to 6 µm wide (3 TE modes, 2 TM modes), gradually increasing to 10 modes in the widest 17.5 µm wide guides. Again, the actual reduction in the final core index, $n_{core}$, due to upper-cladding stress causes some overestimation of the simulated modes since we used the as-deposited core indices. This is confirmed by observation of the transmitted modes via the IR camera setup

previously described, which showed 1 TM & 1 TE mode in the narrowest, 5.0 µm wide guide, 2 TE modes & 1 TM mode for the 5.5 µm width and 2 TE & 2 TM modes for the 5.5 µm width - slightly fewer modes than simulated due to lower final core index than deposited. The scatter in $n_g$ values for wider widths is likely due to the fact that numerous modes with different velocities are contained within the OFDR output facet peak, such that the peak location could be identifying any one of the propagating modes.

Propagation losses for each width and polarization were obtained by fitting the relatively scatter-free regions of each waveguide, although slight oscillations due to mask plate scum and numerous scatterers from particulates/defects impart significant error to the linear fits. Figure 4.19 shows a consistently lower loss for the TM mode, which corroborates the group index hypothesis that the TM mode is less confined, which lowers the sidewall scattering loss.
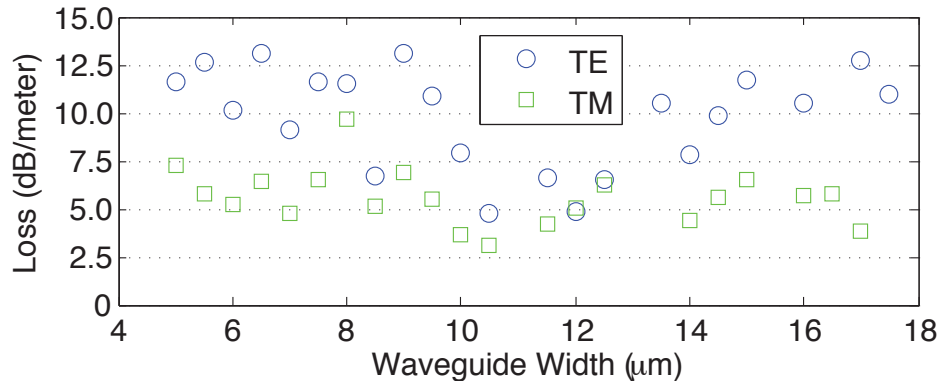


**Figure 4.19:** *$Si_3N_4$-core losses for each waveguide width. The 10.5 µm and 17.0µm wide guides show the lowest TM-mode losses, of 3.1 dB/m and 3.9 dB/m, respectively.*

The minimum losses measured here were for TM modes, with results of 3.1 dB/m for the 10.5 µm wide core, which also appeared to be free of
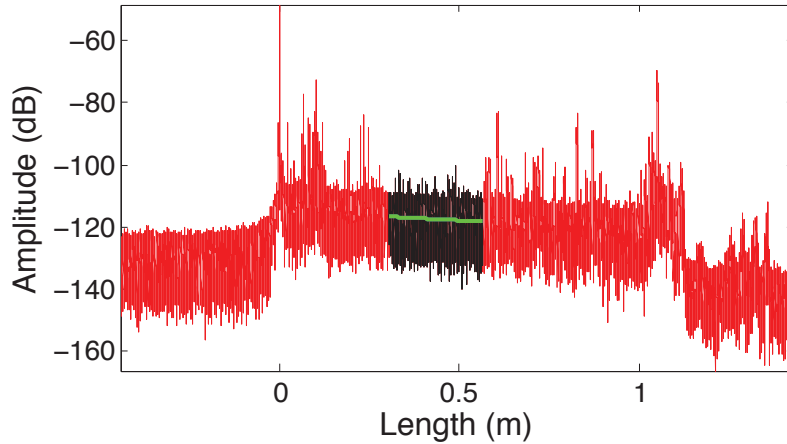
**Figure 4.20:** *Linear loss fit for the 10.5 µm wide guide, showing a loss of 3.078 ± 0.056 dB/m in the longest high quality region.*

lithography roughness oscillations. The linear fit is shown in Figure 4.20. The 10.0 µm guide and 17.0 µm guides also showed low TM propagation losses, of 3.6 dB/m and 3.8 dB/m, respectively.

Since polarization was not chosen at the input, but instead only observed at the output of the guide, we were concerned that the scatter between TE and TM mode losses might actually be attributed to polarization rotation as light propagates in the waveguide. After obtaining these OBR traces, the waveguide was re-measured to check for polarization rotation.

This was done by observing the output of a cleaved fiber with the polarizing beam splitter in-place, and maximizing the TM transmission (and minimizing TE transmission). Polarization control was performed with an Agilent 8169A POlarization Controller (PC), which polarizes the source light with an adjustable polarizer (maximized prior to measurements only), and then transmits the result through mechanically rotatable quarter–wave and half–wave retardation plates on birefringent crystal. The angles of the digitally–controlled quarter-wave and half-wave plates were recorded, which repre-

sent the polarization controller values required for TM polarized light at the launch site. The waveguide chip was then coupled to the fiber, without moving the fiber or altering the launch polarization. The polarization controller was then modified to maximize TM transmission through the chip, for the first few waveguide widths. Any change in the PC plates would indicate that the input polarization does not match the output polarization.

Interestingly, the half-wave plate appeared to make only small differences in maximizing or minimizing a particular polarization, and exhibited 8 period of maxima over the entire rotational range of -360°to +360° (ie. 2 full rotations of the plate). The $\lambda/2$–plate show a maximum in TM transmission every 91.1±2.2°. The half-wave plate caused the largest effect in maximizing or minimizing an observed polarization.

For the first 6 narrowest waveguides, from 5.0 µm to 7.5 µm, we found that the PC position remained almost constant for maximum TM throughput, at a value very close to that optimized for TM transmission on the cleaved fiber alone. Table 4.1 shows the rotational states of each waveplate for maximized TM transmission. All guides observed here were multimode, except for the narrowest, 5.0 µm wide core.

The average $\lambda/4$–plate value was -205.3±3.7° and the average $\lambda/2$–plate was 23.0±1.6°. The standard error calculated across all waveguides shows that very little polarization change occurred across waveguide widths. If polarization was indeed rotating, we would expect the width to have a large impact on the degree of rotation. Thus we believe that polarization is maintained.

This means that the scatter in the loss values is not impacted by polarization rotation, and thus is likely due to the error in slope fitting due to scatterers and lithographic roughness.

**Table 4.1:** *Polarization Controller states for maximum TM throughput for the launch fiber and 6 narrowest waveguides. Only the 5.0 µm width is single-mode for both TE & TM.*

| Waveguide | $\lambda/4$–plate | $\lambda/2$–plate |
|---|---|---|
| Cleaved Fiber | -195.3±0.3 | +13.9±0.8 |
| 5.0 µm | -209.5 | 28.8 |
| 5.5 µm | -197.5 | 25.3 |
| 6.0 µm | -195.9 | 22.1 |
| 6.5 µm | -199.0 | 22.1 |
| 7.0 µm | -198.4 | 22.1 |
| 7.5 µm | -216.4 | 15.5 |

### 4.3.3 Narrow-band OFDR Measurements

Each of the aforementioned $n_g$ and Loss values were effectively averaged over the entire wavelength range of the Luna OBR, from about 1525 nm to 1610 nm. In Section 3.2.2 we showed that the presence of SiN−H and SiO−H bonds can produce a wavelength-dependent loss via vibrational overtones, with resonance peaks for the SiO−H bond at about 1360–1380 nm, O−H at 1415–1430 nm, and N−H bonds at 1490–1520 nm and 1610 nm. The N−H peaks near 1510 nm tend to have the largest magnitude due to it's nature as a first overtone, as compared with the 2nd overtone nature of the other resonances in the communications band.

We realized that we could post-process the full-$\lambda$-range OBR binary data files to reconstruct narrow-band OBR traces from the full-range scans, by simply performing the FFTs on smaller wavelength ranges ranges of the initial data.

The benefit is that we can construct a loss vs. wavelength curve, which immediately reveals the presence of molecular vibrational resonances, and also allows us to fit the wavelength dependent losses to determine what the limiting loss mechanism is. We accomplish this by choosing a small range of wavelengths to reconstruct OBR data from (within the full-range 1525–1610 nm), and perform the standard group index and loss fits to that narrow-band OBR trace. We then move this narrow-wavelength window across the entire range in stepped windows, to obtain new OBR traces at wavelength range. We designate the OFDR wavelength range as $\Delta\lambda$, and the step size at which this range is swept across the acquired range as $d\lambda$.

Each time a new, reduced, wavelength window is chosen, the OFDR plot is recreated, and the typical procedure is followed - group index correction

via user-location of the facets followed by linear fit of a fitting region. For consistency, the fitting region is chosen at the start of the analysis, so the same region is always fit at each wavelength. For very high-loss wavelength ranges (eg. those close to a molecular vibrational resonance peak), the loss can be so high that some of the device and output facet lies below the noise floor, preventing accurate fitting at that range. For this reason, some low-wavelength points are often missing from the whole range, where the N−H bond resonance can cause losses to increase by orders of magnitude.

I described in Section 4.2.1 on page 112 that the smaller the scanned frequency range, the larger the time-delay spacing between acquired data points. Since some measurement error can be traced back to accurate determination of the group index, the spacing between datapoints directly affects the loss measurement error. Losses obtained with a small $\Delta\lambda$ will inherently have larger error. To illustrate this point, the lowest-loss TM-mode transmission for the 10.5 µm wide waveguide was analyzed with 3 different wavelength windows sizes of $\Delta\lambda$ = 2 nm, 4 nm and 10 nm. The step sizes corresponding to these window sizes are simply $d\lambda = \frac{1}{2}\Delta\lambda$ = 1 nm, 2 nm and 5 nm.

All three analyses are overlaid in Figure 4.21, which clearly shows the increased data scatter for narrower wavelength ranges. The average of losses for the 2 nm window is 3.3 dB/m, while the average for the 5 nm window (which excludes $\lambda$ < 1545 nm) is 2.70 dB/m. It is clear that the average losses are lower at higher wavelengths.

Averaging all loss values above $\lambda$=1595 nm, we calculate average losses (and standard errors) of 2.45 ± 0.34 dB/m, 1.83 ± 0.19 dB/m and 1.73 ±0.17 dB/m for $\Delta\lambda$ of 2 nm, 4 nm and 10 nm, respectively.

This data contains a lot of scatter for small $\Delta\lambda$, partly due to the litho-
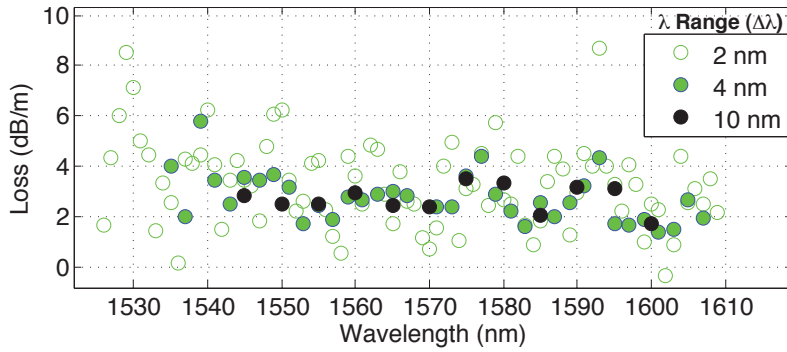
**Figure 4.21:** *Three different narrow wavelength range analyses overlaid, illustrating increased error with reduced wavelength range.*

graphic point-scatterers which reduce the fittable length-range, but also increased by the uncertainty in facet position from reduced spatial resolution. However, we can still visually identify at least 3 peaks in the spectrum, the largest of which appears to peak at lower wavelength than the acquired data. The left-most peak must correspond to the H−N−H stretching vibration identified by numerous researchers, which has been attributed to an increase in losses up to the dB/cm range around 1510–1520 nm (see previous discussion of molecular vibrational resonances on page 87)). A single gaussian curve can be used to fit this peak, with the center (peak) wavelength chosen as 1510 nm. The amplitude and width can then be varied to fit the data.

The two peaks near 1577 nm and 1593 nm don't correspond to molecular vibrational resonance peaks, and should not be assumed to be as such. (It is important that any gaussians chosen have a known physical cause, rather than simply adding more gaussians to obtain a better fit.) We believe that these two peaks represent a fabry-perot cavity of sorts created by scatterers or defects in the waveguide. The analysis of different widths, as shown in Figure 4.23 & Figure 4.22, shows almost the same positions for these spu-

rious peaks for very similar group indices, and seem to repeat across the whole spectrum, corroborating this theory and confirming that these repeating peaks should not be fit with gaussians for vibrational resonances. The period between resonance peaks corresponds to about a 35 µm cavity.

On top of these features is a general downward trend towards higher wavelengths, which is due to the wavelength-dependence of scattering loss (discussed in Section 2.1:*Sidewall/Surface Scattering Loss* on page 21). Rearranging the analytical expressions of Payne & Lacey shows that scattering loss should follow a $\frac{1}{\lambda^3}$ dependence, so a Laurent polynomial of order $-3$ was used to generate the scatter curve, and the coefficients of the scattering polynomial & N$-$H bond gaussian were varied to obtain the best fit to measured data (although no physical meaning to these coefficients can be inferred without more rigorous modeling of polarization, bend-modes and the resulting roughness and material overlaps).

Plotting both of these contributions along with the sum allows us to determine if either of these contributions limit the losses in different wavelength regimes.

The measurement error clearly makes definitive N$-$H curve-fitting approximate at best. In fact, although higher losses do appear to exist at lower wavelengths, the N$-$H contribution is much smaller than shown by previous researchers that utilized $SiO_xN_y$ cores. The use of sputtered $Si_3N_4$ appears to have reduced the Hydrogen-based losses down to the level of scattering losses. Additionally, the OBR spectral range does not encompass the N$-$H absorption peak, only the high-wavelength tail, which makes deterministic fitting impossible since the amplitude and width are indistinguishable without clear observation of the gaussian peak value or inflection points. For the 10.5 µm wide core, we did not include the N$-$H gaussian. Although it may

140
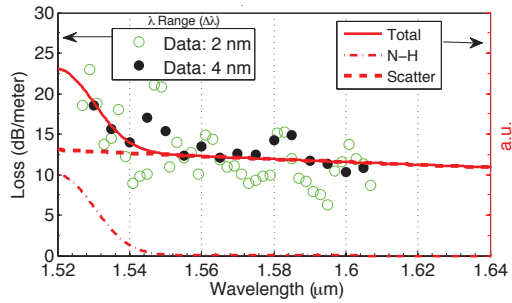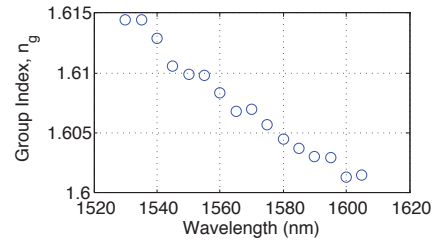
**Figure 4.22:** *(a) Fits of wavelength-dependent scatter and N−H absorption fits for the 5.5 µm wide guide for TE mode transmission. (b) $n_g$ vs. $\lambda$ for the same device & analysis.*
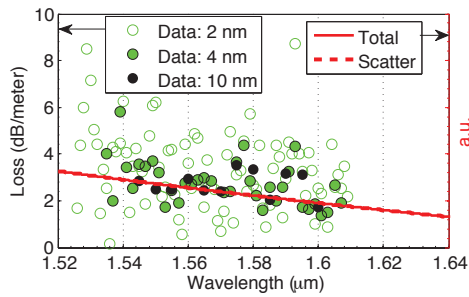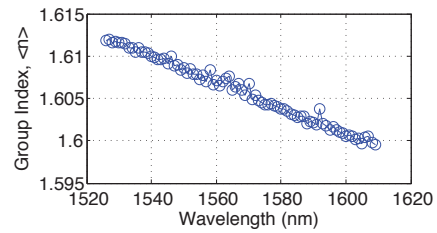


**Figure 4.23:** *(a) Similar fits for the 10.5 µm wide waveguide with TM mode transmission. (b) $n_g$ vs. $\lambda$ obtained during the analysis.*

affect losses at low wavelengths, the fitting error precludes the identification of a distinguishable peak.

The 5.5 µm wide core appears to be limited by N−H bond resonances below about 1560 nm, while both of these wavelength-dependent loss fits show that the losses are limited by roughness/scattering above 1560 nm.

## 4.4 Chapter Summary

In this chapter I showed that Optical Frequency Domain Reflectometry (OFDR) provided the most versatile, non-destructive and rapid measurement of waveguide losses, with the ability to measure losses into the fiber-like loss regime (sub-dB/m).

I described the theory of operation, and presented the analysis techniques for utilizing a commercial system to perform such measurements, the Luna OBR 4400.

The technique enables the measurement of effective group index ($n_g$) of propagating modes in addition to propagation loss, which provides a lot of information about the characteristics of a waveguide design. In particular, this yields information on the degree of modal confinement within the core material, for each waveguide measured.

Measurement techniques for obtaining separate OFDR acquisition of TE and TM modes, were described, enabling measurement of polarization-dependent propagation loss and group index.

Devices were fabricated with the knowledge obtained from previous chapters, utilizing 100 nm thick sputtered-$Si_3N_4$ cores, thermal oxide lower claddings and deposited ICP-PECVD upper claddings. Yield issues were discussed, illuminated by the position-dependent OFDR plots, which revealed the lo-

cations of scum on contact mask plates, present due to the large number of contacts undergone by a single plate.

Measurements of these devices showed relatively consistent $n_g$ values vs. core width, although error due to lithographic defect led to significant scatter in the data. The lack of significantly rising or dropping group indices indicated that confinement was relatively similar between waveguide widths. The multi-mode nature of most core widths also led to additional scatter due to the disparate effective indices of each higher–order mode. The TM mode seemed to have similar or lower confinement for each width, as indicated by the lower $n_g$ value.

Loss measurements for each waveguide width revealed that the TM mode consistently showed lower loss values, due to the lower confinement of TM modes (which was simulated in Figure 2.8 on p. 33). Lower loss due to lower confinement indicates either the prevalence of scattering due to roughness, or higher loss in the core material, presumably due to N−H bonds (which are not present in the cladding). The TM mode for a 10.5 µm core showed the lowest loss of 3.1 dB/m.

A narrow-wavelength OFDR technique was developed and used to obtain wavelength-dependent $n_g$ and Loss for two of the widths. This analysis, although made difficult by the measurement error, revealed a slightly higher loss at low wavelengths for the 10.5 µm & 5.5 µm wide guides, for TE and TM transmission, respectively. With this narrow-band technique, the losses were shown to be dominated by scattering loss above 1560 nm for the two widths analyzed, and possibly by N−H absorption below 1560 nm for the 5.5 µm wide core. Minimum losses, again for the TM-mode 10.5 µm wide core, were calculated as 1.73 ±0.17 dB/m when averaged over $\lambda$=1590–1600 nm (for $\Delta\lambda = 10\ nm$).

We have shown that, even at these large bend radii, the minimum losses are still dominated by scattering losses, which is corroborated by our work with identical geometries fabricated via an external foundry [11].

Thus, in the following chapters, we pursue novel methods for the reduction of sidewall roughness in the glass waveguide platform. According to the Loss vs. Bend Radius limit, this is also necessary to enable low loss for small-footprint devices, as scattering dominates waveguides with small bend radii.

# References

[1] R. Adar, Y. Shani, C. Henry, R. Kistler, G. Blonder, and N. Olsson, Measurement of very low?loss silica on silicon waveguides with a ring resonator, *Applied Physics Letters*, vol. 58, no. 5, pp. 444445, 1991.

[2] Y. Inoue, T. Kominato, and Y. Tachikawa, Finesse evaluation of integrated-optic ring resonators with heterodyne detection technique, *Electronics Letters*, 1992.

[3] T. Feuchter and C. Thirstrup, High precision planar waveguide propagation loss measurement technique using a Fabry-Perot cavity, *IEEE Photonics Technology Letters*, vol. 6, no. 10, pp. 12441247, 1994.

[4] B. J. Soller, D. K. Gifford, M. S. Wolfe, and M. E. Frogatt, High resolution optical frequency domain reflectometry for characterization of components and assemblies, *Optics Express*, vol. 13, no. 2, pp. 666674, Jan. 2005.

[5] Jozef Jasenek, "The theory and application of fiber optic sensors with spread parameters," Slovenská Technická Univerzita, Bratislava, Slovakia [Online.] Available: http://www.eaeeie.org/theiere_bratislava/3.html (Accessed 3/8/2012)

[6] J. K. Barnoski, S. M. Jensen, "Fiber waveguides: A novel technique for investigation attenuation characteristics", *Appl. Opt.*, vol. 15, pp. 2112 - 2115, 1976

[7] W. Eickhoff and R. Ulrich, Optical frequency domain reflectometry in single-mode fiber, *Applied Physics Letters*, vol. 39, no. 9, pp. 693695, 1981.

[8] Luna Innovations Inc., VA. (8/21/2009) "OBR 4400 Datasheet (Web)", LTOBR4400.REV.006.

[9] J. F. Bauters, M. Heck, D. John, and J. S. Barton, Planar waveguides with less than 0.1 dB/m propagation loss fabricated with wafer bonding, *Optics Express*, vol. 19, no. 24, pp. 2409024101, Nov. 2011.

[10] "Standard Practice for Conversion Between Resistivity and Dopant Density for Boron-Doped, Phosphorus-Doped, and Arsenic-Doped Silicon," ASTM Standards, No. F 723-99, 1999.

[11] J. F. Bauters et. al, "Ultra-low-loss high-aspect-ratio Si3N4 wavequides," *Optics Express*, vol. 19, no. 4, pp. 31633174, Feb. 2011.

# Chapter 5

# Etchless Definition of Waveguide Cores

Roughness has long been considered one of the largest contributors to waveguide loss [1, 2, 3]. In Section 2.4:*Loss vs. Bend Radius* on page 50 we showed that this is particularly true for designs aimed at tight bend radii and small footprint, where high-confinement geometries lead to high field values at the etched sidewalls. Additionally, the direct-etched $Si_3N_4$-core devices reported in the previous section were shown to be limited by scattering at most wavelengths.

Figure 2.17 (p. 51) reveals that although a very high width to height ratio can overcome the scattering loss limit, this always comes at the expense of bend radius and footprint [4]. This limiting roughness originates from lithographic roughness of photoresist and the ensuing dry etch. We concluded that the only way to enable ultra-low loss at small, millimeter-scale bend radii, was to reduce the scattering losses via sidewall roughness reduction.

Numerous methods have been developed to reduce the sidewall roughness of silicon-on-insulator waveguides [8, 9, 10, 11, 12], often based on the local

oxidation of silicon (LOCOS) process that is common to the CMOS electronics industry [13]. These methods only apply to silicon-core waveguides, and limited methods exist for the sidewall smoothing of glass-core waveguides (often referred to as Planar Lightwave Circuits, or PLCs) [5, 6, 7]. PLCs often utilize Silicon Oxynitride ($SiO_xN_y$) as the core material due to the tunability of refractive index via the mole ratio. It was shown in 1988 by Kuiper *et al.* that $SiO_xN_y$ and $Si_3N_4$ are also able to be thermally oxidized, although to our knowledge this fact has only been applied to Silicon LOCOS processes [14].

## 5.1   Fabrication Method

$SiO_xN_y$ is a common material for glass waveguide cores due to the easily tuned refractive index ($n$) from that of $SiO_2$ to $Si_3N_4$ (approximately 1.45 to 1.99), allowing a waveguide designer to control the optical mode confinement and propagation characteristics with ease. An $SiO_2$ cladding typically surrounds this core to provide the necessary index contrast. In this paper will refer to the entire spectrum of silicon oxynitrides, including stoichiometric $Si_3N_4$, as $SiO_xN_y$ or just oxynitride. A few researchers have investigated the oxidation of $SiO_xN_y$ with the intention of applying these materials as masks for the oxidation of silicon [15, 16, 14]. It has been shown that in a "wet" oxidizing ambient (containing water vapor) $SiO_xN_y$ will oxidize, showing a significant reduction in nitrogen content and consequent conversion of the material into $SiO_2$. It serves to reason that one could perform a diffusion-based oxidation of $SiO_xN_y$ waveguide core material, to selectively convert oxidized areas into cladding silica.

A typical LOCOS process uses Silicon Nitride ($Si_3N_4$) to mask areas of

148

a Silicon substrate, such that exposure to a high temperature ambient of oxygen or water vapor generates silicon dioxide ($SiO_2$) only in unmasked areas. The technique operates on the fact that $Si_3N_4$ has an extremely low diffusion coefficient for $H_2O$ or $O_2$ as compared with $SiO_2$, such that the oxidants will diffuse rapidly through the generated field oxide, but will be blocked in the masked nitride areas. Figure 5.1 shows the translation of the LOCOS process into a local oxidation of oxynitride (LOO) process, where thermally oxidized silicon is used as a lower cladding and $SiO_xN_y$ of arbitrary index is used as a waveguide core.

A stoichiometric $Si_3N_4$ film (with very low oxidation rate) is deposited and patterned as an oxidation mask, and a thin $SiO_2$ buffer layer is used to prevent direct etching of the core during this patterning. Standard contact lithography and dry etching techniques are employed in patterning of the nitride oxidation mask.

Thermal oxidation is carried out at temperatures ranging from 700°C to 1050°C in a quartz tube with an ambient of heated water vapor and high purity $O_2$, until the core is fully oxidized in the field. The nitride oxidation mask will also undergo oxidation, as indicated in Figure 5.1b, and so must be sufficiently thick to last throughout the oxidation step. Watch samples from the core deposition can be used to probe the oxidation step, to ensure that the desired core thickness reduction was achieved. Lastly the oxidation mask is removed with the same dry etch, and upper cladding is deposited via Plasma Enhanced Chemical Vapor Deposition (PECVD).

The full process follower is detailed in Appendix C.2 on page 270.
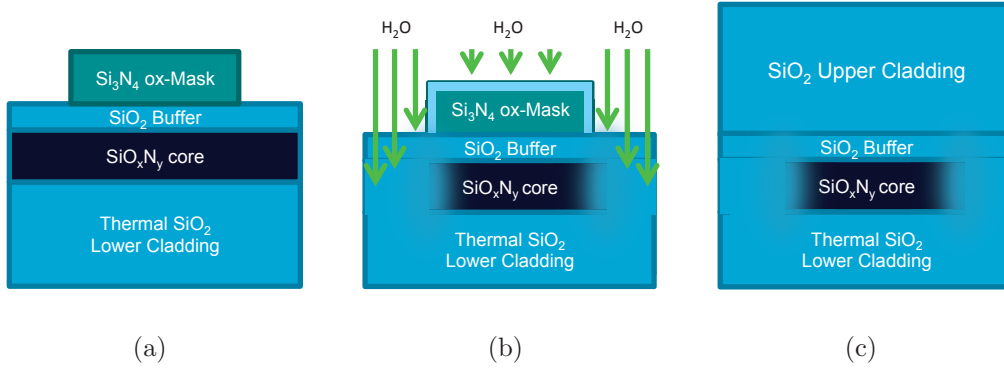
**Figure 5.1:** *(a) Fabricated Structure prior to oxidation, with core undefined laterally and oxidation mask defined via etching. (b) During wet oxidation the slow oxidation rate of $Si_3N_4$ blocks water vapor in the waveguide regions. (c) After the core is defined, the nitride oxidation mask is removed and upper cladding deposited.*

## 5.2 Roughness Reduction

Although previous researchers have used oxidation processes to improve waveguide sidewall roughness, little theoretical work has been done to analyze the mechanism in which this improvement occurs. Cardenas *et al.* were able to perform a qualitative post-fabrication roughness comparison between direct-etched and oxidized "etchless" silicon microstrip processes, showing an RMS surface roughness ($\sigma$) of 0.3 nm for the oxidized silicon core [11]. This appears to be lower than literature values of etched sidewall RMS [1], although their measurement is of planar surface roughness rather than sidewall roughness specifically.

In this section we will model this roughness reduction by envisioning the diffusion of oxidant into a surface as if the surface were covered with infinitesimally small point sources of oxidant, which diffuse spherically into the material. Considering the anisotropic nature of thermally driven molecular

diffusion, and the common assumption made in the Deal-Grove oxidation model that any oxidant reaching an oxidation site will react, the spherical point-source model seems reasonable to a first approximation. This model would move the entire oxidation front through the material with an abrupt interface between the oxidized and unoxidized materials. When applied to a local oxidation, where an oxidation mask is used (Figure 5.2a), spherical diffusion will proceed from the etched line-edge of the oxidation mask. The radial nature of this diffusion will cause the pattern transfer of the etched line edge to be smoothed as it is replicated in the oxidation front.

In Figure 5.2b, we obtained the line-edge roughness of an etched 50 nm $Si_3N_4$ oxidation mask with atomic force microscopy (AFM) and an edge-detection algorithm. The points along the line-edge were used as the centers of circles with radius 20 nm (for illustration purposes), of which the superposition represents the oxidation front advancing towards the waveguide core, as indicated by the red dashed line. This is the new line-edge roughness of the waveguide core.

The radii of these diffusion fronts can be physically altered by varying the $SiO_2$ buffer thickness, which effectively controls how far past the etched line-edge oxidant must travel before it reaches the core material. In reality a diffusion radius much larger than 20 nm must be used, as the oxidation buffer layer must also allow for slight overetching of the oxidation mask while protecting the core layer from direct etching. In practice, a minimum buffer of 200 nm was used, with an upper limit of a few microns before thin-film stress becomes an issue at elevated oxidation temperatures. Figure 5.3a shows the simulated line-edges for various diffusion radii extending from the etched line-edge.

The root-mean square (RMS) roughness, $\sigma$, and correlation length, $L_c$,
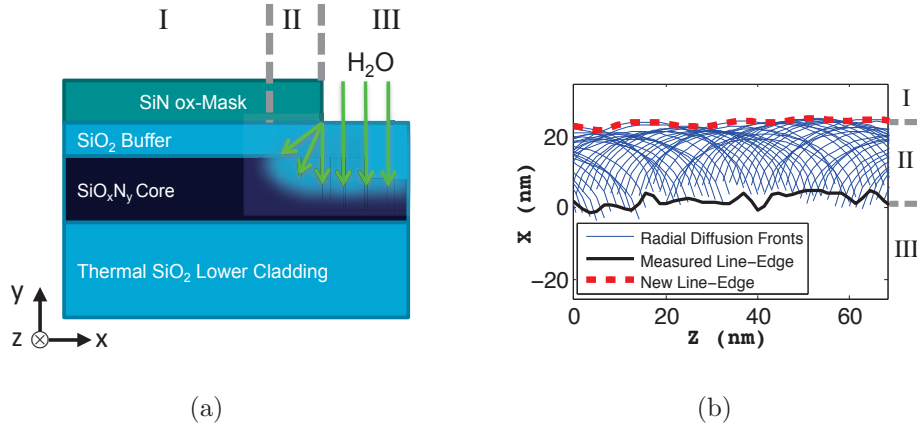
**Figure 5.2:** *(a) Schematic of the diffusion of water vapor from the edge of the oxidation mask, converting the core material into cladding silica. Region I and III will be the core and cladding regions, respectively, while region II is where oxidant radially diffuses under the oxidation mask, defining the core sidewall. (b) Simulation method for determining the line-edge roughness of the waveguide core, where Z is the direction of light propagation within the waveguide. The blue lines represent the spherical diffusion fronts of oxidant, for a 20 nm radius, which combine to form the oxidation front at the red dashed line.*

(a)                      (b)
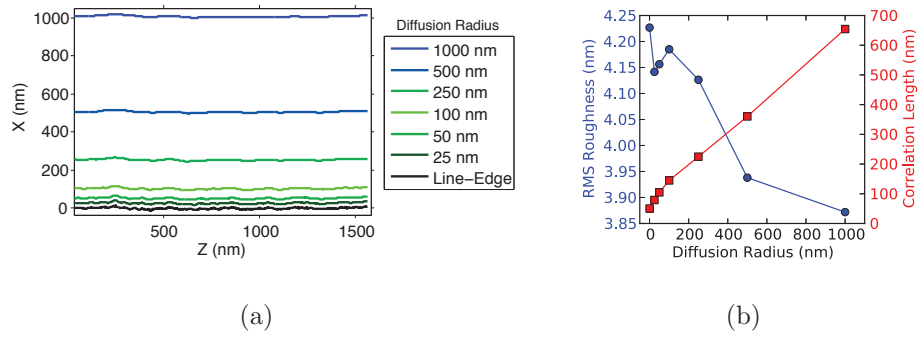
**Figure 5.3:** *(a) Simulated line-edge for various diffusion radii, and (b) the corresponding RMS roughnesses (circles and exponential correlation lengths (squares). Diffusion radius is approximately analogous to the thickness of the $SiO_2$ oxidation buffer layer.*

were extracted via the standard deviation and Wiener-Khintchine relations, respectively [23]. Only exponential autocorrelation functions (ACFs) are reported here, as Gaussian ACFs did not yield reasonable fits, which indicates the prevalence of small-scale roughness [24]. The initial etched line-edge possessed roughness values of $\sigma = 4.23$ nm and $L_c = 51.42$ nm (which agrees well with reported values), as shown in Figure 5.3b.

The figure reveals reduction in the RMS roughness with increasing diffusion radius, along with a drastic increase in correlation length, which is may have a much larger impact on the scattering loss than $\sigma$ alone, as shown by the simulations in Figure 5.4.

Depending on the fabrication process, fabrication could yield edges with much finer roughness that the photoresist line-edge shown above. For example, very deep etches of $SiO_2$ or $SiO_xN_y$ often require metal hard masks such as Chromium for their high selectivity to fluorocarbon etchants. Figure 5.5 shows an SEM of electron-beam evaporated Cr, and the resulting nanoscale grain, which can result in sidewall roughness with finer roughness.

153
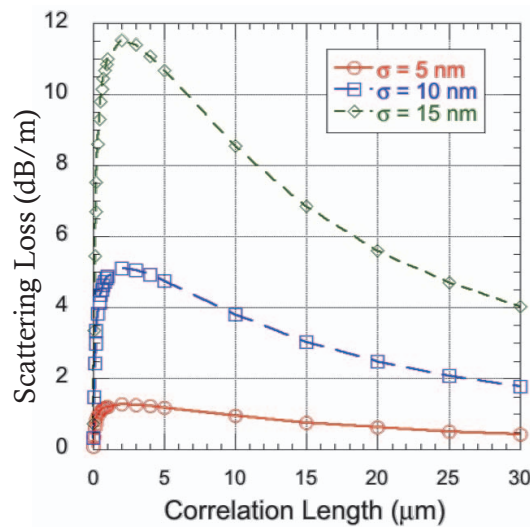
**Figure 5.4:** *Simulated scattering loss with sidewall roughness $\sigma$ & $L_c$.*
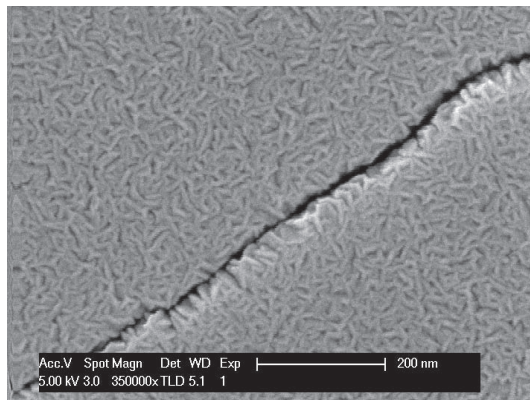


**Figure 5.5:** *Chromium deposited with electron-beam evaporation for use as an etch mask, showing very fine grain roughness.*

In this case, the line-edge can experience a much greater improvement when an oxidation process is used to smooth the transferred pattern. Figure 5.6 presents simulations of a much rougher line-edge, with higher initial RMS values. Curve-fits of the ACFs for these scans were not adequate for determination of correlation lengths at each diffusion radius.

Of note is the fact that the oxidation quickly reduces the RMS roughness
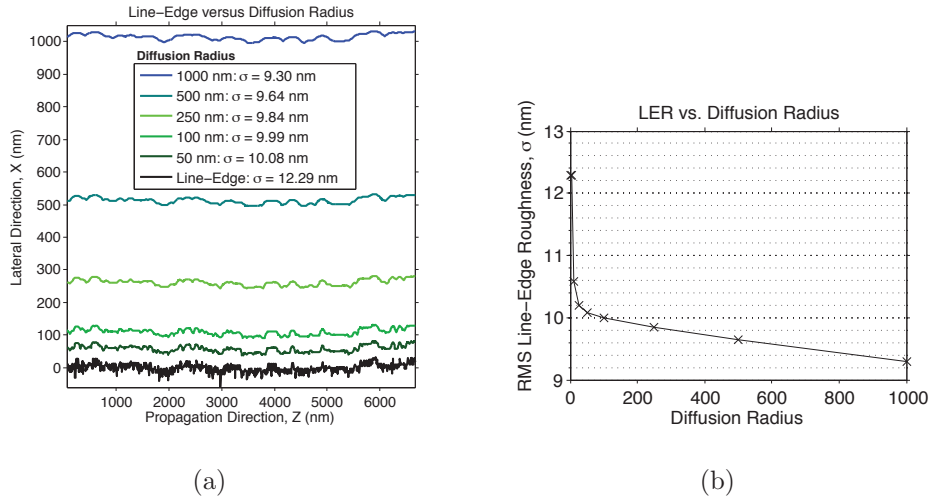
**Figure 5.6:** *(a) Smoothed line-edges created with varying diffusion radius. Line-edges are calculated with the originating point sources along the initial measured line-edge (in black). (b) Reduction of RMS line-edge roughness with increasing diffusion radius. Radius of zero represents the original, etched line-edge.*

by about 25% after only 100 nm of oxidation, but $\sigma$ is reduced by less for increasing radius (illustrated by Figure 5.6b).

The diffusion radius simulated here can physically be controlled by choosing the thickness of the oxidation buffer, which determines how far diffused $H_2O$ must travel before it reaches the material to be oxidized (either $Si_3N_4$ or $SiO_xN_y$). Care must be taken to ensure the oxidation buffer is thick enough to prevent direct etching of the core during removal of the oxidation mask, as dry-etches of $Si_3N_4$ do in fact etch $SiO_2$, often faster than $Si_3N_4$.

## 5.3 Thermal Oxidation of $SiO_xN_y$

### 5.3.1 Oxidation Rate

Kuiper *et al.* found in [16] that that the mechanism that transforms $Si_3N_4$ into $SiO_2$ requires water vapor. They note that in a dry oxidation (utilizing only gaseous $O_2$) $Si_3N_4$ does not oxidize, and $N_2$ implanted in silicon does not react when annealed while $NH_3$ does combine with silicon, so the hydrogen component is necessary for the oxidation reaction to proceed. The previous research into the oxidation of $SiO_xN_y$ films used ERD and RBS (Elastic Recoil Detection and Rutherford Backscattering Spectrometry) and confirmed that the oxidation process relies upon the presence of $H_2O$ and generates ammonia as a by-product ($NH_3$). The chemical reaction is thus believed to proceed as follows:

$$Si_3N_4(s) + 6\,H_2O(g) \longrightarrow 3\,SiO_2(s) + 4\,NH_3(g) \tag{5.1}$$
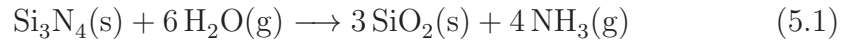
This equation states that the gaseous oxidant, water vapor, replaces nitrogen within a solid silicon nitride molecule, creating solid silica and gaseous ammonia as a byproduct. In the case of $SiO_xN_y$, we can envision this oxidation as occurring to single $Si-N$ bonds within the various $Si-O-N$ bonds present in the material.

Kuiper *et al.* concluded that the rate of $Si_3N_4$ oxidation is reaction-limited, in light of the high bond strength of $Si-N$ as compared to $Si-Si$. They also found that the removal rate of the large gaseous oxidation products ($NH_3$) from the reaction interface played a significant role, by shifting the equilibrium of (5.1). This can be visualized as the generated ammonia molecules blocking oxidant at the reaction sites until they are removed.

Thus the oxidation rate proceeds linearly with time (at least for thin films). Since these rate limiting $NH_3$ molecules are generated at the breaking of each Si-N bond, the oxidation rate is highly dependent on the $SiO_xN_y$ mole ratio, where higher nitrogen content (and higher refractive index) will result in lower oxidation rates. Of course, the temperature dependence follows an Arrhenius equation owing to the dependence on diffusion for transporting both the oxidant and reaction products.

In those early studies, the exact thickness of oxide generated had to be inferred from the atomic concentrations measured by ERD and RBS. Additionally, little knowledge was gained on the refractive indices of the remaining oxynitride or generated oxide.

In order to apply this technique to the fabrication of optical waveguides, we performed a similar oxidation characterization but used spectroscopic, variable-angle ellipsometry to measure the thickness and index of the $SiO_xN_y$ and thermal oxide. We found that a two-film Cauchy model accurately described the ellipsometry measurements of partially oxidized $SiO_xN_y$ films (on either Silicon or Sapphire substrates), where the top-most film represented thermally generated oxide and the lower film is the remaining oxynitride film. Ellipsometric curve-fitting of partially oxidized films yielded top layers with refractive indices of about 1.45, while the lower layer exhibited indices closely matching those of the original film, indicating that the interface between the deposited oxynitride and the generated thermal oxide is relatively abrupt (similar to the oxidation of silicon). $SiO_xN_y$ films were prepared by the high-density ion beam assisted sputter deposition (IBD) described in[17], with a variable $O_2/N_2$ gas flow ratio into the assist ion beam chosen to produce different refractive indices. All samples underwent a post-deposition anneal at 1050°C in an inert nitrogen environment to relax these high density films,

157

which results in a reduction in refractive index of about 0.03-0.05, owing to the Lorentz-Lorenz relationship between density and refractive index. Film thicknesses were kept below 350 nm to avoid film delamination at the high oxidation temperatures.

Oxidations were performed in an Tystar Tube Oxidation/Annealing system with quartz hardware able to accomodate 200 mm wafers. A standard steam oxidation recipe was used, with 200 sccm of $O_2$ bubbled through deionized water heated to 250°C, with a water drip rate of 3 mL/min.

Spectroscopic ellipsometry was used to characterize the oxidations rates at 700°C, 950°C and 1050°C, for oxynitrides of various indices, where the refractive index correlates to the Oxygen to Nitrogen ratio of each film (ie. higher index indicates higher nitrogen content)[18]. Figure 5.7 shows representative plots of 950°C oxidations of three different oxynitrides, including $Si_3N_4$ (refractive index at 1550 nm, $n_{1550} = 1.96$). The three curves plotted show the measured thermal oxide thickness, the reduction in thickness of the $SiO_xN_y$ (amount of $SiO_xN_y$ consumed), and the increase in the total film thickness. The latter is included because we observed that the sum of the two glass films exceeds the thickness of the original film, indicating either that oxide occupies a larger volume than oxynitrides, or that the film contains significant amounts of water or ammonia after the treatment. Oxidation rates are determined with linear fits, as indicated, although in the case of Silicon Nitride oxidation at 950°C a slight deviation may be present, indicating rate-limiting by diffusion of oxidant through the thermal oxide.

The oxidation rate strongly depends on the index of the original film, as shown in Figure 5.8, which may also be attributed to the fact that higher concentrations of Si-N bonds in more nitride-like films will produce more $NH_3$ upon oxidation, slowing the diffusion of oxidant. The temperature de-

Thermal Oxide Thickness

$n_{1550}$

▲1.59

◆1.67

■1.96

Thickness (nm)

147 nm/hr

18.1 nm/hr

2.52 nm/hr

Oxidation Time (hrs)

Consumed SiO$_x$N$_y$

Thickness (nm)

121 nm/hr

14.3 nm/hr

1.81 nm/hr

Oxidation Time (hrs)

Total Thickness Increase

Thickness (nm)

25.3 nm/hr

3.75 nm/hr

0.933 nm/hr
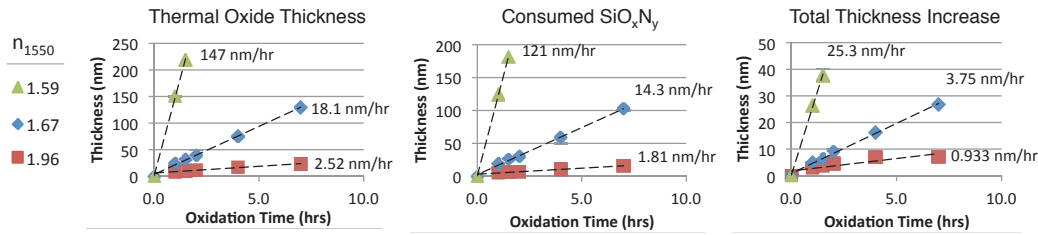
Oxidation Time (hrs)

**Figure 5.7:** *A representative dataset for steam oxidation at 950C is shown for three refractive indices with linear rates indicated. (a) Shows the thickness of generated of thermal oxide versus oxidation time, (b) plots the rate of SiOxNy consumption, and (c) shows the increase in total film thickness (SiO2 + SiOxNy) relative to the initial film thickness. Similar curves were acquired for other temperatures and refractive indices.*

pendence can also be seen in Figure 5.8, although the oxidation rates were too small to be detected for high-index nitride at the lowest temperature of 700°C, and the rates for low index films ($n_{1550} \leq 1.60$) at 1050°C were so high that the 300 nm films were fully oxidized after even the minimum stable oxidation time of 30 m (greater than 600 nm/hr).

## 5.3.2 Role of Ammonia

All dual-film fits showed the expected refractive index of 1.44 to 1.45 for the generated oxide except for the 700°C oxidations of Si$_3$N$_4$ and the SiO$_x$N$_y$ with $n_{1550}$=1.67 (SiO$_x$N$_y$$^{1.67}$), both of which showed thermal oxides of higher indices. 700°C thermal oxide for the SiO$_x$N$_y$$^{1.67}$ film had an index of 1.50-1.58, while the oxide for Si$_3$N$_4$ showed an index of 1.83 after 5 hours of oxidation at 700°C, which gradually dropped to 1.60 after 22 hours. The Si$_3$N$_4$ film did not exhibit oxide generation beyond 5 nm, even though the index of the oxide continued to fall.

159

Thus it appears that, at 700°C and for higher concentrations of Si−N bonds, the oxidized film retains a considerable nitrogen content. In both cases some oxidation appears to have occurred, as exhibited by the reduced refractive index of the thermal oxide. Either the top



**Figure 5.8:** *Linear oxidation rates for a range of temperatures and indices.*

film did not absorb enough $H_2O$ to fully oxidize it or the out-diffusing ammonia was not mobile enough to exit the film and allowed the $NH_3$ to re-bond to the solid glass. For the $n_{1550}=1.67$ oxynitride, the latter seems more viable as it has been shown that the diffusion coefficient of ammonia is far lower than that of water vapor, and that ammonia causes the nitridation of silica at high temperatures [14, 19].

For the $Si_3N_4$, however, it is possible that both situations are at play simultaneously, such that the higher production of ammonia in this nitrogen-rich film required a longer time for the oxidant and product diffusions to reach equilibrium transport. That is, water vapor diffusing slowly into the film performs oxidation while the out-diffusion of ammonia builds up, until the flows stabilize with both oxidation and nitridation reactions occurring.

### 5.3.3   Thickness Increase Due to Oxidation

We have found that the oxidized $SiO_xN_y$ occupies more space than the original $SiO_xN_y$ film, as exemplified by the thickness increases in Figure 5.7c. That is, the Si-O bond appears to be larger in volume than the Si-N bond. In the silicon LOCOS process, the same effect results in the formation of a "birds beak" profile in the masked silicon, due to deformation of the oxi-

**Figure 5.9:** *Percentage expansion of thermally oxidized $SiO_xN_y$.*
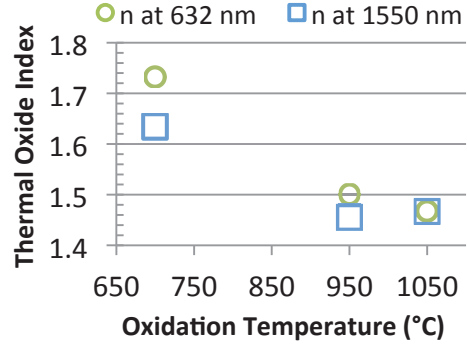
**Figure 5.10:** *Thermal oxide index vs. oxidation temperature for $Si_3N_4$.*

dation mask as the oxidized silicon expands. We expect a similar effect to occur in our local oxidation of $SiO_xN_y$ process. This will inevitably lead to changes in the waveguide core geometry and sidewall profile, and is worth investigating further.

It is a reasonable assumption that the underlying oxynitride does not contribute to the observed thickness increase, as any significant absorption of oxidant should be accompanied by a refractive index change, which was not detected. Consequently, if the thermally generated oxide is solely responsible for the thickness increase, then the increase in total film thickness divided by the amount of oxynitride consumed yields the percentage thickness increase of the thermal oxide alone.

The theoretical increase in thickness upon oxidation can be found by taking the ratio of molar volumes for $SiO_2$ and $Si_3N_4$ and the appropriate number of moles from (5.1) (thanks to Brandon Knott for help with this calculation). The molar volume, $V_M$, for a particular compound is given by

$$V_{M_x} \ (cm^2/mol.) \ = \ \frac{atomic \ mass \ (g/mol.)}{mass \ density \ (g/cm^3)} = \frac{M_x}{\rho_x} \qquad (5.2)$$

which indicates how much space a mole of the compound occupies. The

balanced chemical equation in (5.1) shows that the mole ratio of $SiO_2$:$Si_3N_4$ is 3:1, so the expected volume expansion when $Si_3N_4$ is converted to $SiO_2$ is given by:

$$Expansion\ Ratio = \frac{3\ V_{M_{SiO_2}}}{1\ V_{M_{Si_3N_4}}} = \frac{3\left(M_{Si} + 2M_O\right)/\rho_{SiO_2}}{1\left(3M_{Si} + 4M_N\right)/\rho_{Si_3N_4}} \tag{5.3}$$

Mass density of thin-films varies considerably depending on the deposition technique and parameters, which causes some variation in the calculation. Depending on the sources used to report mass density information, the percentage volume increase is calculated to be between 62.3% and 81.0% [17, 20, 21]. This value of expansion ratio would be exhibited in the oxidation of stoichiometric $Si_3N_4$ only, and should be less for $SiO_xN_y$ films with lower nitrogen content.

Figure 5.9 shows the average thickness expansion measured for the range of temperatures and indices oxidized in this study. The $Si_3N_4$ films $(n_{1550}{=}1.95)$ oxidized at 1050°C falls within the expected range. The $Si_3N_4$ oxidized at 950°C, however, appears to have expanded slightly less than predicted, signifying that at 950°C the thermal oxide likely contains residual Si-N bonds that were not oxidized. If this were true, analysis of the refractive indices should yield some information on whether these unoxidized Si–N bonds are present in the thermal oxide.

Sure enough, closer inspection of the thermal oxide refractive indices at each temperature show that the lower the oxidation temperature, the higher the index, indicating higher residual nitride concentrations in the generated oxide (shown in Figure 5.10). As aforementioned, previous researchers have shown that $SiO_2$ can undergo nitridation in ammonia environments, and also that ammonia (being a larger molecule than water) has a lower diffusion

coefficient [19, 14]. It is possible, therefore, that the large $NH_3$ molecule requires high temperatures to efficiently diffuse through the thermal oxide – but at lower temperatures, the molecule has a higher probability of re-bonding within the $SiO_2$ film, resulting in $SiO_xN_y$ in the top layer. Thus, a higher temperature is necessary to ensure production of pure $SiO_2$, due to more efficient removal of ammonia at higher temperatures.

### 5.3.4 Application to Waveguide Core Definition

In regards to the fabrication of waveguides, the previous characterization yields a few important observations. First, that depending on the refractive index of the oxynitride used, a different oxidation temperature may be appropriate. In particular, for higher nitride concentrations with refractive indices above about 1.68, temperatures of 950°C and above are best, while for lower nitride concentrations, temperatures below 950°C should be utilized for accurate process control (requiring oxidation times greater than 30 min). Additionally, utilizing the highest temperature feasible will result in a lower index $SiO_2$ film being produced, as opposed to a partially nitride film. Ideally, this lateral oxynitride slab should be accounted for in the waveguide design, as bend loss would be impacted.

Secondly, a significant concentration of hydrogen-based molecules ($H_2O$ and $NH_3$) may be left in the films, which will increase propagation losses due to O-H and N-H molecular vibrations. Performing the oxidation at higher temperatures will reduce this effect (by reducing residual ammonia), and additional annealing in an inert environment after the oxidation step can desorb much of this residual hydrogen [22].

Lastly, the "birds beak" effect from the volume expansion of oxidized oxynitride will affect the sidewall geometry for a core defined by the local

oxidation of $SiO_xN_y$. This effect can be simulated in process simulation software such as Silvaco Athena, with the appropriate rate and expansion ratio obtained from Figure 5.9, allowing for more accurate prediction of the optical propagation characteristics.

A similar oxidation experiment was carried out for ICP-PECVD $SiO_xN_y$, but ellipsometry results were not nearly as conclusive. The simple two-layer Cauchy model did not yield predictable oxidation rates and indices for anything other than low nitrogen-content $SiO_xN_y$, for $n_{1550} \leq 1.60$, perhaps due to the high hydrogen content of these films – although the exact mechanism remains to be investigated. However, for low refractive indices, ICP-PECVD films may be used and oxidized in a repeatable manner.

### 5.3.5 SILVACO Parameter extraction

In order to obtain digital index profiles that accurately describe these waveguides, we utilized the characterizations in Section 5.3 to determine the necessary coefficients governing oxidation simulations in SILVACO Athena, based on the Deal-Grove Model [25].

The rate coefficients are defined as so:

$$T_{ox} \approx \left( \frac{B}{A} \right) \ (t + \tau) \tag{5.4}$$

and

$$T_{ox}^2 \approx B \ (t + \tau) \tag{5.5}$$

which describe the linear and parabolic oxidation rates, respectively. $T_{ox}$ is the grown oxide thickness, $t$ is the oxidation time and $\tau$ is the time required to generate any existing oxide [26]. The empirical values $\left( \frac{B}{A} \right)$ and $B$ are called the linear and parabolic rate coefficients, respectively.

164

Since the rates we measured were predominantly linear, the parabolic rate coefficients can be set to zero. Additionally, $\tau$ can be set to zero, as the value is typically used to account for the native oxide on a silicon surface, which is nonexistent or negligible for an $SiO_xN_y$ surface.

The temperature dependence of the rate is defined by an Arrhenius equation, which, for the linear rate coefficient, is as follows:

$$Rate = \left(\frac{B}{A}\right) = C \ e^{\frac{-E_A}{k_b \ T}} \tag{5.6}$$

An exponential curve-fit of the oxidation rates at different temperatures from Figure 5.8 will yield the activation energy, $E_A$ and the "exponential prefactor", $C$ for a particular refractive index. $k_b$ is the Boltzmann constant and $T$ is the oxidation temperature. Units should be in micrometers/hour, electron volts and °Kelvin for the rate, activation energy and temperature, respectively. $E_A$ and $C$ translate into the Athena oxidation variables $LIN.L.E$ and $LIN.L.0$, respectively, assuming that the Break temperature ($L.BREAK$) is chosen to be higher than the oxidation temperatures involved here (so that only the "low" rate coefficients are used).

For the case of $n_{1550} = 1.626$ (ie. $SiO_xN_y{}^{1.63}$), we calculated $C = 8 \cdot 10^4 \frac{\mu m}{hr.}$ and $E_A = 1.51 eV$.

The expansion ratio, can be determined from Figure 5.9, to calibrate the $ALPHA$ parameter (also set in the $OXIDE$ statement), which should be set to correspond with the 22% expansion ratio found for the same refractive index $SiO_xN_y$.

Simulation of this system must be performed with polysilicon used in-place of the $SiO_xN_y$ material, as the tool can only oxidize silicon or polysilicon. The tool is also unable to simulate the oxidation of the $Si_3N_4$ oxidation
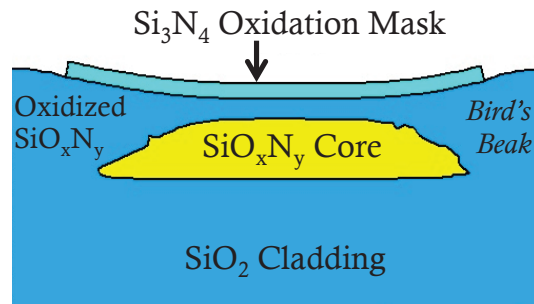
**Figure 5.11:** *Simulated core geometry for a 500 nm thick core defined by selective oxidation with a 4 µm wide oxidation mask.*

mask during a wet oxidation - an effect which could impact even CMOS process simulation. However, the very low rate of mask oxidation has only a small effect on the resulting core shape, which is dominated by the effect of volume expansion during oxidation.

The simulated core geometry is shown in Figure 5.11, with the "bird's beak" indicated by the shape of generate oxide on either side of the waveguide core. Despite it's limitations, the simulator does appear to predict the correct shape of the resulting core (see Figure 5.12 on p. 169). Our simulation tools are all currently setup to simulate perfectly rectangular core shapes, which clearly does not correspond with the shapes produced by this oxidation process. Thus, the use of SILVACO Athena can enable the simulation of real core geometries with tapered sidewalls, by setting up the simulation tool to import SILVACO structure files.

### 5.3.6  Fabricated Devices

Waveguides fabricated via the LOO Process were fabricated using the same lithography mask plate as in Section 4.3.1:*Fabricated Devices* on page 128, with 26 waveguide widths from 5.0 µm to 17.5 µm in a 1.115 meter spiral

Archimedean spiral configuration.

A 1 mm thick silicon substrate with 15 µm of thermal oxide was used for the lower cladding. ICP-PECVD (PECVD with an inductively coupled plasma) was used to deposit 940 nm of $SiO_xN_y$ waveguide core layer, with the $O_2/N_2$ gas flow ratio chosen to produce a refractive index of 1.600 at 1550 nm) followed by an $SiO_2$ oxidation buffer of 200 nm. An $Si_3N_4$ oxidation mask of 100 nm was sputter deposited with IBD.

As aforementioned, low nitrogen content PECVD films are relatively well behaved and predictable during oxidation, but PECVD nitride is not, so sputter deposited nitride was used for the oxidation mask to ensure effective blocking of oxidant. This produces an additional benefit owing to the fact that sputtered nitride exhibits a considerably lower oxidation rate than the PECVD $SiO_xN_y$ films, and thus requires less physical etching to pattern in this case a *core thickness*:*etch depth* ratio of 9:1. This provides a way to fabricate very thick waveguide cores with very little etching, eliminating the need for metal hard masks or thick photoresists (and the resulting polymer removal) for the dry etch steps.

Standard contact lithography and dry-etching techniques were used to pattern the oxidation mask. Core definition proceeded by subjecting the wafer to steam oxidation for 5 hours at 950°C (with all other parameters identical to those in Section 5.3.1). The nitride oxidation mask was then removed via dry etch, and 10 µm of PECVD $SiO_2$ upper cladding was deposited in batches, with 1050°C, 3 hr. anneals performed after every 4 µm of deposition. The spiral facets were diced according to the lithographically defined dicing guides with 200 µm thick resin blades of 22 µm embedded diamond grit.

The full process is described by the follower in Section C.2:$SiO_xN_y$ *Waveg-*

167

### 5.3.6.1 Resulting Core Geometry

The LOO Process results in a waveguide core shape that is not rectangular due to the bird's beak effect, which, again, is a result of the expansion of oxidized material that pushes the oxidation mask up at the edges. Figure 5.12 shows a waveguide core as defined by the LOO Process, clearly showing the characteristic tapered edge of a feature defined by a bird's beak effect. Additionally, it will be narrower than the lithographically defined oxidation mask due to the diffusion of oxidant under the mask material.

The core geometry can be fairly well characterized via SEM of cleaved facets with a thin Au/Pd coating and the use of a low-angle backscatter electron detector to reduce charging effects in the resulting image. The SEM shown exhibits a width, as measured from the tips of the tapered edges, of 9.46 µm, and corresponds to a lithographic width of 10 µm. Core thickness was measured to be 0.80 µm, although this value decreases for the narrowest few waveguides. The same measurements was performed for all 26 waveguide widths, the result of which is plotted in Figure 5.13. SEM magnification and resulting measurement resolution causes both the jump at 8µm and the scatter above 15µm, and the average reduction in core width is 0.49 µm, with respect to the dimensions as designed on the lithography mask plate.

This geometry raises some interesting issues. Firstly, the sophisticated scattering loss, bend loss and other models we have developed all assume a rectangular waveguide core, which is clearly not the case here. The slanted sidewall effectively mixes the two cases of sidewall and surface roughness, such that the sidewall roughness is either distributed over the slanted area, or exists only at the very edge of the taper. It is likely that it is distributed
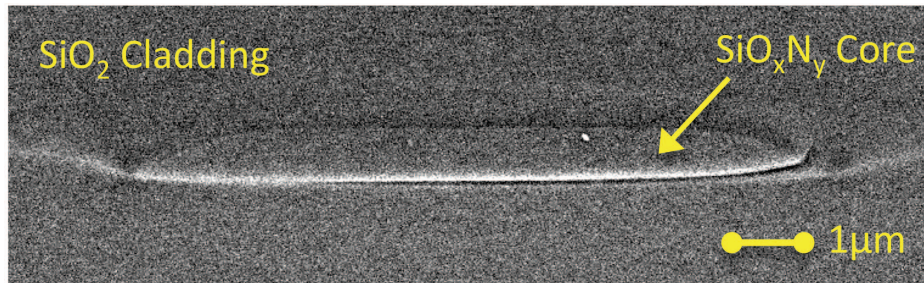
**Figure 5.12:** *An SEM of a waveguide core as defined by the selective oxidation of oxynitride process. The width from tip to tip is 9.46µm, for an oxidation mask width of 10µm.*
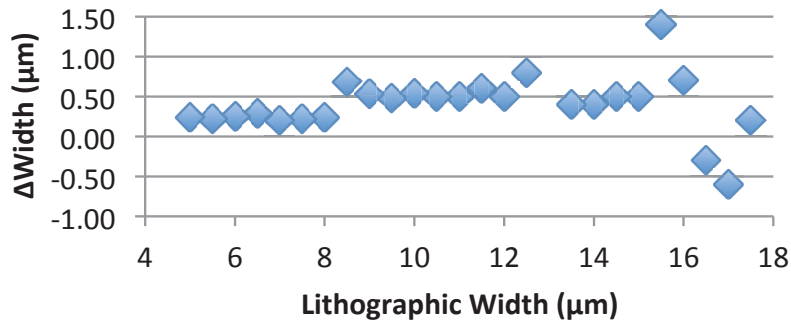


**Figure 5.13:** *The deviation in width from the lithographically defined dimensions. The average width reduction was 0.49µm.*

over the slant, although we have not found 3-D simulation software that can effectively simulate the transfer of roughness in this way, including the bird's beak effect.

Secondly, on a bend the waveguide mode moves towards the outside of the waveguide, which in this case would push the mode into the taper, and lower the confinement.

Lastly, the tapered sidewall could result in dramatically lowered loss by itself, simply by thinning gradually such that the waveguide mode power is squeezed out prior to the point at which core/cladding index contrast occurs

at the edge. The power overlap at the waveguide edge should be reduced solely by this geometry, similar to a sidewall with graded index .

It is possible to create such a geometry without an oxidation process, for example by reflowing resist after lithography and adjusting the etch selectivity to accentuate sidewall slant. However, in this case the entire slanted surface would be defined by ion bombardment in a direct etch, which is be expected to exhibit higher roughness than the diffusion controlled LOO Process.

## 5.4 Core Trimming with Reoxidation

There are many variables in waveguide fabrication that prevent simulations from completely predicting the properties of fabricated waveguides - width, index and thickness variations, not to mention the dramatic effects that thin-film stress and annealing have on the refractive indices of the deposited films (which will be further discussed in Section 6).

Thus it is helpful to be able to modify waveguide geometry after loss measurements, and continue to modify the device until the desired properties are achieved - in this case, low propagation loss, although other properties such as velocity ($\langle n \rangle$) could also be targeted.

The oxidation process for waveguide definition enables the ability to post-process the waveguide devices in this way. We showed in Section 5.3.1 that the oxidation rates were linear with time, which means that that the thickness of $SiO_2$ that oxidant must diffuse through does not appreciably affect the oxidation rate. Of course, this was only measured for oxide thicknesses less than one micron. However, the linear rates do suggest that it would be feasible to reoxidize the waveguides through the 10 µm upper cladding $SiO_2$

170
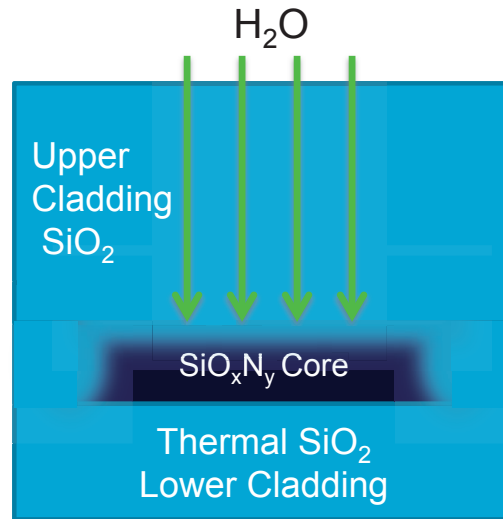
**Figure 5.14:** *Thinning of the $SiO_xN_y$ core with unmasked oxidation through Upper Cladding silica.*

deposition, as shown in Figure 5.14. This unmasked oxidation would oxidize the the $SiO_xN_y$ core from the top and sides, both thinning and narrowing the core, as shown in Figure 5.14.

With this in mind, we can produce waveguides with initially thicker cores than desired, and after completing the device and measuring propagation losses, we can iteratively reoxidize to thin the core, and remeasure the losses until the minimum possible losses are achieved.

Figure 5.15a shows the reduction in core thickness of an ICP-PECVD $SiO_xN_y{}^{1.59}$ core embedded in 10µm of upper cladding after repeated wet oxidation at 1000°C.

Figure 5.15b shows the reduction in core width with respect to the lithographic widths as laid out on the lithography mask plate. The initial reduction of 0.5µm is due to the original width reduction from the baseline core definition with a 200 nm oxidation buffer. The core thickness and width was
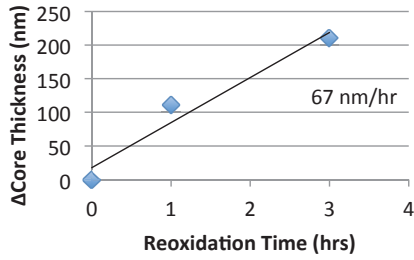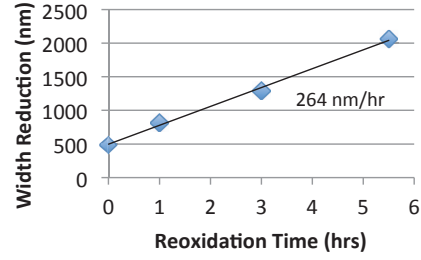
**Figure 5.15:** *(a) Core thickness reduction versus reoxidation time as measured with SEM of cleaved facets, for 1000°C wet oxidations, and (b) the average reduction in core width for the same.*

again measured via SEM of cleaved facets. Although the core width is also reduced in a predictable manner (Figure 5.16), the rate appear higher than for the thinning. This is presumably because the oxidant is attacking the core edges from many directions, and ammonia can additionally diffuse away in more directions than for a flat surface. That is, the increased surface area of the core edge allows it to oxidize faster than the planar surface - a similar mechanism to the smoothing process, in which sharper feature oxidize faster than flat features.

172
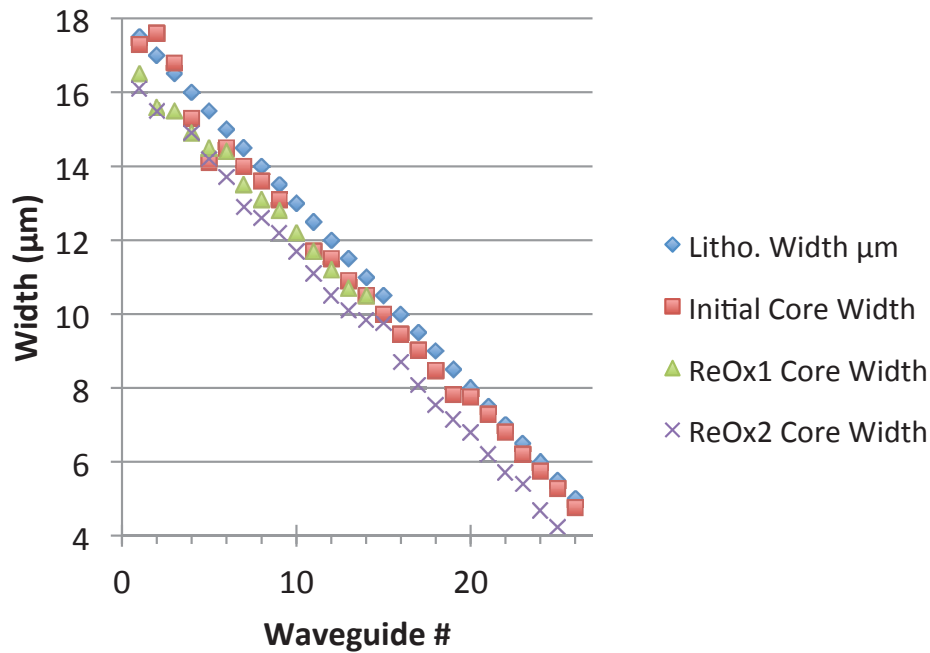
**Figure 5.16:** *Widths of each waveguide as defined lithographically, and for each oxidation/re-oxidation.*

## 5.5 OFDR Measurement of LOO Waveguides

### 5.5.1 Group Index

Our lithographic mask plate has dicing guides for a facet-to-facet spiral length of 1114.9 mm, as described in Section 5.3.6. The techniques described in Section 4.2.3.1 were used to determine the group indices, $n_g$, for each waveguide width, the result of which are shown in Figure 5.17.

The plot shows a consistently lower group index for the TM mode than for the TE mode. This can be attributed to the lower confinement (larger mode size) of the TM mode. Additionally, the group index drops monotonically as the width is reduced below 8 µm, illustrating the modal "squeeze-out" at narrow widths.
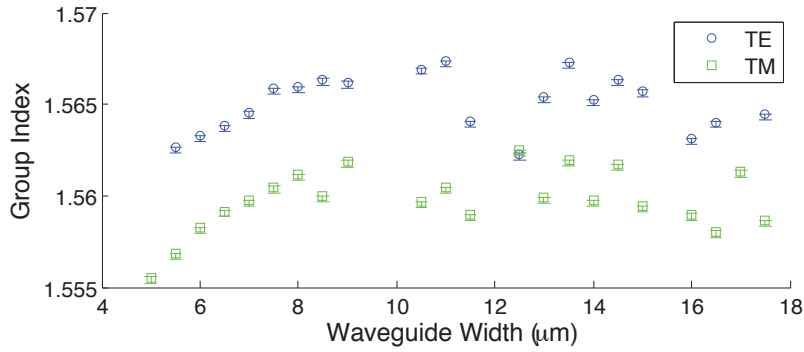
**Figure 5.17:** *Measured $n_g$ versus waveguide width for TE & TM polarizations.*
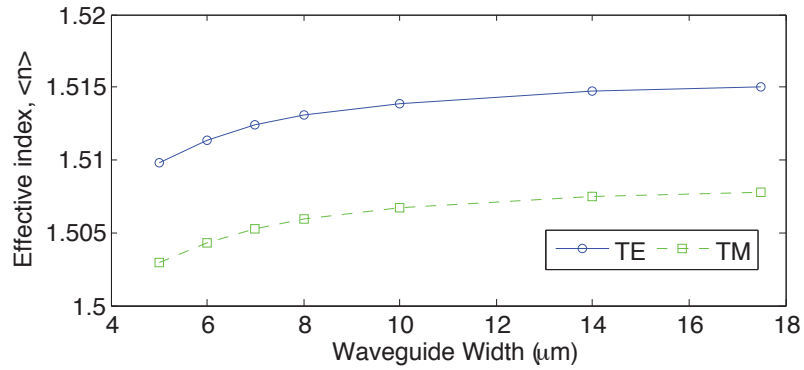


**Figure 5.18:** *Simulated modal indices at 1550 nm, $\langle n \rangle_{1550}$, versus waveguide width for the same geometry as fabricated.*

Simulations of the modal indices, $\langle n \rangle$, in Figure 5.18 for the same core indices and thickness and varying widths shows a similar trend. The conversion to $n_g$ requires many more simulations to obtain $\langle n \rangle$ vs. $\lambda$, which were not performed here. $\langle n \rangle$ vs. $\lambda$ can be subsequently converted to $n_g$ via the relation $n_g = \langle n \rangle - \lambda \cdot \frac{\delta \langle n \rangle}{\delta (\lambda)}$.

Observations of transmitted modes with an IR camera showed that all widths below 7.0 µm were single mode (with one TE and one TM mode

174
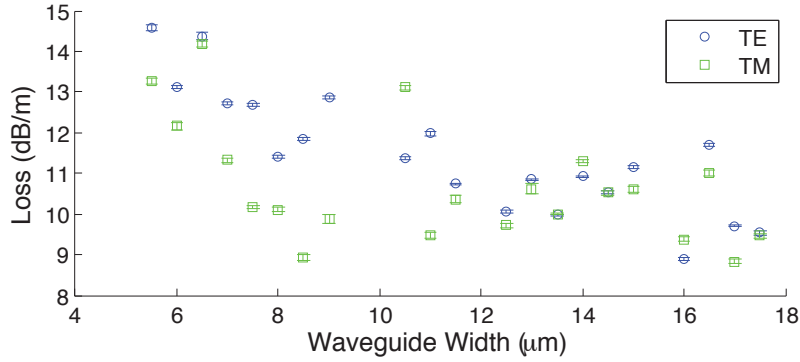
**Figure 5.19:** *Measured losses for each polarization and width with error of 1 dB/m.*

transmitted). The 7.5 µm wide guide supported one additional TE mode, and the next widest guide supported two modes for both polarizations.

The scatter in the $n_g$ data above 7.5 µm is thus due to the the existence of higher-order modes. The different modes have different propagation velocities, causing the OFDR peak at the output facet to contain more than one time-domain reflection peak. The user does not know which mode is creating the selected peak, creating the observed scatter in the $n_g$ data.

The lowered $n_g$ at smaller widths, however, can definitely be attributed to "squeeze-out" of the mode at narrower widths, as also shown in [27].

## 5.5.2 Propagation Loss

The aforementioned OFDR analysis techniques were used to characterize the losses of the devices described in Section 5.3.6. With the corrected group indices for each waveguide width, and for each transmitted polarization, we measured the losses shown in Figure 5.19.

Some of this scatter in the data can be attributed to the $n_g$ scatter, as that relates directly to propagation loss. However, a larger component is

175

likely the large number of scatterers incurred during fabrication, limiting the viable fitting range. Coupled with the variability in measured loss due to the aforementioned localized lithography roughness, loss values have an error of about 1 dB/meter for this device.

The scatter in this Loss vs. Width data is very similar to that shown for the direct-etched device, which was patterned with the same mask plate. Variations of ~6 dB/m in the difference between TE & TM mode losses can also be seen in those measurements on p. 133. We showed there that the scatter was not due to polarization rotation, and similar measurements on this LOO device indicated the same, that polarization is not randomized during propagation.

In combination with the irregular core shape, the measurement error from defects makes correlation to simulated losses fairly difficult. The lowest propagation losses measured here are 9.0 dB/m for both TE and TM modes, for the widest, multi-mode waveguides.

### 5.5.3 Wavelength-dependent Measurements

Since this device utilizes ICP-PECVD $SiO_xN_y$, which we showed has an appreciable hydrogen content (p. 91), it is instructive to perform the same wavelength-dependent loss analysis as on the prior, direct-etched, sputtered $Si_3N_4$ device (see Section 4.3.3 on page 137). Even though the device was annealed for 14 hours at 950°C immediately after oxidation, it is possible for there to be some residual hydrogen in the films, which would manifest most obviously as a gaussian absorption peak near 1510 nm due to the $N-H$ stretching molecular vibration overtone.

Figure 5.20 shows the Loss vs. Wavelength for the 17.0 µm wide cores for TE transmission. As expected, we observe a two- or three-fold loss increase at
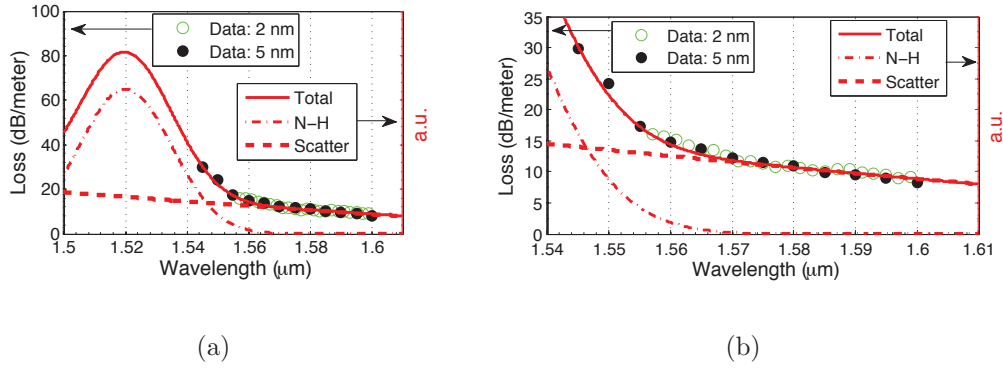
**Figure 5.20:** *(a) Loss vs. λ for TE transmission in the 17.0 µm wide core, with N−H and scatter fits. (b) A zoom-in on the region containing measured data at each Δλ.*

low wavelengths, and a relatively linear drop at higher $\lambda$. The N−H gaussian required to fit the data (without dramatically increasing the width) reveals a potentially large N−H peak, although the exact fit of this gaussian is not possible without capturing the peak location (prevented by the minimum OBR $\lambda$ of 1525 nm).

Similar high-losses were observed for other widths analyzed with this technique, showing 25–40 dB/m at wavelengths lower than about 1.55 µm. Even the long 950°C anneal after core oxidation left some hydrogen within the core films, resulting in residual N−H bonds. This confirms the theory posited in Section 3.2.3 that the annealing of high-hydrogen films does not remove all of the hydrogen, even though the FTIR results (p. 87) indicate a significant reduction.

### 5.5.4 Reoxidation to Optimize Loss

The initial core thickness of this device was chosen to be thicker than the theoretical optimal design, so that a cycle of core thinning and testing could
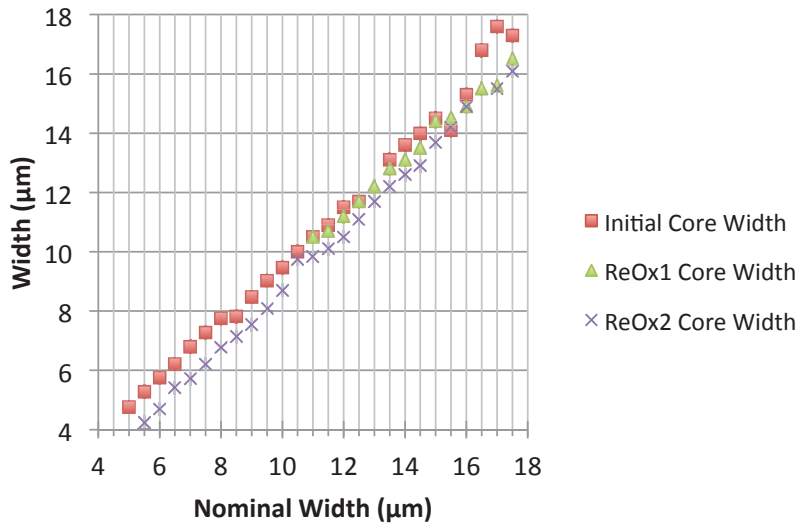
**Figure 5.21:** *Core widths for each reoxidation, with respect to the lithographically defined widths.*

be performed to attempt to locate the optimal geometry.

The original core definition was performed with a 950°C wet oxidation, with only a 200 nm $SiO_2$ oxidation buffer impeding the flow of oxidant. After initial loss testing, reoxidation was performed at 1000°C, to increase the flow of oxidant through the 10µm upper cladding. This was previously described in Section 5.4 on page 170, along with the rate of reoxidation for core thickness and width. The resulting core widths and thicknesses, as measured with SEMs of cleaved facets, are shown in Figure 5.21 and Figure 5.22.

Figure 5.23 shows the progression of losses versus waveguide width as each oxidation is performed, comparing only two successive oxidations at a time. The measurement scatter due to local scatterers makes the trends somewhat difficult to observe, so arrows have been inserted to illustrate general trends.

Perhaps more instructive is to plot the *change* in loss from run to run. In Figure 5.24, the change in loss ($\Delta Loss$) for each waveguide width is plotted,

178
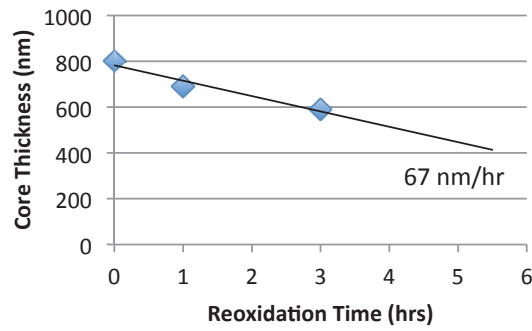
**Figure 5.22:** *Core thickness versus Reoxidation time, corresponding to Initial, ReOx1 and ReOx2.*

with negative values indicating a decrease in propagation loss. The average change is also indicated.

Both Figures 5.23 & 5.24 tell an interesting story, combining the effects of a few different loss contributions as the waveguide cores are made smaller by successive reoxidations.

Firstly, if the initial waveguides are thicker than the modal squeeze-out point, as they are thinned and narrowed, the modes in all widths should become slightly less confined. This will lower the mode overlap with sidewall roughness, and lower the loss. For the narrowest guides, however, this reduced confinement can also start to increase bend loss due to the reduced lateral confinement. In (a) it seems the initial thickness was large enough such that this did not occur.

However, the subsequent reoxidation (*ReOx2*) in (b) does show the onset of bend loss limiting to some degree, accompanied by a small region of little to no change, for waveguides that are right on the cusp of becoming bend-loss limited. Wider guides with enough lateral confinement to obviate bend loss limiting continue to decrease in loss, due to reduced confinement and lower sidewall scattering.

179
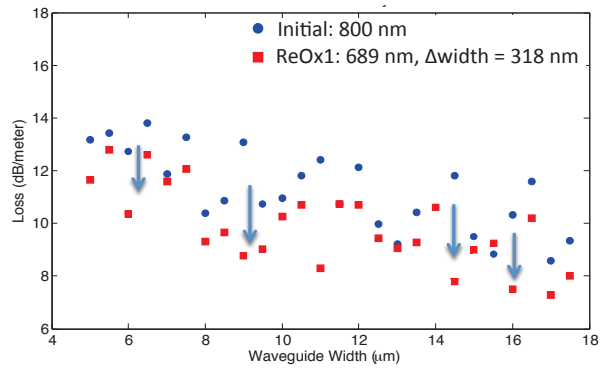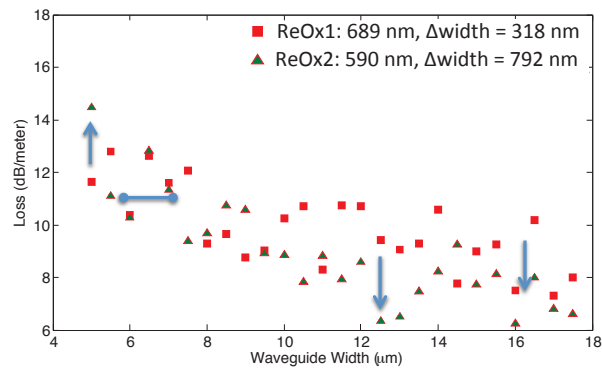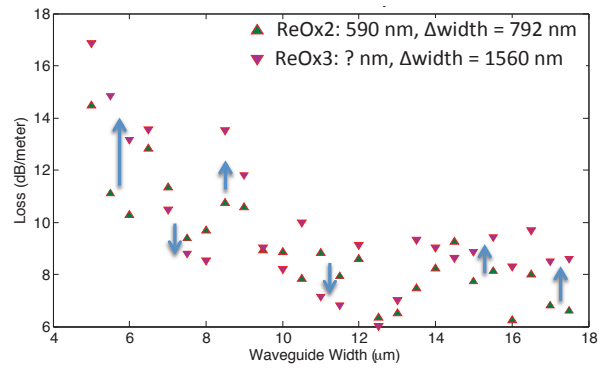
**Figure 5.23:** *(a) The initial measurement juxtaposed with the first reoxidation "ReOx1", with core thickness and average width reduction indicated on the legend, showing a global reduction in losses. (b) "ReOx1" and "ReOx2" compared, and. (c) "ReOx2" and "ReOx3" compared.*
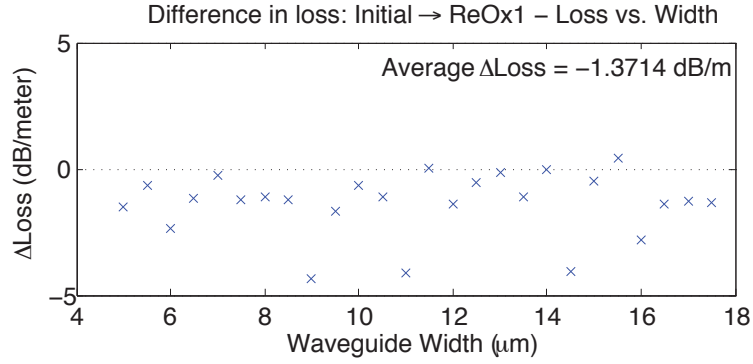
(a)
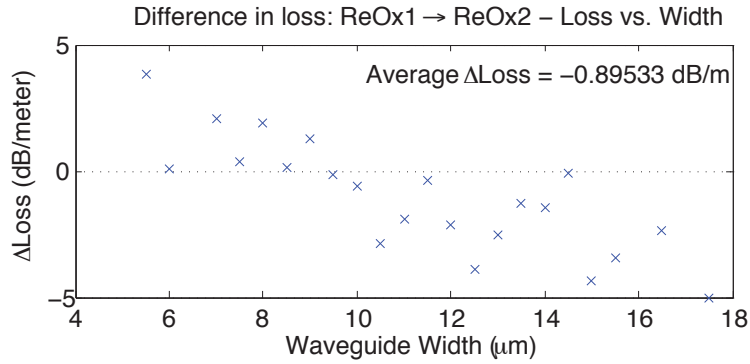


(b)
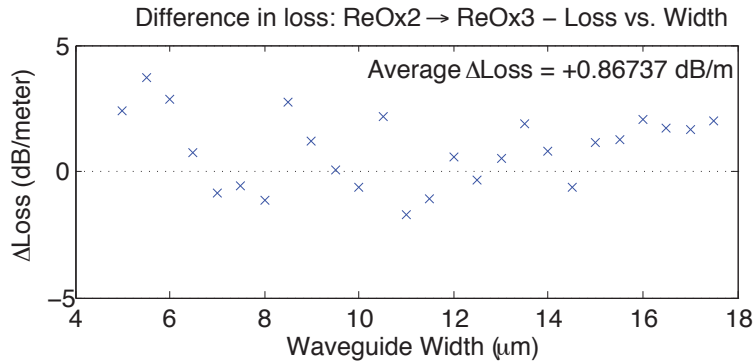


(c)

**Figure 5.24:** *(a) The change in loss for Initial $\rightarrow$ ReOx1 (1000°C, 1.0 hr). (b) ReOx1 $\rightarrow$ ReOx2 (1000°C, 2.0 hr). (c) ReOx2 $\rightarrow$ ReOx3 (1000°C, 2.5 hr).*

As the guides are further reduced in size in (c), the narrowest guides continue to increase in loss due to bend loss. We see almost all guides show a modest increase in the loss. An interesting effect was observed as the cores were thinned - the presence and magnitude of scatterers appeared to increase. If scatterers are present mostly in the upper cladding, then the impact of scatterers would increase as the mode is squeezed out further. Additionally, some of the reduced vertical confinement may increase substrate leakage. Any points that continue to decrease should be the cores just large enough to not be bend loss limited, and any further thinning will likely cause them to increase in loss as the mode is lost to bend radiation.

The reoxidation technique appears to work as expected, allowing a designer to overshoot their designed core thickness during initial fabrication and subsequently "trim" it via loss (or other) measurements until the desired properties are achieved. In theory a finer resolution could be attained, by utilizing shorter oxidation times or lower temperatures than I used here.

## 5.6 Chapter Summary

We have proposed and demonstrated a method to define $SiO_xN_y$ waveguide cores without direct etching, utilizing a selective oxidation of silicon oxynitride for the first time. The local oxidation of oxynitride, or LOO Process, utilizes the conversion of core $SiO_xN_y$ into lateral cladding $SiO_2$ via a high-temperature steam oxidation, instead of direct etching.

We developed a one-dimensional method to simulate the sidewall smoothing performed by a diffusion process, and used the measured line-edge of an optimized lithography process to simulate the resulting sidewall roughness parameters, $\sigma$ and $L_c$. The roughness parameters were calculated for vary-

ing diffusion radii, which corresponds to the physical distance oxidant must travel to reach the core material, as determined by the $SiO_2$ oxidation buffer thickness. Additionally, it was shown that sidewalls with small-scale roughness would benefit most from this process.

We have thoroughly characterized the thermal oxidation of $SiO_xN_y$, for various refractive indices and temperatures, utilizing spectroscopic ellipsometry with a two-layer Cauchy model. This builds upon previous oxidation experiments from the late 1980's by quantifying the refractive indices of the generated thermal oxide. We determined the oxidation rate of $SiO_xN_y$ versus refractive index and temperature. Additionally, the thermal oxide was found to occupy a larger volume than the original $SiO_xN_y$ film, and so the volume expansion ratio of various $SiO_xN_y$'s were calculated.

The oxidation characterizations were related to the generation of ammonia through observation of the refractive indices of the created thermal oxide, which was found to exhibit higher index when produced with lower temperatures. We surmise that this is a result of the re-nitridation of the thermal oxide as the large ammonia molecules attempt to diffuse through it, but instead re-bond with $SiO_2$ molecules, backed up by the fact that $NH_3$ has a lower diffusion coefficient than $H_2O$ and was shown to be the rate-limiting factor in the oxidation reaction [19, 16]. Additionally, the activation energy and exponential coefficients were determined for the target core index $SiO_xN_y^{1.63}$.

A waveguide fabrication process was fully described to utilize the LOO Process, and waveguides were fabricated using ICP-PECVD $SiO_xN_y$ for the waveguide core and sputtered $Si_3N_4$ for the oxidation mask. This yielded an additional benefit of the process, in that only a 100 nm $Si_3N_4$ was necessary to define a 940 nm thick $SiO_xN_y$ core. This *corethickness*:*etchdepth* ratio of

9:1 would obviate the use of metal hard masks or other techniques to define thick waveguide cores.

The resulting core geometry was inspected with SEM of cleaved facets. The core shape corresponds with the "bird's beak" effect, in which expansion of oxidized material pushes the oxidation mask upwards during the oxidation. The average width reduction was found to be 0.5 µm for a 200 nm oxidation buffer thickness.

Lastly, a post-measurement trimming of the waveguide cores was proposed and characterized, in which the core widths and thicknesses are controllably reduced via unmasked oxidation through the deposited upper cladding. When utilized in tandem with a non-destructive waveguide measurement technique (ie. propagation loss or other properties), this enables the waveguides to be repeatedly trimmed until the desired properties are achieved. The width and thickness reduction rates were determined for the reoxidation process as performed on the fabricated devices.

Loss measurements for the LOO Process and the subsequent reoxidations were presented, showing initial losses of about 9.0 dB/m for both the TE & TM modes.

Wavelength-dependent loss measurements revealed the presence of strong $N-H$ absorption peaks, limiting the losses below 1560 nm. Losses at higher wavelengths appear to be limited by scattering, likely dominated by the lithography roughness due to mask plate scum.

The sensitivity of the narrow-band OFDR loss measurement to small hydrogen impurities may in fact be very high compared to common spectroscopy techniques like FTIR, owing to the fact that absorption is experienced over a full meter of optical propagation. Correction of the absorption via the optical power overlap with each material could yield quantified concentrations

with high sensitivity, perhaps on the level of SIMS measurements. The difficulty here is calibration of the molar absorptivity at these N−H overtone wavelengths, which have not been well quantified up to this point.

The non-destructive OFDR measurement technique enabled the use of reoxidation for the trimming of waveguide geometry after measurement, enabling the designer to optimize their device using measurements of the desired properties.

Reoxidations at 1000°C showed thickness and width reduction rates of 67 nm/hr and 264 nm/hr, respectively. We surmise that the higher rate of width reduction is due to large area into which generated ammonia can escape at the sharp, angular sidewalls, as compared with the core's flat top surfaces.

Reoxidations initially showed an average reduction in loss of 1.4 dB/m for all waveguide widths, after 1 hour of thinning. This can be attributed to squeezing out the optical mode, lower the power overlap with roughness. Further thinning for 2.0 hrs. lowered losses for wide waveguides, as the modes were squeezed out further, but increased losses for narrow waveguides, presumably due to an increase in bending loss. The losses decrease on average by 1.4 dB/m, with the minimum losses for the 12.5 – 17.5 µm wide waveguides at 6.5 dB/m. The final reoxidation for 2.5 hrs. increased losses for the majority of widths by an average of 0.9 dB/m, with a larger loss increase at the narrowest widths, again due to bend loss. Minimum loss for the 11.5 – 13.0 µm wide guides were 7.0 dB/m.

The LOO Process has thus been shown to produce a viable waveguide technology, with losses in the dB/meter range, and enables a loss–optimization down to 6.5 dB/m even for the rough contact lithography used in this study.

# References

[1] C. Ciminelli, F. Dellolio, V. M. N. Passaro, and M. N. Armenise, "Fully three-dimensional accurate modeling of scattering loss in optical waveguides," *Opt Quant Electron*, vol. 41, no. 4, pp. 285298, Mar. 2009.

[2] F. Grillot, L. Vivien, E. Cassan, and S. Laval, "Influence of waveguide geometry on scattering loss effects in submicron strip silicon-on-insulator waveguides," *IET Optoelectron.*, vol. 2, no. 1, p. 1, 2008.

[3] K. K. Lee, D. R. Lim, H.-C. Luan, A. Agarwal, J. Foresi, and L. C. Kimerling, "Effect of size and roughness on light transmission in a Si/SiO2 waveguide: Experiments and model," *Applied Physics Letters*, vol. 77, no. 11, pp. 16171619, Sep. 2000.

[4] Bauters *et al.*, "Ultra-low-loss high-aspect-ratio Si3N4 waveguides," *Optics Express*, vol. 19, no. 4, pp. 3163-3174, 2011.

[5] R. Adar and M. Serbin, "Extremely low coupling and propagation losses with modified silica on silicon waveguides," *Lasers and Electro-Optics Society Annual Meeting, 1993 (LEOS '93) Conference Proceedings*, pp. 153-154, 1993.

[6] M. Kohtoku, T. Kominato, Y. Nasu, and T. Shibata, "New Waveguide Fabrication Techniques for Next-generation PLCs," *NTT Technical Review*, vol. 3, no. 7, pp. 37-41, 2005.

[7] A. Maker and A. M. Armani, "Low-loss silica-on-silicon waveguides," *Optics Letters*, vol. 36, no. 19, pp. 3729-3731, 2011.

[8] Q. Xia, P. Murphy, H. Gao, and S. Y. Chou, "Ultrafast and selective reduction of sidewall roughness in silicon waveguides using self-perfection by liquefaction," *Nanotechnology*, vol. 20, no. 345302, pp. 1-5, 2009.

[9] L. Rowe, M. Elsey, N. Tarr, A. P. Knights, and E. Post, "CMOS-compatible optical rib waveguides defined by local oxidation of silicon," *Electronics Letters*, vol. 43, no. 7, pp. 392-393, 2007.

[10] R. Pafchek, R. Tummidi, J. Li, M. A. Webster, E. Chen, and T. L. Koch, "Low-loss silicon-on-insulator shallow-ridge TE and TM waveguides formed using thermal oxidation," *Applied Optics*, vol. 48, no. 5, pp. 958-963, 2009.

[11] J. Cardenas, C. B. Poitras, J. T. Robinson, K. Preston, L. Chen, and M. Lipson, "Low loss etchless silicon photonic waveguides," *Optics Express*, vol. 17, no. 6, pp. 4752-4757, Mar. 2009.

[12] M. P. Nezhad, O. Bondarenko, M. Khajavikhan, A. Simic, and Y. Fainman, "Etch-free low loss silicon waveguides using hydrogen silsesquioxane oxidation masks," *Optics Express*, vol. 19, no. 20, pp. 1882718827, 2011.

[13] J. Appels, E. Kooi, M. M. Paffen, J. J. H. Schatorje, and W. H. C. G. Verkuylen, "Local oxidation of silicon and its application in semiconductor-device technology," *Philips Research Reports*, vol. 25, no. 2, pp. 118-132, 1970

[14] A. Kuiper, M. Willemsen, J. Bax, and F. Habraken, "Oxidation behaviour of LPCVD silicon oxynitride films," *Applied Surface Science*, vol. 33, no. 34, pp. 757-764, Sep. 1988.

[15] D. Choi, D. B. Fischbach, and W. D. Scott, "Oxidation of Chemically Vapor Deposited Silicon Nitride and Single-Crystal Silicon," *Journal of the American Ceramics Society*, vol. 72, no. 7, pp. 11181123, 1989.

[16] A. Kuiper, M. F. C. Willemsen, J. M. L. Mulder, JB Oude Elferink, F. H. P. M. Habraken, and WF van der Weg, "Thermal oxidation of silicon nitride and silicon oxynitride films," *J. Vac. Sci. Technol. B*, vol. 7, no. 3, pp. 455465, May 1989.

[17] D. D. John, J. F. Bauters, J. Nedy, W. Li, R. Moreira, J. S. Barton, J. E. Bowers, and D. J. Blumenthal, "Fabrication and Demonstration of a Pure Silica-Core Waveguide Utilizing a Density-Based Index Contrast," *Proc. of OFC/NFOEC 2011*, Los Angeles, California, U.S.A., paper OWS3, Mar. 2011.

[18] A. Del Prado, E. San Andrés, F. Martinez, and I. Mártil, G. González-Díaz, W. Bohne, J. Röhrich, B. Selle, and M. Fernández, "Composition and optical properties of silicon oxynitride films deposited by electron cyclotron resonance," *Vacuum*, vol. 67, pp. 507512, 2002.

[19] Brow and Pantano, "Thermochemical nitridation of microporous silica films in ammonia," *Journal of the American Ceramic Society*, vol. 70, no. 1, pp. 9-14, 1987

[20] A. Stoffel, A. Kovacs, W. Kronast, and B. Müller "LPCVD against PECVD for micromechanical applications," *J. of Micromech. Microeng.*, vol. 6, pp. 1-13, 1996

[21] J. F . Shackelford and W. Alexander, *CRC Materials Science and Engineering Handbook*, Third Edition, CRC Press, 2000

[22] F. Ay and A. Aydinli, "Comparative investigation of hydrogen bonding in silicon based PECVD grown dielectrics for optical waveguides," *Optical Materials*, vol. 26, no. 1, pp. 33-46, 2004

[23] F. Ladoceur, J. D. Love, and T. J. Senden, "Effect of side wall roughness in buried channel," *IEEE Proc. Optoelectron.*, vol. 141, no. 4, pp. 242248, Aug. 1994.

[24] J. A. Ogilvy and J. R. Foster, "Rough surfaces: gaussian or exponential statistics?," *Jnl. Phys. D: Appl. Phys.*, vol. 22, pp. 12431251, 1989.

[25] B. E. Deal and A. S. Grove, "General Relationship for the Thermal Oxidation of Silicon," *Journal of Applied Physics*, vol. 36, no. 12, p. 3770, 1965.

[26] Stephen A. Campbell, *The Science and Engineering of Microelectronic Fabrication*, 2nd ed., Oxford University Press, New York, 2001.

[27] J. F. Bauters, M. Heck, D. D. John, D. Dai, M. C. Tien, J. S. Barton, A. Leinse, R. G. Heideman, D. J. Blumenthal, and J. E. Bowers, "Ultra-low-loss high-aspect-ratio Si3N4 wavequides," *Optics Express*, vol. 19, no. 4, pp. 31633174, Feb. 2011.

# Chapter 6

# The Stress-optic Effect in Glass Waveguides

Numerous researchers have previously shown that thin-film stress in glass layers is responsible for a large birefringence, ie. a different propagation velocity and $\langle n \rangle$ for the TE versus TM modes of propagation [1, 2]. Although this modal birefringence is indeed present, we began to suspect that an additional effect of thin film stress is to lower the index contrast between the core and cladding materials. We observed that annealing could drastically increase the bend losses in low index-contrast ($n_{core}/n_{clad}$=1.50/1.44) waveguides (coupled with the observation that the resulting substrate in these cases would have a bow of more than 1 mm).

An experiment was carried out that uncovered the effect of stress on core index. The original goal of the experiment was to investigate a multi-layer waveguide platform based on the recently demonstrated record low losses in $Si_3N_4/SiO_2$-based planar waveguide technology [3, 4]. The technology allows for the creation of optical delay line lengths not previously possible on a chip-scale integrated platform. These low losses enable the use of integrated

optical waveguides in otherwise unfeasible applications.

Fiber optic gyroscopes (FOGs) are a particularly interesting application, as the interferometric variety require long optical loops, 10's of meters or more, for increased angular sensitivity[5]. These are currently created with optical fiber, which exhibit the necessary low-loss but require management of polarization birefringence and vibrations.

Our previous waveguide delay demonstrations are highly polarization-maintaining and appear to be well suited for use in FOGs. These designs used Archimedean spirals in which a central "s-bend" reverses the spiral direction. This retrograde spiraling, however, is not compatible with FOG applications, which require that launched light propagate in only one rotational direction[6]. One approach to eliminate retrograde spiraling is to couple light to a second parallel waveguide plane, which would also enable the removal of the tight bend-radius s-bend and consequently enable a longer delay.

Little & Kokubun applied vertically coupled waveguide layers to ring resonators, demonstrating reduced sensitivity to lateral alignment and improved fabrication tolerance due to tight control of layer thicknesses[7, 8].

To investigate this option, a mask plate and set of devices were fabricated with test structures for probing the interactions between multi-layer waveguides, including vertical directional coupling. The waveguide geometries fabricated are based on our previously demonstrated ultra-low loss Silicon Nitride platform shown in [3], in which high aspect ratio geometries were used for both single and multi-mode guides.

For the initial demonstrations presented here we used standard PECVD (Plasma Enhanced Chemical Vapor Deposition) films and deposited claddings, rather than LPCVD (Low Pressure CVD) and bonded claddings. This leads

191

to higher propagation losses due to increased hydrogen content, but will still allow us to uncover fabrication or experimental issues we may face in the final implementation of this multi-layer platform.

## 6.1 Test Structures for Multi-Layer Waveguide Interactions

Figure 6.1 shows the mask design for the various test structures fabricated, where red indicates devices on the lower waveguide layer (WG1) and blue indicates patterns on the upper layer (WG2), corresponding to the two vertically separated layers shown in Figure 6.2.

To probe the loss and group index of each waveguide layer with the Luna OBR 4400, 1.23 meter spiral structures with lithographically defined terminations were designed. Two waveguide widths, of 4 µm and 15 µm, were designed, to investigate both single-mode and multi-mode geometries. These OFDR test structures were laid out on both waveguide layers, to investigate any differences in loss or group index of the two layers. Additionally, looking ahead to the realization of overlapping spirals and access waveguides, spirals with perpendicular crossings on the adjacent waveguide layer were designed, as shown in Figure 6.3. These enable us to probe reflections or losses incurred by the adjacent layer through analysis of an OFDR backscatter plot.

Figure 6.5 shows a schematic of the vertical directional couplers fabricated, in which the coupling region is designated by a selective vertical overlap area. The coupling coefficient of a directional coupler is typically designed via the spacing between waveguides, which in this case is the deposited $SiO_2$ between waveguide layers, referred to here as the coupling gap. In the case of vertical couplers we have an additional degree of freedom, the lateral offset,
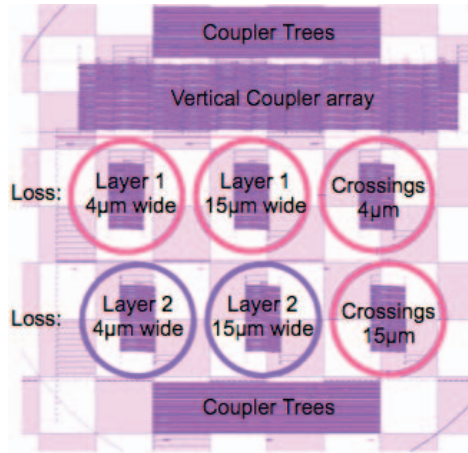
**Figure 6.1:** *Overall wafer layout for the multi-layer test structure mask, with device name/purpose indicated.*
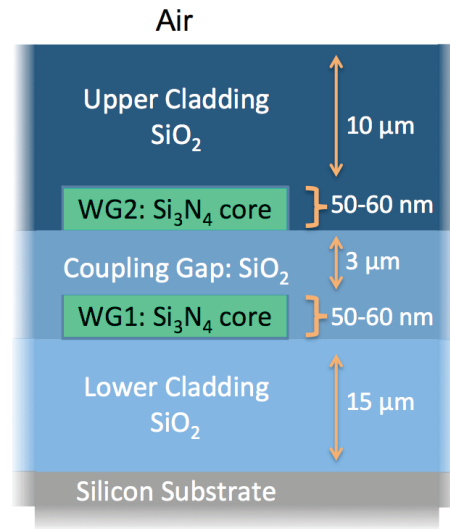


**Figure 6.2:** *Layer structure for the multi-layer waveguide platform.*

to control the coupling coefficient. This is a lithographically defined shift of the overlapping waveguide sections. The coupling length is defined as the length of straight waveguide in the overlap region, although technically there will also be some coupling in the waveguide bends at the entrance and exit of the coupler.

To characterize the couplers, a large array of vertical couplers with 11 varying coupling lengths and 8 lateral offsets were fabricated, one "set" of which is shown in Figure 6.4. This yields the coupling loss along with other characteristic curves.

193
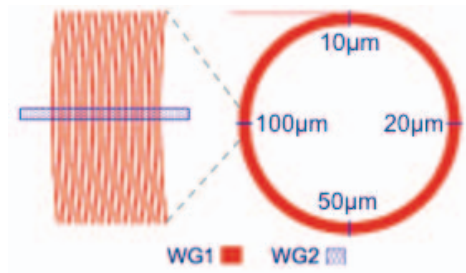
**Figure 6.3:** *Spiral with perpendicular crossings on vertically separated layer, of four different widths.*
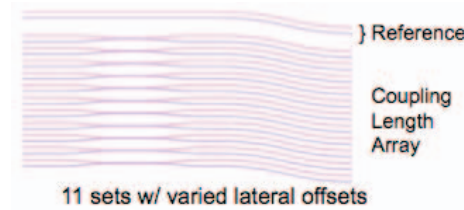


**Figure 6.4:** *One "set" of the vertical coupler array, of a single lateral offset value.*
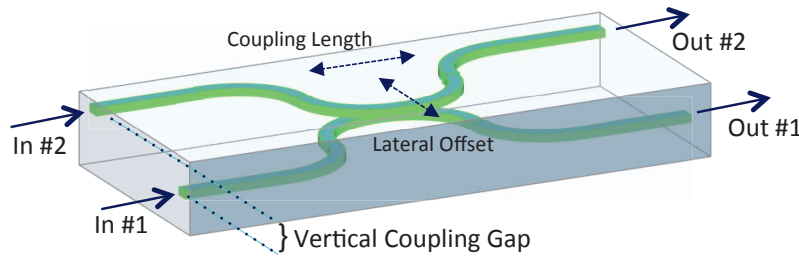


**Figure 6.5:** *Schematic of the vertical direction coupler.*

## 6.2   Multi-layer Waveguide Fabrication

We fabricated Nitride-strip geometries of two widths: 4 µm & 15 µm per device, with the film thicknesses & refractive indices shown in Table 6.1, as measured with multi-angle spectroscopic ellipsometry on deposition watch samples.

The two waveguide widths are single and multi-mode, respectively. Figure 6.2 shows a cross-sectional schematic of the vertical coupling scheme and associated thin-films. Thermally grown oxide was used for the lower cladding, with a refractive index of 1.4458 at 1550 nm. PECVD was used to deposit the 1st $Si_3N_4$ waveguide core (WG1), the Coupling Gap oxide and 2nd $Si_3N_4$ waveguide core (WG2). For device Wafer 1, 50 nm $Si_3N_4$ cores

were deposited, separated by a 3 µm SiO$_2$ coupling gap. Wafer 2 utilized 60 nm thick waveguide cores with the same coupling gap. Each waveguide core layer was patterned with standard contact lithography and ICP-RIE etching techniques (Reactive Ion Etching with an Inductively Coupled Plasma). 10 µm of SiO$_2$ upper cladding was deposited with ICP-PECVD for all three samples. Lastly, to relax the films and reduce the hydrogen content in the PECVD films, the wafers were annealed for 3 hours at 900°C for Wafer 1 and 1000°C for Wafer 2. This anneal reduces the PECVD film thickness by about 5%, which was accounted for during the initial depositions to achieve the desired final thicknesses. The thicknesses and refractive indices in Table 6.1 reflect those of watch samples after annealing.

**Table 6.1:** *Measurements of thin-films used in fabricated couplers.*

|  | Waveguide Function | Film Thickness | Refractive Index |
|---|---|---|---|
| **Wafer 1** | WG1 Core | 50 nm | 1.939 |
|  | Coupling Gap | 2,952 nm | 1.466 |
|  | WG2 Core | 49 nm | 1.940 |
| **Wafer 2** | WG1 Core | 60 nm | 1.978 |
|  | Coupling Gap | 2,923 nm | 1.472 |
|  | WG2 Core | 62 nm | 1.985 |

## 6.3 Measurements

### 6.3.1 Group Index and Loss

OFDR measurements of the 1.23 m spirals on either layer of Wafer 2 yielded the optical time-delay between the input facet of the chip and the rectangular termination of the spiral, which was then used to determine the group index ($n_g$) of each waveguide via knowledge of the lithographically designed spiral length. Uncertainty of the precise location of the diced facet imparts an error of $\pm 1.20\text{E-}3$ to the group index. Using our previously developed narrow-wavelength OFDR analysis method, we calculated $n_g$ versus wavelength for both layers, with a 20 nm wide spectral window, as shown in Figure 6.6. This shows an average difference in the group index between the two layers of 8.5E-3. This disparity indicates a difference in either core geometry or refractive index. Overlaid on the measured group index data are group indices simulated with the finite-difference method for various core refractive indices. The best fits to the measured data indicate that a difference in core index of about 0.050 exists between the two layers.

Previous work on this Nitride-strip technology in [3] showed that thick deposited PECVD $SiO_2$ significantly reduces the refractive index of the $Si_3N_4$ core through the stress-optic effect, which provides a mechanism for deviation of the core refractive indices from those indicated in Table 6.1. Additionally, Schriemer and Cada show in [9] that deposited upper cladding is the principal contributor to birefringence in planar waveguides, and Klein & Miller show that these stressy films create a vertically varying stress [10].

Therefore, it stands to reason that WG1 experiences a different stress than WG2 due to the vertical stress-gradient created by the upper cladding oxide, which produces a different refractive index in each waveguide plane.
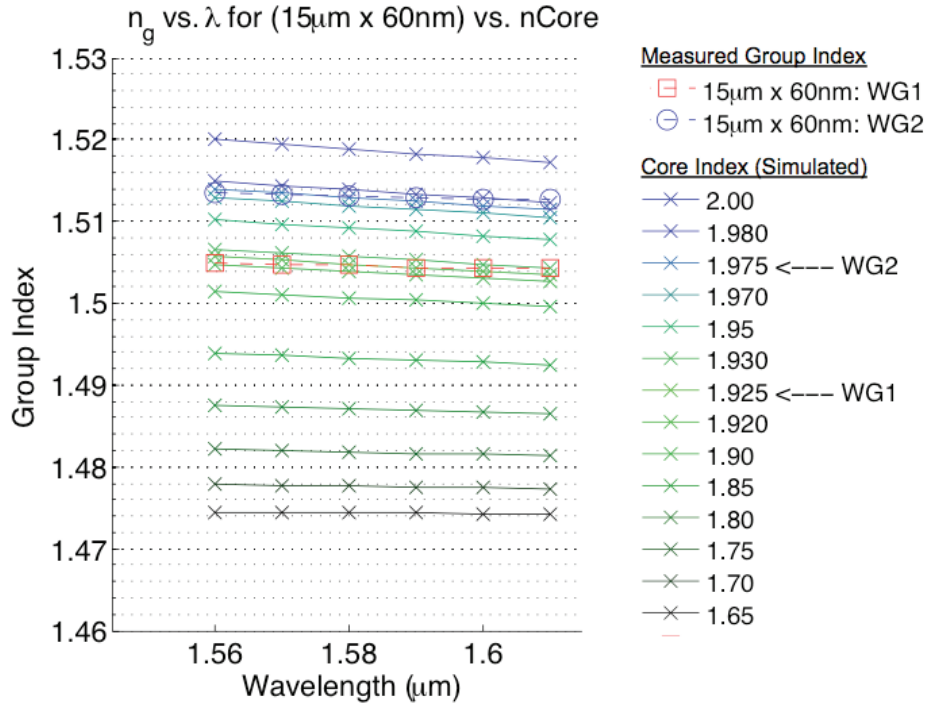
**Figure 6.6:** *Measured group indices of the two waveguide layers, showing a clear difference in modal index. Overlaid are simulate group indices for varying core refractive index, with the best fits indicated.*

This will play a role in the coupling between modes of a vertical directional coupler.

This difference in core refractive index impacts the wavelength-dependent loss significantly, as shown in Figure 6.7. The 20 dB/m loss increase near 1550 nm is characteristic of the first N-H vibrational overtone at 1510 nm, which appears to be more pronounced for the higher-index WG2 guide. This indicates that the higher confinement of WG2 leads to higher mode overlap with the N-H bonds (only present in the core), and thus higher loss at wavelengths closer to the bond resonance overtone.

197
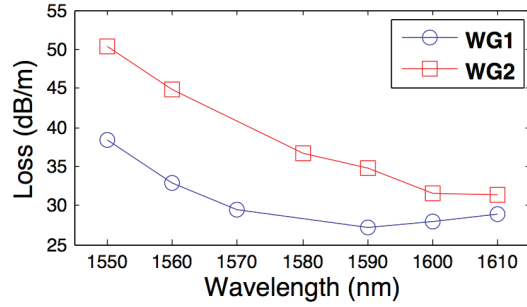
**Figure 6.7:** *Loss versus wavelength for each waveguide layer.*

## 6.3.2 Vertical Coupling Loss

We determined the loss of the vertical directional couplers independently of the coupling ratio and propagation loss using a large array of vertical couplers with varying parameters. The fabricated array consisted of 11 directional couplers, each with varying coupling length from 0 µm to 500 µm in increments of 50 µm. Each set also included non-coupling reference waveguides for both layers. This set was repeated 8 times with varying lateral offset from -1 µm to +1 µm in steps of 0.25 µm. Four of these eight sets were measured on the 4 µm wide guides of Wafer 1, corresponding to lateral offsets of -1.0, -0.25, 0.0 and +0.25 µm, for a total of 39 coupler (156 cross and bar) measurements and 8 reference waveguides (four on each layer). Polarization was optimized for TE mode excitation by observing 1550 nm laser throughput of the reference guides with an infrared camera, using a polarizing beam splitter to differentiate the TE & TM modes.

Coupling loss was calculated as the excess loss of the couplers with respect to the reference waveguides. For launch into a single input waveguide of a given coupler, this is calculated by subtracting the power throughput of the reference guides from the sum of both coupler outputs. We calculated an average coupling loss of 0.19 ± 0.20 dB, where the error from fiber coupling
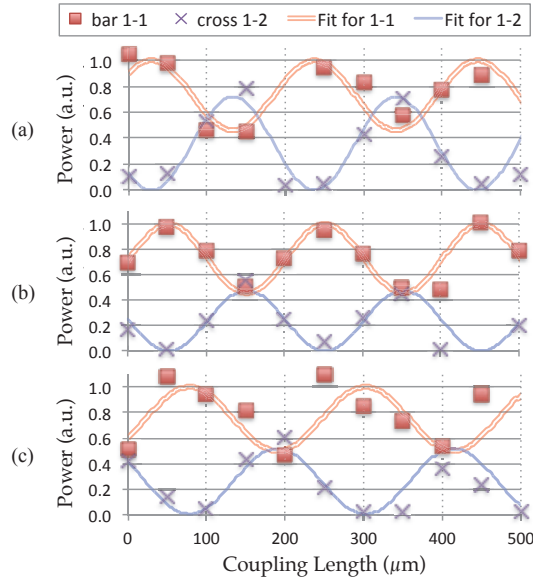
**Figure 6.8:** *Transmitted power (normalized) versus Coupling Length for launch into input #1 to cross (in 1 → out 2) and bar (in 1 → out 1) ports for the (a) -1.0 µm, (b) -0.25 µm and (c) +0.25 µm lateral offsets on Wafer 1.*

was reduced by the large number of measurements performed.

Figure 6.8 shows the power transmitted for launch into layer WG1 and detection on WG2 (cross) and WG1 (bar) for three different lateral offsets. The measurements were performed with lensed fibers and a 1550 nm laser source. Consequently, the plots shown include fiber-to-chip coupling losses and the corresponding uncertainty for each measurement.

Sinusoidal fits were performed by varying the y-offset and amplitude of each sinusoid and minimizing the mean-square error of the fits. The period of the cross & bar curves were kept equal and the phase difference between the two curves was set to $\pi$ radians, the results of which are shown in Figure 6.9.

The sinusoid periods were fit as 208, 200, 174 and 224 µm for the -1.00, -0.25, 0.00 and +0.25 µm offsets, respectively. This indicates that zero offset
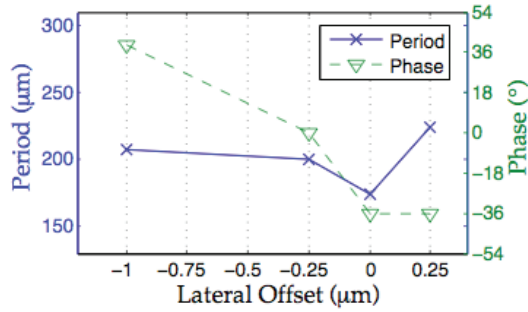
**Figure 6.9:** *Fitted periods and phases for the measured directional coupler arrays on Wafer 1.*

had the largest coupling coefficient, as expected. A steadily increasing phase shift with lateral offset represents an increasing amount of coupling occurring in the bends on either side of the straight coupling section.

Coupling amplitudes of less than 100% indicate that the two parallel waveguide layers are velocity mismatched, a direct result of the stress-related shift in modal indices shown in Section 6.3.1 and described in [12].

The difference in the cross and bar measurements may be additionally accentuated by reduced fiber-to-chip coupling efficiency of WG2, in that a reduction of fiber coupling efficiency would shift the entire 1 → 2 curve down. An asymmetry in fiber coupling between the two layers would still be a result of the stress gradient across the two layers.

Maximum coupling was calculated as the largest percentage of power that leaves the 1 → 1 bar waveguide, with results of 54.0%, 54.7%, 48.8% and 50.0% for the -1.00, -0.25, 0.00 and +0.25 µm offsets, respectively.

Simulations of the cross-coupled power were performed with Photon Design's FIMMWave simulator. We simulated waveguides with the geometries for Wafer 1: 4 µm x 50 nm & 4 µm x 49 nm for WG1 and WG2, respectively. The simulated vertical coupler was composed only of perfectly straight waveg-
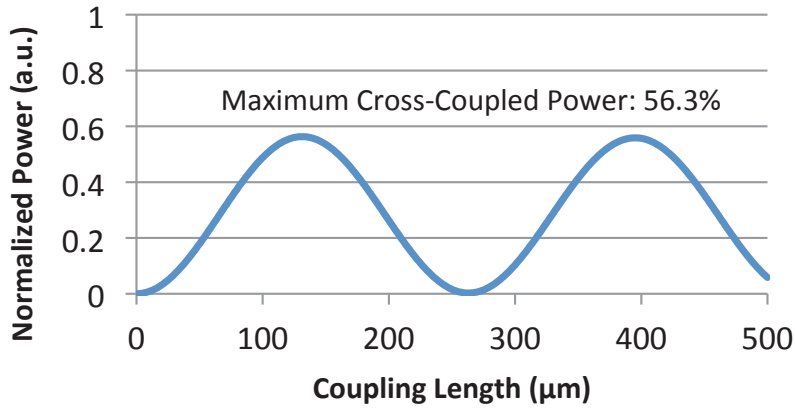
**Figure 6.10:** *Simulated cross-coupling from WG1 → WG2 for $\Delta n = 0.065$.*

uides, with no bends at the entrance and exit, and the waveguides abruptly beginning and ending in the coupling region, which creates some reflection loss at these points.

Sweeping the refractive index of the lower core, WG1, we found that refractive indices of 1.910 and 1.975 for WG1 and WG2, respectively, yielded cross-coupled power of 56%, which is similar to the measured couplers. The cross-coupled power from WG1 → WG2 versus coupling length is shown in Figure 6.10. This shows a slightly larger reduction of refractive indices of 0.065 than the values measured on the spirals with OFDR.

### 6.3.3 Layer Interactions

Figure 6.11(a) shows the power versus distance into the multimode spiral with crossings on Wafer 2 (15 μm x 60 nm cores), where the data was acquired via OFDR and smoothed with a moving-window average. A reflection and drop in power is seen at each crossing, with both the reflection magnitude and transmission loss increasing with crossing width, as one would expect. Loss incurred by each crossing width was calculated by subtracting the re-
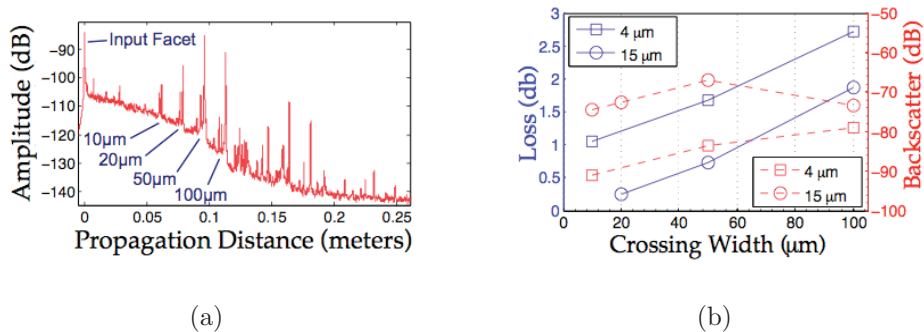
**Figure 6.11:** *(a) OFDR of the spiral with crossing locations and widths indicated for the 15 µm x 60 nm guides on Wafer 2. (b) Losses (solid) and mode-coupled backscatter (dashed) incurred at each crossing width for the same devices.*

flection amplitude after the crossing from that before the crossing, and then correcting for the propagation loss incurred over that distance. This value was then halved to account for the double-pass of reflected light. We additionally calculate the power scattered into backward-propagating waveguide modes by integrating over each reflection peak.

The losses incurred by each crossing width are plotted in Figure 6.11(b), for both waveguide widths on Wafer 2. Interestingly, for the 15 µm wide guide, the 10 µm wide crossing incurs too little loss to differentiate from the propagation loss and measurement error, which indicates that it is well below 0.254 dB. Higher crossing losses for the 4 µm wide guides are a result of reduced modal confinement from "squeezing out" the mode, resulting in larger field overlap with layer WG2, with a minimum loss of 1.05 dB for the 10 µm wide crossing.

## 6.4   Chapter Summary

Using standard PECVD depositions for rapid turnaround, we fabricated vertically coupled $Si_3N_4$ waveguide layers to probe for unforeseen problems with the theory and fabrication of a multi-layer waveguide platform.

Narrow-band OFDR with a 20 nm wide window revealed that film-stress plays a large role by reducing the core refractive indices. Both waveguide layers showed a reduction in core index from the deposited & annealed watch samples. The layer closest to the air interface, WG2, showed an index reduction of 0.01, while the more deeply embedded layer, WG1, showed a larger reduction of 0.06, resulting in a group index difference between the two parallel waveguide planes of 8.5E- 3. This consequently reduced the maximum coupling of the vertical directional couplers, resulting in a maximum cross-coupling of 54.7%.

Even so, the excess loss of the couplers is shown to be as low as $0.19 \pm 0.20$ dB for a 4 µm x 50 nm geometry, which is likely dominated by the bend loss in the couplers (again, an effect of the reduced core indices).

In order to achieve complete coupling with this type of vertical coupling scheme, the stress-optic effect must be addressed with modal index compensation in the waveguide design, or via wafer bonded cladding oxide to reduce the induced stress. For example, knowledge of the stressed core refractive indices (from Figure 6.6) allows one to modify the core geometry of each layer  lithographically or via layer thickness  to match the modal indices of each layer.

Lastly, we showed that for perpendicular crossings on adjacent layers, transmission loss was lower than 0.25 dB for the multi-mode 15 µm x 60 nm waveguide structure. For the single-mode 4 µm x 60 nm geometry, the min-

imum crossing loss was higher, at 1.0 dB for a 10 µm wide crossing. For the intended application of two overlapped spirals, the waveguides on adjacent layers will be closer to parallel than perpendicular, so this measurement indicates the extreme if an adjacent layer is treated as a a scatterer, rather than as a directional coupler.

The primary issue uncovered during this investigation of a multi-layer glass waveguide platform is the existence of a stress-optic effect that varies in magnitude in the vertical direction. Additionally, for the compressive stresses incurred by our deposited claddings, we find that the core refractive index appears to be reduced from the as-deposited value, due to the stress of the upper cladding. The $Si_3N_4$ waveguide with 10 µm of upper cladding showed a smaller index reduction that a lower waveguide with an additional 3 µm of silica above it, corroborating the fact that higher total stress leads to lower core index.

The stress mechanism can be envisioned as a boundary-value problem, in which the combined upper and lower claddings form a slab of $SiO_2$ which is clamped at the silicon substrate, but free to expand at the unclamped air interface. When the wafer is ramped up to high temperatures and subsequently cooled, the $SiO_2$/Silicon interface experiences large stresses due to the mismatched thermal expansion coefficients of the two materials. On the other hand, the $SiO_2$/Air interface can expand and contract freely, so that little energy is bound at this interface.

The result is that the stress - and thus refractive change - of material closer to the air interface is minimal, while the stress buildup at the silicon interface is relatively high. All points in between the silicon and air interfaces will thus exhibit a gradually varying stress, varying from the high value at the substrate, to the low value at air.
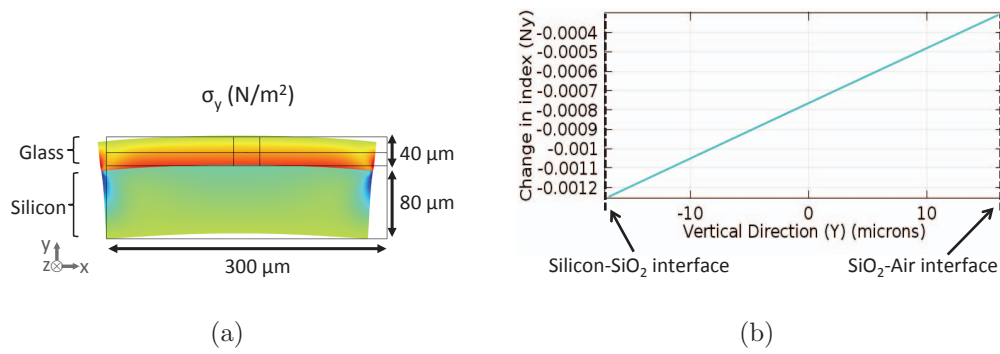
**Figure 6.12:** *(a) The stress component in the vertical (y) direction for annealed $SiO_2$ on Si. (Courtesy J. Bauters) (b) The change in cladding $SiO_2$ refractive index from as-deposited $n_{SiO_2}$ in the vertical direction.*

Finite-element simulations performed with COMSOL Multiphysics corroborate this thought process [11]. Using the built-in material parameters and reduced dimensions to allow for reasonable simulation times, the stress components in each direction were calculated for a 2-D material profile of $SiO_2$ on Si. The color-coded surface in Figure 6.12a shows the vertical stress component, $\sigma_y$, which varies in the vertical direction. Wafer deformation is also present, as indicated by deviation from the initial structure, which is shown by the black outline.

The stress simulation is performed as if the system began at 1000°C, and then cooled to room temperature, creating the thermal-expansion driven stresses. Of course, in actuality the sample is heated and then cooled – so this simulation assumes that the sample was heated for so long that the materials reflowed until reaching equilibrium, which is likely not the case given the solidity of $SiO_2$, even at 1000°C for three hours. However, the effect of vertically varying stress and of lateral deformation is still shown in the color contours.

Figure 6.12b shows the calculated change in refractive index of the glass
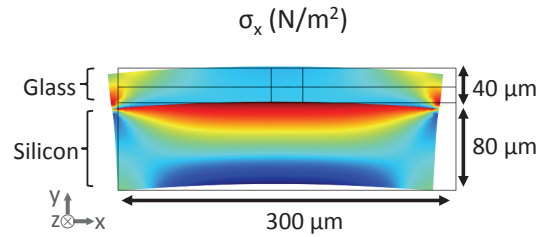
**Figure 6.13:** *The horizontal (x) stress component for annealed SiO$_2$ on Si. (Courtesy J. Bauters)*

layer, for a vertical slice at the middle of the wafer. This shows a linearly varying index, which is a result of the stress in the vertical direction, caused by contraction of the silicon substrate upon cooling. Due to the number of unknown material parameters (all of which have been assumed by the simulator), only the existence of the vertically-varying-stress (and index) can be taken from this plot, not absolute refractive index values, although the simulation corroborates the physical interpretation posited above.

It should be noted that the stress in the lateral direction, shown in Figure 6.13, is what primarily causes the substrate deformation and wafer bow. This deformation can cause the silicon substrate to cleave, or cause the film to delaminate as the shape is changed during heating or cooling.

Stress compensation via backside depositions is often used to flatten wafers that are bowed by high-stress depositions. However, it should be noted that only the laterally varying stress ($\sigma_x$) is compensated with this technique – the vertically varying stress ($\sigma_y$) still exists. This is the case for even thermally grown oxide, which is generally considered to be automatically "stress compensated" – the final substrate remains flat because the oxide grows on both sides simultaneously. The film is *not*, however, "stress–free".

# References

[1] M. Huang, "Analytical solutions for thermal stresses in buried channel waveguides," *IEEE Jnl. Quant. Elec.*, vol. 40, no. 11, pp. 15621568, 2004.

[2] P. Dumais, "Birefringence of strained buried-core waveguides," in *2011 ICO International Conference on Information Photonics (IP)*, 2011.

[3] Bauters *et al.*, "Planar waveguides with less than 0.1 dB/m propagation loss fabricated with wafer bonding," *Optics Express*, vol. 19, no.24, pp. 24090-24101, Nov. 2011.

[4] Bauters *et al.*, "Ultra-low-loss high-aspect-ratio Si3N4 wavequides," *Optics Express*, vol. 19, no. 4, pp. 3163-3174, Feb. 2011.

[5] Armenise *et al.*, *Advances in Gyroscope Technologies.* Berlin: Springer-Verlag, 2010, pp. 32-27.

[6] Bergh *et al.* , "All-single-mode fiber-optic gyroscope,", *Optics Letters*, vol. 6, no. 4, pp. 198-200, Apr. 1981.

[7] Little *et al.*, "Vertically coupled glass microring resonator channel dropping filters," *Phot. Tech. Lett.*, vol. 11, no. 2, pp. 215-217, Feb. 1999.

[8] Kokubun *et al.*, "Polarisation-independent vertically coupled microring resonator filter," *Electronics Letters*, vol. 37, no. 2, pp. 90-92, Jan. 2001.

[9] H. P. Schriemer, M. Cada, "Modal birefringence and power density distribution in strained buried-core square waveguides," *Quantum Electronics*, vol. 40, no. 8, pp. 1131-1139, Aug. 2004.

[10] C. Klein, R. Miller, "Strains and stresses in multilayered elastic structures: The case of chemically vapor-deposited ZnS/ZnSe laminates," *Journal of Applied Physics*, vol. 87, no. 5, pp. 2265-2272, Mar. 2000.

[11] *FEMLAB Electromagnetics Module: Stress-Optical Effects in a Photonic Waveguide*, COMSOL AB, Stockholm, Sweden, 2002.

[12] L. A. Coldren and S. W. Corzine, *Diode Lasers and Photonic Integrated Circuits*, New York, NY: Wiley & Sons, 1995, pp. 286.

# Chapter 7

# Summary & Future Work

This thesis has been effectively split into two separate, related, sections. The first focused on determination of the optimal design and materials for the fabrication of a low-loss glass waveguide. We determined that low-loss requires very large bend radii and device sizes, unless waveguide roughness is reduced. Therefore, we secondly developed a novel fabrication process in an attempt to reduce the sidewall roughness of glass waveguides, following the oxidation techniques used in silicon waveguide fabrication.

In the first chapters of this thesis, we investigated the sources of loss incurred in chip-scale optical waveguides, with the intent to uncover a path to realizing low-loss waveguides, with optical fibers representing the ultimate goal (Chapter 2 on page 20). Simulation tools were developed, allowing for simultaneous simulation of each investigated "waveguide" loss mechanism.

Sidewall and surface scattering were initially simulated using the 2-D analytical expressions of Payne & Lacey [1], and later by a fully 3-D simulation after Barwicz & Haus [2] (p. 21). We reached the conclusion that designs with low core confinement result in reduced mode-overlap with the rough sidewalls, and thus reduced scattering losses (see Figure 2.3 on p. 29). Addi-

tionally, we observed that sidewall scattering should produce a much larger optical loss than surface roughness, simply due to the much larger RMS values (both experimentally and in literature) of etched sidewall roughness than polished and deposited surfaces (p. 26). This led us to the insight that a very thin waveguide will have reduced sidewall roughness loss contribution, thus a high ratio of *width:height* would result in the lowest scattering losses, and simulations confirmed this theory. The mode overlap with horizontal surfaces would be increased, however, and thus the surface scattering loss will also become a larger loss contribution as the waveguide is made wider and thinner (p. 32).

Additionally, we simulated bend losses using the accepted method of conformal index transformation. This revealed that, on a dB scale, bend loss dramatically increases at some minimum bend radius, which we label the "bend loss knee". Any design at significantly smaller bend radii will be bend-loss limited.

These simulations resulted in an understanding of the tradeoff between bend loss and scattering loss, which requires careful management to obtain the lowest possible loss (p. 51). Other parameters, such as waveguide separation (p. 56) and cladding thicknesses (p. 47) were simulated and chosen to be large enough such that the loss impact would be negligible within our approximate design space. We chose a thickness that would minimize modal confinement while still enabling low-loss propagation around the bend radii allowable by our substrate wafer size.

We then performed an investigation into the various glasses available at the UCSB Nanofabrication Facility, analyzing and comparing the material properties of various glasses.

We discussed the optical absorption mechanism of molecular vibrational

absorption, in which Hydrogen bonds can absorb optical power near telecom wavelengths (p. 87). FTIR showed that sputter-deposited and thermally oxidized glassed had the lowest hydrogen, and that annealing of high-hydrogen films could reduce the hydrogen content to below the detection limit of the FTIR, below 20 atoms/cm$^3$.

XPS measurements only detected trace argon and xenon within the IBD sputtered films, both of which are below 0.5 at.%. Much more sensitive SIMS measurements found a number of metal impurities in the IBD sputtered films, along with Hydrogen below the FTIR detection limit (p. 93). The thermally oxidized films appeared to have more hydrogen than the IBD films, although this was unquantified. Unannealed PECVD-based films contained large hydrogen contents, along with fluorine and helium. At this time we have not developed simulations of the expected loss contribution from these material impurities, although, apart from hydrogen, they are expected to be overshadowed by the losses due to roughness.

Measurements of film roughness showed than IBD sputtered films produced the smoothest thin films, appropriate for waveguide cores, while thermal oxidation produced the smoothest thick oxides, applicable to claddings (p. 83).

We additionally developed methods for non-destructively measuring the sidewall roughness via SEM & AFM (p. 34). We found that top-down imaging via SEM undersamples small-scale roughness, but the large acquisition window produces reasonable ACF fits for determination of the correlation length, $L_c$. The undersampling is thought to be due to charging effects, present even in metal-coated samples. The AFM produced more accurate, higher RMS roughness values, but worse $L_c$ curve-fits, most likely due to the small scan length obtainable with this method. The AFM $\sigma$ values were used

as feedback to optimize the roughness due to lithography, achieving minimum values of about $\sigma$=4.4 nm. This roughness is similar to that of commercially-produce waveguides that we obtained and measured in the same way.

Numerous methods to measure waveguide losses on the dB/m scale were attempted, and OFDR with a commercial Luna OBR 4400 was determined to be the most versatile non-destructive testing method with applicability to sub-dB/m losses (p. 111). We developed custom methods to analyze the raw data, providing a Matlab-based API for obtaining the group index, loss and wavelength-dependent loss of a measured waveguide.

The developments described above were used to fabricate $Si_3N_4$-core/$SiO_2$-clad waveguides with measured losses as low as 1.73 $\pm$0.17 dB/m, for the high-wavelength range (1590–1600 nm) of the TM mode of a multi-mode 10.5 µm x 100 nm waveguide (p. 128). The lack of prominent absorption peaks indicates that the losses of these waveguides are limited by scattering. This, in addition to the prior observation that very small devices (mm-scale) are inherently scatter-loss limited, led us to pursue novel roughness reduction techniques for application to glass waveguides.

We then developed a fabrication method intended to reduce sidewall scattering, for the first time employing the selective oxidation of silicon oxynitride. We further apply this technique to the fabrication of silica-based waveguides (Chapter 5 on p. 147).

We created a 2-D simulation of the sidewall smoothing mechanism, and found that the calculated roughness parameters in the resulting waveguide core show that waveguide loss should be reduced. We also found that very small-scale roughness would see the largest improvement from a selective oxidation process.

The oxidation of sputter-deposited $SiO_xN_y$ of varying indices (including

stoichiometric $Si_3N_4$) shed light on the interesting chemistry taking place. The most important effects were that of the volume expansion of $Si-N$ bonds upon oxidation, and the role of residual ammonia, which causes the generated oxide to exhibit slightly higher refractive indices due to re-nitridation. The core geometries were simulated with SILVACO Athena, revealing that expansion ratio would result in a tapered sidewall, which is not accounted for by our simulation tools (which address only rectangular shapes).

Devices were fabricated using the Local Oxidation of Oxynitride (or LOO) process, which enabled the definition of very thick ~1 µm cores with only 100 nm of etching, eliminating the need for metal hard masks and polymer removal processes. We fabricated the same spiral configuration and widths as the previous direct-etched $Si_3N_4$-core devices. The major difference is that we used $SiO_xN_y$-cores for their higher oxidation rates as compared with the sputtered $Si_3N_4$ oxidation mask, which enables this high 8:1 *core thickness* : *etch depth* ratio. The core geometry was very similar to that simulated with SILVACO Athena, with thickness and width reductions corresponding to the upper cladding stress and bird's beak effect, respectively (described on p. 169).

These devices exhibited minimum initial losses of 9.0 dB/m for both TE & TM modes, and showed clear $N-H$ absorption peaks at lower wavelengths. The losses below 1560 nm were determined to be limited by these bond resonances, while still scattering loss limited at higher wavelengths (Figure 5.19 on p. 175).

Lastly, an iterative optimization procedure was utilized to progressively lower the losses. This method was enabled by the non-destructive nature of OFDR loss & $n_g$ measurement, and an unmasked reoxidation of the waveguide devices, which thins and narrows the waveguide cores (p. 177). The

lowest losses obtained with this process were 6.5 dB/m for the wide, multi-mode waveguides between 12.5 µm and 17.5 µm and 590 nm thickness.

## 7.1 Future Work

The LOO Process was originally pursued in order to reduce sidewall roughness. The reduction in roughness was deemed necessary to enable low loss propagation in very small devices, although in this work only very large devices of 10 mm bend radii were fabricated. The novel processes developed here should be applied to the fabrication of low-loss waveguides at millimeter or sub-mm bend radii. In fact, the use of contact lithography was really necessitated by the large die sizes, which were much larger than the field size of available projection lithography tools. Fabrication of small devices that can be patterned via stepper lithography would lower sidewall roughness and entirely remove the issue of maskplate scum (p. 127).

Additionally, the lowest-loss direct-etched waveguide have, surprisingly, used high-index cores, and achieved low confinement via thin cores with a very high $width : height$ ratio (see both reference [5] and p. 128). The LOO devices shown on p. 166, on the other hand, used lower index cores, which then necessitated thicker cores. The benefit is that they are far less polarization dependent, as exhibited by the similar losses of the TE & TM modes. However, it stands to reason that high-index $Si_3N_4$-cores could be produced with this oxidation process. This simply requires using a thicker $Si_3N_4$ oxidation mask than the $Si_3N_4$ core thickness used, eg. a 150 nm thick oxidation mask to define a 100 nm thick core. This was in fact attempted, although the fabrication yield was too low to produce measurable devices. In one case, particulate deposition from the IBD led to very high-loss scatterers

across the wafer, while the last attempt was overoxidized (despite careful observation of watch samples at various points), resulting in no waveguiding at all. Neither of these are insurmountable problems, and further attempts to replicate the low loss $Si_3N_4$-core geometries with the etchless core-definition process should be attempted. (One further observes that the lowest loss waveguides to date in [5] also obviated the stress-optic effect by using bonded thermal oxide for the upper cladding).

The reoxidation process demonstrated here is actually applicable to any $SiO_xN_y$-based glass waveguide technology, even if direct-etching is employed. For example, the 100 nm thick $Si_3N_4$-cores that are shown in Section 4.3 on page 128 could now be subjected to high-temperature steam oxidation, to thin the cores. Since those devices are currently scatter-loss limited and don't appear to show the onset of bend loss limiting, a reduction in confinement via reoxidation would be expected to lower losses further. The iterative optimization process should be used to locate the optimal geometry for low loss. Of course, wavelength-dependent losses should be analyzed to ensure that $N-H$ bonds are kept low, perhaps requiring mitigation via long anneals.

Even our foundry-fabricated devices are open to improvement via reoxidation, as long as silica is employed for the upper cladding (as opposed to the bonded silicon substrates more recently shown in [5]). Apart from simply allowing post-measurement trimming of core geometry, for a direct-etched device, the sidewall roughness may also see improvement via the diffusion process, as shown on p. 152.

The non-rectangular core geometry produced with the LOO Process is expected to play a large role in the propagation characteristics (p. 166). The tapered sidewall produced by this process likely squeezes-out the optical mode, which would manifest as an effective-index version of a graded-index

sidewall. The impact on propagation characteristics should be simulated by importing core geometries generated with SILVACO Athena into the simulations tools we have developed, namely the mode, bend loss and scattering loss calculators.

Sharply tapered sidewalls have also found use in whispering gallery resonators, with impressive results [4]. These tapers, when applied to the conformal index transformation shown in Figure 2.15 (p. 47), result in a broadened core index peak, allowing for a mode that is guided only at the outer edge of the core. The oxidation process could be used to fabricate waveguide-coupled whispering gallery mode ring resonators, although the width reductions would need to be accounted for in order to produce the expected coupling gap between bus waveguides and the ring resonators.

A final example is the tuning of modal index via reoxidation, rather than just loss. For example, a ring resonator could be repeatedly oxidized to move the resonance frequency to within a very tight tolerance. For a $Si_3N_4$-based waveguide, oxidation rates are so slow that one would have nanometer-level accuracy in the core geometry, and thus very fine tuning in the resulting modal index & resonance frequency.

In general, the concept of oxidizing $SiO_xN_y$ or $Si_3N_4$ intentionally, and doing so through the thick upper cladding oxide after device measurement, is applicable to a myriad of oxynitride-based glass waveguide devices.

# References

[1] J. Lacey and F. Payne, "Radiation loss from planar waveguides with random wall imperfections," *IEEE Proceedings*, vol. 137, no. 4, pp. 282288, Aug. 1990.

[2] T. Barwicz and H. A. Haus, "Three-dimensional analysis of scattering losses due to sidewall roughness in microphotonic waveguides," *IEEE Jnl. Lightwave Tech.*, vol. 23, no. 9, pp. 27192732, 2005.

[3] L A Coldren and S W Corzine, *Diode Lasers and Photonic Integrated Circuits.* New York, NY: John Wiley & Sons, Inc., 1995, p.322

[4] S. Spillane, D. Armani, and K. Vahala, "Fabrication and coupling to planar high-Q silica disk microcavities," *Applied Physics*, 2003.

[5] J. F. Bauters, M. Heck, D. John, and J. S. Barton, "Planar waveguides with less than 0.1 dB/m propagation loss fabricated with wafer bonding," *Optics Express*, vol. 19, no. 24, pp. 2409024101, Nov. 2011.

# Appendix A

# Fabricated Devices: Losses & Failures

During the course of my foray into glass waveguide fabrication, I documented the devices being fabricated on an ongoing spreadsheet. A huge number of devices failed, for various reasons, and this table documenting 3 years worth of devices allows one to comprehend how difficult some of these issues turned out to be. It may be easy to dismiss the effects of thin-film stress, until you notice that almost 10% of the devices failed due to cleaving, usually from the high stresses incurred by deposited upper claddings.

The Histogram of Failure, Figure A.1, shows a histogram encompassing about half of the devices we attempted to fabricate, binned by general failure mode. This actually includes some devices that were fully fabricated, but then did not guide, or failed optically in some way. Clearly, it took a long time for us to understand that the stress-optic effect, created by the stress of thick deposited upper claddings, was responsible for the recurring bend loss-limited devices we kept fabricating.

For more insight into how these general failure modes actually manifested,

## Reasons for Device Failure
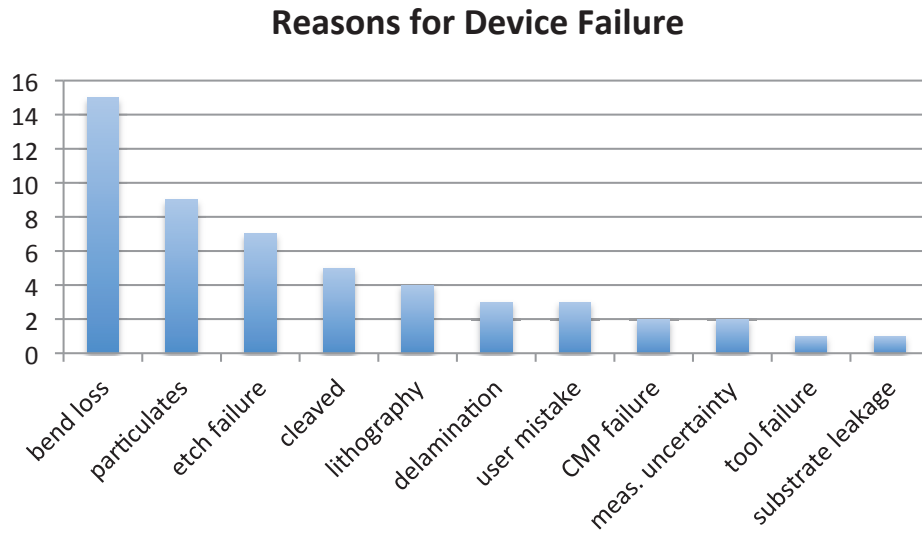


**Figure A.1:** *The Histogram of Failure: failure modes of 52 devices, out of the 97 listed in Table A.1.*

take a look through the following table, Table A.1, which lists (most) of the fabricated waveguide devices chronologically. 97 devices are listed here, fabricated mostly by myself, but also by Dr. Jonathon Barton & Renan Moreira. 52 of these were included in the aforementioned histogram of failure, if the failure mechanism was able to be inferred. Losses and failure mechanisms are included, with some insight into exactly what we believe caused the failure. Green sample names indicate devices that were fully fabricated, while Red sample names indicate a device destroyed before measurement. Red is also used in the Conclusions column for devices that were fabricated successfully, but failed due to lack of guiding or ability to measure.

**Table A.1:** *List of devices fabricated from Jan. 2009 to March 2012*

<div align="center">Table A.1</div>

| Sample Name green=done red=aborted/fail | Waveguide Structure | Notes on process Unique Traits of Device | Loss Measured (dB/meter) | Measurement Method | Structure Tested | Comments/Conclusions | Lowest Loss Measured (dB/m) | Failure Reason | Failure Specific |
|---|---|---|---|---|---|---|---|---|---|
| SiNox#30.1 | Core: AJA SiN 100nm oxBuff: 418nm AJA SiO2 | oxidized SiN-core oxMask: 180nm AJA SiN WetVar: 1050°C, 34h20m IPhOD 2_5 | | | | Since AJA does not have particulate issue | | | |
| SiNox#30 | Core: IBD SiN 100nm | oxidized | | | | IBD dep'd too little and then died.. abort. | | tool failure | |
| SiONox#30 | Core: Unaxis 5/5: n=1.560, ~970nm oxBuff: ~1000 nm | | | | | | | | |
| ox180 | AJA-SiN: 183.67 nm n=2.04874 (unannealed) | | | | | particulates (AJA or avpecvd_b.s.) | | particulates | AVPECVD |
| et180 | AJA-SiN: ~180nm | | | | | | | | |
| et400 | Unaxis 5/5 | | | | | | | | |
| ox600 | | | | | | unax/avpecvd particulates | | particulates | AVPECVD |
| et600 | | | | | | unax/avpecvd particulates | | particulates | AVPECVD |
| ox100-ibd | | | | | | ibd particulates | | particulates | IBD |
| et100-ibd | Core: IBD SiN ~100nm | | | | | | | | |
| et90-ibd | Core: IBD SiN ~90nm | | | | | | | | |
| DJ02-B (IBD, ox) | Core: IBD SiON d=601.099 nm n=1.61542 - oxBuff: Unax 284.044 nm - oxMask: IBD SiN 52.580nm | Bonded UClad | | | | IBD core particulates | | particulates | IBD |
| DJ02-A (IBD, etch) | Core: 606.236nm n=1.61682 (1.614, 0.00714, 1.126e-5) | Bonded UClad HF etched core | | | | | | | |
| DJ01-B (Unax, ox) | - Core; Unax 5/5: d=605.137 nm n=1.56114 (1.555, 0.006, 4.5282e-7) - oxBuff: Unax 300.164 nm - oxMask: IBD SiN 52.580nm | Oxidized Core Bonded UClad | | | | IBD oxMask particulates | | particulates | IBD |
| DJ01-A (Unax, etch) | Core; Unax 5/5: d=606.280 nm n=1.55757 (1.555, 0.006, 4.5282e-7) | Direct etch | | | | lost PR during core etch Etch depth too deep/etch selectivity inadequate | | etch failure | Selectivity to PR too low |
| SiNstrip#8 3/14/12 | Mask: In-House 2_5 core: AJA SiN 100 nm LClad: 15µm KST (450µm?) UClad: Unax 10µm (4µm + 1050°C anneal...) | 1µm AJA SiO2 Partial UClad + 1050°C, 3hr anneal | Lowest: 10.5µm: 1.73 dB/meter (TM >1550nm), 2.0 dB/m avg TM | OBR | Spiral, 1.11m | Lowest Loss to-date! In-house loss matches or beats simalr design at LiONiX! | 1.73 | | |
| SiNstrip#7 | core: IBD SiN 110nm | | | | | particulates (IBD) | | particulates | IBD |

Table A.1

| Sample Name green=done red=aborted/fail | Waveguide Structure | Notes on process Unique Traits of Device | Loss Measured (dB/meter) | Measurement Method | Structure Tested | Comments/Conclusions | Lowest Loss Measured (dB/m) | Failure Reason | Failure Specific |
|---|---|---|---|---|---|---|---|---|---|
| SiNstrip#6 | mask: in-house 2.5 65nm IBD SiN core L/UClad = 15um KST Dep'd UClad: 10μm | Thicker core IBD partial UClad Bonded UClad ~550um Si substrate (KST 15um ox) | Bend loss limited - lost light at angled/tight BR input waveguides | IR camera | spiral | worked tight bends on inputs radiate all the light - think it's bend loss limited due to core index reduction (stress of UClad) | | bend loss | mask plate: too tight bends at input |
| SiNstrip#5 | mask: in-house 2.5 55nm IBD SiN core L/UClad = 15um KST | | | | | Needs: •CMP + Bond | | | |
| SiNox#4 | mask: in-house 2.5 65 nm IBD SiN core L/UClad = 15um KST Depd' UClad: 10μm | oxBuff = ~200nm IBD SiO2 Bonded UClad ~550um Si substrate (KST 15um ox) | Bend loss limited - lost light at angled/tight BR input waveguides | IR camera | spiral | worked - seemed lower loss (w/ Red light) than SiNstrip#6 (identical structure otherwise) | | bend loss | mask plate: too tight bends at input |
| SiONox #23 11/17/11 | Oxidized SiOxNy + Bonded UClad t = 938.70 nm (as dep'd) w = 4.5-15.0μm n_core= 1.59858 (as dep'd) t/n_LClad=15um / 1.445 (KST ThermOx) t/n_UClad=15um / 1.445 (KST ThermOx) | 1mm substrate oxBuff = 233.123 nm (Unaxis) Core = Unaxis SiON • WetVar 950°C, 5hr • Post-WetVar Anneal: 1050°C, 14hr --> glass damaged! | | | | large Nitride squares caused glass to delaminate above it upon anneal. Not good for bonded cladding 1mm thick substrate prevent energy release by bowing, so films delaminated instead. | | delamination | oxidation anneal |
| SiONox#22 06 - ReOx#3 | | WetVar 1000°C, 2h30m | 7.0 | OBR | Spiral | Loss increased | | | |
| SiONox#22 05 - ReOx#2 | core_t = 0.590 nm | WetVar 1000°C, 2hr | 6.247 dB/m and up | OBR | Spiral | optimal reoxidation | 6.30 | | |
| SiONox#22 04 - ReOx1 Anneal | | Anneal 1000°C, 5hr | 9.54 dB/m loss increased! | OBR | Spiral | I believe oxidation lowers the density (by increasing the hydrogen), lowers the index, lowers the confinement, lowers the scattering and thus lowers the loss. The increased H2 marginally increases the loss. The anneal undoes all that - so even though the core is thinner, it goes back to increased scattering (and decreased H2 is minimal contribution) | 9.50 | | |
| SiNox #22 03 - ReOx #1 | core_t = 689nm | WetVar 1000°C, 1hr | 17.0μm: 7.29 dB/m and up | OBR | Spiral | | 7.30 | | |
| SiONox #22 02 - Anneal#1 | | Anneal 950°C, 7sec (tool error) | no change | OBR | Spiral | | | | |

| Sample Name green=done red=aborted/fail | Waveguide Structure | Notes on process Unique Traits of Device | Loss Measured (dB/meter) | Measurement Method | Structure Tested | Comments/Conclusions | Lowest Loss Measured (dB/m) | Failure Reason | Failure Specific |
|---|---|---|---|---|---|---|---|---|---|
| SiONox #22 11/17/11 01 - Initial | Oxidized SiOxNy + Bonded UClad t = ~0.80 µm (SEMd) w = 5.0-17.5µm n_core= 1.59858 (as dep'd) t/n_LClad=15um / 1.445 (KST ThermOx) t/n_UClad=10um / 1.445 (Unax Dep) | 1mm substrate oxBuff = 233.123 nm (Unaxis) Core = Unaxis SiON (5/5) • WetVar 950°C, 5hr • Post-WetVar Anneal: 950°C, 14hr  No Partial UClad (sputtered) 10µm Unaxis Dep'd UClad (4µm batches w/ 1050°C, 3h anneal between) | prelim: ~8.59 dB/m and up | OBR | Spiral | Good SiONox! | 8.60 | | |
| SiN-VC-05 | SiN-strip, Vertical Coupler t/nCore = ~60nm / ~1.997 | AV-PECVD Cores, Coupling Gap Unaxis 10um UClad | | IR camera | spiral | | | bend loss | too thin core stress-optic effect |
| SiN-VC-04 | SiN-strip, Vertical Coupler t/nCore = ~100nm / ~1.997 | | | OBR | Spiral | | | lithography | PR sticking to Maks Plate |
| SiN-VC-02 | SiN-strip, Vertical Coupler t/nCore = ~50nm / ~1.997 | | | IR camera | vertical couplers | propagates in straight WGs ok, but loses light when entering the bends. | 26.00 | bend loss | too thin core stress-optic effect |
| SiON-ox #21 10/1/2011 | ~900nm Core (N/O=1.0) | Bonded UClad - 15um thick 250nm thick oxBuff | ~20dB/m | OBR | Spiral | bubbles in bonding - not CMP planarized enough | 20.00 | CMP failure | non-planar prior to bond |
| SiON-ox #20 10/1/2011 | ~600nm Core (N/O=1.0) | Bonded UClad - 15um thick 250nm thick oxBuff | hard to couple | OBR | Spiral | bubbles in bonding - not CMP planarized enough | | CMP Failure | non-planar prior to bond |
| SiON-ox #19 9/16/2011 | Oxidized SiOxNy - Unaxis: t = ~970nm rib (not fully ox'd) w = 4.5-15.0µm n_core=~1.58 n_LClad=1.448 t_LClad=15um WetOx, FZ-Si n_UClad=1.45? (Unax) | -- Much thicker oxBuff - ~1000nm • Thicker core for optimization via ReOx core: 970.127nm, n1550=1.573 ox mask: 50nm SiN uclad: 4um/1050, 3h/4um/1050, 3h/2um/1050, 3h (no B.S.)  core ox: 950, 3hr 1st reox: 950 1hr 2nd reox: 1050 3hr 3rd reox: 1050, 3hr  • IPhOD#2 mask after Photronics clean + Suss MPT coating | ~15 dB/meter | OBR | Spiral | Very slight oscillation in OBR plots much longer period than previous oscillations - possibly longer than spiral roundtrip Lots of scatterers | 15.00 | lithography | mask plate dirt |

| Sample Name green=done red=aborted/fail | Waveguide Structure | Notes on process Unique Traits of Device | Loss Measured (dB/meter) | Measurement Method | Structure Tested | Comments/Conclusions | Lowest Loss Measured (dB/m) | Failure Reason | Failure Specific |
|---|---|---|---|---|---|---|---|---|---|
| SiON-ox #18 05/25/11 | Oxidized SiOxNy - Unaxis: t = w = 4.5-15.0µm n_core= n_LClad=1.448 t_LClad=15um WetOx, FZ-Si n_UClad=1.45? (Unax) | -- Much thicker oxBuff - ~1000nm • Otherwise, same as 17.1/17.2 • IPhOD#2 mask (more widths) | | | | • Cleaved through spiral upon handling after UClad anneal -- Should have done partial UClad deps/stress comp/anneals (5µm each), or less B.S. comp • NO flaking/delamination on anneal!  Stress compensation method is good for 15µm UClad, but must be done in steps to avoid overcompensating | | cleaved | upper cladding stress |
| SiON-ox #17.1 --ReOx#1 05/30/11 | | WetVar on Spiral (upright), 1050°C, 1hr • Got XXX additional UClad (Total = XXX) | ReOx 1050°C 1hr: | | | Cleaved thru Spiral during Bow meas - picked up on notch and knocked tweezers against tool • Core thinned by XX nm (~50nm) after WetVar 1050°C 1hr • Anneal 1050°C, 30hr significantly altered stress - severely negative bow | | cleaved | upper cladding stress |
| SiON-ox #17.1 05/27/11 | Oxidized SiOxNy - Unaxis: t = <renan> w = 4.5-15.0µm n_core= <renan> n_LClad=1.448 t_LClad=15um WetOx, FZ-Si n_UClad=1.45? (Unax) | • Unaxis Core ~1.505 -- Thicker, to compensate for high-temp densification • 200nm oxBuff (standard) • IPhOD#2 mask (more widths) | 14.0 TE: 22.00 // TM: 18.11 13.5 TE: 23.06 // TM: 17.41 13.0 TE: 23.89 // TM: 17.65 12.5 TE: 23.80 // TM: 17.88 10.5 TE: 24.94 // TM: 21.37 8.0 TE: 22.56 // TM: 28.36 | OBR | Spiral | Higher loss - due to thinner oxBuff?  If so, then theory is confirmed, and next sample should have even thicker oxBuff | 17.41 | 13.5µm TM | |
| SiON-ox #17.2 --ReOx#3 06/8/11 | | WetVar on Spiral (upright), 1050°C, 2hr • Got XXX additional UClad (Total = XXX) | ReOx 1050°C 2hr: | | | • WetVar 1050°C 2hr: upper cladding flaked off on 1/2 of the wafer | | delamination | oxidation |
| SiON-ox #17.2 --ReOx#3 05/30/11 | | WetVar on Spiral (upright), 1050°C, 1hr | ReOx 1050°C 1hr: | OBR | Spiral | • Core thinned by XX nm (~50nm) after WetVar 1050°C 1hr • Anneal 1050°C, 30hr significantly altered stress - severely negative bow | | | |
| SiON-ox #17.2 --ReOx#2 05/20/11 | | WetVar on Spiral (upright), 1000degC, 1hr | ReOx 1000°C 1hr (1.5h total): no change? values pending | OBR | Spiral | no change in core thickness (SEM) | | | |
| SiON-ox #17.2 --ReOx#1 05/16/11 | | WetVar on Spiral (upright), 1000degC, 30m | ReOx 1000°C, 30m: no change? values pending | OBR | Spiral | no change in thickness (SEM) | | | |

Table A.1

| Sample Name green=done red=aborted/fail | Waveguide Structure | Notes on process Unique Traits of Device | Loss Measured (dB/meter) | Measurement Method | Structure Tested | Comments/Conclusions | Lowest Loss Measured (dB/m) | Failure Reason | Failure Specific |
|---|---|---|---|---|---|---|---|---|---|
| SiON-ox #17.2 05/4/11 | Oxidized SiOxNy - Unaxis: t = 550nm (SEM) w = 2.5-15.0µm n_core= <renan> n_LClad=1.448 t_LClad=15um WetOx, FZ-Si n_UClad=1.45? (Unax) | • Unaxis Core ~1.505 – Thicker, to compensate for high-temp densification • 500nm oxBuff • oxMask: 50nm AV-PECVD SiN | initial: 11.5µm TE: 11.62 // TM: 9.54 12.0µm TE: 10.72 // TM: 8.82 13.0µm TE: 10.86 // TM: 7.76 14.5µm TE: 10.87 // TM: 9.91 average of WG#5 (5th largest): 6.95 WetVar 1050°C, 1hr: | OBR | Spiral | • SEMs of intial facets: ~550nm thick (42% reduction) • Lower loss than 17.1 (thinner oxBuff): thicker oxBuff lowers loss? – could be due to 17.1 having particulates, even though both samples were in all the same depositions at the same time on AV-PECVD | 6.95 | | |
| SiNox #3 4/25/2011 | Oxidized SiN-strip | Same as LiONiX geometry, core-definition via Oxidation • Doubled Oxidation Buffer (incr. Correl.Length) IBD films core: ~50nm, n_core~2.007 oxBuff: ~400nm (& Annealed 1150°C, 3h) | | | | • Difficulty coupling to both #2 & #3 SiNox waveguides | | bend loss | too thin core stress-optic core reduction too tight bends on mask (at input) |
| SiNox #2 4/22/2011 | Oxidized SiN-strip | Same as LiONiX geometry, core-definition via Oxidation IBD films core: ~50nm, n_core~2.007 oxBuff: ~200nm (& Annealed 1150°C, 3h) | | | | | | bend loss | too thin core stress-optic core reduction too tight bends on mask (at input) |
| SiNox #1 (was JB9) 4/20/2011 | Oxidized SiN-strip | Same as LiONiX geometry, core-definition via Oxidation Core PECVD: ~58nm oxBuff: PECVD ~200nm oxMask: PECVD ~75nm | | | | Many Particulates from PlasmaT PECVD - will use for Oxidation test only (not loss meas.) | | particulates | deposition - AVPECVD |
| JB#11e | Oxidized SiOxNy | | | | | | | | |

Table A.1

| Sample Name green=done red=aborted/fail | Waveguide Structure | Notes on process Unique Traits of Device | Loss Measured (dB/meter) | Measurement Method | Structure Tested | Comments/Conclusions | Lowest Loss Measured (dB/m) | Failure Reason | Failure Specific |
|---|---|---|---|---|---|---|---|---|---|
| JB#11d ~5/2/2011 | Oxidized SiOxNy | • Wafer Fusion UClad | ~10dB/m | OBR | Spiral | • Wafer fusion = ok -- did not appear to significantly lower loss | ~10 | | |
| JB#11c | Oxidized SiOxNy | • Wafer Fusion UClad | | | | | | | |
| JB#11b ~4/22/2011 | Oxidized SiOxNy: core th = ___(1350secs) n@1550= | | 6.3688 - 12.9386 | OBR | Spiral | | 6.37 | | |
| SiON-ox #16 04/7/11 | Oxidized SiOxNy: t = 475.444nm (post-anneal) w = 4.5-15.0µm n_core= 1.581 (post-anneal) n_LClad=1.448 t_LClad=15um WetOx, FZ-Si n_UClad=1.45? | • Higher ∆n IBD SiONox - IBD (void-free) partial upper cladding | ~10dB/m | OBR | Spiral | Very little guiding after re-ox - annealing must be reducing index contrast by a lot. Many guides only show cladding modes | ~10 | bend loss | stress-optic effect after anneal/reoxidation |
| SiON-ox #15 02/27/11 | Oxidized SiOxNy - Unaxis: t = 609.634 (pre-anneal) w = 4.5-15.0µm n_core= 1.505 (pre-anneal) n_LClad=1.448 t_LClad=15um WetOx, FZ-Si n_UClad=1.45? (Unax) | • 400nm oxBuff • Unaxis Core ~1.505 (should increase w/ anneal) - IBD (void-free) partial upper cladding • IPhOD#2 mask (more widths) • Unaxis Core, IBD oxBuff/oxMask on top of WetOx LClad - Each film annealled after dep | | | | - defect near middle of wafer - will place in center of spiral to avoid WGs - looks ok - Overcompensated with B.S. SiN - bow ~= -300µm (Unax Core?) • Cleaved thru spiral during dice - only bypass WGs intact | | cleaved | stress during dicing |
| SiNstrip#04 4/5/11 | IBD SiN core n_core= t_core= L_Clad = 15um WetOx, FZ-Si, Annealled & vac sealed before core dep | - Standard single-resist, SiNetch process for baseline - IBD (void-free) partial upper cladding | initial~ 50dB/meter 4µm: ~105.581 dB/m | IR camera | spiral bypass | • some defect on TOP of Uclad (on spiral) - pretty sure this is not a scratch and should be 10µm away from core • Could not see end-fact of ~6cm long bypass WGs | 50.00 | | |
| SiNstrip#03 2/23/11 | IBD SiN core n_core= t_core= L_Clad = 15um WetOx, FZ-Si, Annealled & vac sealed before core dep | - Chrome HardMask/SF6 Glass etch process - Will AFM sidewall roughness to compare - IBD (void-free) partial upper cladding | | | | - Cr etch (4m) not overetched enough - some small (15nm) bumps across wafer  ABANDONED | | etch failure | chromium etch products micromasking |

| Sample Name green=done red=aborted/fail | Waveguide Structure | Notes on process Unique Traits of Device | Loss Measured (dB/meter) | Measurement Method | Structure Tested | Comments/Conclusions | Lowest Loss Measured (dB/m) | Failure Reason | Failure Specific |
|---|---|---|---|---|---|---|---|---|---|
| SiNstrip#02 2/22/11 | IBD SiN core n_core=1.929 (post-anneal) t_core=48.862 nm (post-anneal) <br> L_Clad = 15µm WetOx, FZ-Si | • Wafer fusion Upper Cladding <br> IBD SiN (on both sides of wafer) + Anneal 1050°C, 3hr - Reflowed resist before etch - AFM'd sidewall roughness <br> Barton attempting ThermOx Wafer Fusion for UClad 1um Unax Partial Uclad / CMP / WfBond | ~10dB/m | | | (For WetOx UClad Fusion experiment) | | | |
| JB #11 ~4/8/2011 | oxidized SiOxNy <br> core th = 591.3 nm n@1550nm=1.562 (pre-anneal) Buffer - 430 secs, 195 nm n@1550 = 1.463 UC same material as buffer (SiO2 250C) - 11um | PR removal PEII 2min - 300mTorr, 100W 1165 strip 25 min @ 80C Solvent clean O2 Ash @100C 30 min | | | | ABANDONED - due to overoxidation of core - Core witness sample cracked, don't know post-anneal thickness and index <br> -Did 1050C oxidation instead of 950C <br> -Did not do an ash after nitride mask removal, some polymer might be present | | mistake | oxidized at wrong temperature (too high) core over oxidized |
| JB #08 | Oxidized SiOxNy <br> core 1350 sec N2=5, O2=5 Buffer 450 secs 250C SiO2 11 um of Upper cladding | • IBD SiN oxMask (50nm) <br> 3 um of UC anneal 1150 3hr 4 um of UC 2 um of back comp. anneal 1150 3hr 4 um of UC 4 um of back comp. anneal 1150 3hr | initial: ~5dB/meter | | | • Notch on wafer after last Anneal caused autocleave during dicing, breaking spiral. --> Possibly due to TyStar door shaking during load/unload • micrometer Bow ~ 700µm during dice - should B.S. stress comp more to alleviate. | ~5 | cleaved | upper cladding stress cleaved during dicing |
| JB #07 reox | Reoxidized (thinned) core: WetVar 1050°C, 1hr | | | | | | 4.44 | reoxidized | |
| JB #07 | Oxidized SiOxNy: t=~400 nm w = 4.5-15.0µm n_core= ~1.550 n_LClad=1.448 t_LClad=15um WetOx, FZ-Si n_UClad=1.45? (Unax250CNoAr) | Got backside stress comp. (PlasmaTherm SiO2) after every 4µm of Upper Cladding SiO2 | reox 1050°C 1hr: 4.4437 - 13.4944 <br> orig: 8.1097 - 15.4495 | OBR | Spiral | Oscillations in OBR trace due to lithography issues (dirt on mask) | 8.11 | lithography | dirt on mask burnt photoresist in oxidation furnace (JB) |

226

Table A.1

| Sample Name green=done red=aborted/fail | Waveguide Structure | Notes on process Unique Traits of Device | Loss Measured (dB/meter) | Measurement Method | Structure Tested | Comments/Conclusions | Lowest Loss Measured (dB/m) | Failure Reason | Failure Specific |
|---|---|---|---|---|---|---|---|---|---|
| LiONiX Run#002 2/27/2010 | SiN-strip: t = 20nm, 30nm, 40nm, 50nm; w = range? um; n_core~ 1.9835; n_clad~ 1.4456; L-Clad t= 15 um; U-Clad t= 15 um | Fabricated at Foundry: LioniX BV (Holland); • Resist reflow; • Double TEOS partial UClad; • More widths (wider), thinner cores; • Thicker Upper/Lower claddings (15µm) | Reanalyze with narrow bandwidth; 50? nm x X.X µm? 1580nm: <0.1 dB/m ± ~0.1 dB/m; OBR meas /88nm Bandwidth: •12.5µm x 50nm: --MM=1.047±0.017 dB/m --SM=0.738±0.031 dB/m | OBR | Spiral | • 40nm WG had polishing grit on half of spiral; • 20, 30nm WGs did not guide 1550nm; widths = 5.3, 6.5, 8.5, 9.0, 9.5, 12.5, 13.0, 13.5, 14.0, and 14.5; thicknesses = 50nm, 40nm, 30nm, 20nm; SEMs indicate cores are possibly 5nm thinner than expected | 0.34 | | |
| SiON-ox #14 02/09/11 | Oxidized SiOxNy: t = 533.75nm (post-anneal); w = 4.5-15.0µm; n_core= 1.505 (post-anneal); n_LClad=1.448; t_LClad=15um WetOx, FZ-Si; n_UClad=1.45? (Unax100CNoAr) | • Annealed Core @1050°C, 3hr; (No L-Clad Anneal); • Same as #13; • IPhOD#2 mask (more widths); • All IBD films on top of WetOx LClad (mult deps) | | | | | | bend loss | too low core index; stress-optic core reduction |
| SiON-ox #13 02/09/11 | Oxidized SiOxNy: t = 565.418nm (post-anneal); w = 4.5-15.0µm; n_core = 1.497 (post-anneal); n_LClad=1.448; t_LClad=15um WetOx, FZ-Si; n_UClad=1.45? (Unax100CNoAr) | • Annealed Core @1050°C, 3hr; • Annealed L-Clad @ 1050°C, 3hr; • 2nd lowest loss design: 560nm, n=1.50; • IPhOD#2 mask (more widths); • All IBD films on top of WetOx LClad (mult deps) | | IR camera | bypass | too low index - core will not guide after anneal | | bend loss | too low core index; stress-optic core reduction |

Table A.1

| Sample Name green=done red=aborted/fail | Waveguide Structure | Notes on process Unique Traits of Device | Loss Measured (dB/meter) | Measurement Method | Structure Tested | Comments/Conclusions | Lowest Loss Measured (dB/m) | Failure Reason | Failure Specific |
|---|---|---|---|---|---|---|---|---|---|
| SiON-ox #12 02/01/11 | Oxidized SiOxNy: t~=200nm w = 4.5-15.0µm n_core~= 1.500 n_LClad=1.448 t_LClad=15um WetOx, FZ-Si n_UClad=1.457? (Unax100CNoAr) | • Got 4µm top-side SiO2, then 1.6µm backside IBD SiO2, then anneal 900°C 4h, then topside SiO2 4µm, then backside PECVD SiO2 ~2.5µm (check) & 2µm topside UClad to complete<br>• Annealed Core before other deps, to relax films (700°C, 8hrs)<br>• Thinner core (~200nm) - 2nd lowest loss design<br>• 2x thicker SiO2 ox-Buffer (aka. Spacer) = 368.4nm<br>• IPhOD#2 mask (more widths)<br>• All IBD films on top of WetOx LClad (mult deps) (No L-Clad anneal) | | IR camera | bypass | No lateral guiding again - stress compensation inadequate? SHould increase core index | | bend loss | too low low core index stress-optic core reduction |
| JB#06 01/23/11 | Oxidized SiOxNy: t=618.262 nm (pre-anneal) w = 4.5-15.0µm n_core= 1.550 (pre-anneal) n_LClad=1.448 t_LClad=15um WetOx, FZ-Si n_UClad=1.457? (Unax100CNoAr) | Core: Unaxis SiON 250°C: O2/N2=5/5, 918sec. A = 1.548, B = 0.00447, C = 9.3997e-5; th = 6182.62, n1550 = 1.550, n632 = 1.560. OxBuff - Unaxis SiO2: 450sec, 250°C | | | | Cracked during anneal - 1150 C for 3 hr | | cleaved | upper cladding anneal |
| JB#05 01/23/11 | Oxidized SiOxNy: t=XXXnm (post-anneal) w = 4.5-15.0µm n_core= XXX (post-anneal) n_LClad=1.448 t_LClad=15um WetOx, FZ-Si n_UClad=1.457? (Unax100CNoAr) | Core: Unaxis SiON 250°C: O2/N2=5/5, 918sec. OxBuff - Unaxis SiO2: 450sec, 250°C | | | | Abandoned? Attempted hot H3PO4 - did not etch after 11min. Tried 162C, tried 172, 180C, 185C on the thermometer | | etch failure | H3PO4 etch did not remove SiN fully bad ICP etch (did not verify etch params (RM/JB) |
| SiON-ox #11 01/20/11 | Oxidized SiOxNy: t=361.420nm (post-anneal) w = 4.5-15.0µm n_core= 1.496 (post-anneal) n_LClad=1.448 t_LClad=15um WetOx, FZ-Si n_UClad=1.457? (Unax100CNoAr) | • Annealed Core before other deps, to relax films (700°C, 8hrs)<br>• IPhOD#2 mask (more widths) (same as #5, but with Oxidation rate) core = higher index & thinner<br>• All IBD films on top of WetOx LClad (mult deps) | | IR camera | bypass | too low index - core will not guide after anneal | | bend loss | too low core index stress-optic core reduction |

| Sample Name green=done red=aborted/fail | Waveguide Structure | Notes on process Unique Traits of Device | Loss Measured (dB/meter) | Measurement Method | Structure Tested | Comments/Conclusions | Lowest Loss Measured (dB/m) | Failure Reason | Failure Specific |
|---|---|---|---|---|---|---|---|---|---|
| SiON-ox #10 01/15/11 | Oxidized SiOxNy: t=359.749nm (pre-anneal) w = 4.5-15.0µm n_core= 1.514 (pre-anneal) n_LClad=1.448 t_LClad=15µm WetOx, FZ-Si n_UClad=1.45? (Unax100CNoAr) | • IPhOD#2 mask (more widths) (same as #5, but with Oxidation rate) core = higher index & thinner • All IBD films on top of WetOx LClad (1dep) oxMask=146nm, oxBuff=117nm | | | | Hot H2PO4 etch would not etch off the SiN - this is because the SiN is covered with SiO2 from the oxidation! Hot H2PO4 etch is not worth the difficulty two spiral breaks due to PR sticking to maskplate | | etch failure | H3PO4 etch did not remove SiN fully (due to oxidized SiN) |
| SiON-ox #9 01/12/11 | Oxidized SiOxNy: t=490.730nm (pre-anneal) w = 4.5-15.0µm n_core= 1.694 (pre-anneal) n_LClad=1.448 t_LClad=15µm WetOx, FZ-Si n_UClad=1.45? (Unax100CNoAr) | • IPhOD#2 mask (more widths) (same as #5, but with Oxidation rate) core = higher index & thinner • All IBD films on top of WetOx LClad (1dep) • redo #5/6 w/ corrected oxidation rate | | | | two spiral breaks due to PR sticking to maskplate | | lithography | PR sticking to mask plate |
| SiON-ox #8 12/22/10 | Oxidized SiOxNy + GRIN U/L-clad: w = 4.5-15.0µm t_Core=528.687nm (post-anneal) t_GRIN = ~40nm x 5 = ~200nm n_core=1.507 (post-anneal) n_LClad=1.448 n_UClad=1.45? (Unax100CNoAr) | • U/L Cladding has Graded Index • 50nm oxMask (reduced) • IPhOD#2 mask (4.5-15µm widths) • All IBD films on top of WetOx LClad (mult deps) • dep'd with sample removal+cooldowns between various layers to prevent particulates. • Annealed L-Clad (1050°C, X hrs) prior to other deps | | IR camera | bypass | • No guided mode (cladding only) - backside stress comp. w/ AJA Sputter#3 SiO2 to see if it fixes it | | bend loss | too low core index stress-optic core reduction |
| SiON-ox #7 12/14/10 | Oxidized SiOxNy: t=554.029 (post-anneal) w = 4.5-15.0µm n_core= 1.503 (post-anneal) n_LClad=1.448 t_LClad=15µm WetOx, FZ-Si n_UClad=1.45? (Unax100CNoAr) t_UClad ~=15µm | • 2nd lowest-loss design (w/ litho roughnesses) → slightly higher index core, thinner core • 50nm oxMask (reduced) (old mask - ULLWG3) • All IBD films on top of WetOx LClad (1dep) | 5µm: 35.8 +/- 1.320 dB/meter 6µm: 38.6 +/- 3.045 dB/meter 7µm: 34.2 +/- 3.276 dB/meter | OBR - ±2dB/meter | straight/spiral | lower losses than JB#1, but no observable trend in loss vs. width & large deviation between similar waveguides. Annealed 700°C, 12hr: mode is sucked towards substrate w/ high losses - core reduced in index greatly during final UCLad anneal? | 34.20 | bend loss | low core index stress-optic core reduction |

Table A.1

| Sample Name green=done red=aborted/fail | Waveguide Structure | Notes on process Unique Traits of Device | Loss Measured (dB/meter) | Measurement Method | Structure Tested | Comments/Conclusions | Lowest Loss Measured (dB/m) | Failure Reason | Failure Specific |
|---|---|---|---|---|---|---|---|---|---|
| SiON-ox #6 12/14/10 | Oxidized SiOxNy: t=500nm, w = 4.5-15.0µm, n_core=~1.67 (confirm), n_LClad=1.448, t_LClad=15um WetOx, FZ-Si, n_UClad=1.45?, (Unax100CNoAr) | • WetVar 950°C, 2hrs (40% of SiON-ox #5), • IPhOD#2 mask (more widths), (same as #5, but AFM'd core), core = higher index & thinner, • All IBD films on top of WetOx LClad | | | | ABORTED Since SiONox #05 was underox'd, this is definitely underox'd | | mistake | underoxidized - rate not characterized prior |
| SiON-ox #5 | Oxidized SiOxNy: t=~500nm, w = 5,6,7µm, n_core=~1.67 (confirm), n_LClad=1.448, t_LClad=15um WetOx, FZ-Si, n_UClad=1.45?, (Unax100CNoAr), t_UClad=~15um | • higher index, thinner core (to be similar to JB#1), • 3 x 2hr WetVar, 950°C (used Stanford ThermOx Calculator), • All IBD films on top of WetOx LClad | | IR camera | bypass | Waveguides work - although 6 & 7um widths are multimode (5µm may be Single mode) UNDEROXIDIZED Definitely a Rib waveguide - only ~50nm oxidized SiON in cladding | | mistake | underoxidized - rate not characterized prior |
| SiON-ox #4 | Oxidized SiOxNy + GRIN U/L-clad: t=200nm, w = 5,6,7µm, n_core=1.500 (check, pre-anneal), n_LClad=1.448, t_LClad=15um WetOx, FZ-Si, n_UClad=1.45?, (Unax100CNoAr), t_UClad=~15um | Graded Index above & below core, GRIN thickness ~250nm on either side, • All IBD films on top of WetOx LClad | | | | Not working on this, as litho/etch re-do is iffy, and has particulates embedded in film. SiONox#08 is a much better re-run of this wafer | | particulates | IBD |
| JB#04 | Oxidized SiOxNy: t=210nm, w = 5,6,7µm, n_core=1.650, n_Lclad=1.448 (WetOx), n_Uclad=1.45?, (Unax100CNoAr) | (same as #3, but AFM'd core), WetVar, 950°C, 1.5hrs, • Unaxis/PECVD OxMask | | | | Upper cladding Cracked on annealling (before testing) Dep only partial U-Clad before annealling! ~3µm? core index may have dropped after ox/anneal pre-anneal n_core=1.55, post ~=1.54? | | delamination | upper cladding anneal |
| JB#03 | Oxidized SiOxNy: t=210nm, w = 5,6,7µm, n_core=1.650, n_Lclad=1.448 (WetOx), n_Uclad=1.45?, (Unax100CNoAr) | • Unaxis/PECVD OxMask | | | | core index may have dropped after ox/anneal pre-anneal n_core=1.55, post ~=1.54? | | | |

| Sample Name green=done red=aborted/fail | Waveguide Structure | Notes on process Unique Traits of Device | Loss Measured (dB/meter) | Measurement Method | Structure Tested | Comments/Conclusions | Lowest Loss Measured (dB/m) | Failure Reason | Failure Specific |
|---|---|---|---|---|---|---|---|---|---|
| SiON-ox #03 | Oxidized SiOxNy: t=700nm w = 5,6,7µm n_core=1.500 n_LClad=1.448 n_UClad=1.45? (Unax100CNoAr) | all IBD films, dep'd in one sitting onto WetOx15um wafers ~ 150nm oxMask ~ 200nm oxBuffer Pana#2 etch w/ VikSINetch (1m) Pana#1 O2 ash prior to Oxidation (30m, 100°C) | ~ 300 dB/m | OBR | spiral | SiN ox-Mask was not fully removed - Core likely not oxidized at all | 300.00 | etch failure | did not fully remove SiN rate not known prior |
| JB #02 | Oxidized SiOxNy: t=210nm w = 5,6,7µm n_core=1.650 n_Lclad=1.448 (WetOx) n_Uclad=1.45? (Unax100CNoAr) | Wet Var, 950°C, 3hrs (too long) • Unaxis/PECVD OxMask | ~ 100 dB/meter | OBR | spiral | • overoxidized!! had to dice off angled facets waveguide widths were narrower than expected (see SEMs) | 100.00 | bend loss | overoxidized cores too narrow |
| PSCW #03 | Pure Silica Core/Clad: t=700nm w=5,6,7um n_core=1.4778 n_Lclad=1.446 (WetOx) n_Uclad=1.45? (Unax100C+Ar) 10um U/L-Clad | Improved Cr/SiO2 etching process Resolution/Contact still non-uniform Turned out to have Silica roughness (only observed in U-Clad dep) WetOx Lower Cladding | 300 dB/meter | OBR | spiral bypass - straight waveguides | bend loss? | 300.00 | etch failure bend loss | Chromium etch products/micro masking too low index contrast/stress-optic effect |
| JB#01 | Re-oxidized t= | 950°C; WetVar, ___ hr | | OBR | | | | | |
| JB#01 11/15/2010 | Oxidized SiOxNy: t= 510nm w = 5,6,7µm n_core= 1.65 (Unaxis) n_Lclad=1.448 (WetOx) n_Uclad=1.45? (Unax100CNoAr) | First SiON-ox run: 200nm SiO2 ox-Buffer 250 nm SiN ox-Mask 1st ox - 5hrs, 950°C • Unaxis/PECVD OxMask • ULLWG3 Mask (PhOD#1) | (estimated from plot) 5µm: 52 dB/m 6µm: 49 dB/m 7µm: 50 db/m  Annealed 700°C, 1h:5µm: 37 dB/m 6µm: 36 dB/m 7µm: 36 db/m  900°C, 3hr: 5µm: 28 dB/m 6µm: 30 dB/m 7µm: 32 db/m  1050°C + 1150°C, 3hr: 5µm: 16 dB/m 6µm: 14 dB/m 7µm: 15 db/m | OBR | Spiral | Multi-Mode (higher-order modes lost within a few cm)  pre-anneal n_core = 1.55, post=1.65? | 14.00 | | |

| Sample Name green=done red=aborted/fail | Waveguide Structure | Notes on process Unique Traits of Device | Loss Measured (dB/meter) | Measurement Method | Structure Tested | Comments/Conclusions | Lowest Loss Measured (dB/m) | Failure Reason | Failure Specific |
|---|---|---|---|---|---|---|---|---|---|
| **PSCW #02** 10/07/2010 | Pure Silica Core/Clad: t=700nm w=5,6,7um n_core=1.4778 n_clad=1.45? (Unax100C+Ar) 10um U/L-Clad | Unaxis L-Clad (rougher) Had severe Silica etch Roughness issue (in open-field) • ULLWG3 Mask (IPhOD#1) | 5µm: 265.8 ± 12.3 dB/meter 6µm: 242.67 ± 8.32 7µm: 211.95 ± 4.52 | OBR | Straight (n_mode) / Spiral (loss) | | 211.95 | etch failure | Chromium etch products micromasking |
| **LiONiX Run#001** 4/13/2010 | SiN-strip: t = 80nm, 90nm, 100nm w = 2.8 um n_core = 1.9835 n_clad = 1.4456 L-Clad t= 8um U-Clad t = 7.5um | Fabricated at Foundry: LioniX BV (Holland) | 80nm x 2.8µm: 2.84895 ± 9.3e-4 dB/m 90nm x 2.8µm: 4.11473 ± 1.905e-3 dB/m 100nm x 2.8µm: 5.10586 ± 2.23e-3 dB/m | OBR | Spiral | | 2.85 | | |
| **WetOx#11?** | SiOxNy Core, SiO2 Clad: | • ULLWG3 Mask (IPhOD#1) | | | | | | | |
| **FZ#01** 10/03/2009 | PSCW (Pure Silica Core) 3µm x 3µm IBD SiO2 core, Unaxis SiO2 U/L cladding | ULLWG2 Mask (S-Bend faux-cutback) copied Adar/Serbin/Mizrahi Bell Labs design, since Δn is similar | too low to measure (meas. error too high) | faux-cutback | S-Bends | MultiMode Sidewall roughness is huge - very bad Facets diced/polished - lots of chipping Error from coupling loss is much too high to yield usable loss values! | | bad design measurement uncertainty | multimoding and bad facets increase measurement error above loss |
| **PETE03** 4/7/2009 | SiN-strip 3µm x 97nm, 3µm SiO2 L/U-Cladding Unaxis ICP-PECVD & PanalCP#1 etch | Thinned core to barely single mode High aspect ratio SiN-strip: 3 um x 100 nm | 2.409 - 6.103 dB/cm | Cutback - cleaving | Straight WGs | too low reflections @ facets for FP meas (& uncertainty in coupling/reflections) WGs too short for decent certainty in APA meas, & APA polarization averaging is a problem (coupling is varied during measurement) Too high bend loss for ring res meas. (100µm bend radius too tight for squeezed-out single mode) | 2,409.00 | bend loss substrate leakage | thin cladding inadequate for squeezed-out thin core thickness |
| **PETE02** 3/8/3009 | SiN-strip | | | | | | | | |
| **AllP2** 1/15/2009 | SiN-strip Multi-mode | Stepper Lithography ULLWG1 Mask Plate - Jon Barton suggestions, Active/Passive InP/Silica Straight cutback waveguides 50/50 MMI's, 15/85 MMI's, Ring Resonators of 4 bend radii (20µm to 100µm) Coupled Ring Resonators Ring Lasers Mode Locked Lasers | | Agilent APA / Fabry Perot Finesse | Straight WGs | Huge measurement error due to multimoding - can't measure ring resonators or Fabry-perot cleaved resonators. Bad Mask plate design - multimoding not ok | | measurement uncertainty bad design | multimoding not ok for intended measurement methods |

# Appendix B

# AFM Measurement of

# Nanoscale Surface Roughness

**User Guide for the Asylum MFP-3D Atomic Force Microscope**
*Gentle Engagement into Attractive Mode for Surface Roughness Measurement*

Written by Demis John & Géza Kurczveil
Date: July 21<sup>th</sup>, 2010
Version: 2.0

Tool location: CNSI (Elings Hall)
Contact person: Mark Cornish (Not an experienced AFM user)

Sample prep (~20min, do a couple of hours before actual AFM):
    1. Mount sample(s) using x-tal bond wax on a glass slide (1 sample per glass slide).
        a. For depoisition watch samples (~1/4 of a 2" wafer), Demis just places sample directly on glass slide with no bond, and uses magnets either directly on sample, or magnets that clamp 2 additional slides which hold down either side of the sample.
    AFM:
    1. Mount glass slide with magnets on AFM tool. Crudely center sample.
        a. Make sure magnets are mostly on the shiny metal only (not too close to head, and not restricting movement of stage by contacting the black metal).
    2. Place probe holder on black mount. Loosen screw on AFM tip holder just a bit. Mount tip on holder and tighten screw.

a. Do not place tip all the way back/inserted into holder too far - will tilt tip & cause inability to achieve zeroed deflection.

b. Make sure tip is in the groove, approximately center in quartz window (pull forward slightly)

3. On the PC:

a. Open "MFP-3D" software.

4. MFP-3D Controller (Main): on.

a. Laser: on.

5. Illuminator: on & on lowest setting.

6. Flip AFM head upside down and mount probe holder. Flip head again.

7. Raise the front leg of the head by turning the front wheel. Place head on top of sample.

a. Insert back legs first, keeping front raised

b. Watch tip/sample spacing as you lower the front leg - ensure holder does not hit slides, magnets or sample. Turn "Up" knob if needed to correct.

8. Click on TV in bottom right. (on "Bio" system, select Device > Winview or whatever to view through correct camera

9. Adjust knobs at far back of head (camera mirror adjust) to center AFM tip on sample and in TV screen.

10. Level (left-right) head - place bubble level on top of head, adjust height of both rear legs to level

11. Turn on laser. Turn off illuminator (or down to lowest setting).

12. Move laser beam to tip with LDX & LDY adjustments

a. Actual beam is to the left of the oval optics artifact with diffraction pattern in it

13. Adjust LDX to move beam to nearest ro cantilever apex without going past

14. Maximize 'Sum' by adjusting LDY. Adjust PD to get 'Deflection=0'.

a. If you can not get Deflection to zero (it is always at max, or knob hits limit before Deflection reaches 0) then your cantilever is likely too far back in the holder & tilted because of this. You must Re-seat the probe in the holder.

15. Turn Illumination OFF

a. Leaving the illumination on causes thermal drift by heating the cantilever. Depending on desired scan size & quality, you may need to let the temperature stabilize before scanning (observe to see Deflection stop drifting). ˜15-30m for sub-nanometer features.

16. Tune (tab) -> Auto-tune (detune by -5%). You should get a single peak, with phase crossing ˜0 at the amplitude peak.

a. For surface roughness & attractive mode imaging: Target Ampl = 1.0V, Offset = 0%

b. For Olympus AC240 tips, resonance freq ˜= 74 kHz - NOT ˜400kHz.

17. Set "SetPoint" to 95% of the "Amplitude" readback.

a. Eg. "Amplitude" = 1.00V, so Setpoint = 950mV

b. Take note of Free-space phase (~90 if tuning offset = 0)

18. Click "Engage". Z-Voltage will extend to +150V (fully extended)

19. Carefully (seriously, be slow and gentle) lower the front leg.

a. System will "beep"

b. Amplitude will drop from 1 to 0.95 V.

c. Phase will remain unchanged - if so, then tip is only pushing air between sample & tip

d. Z Voltage will drop gently - lower tip until Z-Voltage reaches ~20.

20. Reduce SetPoint to ~95% of new free-space "Amplitude"

a. Repeat - Lower tip until system beeps, Z-voltage drops gradually to ~20

21. Use "Hampster Wheel" to reduce SetPoint slowly - you know sample is interacting with surface when the Z-Voltage stops hard & phase jumps -

a. If Z-Voltage reaches +50 and phase still = free-space phase, then you must repeat step 20 (lower tip), maybe a few times.

b. Upon contact, if Phase > free-space Phase then in Attractive mode, < free-space Phase = Repulsive Mode

i. For 0% Tuning offset, Attractive mode: Phase >90, Repulsive: Phase <90

ii. Increase SetPoint (raise tip) to remain in more gentle Attractive Mode, lower to move into more aggressive Repulsive mode

22. Use tip height adjustment to center Z-Voltage in meter

23. Increase Setpoint (Hampster Wheel) until Z-Voltage retracts to -10 (tip withdrawn)

24. Close chamber.

25. Decrease SetPoint until reach engagement again & desired Phase (attractive or repulsive).


### *Maintaining Attractive Mode - w/ lower drive amplitude & lower force for nm-scale roughness*

While engaged (hopefully in attractive mode, Phase>F.S.Phase, to preserve tip):

26. Lower Drive Amplitude (~two or three clicks of down arrow)

a. Tip will disengage as "Amplitude" Readback drops below SetPoint

27. Decrease SetPoint (Hampster Wheel) until Z-Voltage begins to increase - decrease slowly until re-engaged and Phase jumps to > Free-space Phase (try not to go too far when Phase < F.S. Phase)

28. Repeat by lowering Drive Amp & SetPoint until engagement until Drive Amp ~ 50mV

a. For large roughness, Drive Amp must be larger (so cantilever oscillates enough to capture a bump), and for sub-nm roughness Drive Amp ~=15-25mV.

b. Ability to maintain Attractive mode (Phase > F.S. Phase) is better for lower Drive Amps (lower max velocity during oscillation)

29. Under 'Main' tab, set 'Scan size', 'Scan points', 'Scan lines', and 'Speed'. Then "Do scan".

      a. If the red and blue scans differ - ie. They look laterally offset try the following:

            i. Lower scan speed (<1Hz) - drawback: drift may be more pronounced

            ii. Increase Integral Gain - drawback: noise increases

1. Increase Int. Gain until 'ringing' noise appears, then reduce to just below this point. The tip will respond to height changes faster w/ increased Gain.

30. Type a "Base Name", Note & "Browse" a folder to save into, and check "Save Images"

      a. Files will be saved every time a 'frame' is finished - ie. The scan reaches the top or bottom

      b. To Save a partial scan - click "Withdraw" and then click "Save Prev."

31. When done, hit "Stop!!!".

32. Turn off laser and illuminator.

33. Raise head.

34. Remove tip from head, place head on stand to the left, and remove sample.

35. Fill out log.

**Other comments:**
Integral gain:
· High number -> faster response, higher resolution, more noisy
· Default = 10.
To view plot of data:
· MFP IP -> Browse -> open files. 'M' for flatten, 'A' for analysis (Roughness etc)
· Files -> Save Graphic (of currently selected window) - use const. size


**Demis' Parameters for Surface Roughness:**
AutoTune:
Target Amplitude = 1.00V
Target Percent: 0.00
(50kHz - 200 kHz)
Pre-Engage:
SetPoint = 950mV
Integral Gain = 10.0
Proportional Gain = 0
(Drive Amp & Freq = default from AutoTune)
Scan Size = 1um
Scan Rate = 1.00 Hz
Scan Angle = 90.0 (can make tip more resilient to bumps via torsional flex)
Scan Points = 1024
Width:Height = 2:1
During Scan:
Drive Amplitude  35mV
Integral Gain is maximized but below 'ringing' point - ~5-6 for 500nm scans, 10-15 for 2um scans
SlowScan Axis = Disabled during Gain & Scan Speed optimization (should see vertical lines)
Scan Speed  1.0 Hz (only less if can't reduce Parachuting - lateral blur - w/ Int.Gain

# Appendix C

# Process Followers

## C.1    Direct-Etched Si$_3$N$_4$-strip Waveguide

*Device Name: SiNstrip#8*

**Table C.1:** *Process Follower for Direct-Etched SiN-strip waveguide.*

| Demis John, 4/15/2012 | 4' Si Wafer: SiN WaveGuide Fab w/ Direct Dry-Etch | |
|---|---|---|
| **Step** | **Details / Actual** | |
| Device Name: | **SiNstrip#8** | |
| Device Description: | Sputtered SiN-core, 100nm thick x 5.0µm to 17.5µm Direct-etched core, deposited Upper Cladding | |
| | | |
| | | |
| General Process Notes: | * Keep Wafer face-down in curved wafer tray to minimize dust buildup (electrostatic films can make dust removal difficult) | |
| | * Cleanliness is extremely important for these huge waveguides. – wear face mask, and cover sample if people without masks are talking to you | |

| | |
|---|---|
| | * The Unaxis ICP $SiO_2$ causes radial curvature of the Si wafer - the center is about 2 or 3mm off of the table while all edges are touching. Strain-compensation on the backside is necessary, via backside dep of $SiO_2$ on any tool that can do this safely - PlasmaTherm PECVD, AV-PECVD or IBD. Use Backside coating fixture or glass slides to ensure front is not scratched during this step. |
| | * Deposition Watch Samples are ~1cm x 3-5cm Silicon from IWS. Always HF dip these once at the start of each day that they are needed (can dip one large piece, and keep cleaving off pieces throughout the day) IWS order: Silicon wafers, 2-inch, P/B, <100>, 250-350µm, Single-Side Polished (SSP), Test grade, |
| | |
| Process Follower Notes: | * You should assume that every step is inserted for a reason - skipping steps often results in re-solving an old problem |
| | * This process is specifically for SiN-core, Silica-clad waveguides with deposited upper cladding. Although IBD SiN is preferable, AJA SiN was used due to particulates on the IBD at the time - use Scope (+ Nomarski) to check for these. |
| | | |
| *Lower Cladding* | **Thermally oxidized Silicon** | |

| | | |
|---|---|---|
| Initial substrate purchase | KST World Corp.<br><br>100 mm Silicon, <100><br><br>Thickness = 525 µm<br><br>Front/Backside = Polished/Etched<br><br>P-type doping 5-10 Ohm-cm<br><br>15 µm Oxide +/- 5%<br><br>$n_{1550}$ = 1.4458 +/- 0.0001 | Wafers are about $300 each. In-house oxidation requires about 30 days of continuous oxidation at 1050°C. Boron doping allows some reflow (lower melting point of B-SiO$_2$), and fewer cracks via reduced Thermal Expansion. |
| | | |
| | | |
| **Core Deposition** | **AJA SiN: 98 nm** | Si$_3$N$_4$ core sputter deposition, ˜ 1 hr dep. (unmanned) |
| Tool: AJA Int'l Sputter #3 | ˜3hrs | |
| **Test Deposition** | | |
| prepare silicon test piece | cleave a piece of silicon (>=1cm x 3cm)<br>HF dip for 1m & DI/N2 dry | |
| Mount & Load | Mount onto 4-inch sample holder, with only clips installed (no bars)<br>Load into chamber | Sample Holder should be all the way to the Right on load-arm<br>+ centered rotationally/up and down |

| | | |
|---|---|---|
| Edit Recipe & Run | APEX > process: 'Demis_SiN_dep':<br><br>Sample height = 44mm, Max Rotation (100rpm)<br><br>Gun (Silicon, RF2, #6 usually) Angle = 4mm<br><br>in layer 'Demis_SiN_deposition': set time = 2000 sec<br><br>set Target Pre-Clean = 15m<br><br>set Post-Dep-Clean = 10sec (or delete step)<br><br>DataLogging = On & RUN (turn off ion-guage) | Approx. 1.77 nm/min |
| *Measure Test Dep* | on J.A.Woolam EC-400 | Meas. Program: 'Glass Measurement - 4 Angle 50 to 80'<br>Fitting Program: 'Glass on Si - No NatOx'<br>Fit Thickness & A (300nm to 1700nm, 4 angles 50°-80°). Then fit B & C & Angle.<br>Record Thickness, n(632) & n(1550)<br>Fit k_A and k_exp; Record k(1550) |
| Mount Test Sample | | |
| Measure | Load recipe:<br>"Demis/4–Angle Glass Measurement" | in the 'Measurement' tab, press 'Measure' & 'load'<br>align well - this affects accuracy most |

| Analyze | Load Model: | in the 'Analysis' tab, in the 'Model' window, press 'Open' |
| | Demis/Glass on Si - no NatOx.mod | optionally save the data |
| | | Fit 300nm - 1700nm Make sure at least one peak is shown (or else include lower wavelengths) |
| | | Fit Thickness & A (300nm to 1700nm, 4 angles 50°-80°). Then fit B & C & Angle. Record Thickness, n(632) & n(1550)Fit k_A and k_exp; Record k(1550) |

| | | |
|---|---|---|
| Record Index & Thickness | Recalc time to dep desired core thickness: Target Thickness = 98 nm | Also record MSE, and A,B,C if desired (for later index vs. wavelength modelling) To get more decimal points in Index: Right-click on Layer #1 (Model) & choose 'Graph Optical Constants', right-click on graph and choose 'Copy Data to clipboard' & paste into MS Excel - find index at desired wavelength |
| | | Thickness will increase by ~2% upon annealing |
| *Core Deposition* | | |
| Prepare & Mount Watch Sample | Do this in a litho-bay fume hood with no other users mount WatchSamp at top/bottom, using double clip | |
| Mount 4-inch sample Load into system | N2 blow & inspect for cleanliness & Load into Chamber | mount test-piece first, then mount real sample Nitrogen gun on sample Hold sample face-down while transporting |

| Edit Recipe & Run | Recipe:<br><br>APEX > process: 'Demis_SiN_dep':<br><br>Sample height = 44mm, Max Rotation (100rpm)<br><br>Gun (Silicon, RF2, #6 usually) Angle = 4mm<br><br>in layer 'Demis_SiN_deposition': set time = 98nm ÷ RATE (nm/sec)<br><br>set Target Pre-Clean = 10s (or delete step<br><br>set Post-Dep-Clean = 10min<br><br>DataLogging = On & RUN (turn off ion-guage) | |
|---|---|---|
| | | |
| | | |
| ***Core Stress-Compensation*** | **Backside SiN Dep** | $Si_3N_4$ dep on backside |
| Tool: AV-PECVD #2 or IBD | ~2hrs | This process can increase particulates on core layer, depending on dep. tool cleanliness - skip if paranoid. Beware that bow will increase a low after anneal, which can result in film delamination during cool down. |
| Check Bow | Check wafer bow with Tencor<br><br>Record Bow of wafer top-side | Process: "dj4inSi.prc"<br><br>4 orientations: 0, 30, 60, 90. |

| | | |
|---|---|---|
| Backside Deposition | Deposit $Si_3N_4$ on backside of sample. For either tool, use the IBD backside sample holder. | Ensure core side does not contact platten. Deposit less than core thickness. |
| Check Bow | Re-Check wafer bow with Tencor<br>Calculate rate of bow reduction | 4 orientations: 0°, 30°, 60°, 90°. |
| Repeat until almost flat | Stop before bow changes sign. $Bow \leq 50~\mu m$ is ok. | Do not exceed ~400 nm of $Si_3N_4$. |
| | | |
| | | |
| ***Core Anneal*** | **TyStar Anneal: 1050°C, 3hr** | |
| Tool: TyStar Tube 3 | 7 hrs | |
| Prepare Sample | Place sample on flat quartz boat<br>N2 clean<br>Place under table (above floor) | |
| Load & Run recipe | 'Menu' > 'RL' > 'Anneal.003'<br>S/C/L/IF Temp = 1050°C<br>N2 = 3.00 slpm<br>All other gases = 0.00 slpm<br>Time = 03.00.00 (hh.mm.ss)<br><br>Hit 'Run' - and 'Event' once door is fully open | Total time = Anneal time (3h) + 2hr warmup + 2hr cooldown |
| Load Sample | N2 clean sample while door is closing.<br>When door is halfway closed, place sample boat in system, under Tube #2 door | to shield sample from dust |

| Unload Sample | When tool shows Step=110, press 'Event' to open door<br>As soon as possible, pick up sample boat and place under table.<br>Cool for 10m before putting away. | |
|---|---|---|
| | | |
| | | |
| *Core Litho* | **PhotoLithography, Contact** | |
| Lithography Tool: Karl Suss MA-6 | ˜45m | From Renan Moreira's 'IPhOD Lithography - 2011-10-06.doc' which gives ˜4.47 nm RMS sidewall roughness |
| Set Fisher Oven #4 | Set temp to 300°C, place reservation sign if necessary | |
| Solvent Clean & Dry | Solvent Spinner (left), prog 5: 500s, 400rpm, 100rpm/s<br>ACE/MoL/ISO/N2 Dry<br>Inspect closely in hood for particles | Leave sample spinning for 30s after N2 dry to evaporate backside<br>Bay 6: Prog 8 // Bay 7: Prog 5 |
| *de-H2O Bake* | **300°C, >10m** | In Fischer Over #4 |
| Prepare Spinner | Non-raised spinner (Bay #7)<br>ACE/Non-shedding wipe underside of lid, N2 gun to check for wispy cobwebs<br>Replace napkin - 2 napkins. 4-inch chuck (non-bent, w/rubber o-ring) | |

| | | |
|---|---|---|
| Cool | 2m | Use pliers/monkey wrench to remove Cool at cleaned spinner bench, no other users around |
| Apply HMDS | Coat wafer, small pipette | |
| *HMDS soak* | 30 sec | |
| **Spin HMDS** | Spin Recipe #0 = spin: 5000 rpm, 2000 rpm/s, 60s stop: (0 rpm, 500 rpm/s, 0s) | |
| Remove Top Napkin | Remove sample to tray remove top napkin replace sample | |
| Apply SPR 955 CM-0.9 | Coat wafer, large pipette | |
| **Spin PhotoResist** | Spin Recipe #1 = spread: (100 rpm, 100 rpm/s, 10s) spin: 4000 rpm, 800 rpm/s, 30s stop: (0 rpm, 500 rpm/s, 0s) | Large Pipette, no bubbles, cover wafer Or just Recipe 7: 4000 rpm, 800 rpm/s, 30s The 10sec low-spin spreads PR |
| *Pre-Bake* | **105°C, 1m** | HotPlate w/ Lid Down, Bay 7 |
| Remove Edge Bead | Use smaller plastic bud w/ EBR squirt bottle | only remove ~2-3mm at edge - mask designed with 5mm margin Do on non-shedding wipes, no other users at bench N2 dry afterwards 10 s |

| Prepare MA-6 | Install 5' Plate Holder | (17.2        mW/cm2) |
|---|---|---|
|  | & 4' Vac Chuck | Channel 2 |
|  | Set recipe: Vac-Ct |  |
|  | pre vac: 5 / full vac: 6 / vac purge: 10 |  |
|  | vac sea: 0.35 / WEC press: 0.45 |  |
|  | Al.Gap=50 / WEC Offset=0 / WEC Type=Cont |  |
|  | Time = 7 sec |  |
|  | Alignment Knobs: left=10.0 / right=6.0 |  |
| Lamp Test | NO Sample nearby! Ensure power is correct CH2 = 17.2 mW/cm2 |  |
| Insert Mask Plate | Press 'Change Mask' place mask plate against guides & clip press 'ENTER' to start plate vac |  |

| Load Sample + Expose<br><br>Plate: **"IPHOD IN–HOUSE 2_5"** **Layer 1** | N2 gun the sample, & check plate closely for dust<br><br>After WEC, sample should be centered already<br>Ensure that entrance/exit of spiral is away from Edge-bead removal areas | Calculate Correct Exposure time (sec) from the Lamp Test power reading (mW)<br>Exp = _____ sec = 10.7s x (17.2 mW / _____ mW)<br><br>Set 'BSA Microscope' to prevent uScope from coming down during alignment<br><br>Once aligned, press 'Alignment check' to start vacuum sequence, to observe contact quality.<br>Press 'Exp' if it looks ok |
|---|---|---|
| *Post-Exp-Bake* | **125°C, 2m** | HotPlate in Bay 7 - cover in tin foil if paranoid about dust |
| Cool | 1m | |

| | | |
|---|---|---|
| **Develop**<br>**AZ 726 MiF** | 35 sec | Use 4-inch inner-cassette to hold sample, and 16" x 8" x 2" pyrex 3/4 full with Developer<br>Stop-dev in 150mm x 90mm crystallization dish of DI |
| Spin-Rinse-Dry | Std. Recipe: 90s Rinse @ 1000 rpm, 120s Dry @ 2000 rpm<br>Turn off Water valve during Dry step | Set pump-out to 'Hand' before start & turn on water<br>Set back to 'Auto' at end |
| **uScope In-spection** | **Inspect TestStructure patterns -**<br>**– look for curved/undeveloped PR at bottom of patterns**<br>**– Inspect/photograph resolution dots/L-shapes**<br>**– Look for dirt/obstructed waveguides** | Inspect Non-ius/Vernier marks<br>Ensure uniformity is reasonable (Verniers are similar around spiral) |
| | | |
| *HardBake* | **95°C, 20m** | Doubles selectivity, prevents PR reflow during etch |
| | | |
| | | |
| *Core Etch* | **CF4/O2 etch of SiN** | |
| Tool: Panasonic #2 | ~1.5hr (incl. cleans) | |

| | | |
|---|---|---|
| Mount Sample | Use Santovac oil - ˜2mm dots on 4 corners at edge only<br><br>N2 gun & Cover w/ tray immediately<br><br>Cleave ˜2mm piece off Core dep. WatchSamp & place next to wafer flat | No oil exposed from beneath wafer (preferably) |
| O2 Clean + CF4 Season | P2:#105: 5m + 3m (CLEANING WAFER) | 3m Coat in order to stabilize etch rate prior to etch |
| **CF4/O2 Etch** | P2:#155, 40sec<br><br>Make sure watch sample is fully etched (only silicon) | |
| Post-Etch O2 Clean | #103: 5m Clean | Clean:Etch time = 1:2 |
| Prepare PR Stripper | Place 150mm x 10mm dish of 1165 on 80°C HotPlate | Heat for 10m before using |
| Remove sample from Carrier | In solvent bench fume hood | |
| Backside Solvent Clean | place face-down in carrier, carefully swab ACE to remove oil | |
| **uScope Inspection** | **Inspect edges of TestStructure patterns** | |
| | | |
| | | |
| *P.R. Strip* | **PhotoResist Ash + Strip** | |
| PEII O2 Ash | | |
| O2 Stabilize | 1m, 300mT | Vent=ON: insert Sample<br><br>Vac=ON; when press ˜0.500 T, Gas=ON, stabilize at 0.300T for >=2m |

| O2 Ash | 2m, 100W | Power=ON - make sure 100W, start timer. @end: Power=OFF, Gas=OFF, Vac=OFF, Vent=ON - remove sample Vac=ON; when press ~0.500T, Vac=OFF, log in book |
|---|---|---|
| Strip Resist | | |
| 1165 soak @ 80°C | 10m, 150mm shallow dish on Hotplate | optional: squirt w/ 1165 squirt bottle@ start & end |
| Solvent Spinner Clean | ACE/MoL/ISO/DI & N2 Dry | optional: can squirt backside of sample w/ISO to remove 1165. Do this by spinning with ACE/MoL/ISO, but keep squirting ISO while shutting off spinner. Pick up sample (clean tweezers) and ISO backside Replace sample, and spin with ACE/MoL/ISO  ACE tweezers + dry to clean |

| | | |
|---|---|---|
| Gasonics Ash | Run Test-ash first: Recipe #3 (250°C), 60s<br><br>Run Sample: 3 x Recips #3, 60s | Use carrier with ceramic stops<br><br>If wafer moves during pickup, grab the carrier & let the tool abort!<br><br>If tool is not behaving, use PEII, for 2m |
| Solvent Spinner Clean | ACE/MoL/ISO / N2 dry | |
| Inspect | Check that resist is gone on large features | If anything is left, PRX-127 for ~5m |
| | | |
| **uScope Inspection** | **look for dirt/polymer on pattern edges** | DI/ACE/MoL/ISO/DI again if needed. Can even PEII again 2-5m if see polymer film Observe/photo Vernier width bias / circular resolution marks |
| **Dektak (optional)** | **depth = _____** | can look for 'rabbit Ears' - indicative of residual polymer buildup. O2 ash + solvent soak (1165 @ 80degC, >5m or PRX-127) to remove |
| | | |
| | | |

| Core Rough-ness Mea-surement (optional) | AFM & SEM | measure sidewall roughness and top-surface roughness |
|---|---|---|
| Tool: Dimension D3100 AFM | ~3hrs | |
| AFM top surface of test structures | | |
| Insert New/Reliable-Used Probe | land laser on tip by watching shadow on stage Locate tip & center tip in field of view Focus on sample surface (wafer edge is helpful for coarse focus) Choose 'Focus: Tip Reflection' Center laser behind apex & maximize Signal Sum | |
| AutoTune: find probe resonance | Tune to Ampl=1.00V, Offset=5% ensure resonance matches tip specs | if AutoTune finds incorrect resonance, reduce Tuning range (set back to 100-500kHz afterwards) ~75kHz for Olympus AC240TS |
| Close lid | perhaps find area of interest first | use unetched checkerboard square |
| Use normal engagement procedure | Scan = 3um, 1.00 Hz, Integral Gain = 0.30, Zlimit = 6um (or max), SlowScanAxis = Enabled, Scan Angle = 90°, Aspect Ratio = 1.00, Samples/Line = 1024, SetPoint = ~ 90% of Free Amplitude | Ensure sample & tip are correct focus or will crash tip into sample |

| Optimize parameters | Other (tab) –> Z-Limit = 1um (set back when done) | |
|---|---|---|
| | Drop Setpoint by two or three arrow keys (repulsive mode) | |
| | Disable Y-scan (SlowScan Axis), | |
| | maximize Integral Gain, but below point of adding ringing | |
| | – if see drift, turn off illumination & let system's temperature stabilize (5-20m) | |
| | – if see lateral blur (parachuting: trace & retrace are offset) lower scan speed or increase IntGain | |
| | – if see perfectly even ripples (usually diagonal) decrease IntGain | |
| Capture | Set Acquisition > Capture FileName | capture one to three scans consecutively if see drift (if up versus down are squished differently) |
| | Press 'Capture' (camera) | |
| | Frame Down/Up (whichever has less drift) | |
| | | also check vacuum if sample is drifting - can help |
| Withdraw & remove sample | Analyze images - Browse/Open, Flatten (1st order - minimize), Roughness, File > Export > Export view (as JPEG) | |
| | | |
| | | |

| Tool: JEOL SEM | ~2hrs | THESE INSTRUCTIONS MUST BE MODIFIED ONCE B.MITCHELL GENERATES NEW OPERATING PROCEDURE |
|---|---|---|
| Load Sample (F4 to view IR Camera) | Use appropriate sample holder - secure all screws and tighten set screws so sample/holder is held tight<br>'Vent' load lock & load sample & 'Evac' load lock (hold until button lights)<br>Wait until door opens & chamber pressure drops to 5e-4 Torr (~5m)<br>Use arm to load sample holder - 'HLDR' light=on & sample holder window appears | Take Note of highest point on sample/holder!!! Will need to find this w/ SEM Select correct sample holder, and set appropriate Offset as indicaated |
| Raise sample | reduce Z in 5mm increments until ~ halfway there | |
| Observation = ON | Beam = 2.0kV, SEI detector / SEM mode | |
| Focus on highest point | 'Low Mag': reduce mag & drive around, increase mag & center feature<br>Set WD = ~15mm & CANCEL when prompted! (won't move Z) | can abort sample movement by moving trackball |

| | | |
|---|---|---|
| Set Offset | Offset = (Z - WD) when focused on highest point | ~4.0-6.0 for flat samples. Offset increases for taller samples<br><br>Offset is very important - necessary for software to prevent sample-detector crashes |
| decrease WD, correct Offset | make two or three steps to reach 2mm WD, refocusing & correcting Offset each time | Offset will likely change each time - last time should only change by a hundred microns or so |
| Set GB-mode | Beam = 1.0kV, GH-B mode (max sample bias, 2.0kV) | may need to reduce to 0.8 kV if too much charging |
| Save Image at high res | Wobble (use resolution dots), Astig, Focus & re-do @ higher mag<br>Setup > (something) > set 'Photo' params to higher-res picture<br>Image (tab) > browse to save in folder | image @ 2 or three places on wafer<br><br>res: 2560x2048 px,<br>mag: x14,000 - x33,000 |
| set SEM mode, Observation = OFF<br>Exchange Position<br>unload sample<br>log off,<br>copy pictures from comp | | |
| | | |

| | | |
|---|---|---|
| ***Partial Upper Cladding Dep.*** | **AJA SiO$_2$: 1µm** | To fill voids from deposition seams |
| Tool: AJA Sputter #3 | 5hrs | |
| Prepare & Mount Watch Sample | Do this in a litho-bay fume hood with no other users<br>mount WatchSamp at top/bottom, using double clip | |
| Mount 4-inch sample<br>Load into system | N2 blow & inspect for cleanliness & Load into Chamber | mount test-piece first, then mount real sample<br>Nitrogen gun on sample<br>Hold sample face-down while transporting |
| Edit Recipe & Run | Recipe:<br>APEX > process: 'UCSB_SiO$_2$_dep':<br>Sample height = 25mm, Max Rotation (100rpm)<br>Gun (Silicon, RF2, #6 usually) Angle = 9mm<br><br>in layer 'UCSB_SiO$_2$_deposition': set time = 1000nm  RATE (nm/sec)<br>set Target Pre-Clean = 15m<br>set Post-Dep-Clean = 10m<br>DataLogging = On & RUN (turn off ion-guage) | Approx. 3.63 nm/min |
| Unload Sample | N2 gun | |
| | | |
| | | |

| | | |
|---|---|---|
| ***P.UClad An-neal*** | **TyStar Anneal: 1050°C, 3hr** | Reflows P.Uclad, filling voids and Dep. seams |
| Tool: TyStar Tube 3 | 7 hrs | |
| Prepare Sample | Place sample on flat quartz boat<br>N2 clean<br>Place under table (above floor) | |
| Load & Run recipe | 'Menu' > 'RL' > 'Anneal.003'<br>S/C/L/IF Temp = 1050°C<br>N2 = 3.00 slpm<br>All other gases = 0.00 slpm<br>Time = 03.00.00 (hh.mm.ss)<br><br>Hit 'Run' - and 'Event' once door is fully open | Total time = Anneal time (3h) + 2hr warmup + 2hr cooldown |
| Load Sample | N2 clean sample while door is closing.<br>When door is halfway closed, place sample boat in system, under Tube #2 door | to shield sample from dust |
| Unload Sample | When tool shows Step=110, press 'Event' to open door<br>As soon as possible, pick up sample boat and place under table.<br>Cool for 10m before putting away. | |
| | | |
| | | |
| ***Upper Cladding Dep*** | **Unaxis ICP-PECVD: SiO$_2$ 10µm** | Encapsulate to make device robust - air clad is ok, but dirt and environment affects loss and guiding |

| | | |
|---|---|---|
| Tool: Unaxis ICP Deposition | ~6 hrs | sign up for additional 2-3 hours for cooldown (unmanned) |
| *Follow procedure in sheet:* | 'Sub: Unaxis Dep - No Vent' (p. 266) | |
| dep. 10 microns of $SiO_2$ 4 cycles of steps (1) to (3) | #1: (dep)_____ (clean)_____ #2: (dep)_____ (clean)_____ #3: (dep)_____ (clean)_____ #4: (dep)_____ (clean)_____ #5: (dep)_____ (clean)_____ | |
| | | |
| | | |
| *Dicing Protect/Prep* | **SPR-220-7.0 spin + cure** | provides structural support for ridges during dice |
| Tool: spinner & hotplate | 15 min | |
| **Spin SPR 220-7.0** | Spin Recipe #1 = spread: (100 rpm, 100 rpm/s, 10s) 4000 rpm, 800 rpm/s, 30s stop: (0 rpm, 500 rpm/s, 0s) | Large Pipette, NO BUBBLES Or just Recipe 7: 4000 rpm, 800 rpm/s, 30s The 10sec low-spin spreads PR |
| *Pre-Bake* | **115°C, 5m** | HotPlate w/ Lid Down |
| *Mount to Si carrier wafer* | get 4-inch Si from dicing room | |

| | | |
|---|---|---|
| Measure Thickness of Carrier wafer | Plumb Micrometer: Thickness @ 5 points:<br><br>------<br><br>------ | Can get any relatively clean wafer from the 'Wafer Disposal' bin in bay 2, or a new 'Reclaimed Wafer' from the Panasonic supplies drawer<br><br>Make sure thickness does not deviate more than 100um |
| Heat Carrier | 125C, 2m | |
| Apply wax<br>Mount Sample<br>Remove carrier & cool | apply wax as thinly as possible, to carrier directly<br>enough to contact most of sample in center and very edges<br>press sample edges to make sure sample is fairly level | Do this in a fume hood! PR will release neurotoxins when heated! |
| | | |
| | | |
| *Dice Wafer* | **Dicing Saw w/ Std. Resnoid Blades** | Separate samples by dicing through waveguides, creating facets in the process |
| Tool: ADT Dicing Saw | ˜1 hrs | |
| Prepare Carrier | Use standard UV-release tape and metal frame<br>Prepare the tape and frame by themselves | |

| | | |
|---|---|---|
| Mount Sample | Place sample in center of frame/tape carrier, and press on underside of tape to completely adhere tape to device backside | |
| Load Recipe | Blumenthal > Demis_APC_SiOnWaxonTape<br>–Speed = 0.8 mm/sec,<br>–110mm cut length,<br>–Depth = 0.490 mm<br>–Cut No. = 1 for both Angles 1/0° and 1/90° | Standard Silicon dicing parameters |
| Change Blade | Setup saw for 9RU or 22RU Resnoid blade (stocked)<br>49mm flange (maximum exposure, smallest flange) | 9µm grit preferable |
| Load Sample | 'Wafer Load' (foam chuck) | |
| Align Rotation + 1st cut | 'Manual Wafer Align'<br>Get correct angle with 'rotate for initial align'<br>Correct rotation to long dice lines.<br>Set 'Cut Position' to right-most point of 1st desired cut | |
| Align Blade | 'Manual Y Offset'<br>Choose Cut Pos. 2mm from edge of wafer<br>Align to the cut & 'Finish' | Make sure this cuts fully thru sample but not thru carrier! |
| 1st Cut | 'Partial Wafer Cut'<br>–'Next' if it shows correct Angle (eg. '1/0°')<br>– 'Next' to complete alignment (Cut Pos already chosen for this cut only)<br>– 'Next' to set current Pos. as First Index<br>– 'Next' to set current Pos. as Last Index (eg. Index #1 to #1)<br>– 'Finish' to Cut wafer & exit | |

| | | |
|---|---|---|
| Inspect | At Wafer Unload, hit 'Cancel' to prevent vacuum release<br><br>Click 'I' and up or down arrow, to bring sample to Scope<br><br>Click 'Auto Focus: At Wafer'<br><br>Make sure sample fully cut | |
| 2nd Cut | 'Partial Wafer Cut'<br><br>–'Next' if it shows correct Angle (eg. '1/0°')<br><br>– 'BACK' to Re-do alignment (Need new Cut Pos.)<br><br>– Find 2nd Dice Line, and set Cut Pos. @ Right & 'Finish'<br><br>– 'Next' to complete alignment<br><br>– 'Next' to set current Pos. as First Index<br><br>– 'Next' to set current Pos. as Last Index (eg. Index #1 to #1)<br><br>– 'Finish' to Cut wafer & exit | |
| Inspect | At Wafer Unload, hit 'Cancel' to prevent vacuum release<br><br>Click 'I' and up or down arrow, to bring sample to Scope<br><br>Click 'Auto Focus: At Wafer'<br><br>Make sure sample fully cut | |
| Unload Sample | 'Wafer Unload'<br><br>Water rinse/N2 dry<br><br>'Finish' to release.<br><br>Place in UV exposer<br><br>Time = 60 sec, 'Start'<br><br>Remove Si carrier from tape | |
| | | |
| | | |

| *DicingProtect Removal* | **Clean Samples for testing** | Edge pieces will be used for SEM Facet inspection |
| --- | --- | --- |
| Tool: Fume Hood in Bowers Lab | ˜1 hrs | |
| Remove from Carrier | Set Hotplate to 130°C<br>Place carrier, wait ˜5m<br>Hold carrier with tweezers, Pull piece out sliding with other tweezers<br>Immediately place tilted facedown and let go with tweezers | If tweezers get stuck to sample, heat them up on the hotplate (with sample) and retry |
| Cool | 1m | |
| Solvent Clean | Holding sample aloft, ACE repeatedly until PR + Wax is gone, then MoL/ISO/N2 dry | Any cloudiness is dried ACE or wax residue - redo ACE/MoL/ISO |
| | | |
| | | |
| *Facet Inspection* | **SEM to measure core dimensions** | |
| Tool: JEOL 7600F FESEM | ˜2hrs | |

| | | |
|---|---|---|
| Cleave edge piece | Side pieces with straight waveguides<br><br>Scribe repeatedly on backside, or shallow Dice<br><br>Cleave with glass slides to break<br>Piece should only be ~7.5mm long (x orig width, ~1cm) | Shallow dice on backside works extremely well:<br>–use program 'Demis_APC_SiOnTape'<br>– Place piece face-down on tape/frame carrier<br>– Depth = tape + 100µm - may cleave itself, but usually good facets<br>– break away from top-side (device side) |
| Mount to SEM holder | WG facets face-up, on x/y/z conductive tape, with clip | |
| Metal Coat | Hummer Au/Pd coat: (Volts = 0, DC Plate)<br>[Vac] until 0.060 Torr<br>[Gas] and adust until 0.100 Torr<br>[HV] increase Volts until 10 mA<br>[STOP] once coating @ 10mA for 60 sec | |
| Load + image in SEM | 5 kV, Current=9,<br>5mm distance<br>LABE det. inserted, SEI imaging<br>Locate widest guide (last in set)<br>Optimize Focus & Astigmatism (no skew when de-focused) | |
| Image Core | Once image optimized with SEI, snap image with LABE detector | removes charging artifacts, although using same excitation |

| Save thick-ness + width measurements | repeat for all 26 waveguides | best thickness meas on widest cores |
|---|---|---|

## C.1.1  Unaxis Deposition: No Vent

**Table C.2:** *Process Follower for Subroutine: Unaxis Deposition with No Venting.*

| Subroutine Module: | **Sub_Unaxis Dep - No Vent** | |
|---|---|---|
| for manual wafer re-mapping (to eliminate venting sample to atmosphere). Only necessary for films > 2µm. For films > 1µm & < 2µm, only need re-clamping step (via flow "Demis PM3 Multi"). Films ≤ 1µm use standard method | | |
| | | |
| *Upper Cladding Dep* | **Unaxis ICP-PECVD** | Deposition with multiple Dep/Clean steps without exposing sample to atmosphere |

266

| | | |
|---|---|---|
| Tool: Unaxis ICP Deposition | Signup for BOTH Etch & Dep sides if possible - to prevent venting LoadLock | Place sample wafer in left-Cassette (#1) and 2 cleaning wafers in right-Cassette (#2). Leave a few spaces between each wafer. Be VERY careful about which flow is run on which wafer - Don't SF6-clean your sample!!! Double check your flows before you Execute them |
| Login | OCPN / OCPN | on highest-level menu, bottom-left button. default is process/process |
| Chamber Pre-Season | Wafer = Cleaning (Cassette #2) Flow = "Demis - PM3 Clean + Season" Seq = "Post Dep Clean" + "SiO2 Seasoning 100C" Step = "SF6 Clean Post-Dep" | Run ~30m (1800s) pre-clean |
| 2um Dep + Chamber Clean Cycle | Run cycle 4 times, for ~8um SiO2 dep | |

| 1) SiO2 Deposition | Wafer = Sample (Cassette #1) Flow = "Demis - PM3 Multi" Seq = "SiO2 Deposition 100C" x 2 Step = "SiO2 Deposition 100C" - time=2000sec (33m) | Deposits 1um, removes wafer to TM, then replaces & deposits another 1um - this is to prevent the backside He error due to wafer bowing during dep. - the wafer is reclamped by doing this (2hrs total) Rate ˜= 1053nm/2000sec |
|---|---|---|
| 2) Chamber Clean + Season | Wafer = Cleaning (Cassette #2) Flow = "Demis - PM3 Clean + Season" Seq = "Post Dep Clean" + "SiO2 Seasoning 100C" Step = "SF6 Clean Post-Dep" | Set Cleaning time to 2000nm * 60s / 40nm = 3000sec (50min) This can be queued up as soon as sample dep is started - system will wait for previous flow to complete |

| 3) Remap Wafers | (Only once dep & clean are finished) * Go to screen: Maintenance > Manual Ops * Select LM module (top-left list) * click check box next to "LM Door is Open" (checked) * click "LM Door is Open" <br><br> * click check box next to "Cassette 2 is present" (checked) * click "Cassette 2 is Present" (grey) * click checkbox next to "Cassette 2 is Present" (unchecked) <br><br> * click check box next to "Cassette 1 is present" (checked) * click "Cassette 1 is Present" (grey) * click checkbox next to "Cassette 1 is Present" (unchecked) <br><br> * click checkbox next to "LM Door is Open" (unchecked) | Do this after both dep & clean are completed, and then run the Dep/Clean flows on their respective wafers again |
|---|---|---|
| **Repeat (1) to (3) for additional 2µm SiO2 as needed** | | |
| Last cycle: Do not season chamber | Flow = "PM3 Post-Dep Clean" Seq = "Post Dep Clean" Step = "SF6 Clean Post Dep" | Clean time will already be correct, 3000s |
| Vent LM and re-move sample | Can remove while final clean is running | Don't pick up Cassette 1 or system will error |
| Re-set Login | process / process | |

# C.2 SiO$_x$N$_y$ Waveguide with Etchless Core Definition

*Device Name: SiONox#22*

**Table C.3:** *Process Follower for waveguide with etchless core definition.*

| Demis John, 4/21/2012 | **4' Si Wafer: SiO$_x$N$_y$ WaveGuide Fab w/ Local Oxidation of Oxynitride** | |
|---|---|---|
| **Step** | **Details / Actual** | |
| Device Name: | **SiONox#22** | |
| Device Description: | Sputtered SiON-core, 900nm thick x 5.0µm to 17.5µm etchless core definition, deposited Upper Cladding | |
| | | |
| | | |
| General Process Notes: | * Keep Wafer face-down in curved wafer tray to minimize dust buildup. | |
| | * Cleanliness is extremely important for these huge waveguides. – wear face mask, and cover sample if people without masks are talking to you | |
| | * The Unaxis ICP SiO$_2$ causes radial curvature of the Si wafer - the center is about 2 or 3mm off of the table while all edges are touching. Strain-compensation on the backside is necessary, via backside dep of SiO$_2$ on any tool that can do this safely - PlasmaTherm PECVD, AV-PECVD or IBD. Use Backside coating fixture or glass slides to ensure front is not scratched during this step. | |

| | | |
|---|---|---|
| | * Deposition Watch Samples are ~1 cm x 3-5 cm Silicon. Always HF dip these once at the start of each day that they are needed (can dip one large piece, and keep cleaving off pieces throughout the day) | |
| | IWS order: Silicon wafers, 2-inch, P/B ~10 $\Omega$, <100>, 250-350µm, Single-Side Polished (SSP), Test grade, | |
| | | |
| Process Follower Notes: | * You should assume that every step is inserted for a reason - skipping steps often results in re-solving an old problem | |
| | * This process is specifically for SiN-core, Silica-clad waveguides with deposited upper cladding. Although IBD SiN is preferable, AJA SiN was used due to particulates on the IBD at the time - use Scope (+ Nomarski) to check for these. | |
| | | |
| ***Lower Cladding*** | **Thermally oxidized Silicon** | |
| Initial substrate purchase | KST World Corp. <br><br> 100 mm Silicon, <100> <br><br> Thickness = 525 µm <br><br> Front/Backside = Polished/Etched <br><br> P-type doping 5-10 Ohm-cm <br><br> 15 µm Oxide +/- 5% <br><br> $n_{1550}$ = 1.4458 +/- 0.0001 | Wafers are about $300 each. In-house oxidation requires about 30 days of continuous oxidation at 1050°C. Boron doping allows some reflow (lower melting point of B-SiO$_2$), and fewer cracks via reduced Thermal Expansion. |
| | | |
| | | |

| Core + Buffer Deposition | Unaxis SiON: 900 nm | SiO$_x$N$_y$ core sputter deposition, ~ 1 hr dep. (unmanned) |
|---|---|---|
| Tool: Unaxis ICP-PECVD Deposition | ~3hrs | |
| | *Perform Test Depositions if Needed* | |
| Core Deposition | | |
| prepare silicon test piece | cleave a piece of silicon (>=1cm x 3cm) HF dip for 1m & DI/N2 dry | |
| Load | Place watch sample(s) on Si carrier, and 4" Sample in slot directly below | Wafer flat facing load-lock door include 3 AlN cleaning wafers |
| Chamber Season | Cleaning Wafer Flow: PM3 Multi: Clean + Season Set 2nd sequence to: Category: Demis-SiON Dep Sequence: Demis-SiON Seasoning 250C | Clean "SF6 Clean Post Dep" = 600 sec |
| Core Dep. Edit Recipe & Run | PM3 Category: Demis-SiON Dep Sequence: Demis-SiON Dep Step: Demis-SiON Dep set time = 2000 sec | O2/N2 = 5/5 sccm set "SF6 Clean Post-Dep" = 3000sec Approx. 1.77 nm/min Thickness will decrease by ~15% after annealing & upper cladding dep. |
| Remove one watch sample | | |

| oxBuff Dep.<br>Edit Recipe & Run | PM3<br>Category: SiO2 Deposition(2% SiH4)-250C<br>Sequence: SiO2 Deposition 250C<br>Step: SiO2 Deposition 250C<br>set time = 2000 sec<br>set "SF6 Clean Post-Dep" = 3000sec | Approx.<br>1000 nm/2060 sec |
|---|---|---|
| ***oxMask Deposition***<br>Sputtered $Si_3N_4$<br>100 nm | AJA Sputter #3 | IBD $Si_3N_4$ is also ok, as long as no particulates |
| Prepare & Mount Watch Sample | Do this in a litho-bay fume hood with no other users<br>mount WatchSamp at top/bottom, using double clip | |
| Mount 4-inch sample<br>Load into system | N2 blow & inspect for cleanliness & Load into Chamber | mount test-piece first, then mount real sample<br>Nitrogen gun on sample<br>Hold sample face-down while transporting |

| | | |
|---|---|---|
| Edit Recipe & Run | Recipe: <br><br> APEX > process: 'Demis_SiN_dep': <br><br> Sample height = 44mm, Max Rotation (100rpm) <br><br> Gun (Silicon, RF2, #6 usually) Angle = 4mm <br><br> in layer 'Demis_SiN_deposition': set time = 98nm ÷ RATE (nm/sec) <br><br> set Target Pre-Clean = 10s (or delete step <br> set Post-Dep-Clean = 10min <br> DataLogging = On & RUN (turn off ion-guage) | |
| | | |
| | ***Stress-Compensation if Desired*** | SiO$_2$ dep on backside with AV-PECVD |
| | | |
| | | |
| ***Core Anneal*** | **TyStar Anneal: 1050°C, 3hr** | |
| Tool: TyStar Tube 3 | 7 hrs | |
| Prepare Sample | Place sample on flat quartz boat <br> N2 clean <br> Place under table (above floor) | |
| Load & Run recipe | 'Menu' > 'RL' > 'Anneal.003' <br> S/C/L/IF Temp = 1050°C <br> N2 = 3.00 slpm <br> All other gases = 0.00 slpm <br> Time = 03.00.00 (hh.mm.ss) <br><br> Hit 'Run' - and 'Event' once door is fully open | Total time = Anneal time (3h) + 2hr warmup + 2hr cooldown |

| | | |
|---|---|---|
| Load Sample | N2 clean sample while door is closing.<br>When door is halfway closed, place sample boat in system, under Tube #2 door | to shield sample from dust |
| Unload Sample | When tool shows Step=110, press 'Event' to open door<br>As soon as possible, pick up sample boat and place under table.<br>Cool for 10m before putting away. | |
| | | |
| | | |
| **oxMask Litho** | **PhotoLithography, Contact** | |
| Lithography Tool: Karl Suss MA-6 | ˜45m | From Renan Moreira's 'IPhOD Lithography - 2011-10-06.doc' which gives ˜4.47 nm RMS sidewall roughness |
| Set Fisher Oven #4 | Set temp to 300°C, place reservation sign if necessary | |
| Solvent Clean & Dry | Solvent Spinner (left), prog 5: 500s, 400rpm, 100rpm/s<br>ACE/MoL/ISO/N2 Dry<br>Inspect closely in hood for particles | Leave sample spinning for 30s after N2 dry to evaporate backside<br>Bay 6: Prog 8 // Bay 7: Prog 5 |
| *de-H2O Bake* | **300°C, >10m** | In Fischer Over #4 |
| Prepare Spinner | Non-raised spinner (Bay #7)<br>ACE/Non-shedding wipe underside of lid, N2 gun to check for wispy cobwebs<br>Replace napkin - 2 napkins. 4-inch chuck (non-bent, w/rubber o-ring) | |

| Cool | 2m | Use pliers/monkey wrench to remove Cool at cleaned spinner bench, no other users around |
|---|---|---|
| Apply HMDS | Coat wafer, small pipette | |
| *HMDS soak* | 30 sec | |
| **Spin HMDS** | Spin Recipe #0 = spin: 5000 rpm, 2000 rpm/s, 60s stop: (0 rpm, 500 rpm/s, 0s) | |
| Remove Top Napkin | Remove sample to tray remove top napkin replace sample | |
| Apply SPR 955 CM-0.9 | Coat wafer, large pipette | |
| **Spin PhotoResist** | Spin Recipe #1 = spread: (100 rpm, 100 rpm/s, 10s) spin: 4000 rpm, 800 rpm/s, 30s stop: (0 rpm, 500 rpm/s, 0s) | Large Pipette, no bubbles, cover wafer Or just Recipe 7: 4000 rpm, 800 rpm/s, 30s The 10sec low-spin spreads PR |
| *Pre-Bake* | **105°C, 1m** | HotPlate w/ Lid Down, Bay 7 |
| Remove Edge Bead | Use smaller plastic bud w/ EBR squirt bottle | only remove ˜2-3mm at edge - mask designed with 5mm margin Do on non-shedding wipes, no other users at bench N2 dry afterwards 10 s |

| | | |
|---|---|---|
| Prepare MA-6 | Install 5' Plate Holder | (17.2 mW/cm2) |
| | & 4' Vac Chuck | Channel 2 |
| | Set recipe: Vac-Ct | |
| | pre vac: 5 / full vac: 6 / vac purge: 10 | |
| | vac sea: 0.35 / WEC press: 0.45 | |
| | Al.Gap=50 / WEC Offset=0 / WEC Type=Cont | |
| | Time = 7 sec | |
| | Alignment Knobs: left=10.0 / right=6.0 | |
| Lamp Test | NO Sample nearby! Ensure power is correct | |
| | CH2 = 17.2 mW/cm2 | |
| Insert Mask Plate | Press 'Change Mask' | |
| | place mask plate against guides & clip | |
| | press 'ENTER' to start plate vac | |

| Load Sample + Expose Plate: "IPHOD IN–HOUSE 2_5" Layer 1 | N2 gun the sample, & check plate closely for dust<br><br>After WEC, sample should be centered already<br>Ensure that entrance/exit of spiral is away from Edge-bead removal areas | Calculate Correct Exposure time (sec) from the Lamp Test power reading (mW)<br>Exp = _____ sec = 10.7s x (17.2 mW / _____ mW)<br><br>Set 'BSA Microscope' to prevent uScope from coming down during alignment<br><br>Once aligned, press 'Alignment check' to start vacuum sequence, to observe contact quality.<br>Press 'Exp' if it looks ok |
|---|---|---|
| *Post-Exp-Bake* | **125°C, 2m** | HotPlate in Bay 7 - cover in tin foil if paranoid about dust |
| Cool | 1m | |

| | | |
|---|---|---|
| **Develop AZ 726 MiF** | 35 sec | Use 4-inch inner-cassette to hold sample, and 16" x 8" x 2" pyrex 3/4 full with Developer<br>Stop-dev in 150mm x 90mm crystallization dish of DI |
| Spin-Rinse-Dry | Std. Recipe: 90s Rinse @ 1000 rpm, 120s Dry @ 2000 rpm<br>Turn off Water valve during Dry step | Set pump-out to 'Hand' before start & turn on water<br>Set back to 'Auto' at end |
| **uScope Inspection** | **Inspect TestStructure patterns -**<br>**– look for curved/undeveloped PR at bottom of patterns**<br>**– Inspect/photograph resolution dots/L-shapes**<br>**– Look for dirt/obstructed waveguides** | Inspect Nonius/Vernier marks<br>Ensure uniformity is reasonable (Verniers are similar around spiral) |
| | | |
| *HardBake* | **95°C, 20m** | Doubles selectivity, prevents PR reflow during etch |
| | | |
| | | |
| *oxMask Etch* | **CF4/O2 etch of SiN** | |
| Tool: Panasonic #2 | ~1.5hr (incl. cleans) | |

| | | |
|---|---|---|
| Mount Sample | Use Santovac oil - ~2mm dots on 4 corners at edge only<br>N2 gun & Cover w/ tray immediately<br>Cleave ~2mm piece off oxMask dep. WatchSamp & place next to wafer flat | No oil exposed from beneath wafer (preferably) |
| O2 Clean + CF4 Season | P2:#105: 5m + 3m (CLEANING WAFER) | 3m Coat in order to stabilize etch rate prior to etch |
| **CF4/O2 Etch** | P2:#155, 1m<br>Make sure watch sample is fully etched (only silicon) | |
| Post-Etch O2 Clean | #103: 5m Clean | Clean:Etch time = 1:2 |
| Prepare PR Stripper | Place 150mm x 10mm dish of 1165 on 80°C HotPlate | Heat for 10m before using |
| Remove sample from Carrier | In solvent bench fume hood | |
| Backside Solvent Clean | place face-down in carrier, carefully swab ACE to remove oil | |
| **uScope Inspection** | **Inspect edges of TestStructure patterns** | |
| | | |
| | | |
| *P.R. Strip* | **PhotoResist Ash + Strip** | |
| PEII O2 Ash | | |
| O2 Stabilize | 1m, 300mT | Vent=ON: insert Sample<br>Vac=ON; when press ~0.500 T, Gas=ON, stabilize at 0.300T for >=2m |

| O2 Ash | 2m, 100W | Power=ON - make sure 100W, start timer. @end: Power=OFF, Gas=OFF, Vac=OFF, Vent=ON - remove sample Vac=ON; when press ˜0.500T, Vac=OFF, log in book |
|---|---|---|
| Strip Resist | | |
| 1165 soak @ 80°C | 10m, 150mm shallow dish on Hotplate | optional: squirt w/ 1165 squirt bottle@ start & end |
| Solvent Spinner Clean | ACE/MoL/ISO/DI & N2 Dry | optional: can squirt backside of sample w/ISO to remove 1165. Do this by spinning with ACE/MoL/ISO, but keep squirting ISO while shutting off spinner. Pick up sample (clean tweezers) and ISO backside Replace sample, and spin with ACE/MoL/ISO<br><br>ACE tweezers + dry to clean |

| | | |
|---|---|---|
| Gasonics Ash | Run Test-ash first: Recipe #3 (250°C), 60s<br><br>Run Sample: 3 x Recips #3, 60s | Use carrier with ceramic stops<br>If wafer moves during pickup, grab the carrier & let the tool abort!<br>If tool is not behaving, use PEII, for 2m |
| Solvent Spinner Clean | ACE/MoL/ISO / N2 dry | |
| Inspect | Check that resist is gone on large features | If anything is left, PRX-127 for ~5m |
| | | |
| **uScope Inspection** | **look for dirt/polymer on pattern edges** | DI/ACE/MoL/ISO/DI again if needed. Can even PEII again 2-5m if see polymer film<br>Observe/photo Vernier width bias / circular resolution marks |
| **Dektak (optional)** | **depth = _____** | can look for 'rabbit Ears' - indicative of residual polymer buildup. O2 ash + solvent soak (1165 @ 80degC, >5m or PRX-127) to remove |
| | | |
| | | |

| | | |
|---|---|---|
| | *Core Roughness Measurement if Desired (optional)* | AFM & SEM measure sidewall roughness and top-surface roughness |
| | | |
| | | |
| ***Core Definition: Oxidation*** | **TyStar WetVar: 950°C, 6hr** | |
| Tool: TyStar Tube 3 | 10 hrs | |
| Prepare Sample | Place sample on flat quartz boat<br>N2 clean<br>Place under table (above floor) | |
| Load & Run recipe | 'Menu' > 'RL' > 'WetVar.003'<br>S/C/L/IF Temp = 950°C<br>Time = 06.00.00 (hh.mm.ss)<br><br>Hit 'Run' - and 'Event' once door is fully open | Total time = Oxidation time + 2hr warmup + 2hr cooldown |
| Load Sample | N2 clean sample while door is closing.<br>When door is halfway closed, place sample boat in system, under Tube #2 door | to shield sample from dust |
| Unload Sample | When tool shows Step=110, press 'Event' to open door<br>As soon as possible, pick up sample boat and place under table.<br>Cool for 10m before putting away. | |
| | | |
| | | |

| | | |
|---|---|---|
| *oxMask Removal* | **CF4/O2 etch of SiN** | |
| Tool: Panasonic #2 | ~1.5hr (incl. cleans) | |
| Mount Sample | Use Santovac oil - ~2mm dots on 4 corners at edge only<br>N2 gun & Cover w/ tray immediately<br>Cleave ~2mm piece off oxMask dep. Watch-Samp & place next to wafer flat | No oil exposed from beneath wafer (preferably) |
| O2 Clean + CF4 Season | P2:#105: 5m + 3m (CLEANING WAFER) | 3m Coat in order to stabilize etch rate prior to etch |
| **CF4/O2 Etch** | P2:#155, 1min<br>Make sure watch sample is fully etched (only silicon) | |
| Post-Etch O2 Clean | #103: 5m Clean | Clean:Etch time = 1:2 |
| Remove sample from Carrier | In solvent bench fume hood | |
| Backside Solvent Clean | place face-down in carrier, carefully swab ACE to remove oil | |
| Gasonics Ash | Recipe #3 250°C,<br>60s x 3 | |
| | | |
| | | |
| *Partial Upper Cladding Dep.* | **AJA SiO$_2$: 1μm** | To fill voids from deposition seams |
| Tool: AJA Sputter #3 | 5hrs | |

| | | |
|---|---|---|
| Prepare & Mount Watch Sample | Do this in a litho-bay fume hood with no other users <br> mount WatchSamp at top/bottom, using double clip | |
| Mount 4-inch sample <br> Load into system | N2 blow & inspect for cleanliness & Load into Chamber | mount test-piece first, then mount real sample <br> Nitrogen gun on sample <br> Hold sample face-down while transporting |
| Edit Recipe & Run | Recipe: <br> APEX > process: 'UCSB_SiO$_2$_dep': <br> Sample height = 25mm, Max Rotation (100rpm) <br> Gun (Silicon, RF2, #6 usually) Angle = 9mm <br><br> in layer 'UCSB_SiO$_2$_deposition': set time = 1000nm RATE (nm/sec) <br> set Target Pre-Clean = 15m <br> set Post-Dep-Clean = 10m <br> DataLogging = On & RUN (turn off ion-guage) | Approx. 3.63 nm/min |
| Unload Sample | N2 gun | |
| | | |
| | | |
| ***P.UClad Anneal*** | **TyStar Anneal: 1050°C, 3hr** | Reflows P.Uclad, filling voids and Dep. seams |
| Tool: TyStar Tube 3 | 7 hrs | |

| | | |
|---|---|---|
| Prepare Sample | Place sample on flat quartz boat<br><br>N2 clean<br><br>Place under table (above floor) | |
| Load & Run recipe | 'Menu' > 'RL' > 'Anneal.003'<br><br>S/C/L/IF Temp = 1050°C<br><br>N2 = 3.00 slpm<br><br>All other gases = 0.00 slpm<br><br>Time = 03.00.00 (hh.mm.ss)<br><br>Hit 'Run' - and 'Event' once door is fully open | Total time = Anneal time (3h) + 2hr warmup + 2hr cooldown |
| Load Sample | N2 clean sample while door is closing.<br>When door is halfway closed, place sample boat in system, under Tube #2 door | to shield sample from dust |
| Unload Sample | When tool shows Step=110, press 'Event' to open door<br>As soon as possible, pick up sample boat and place under table.<br>Cool for 10m before putting away. | |
| | | |
| | | |
| *Upper Cladding Dep* | **Unaxis ICP-PECVD: SiO$_2$ 10µm** | Encapsulate to make device robust - air clad is ok, but dirt and environment affects loss and guiding |
| Tool: Unaxis ICP Deposition | ˜6 hrs | sign up for additional 2-3 hours for cooldown (unmanned) |
| *Follow procedure in sheet:* | 'Sub: Unaxis Dep - No Vent' (p. 266) | |

| | | |
|---|---|---|
| dep. 10 microns of SiO$_2$<br><br>5 cycles of steps (1) to (3) | #1: (dep)_____ (clean)_____<br><br>#2: (dep)_____ (clean)_____<br><br>#3: (dep)_____ (clean)_____<br><br>#4: (dep)_____ (clean)_____<br><br>#5: (dep)_____ (clean)_____ | |
| | | |
| | | |
| **Dicing Protect/Prep** | **SPR-220-7.0 spin + cure** | provides structural support for ridges during dice |
| Tool: spinner & hotplate | 15 min | |
| *Spin SPR 220-7.0* | Spin Recipe #1 =<br><br>spread: (100 rpm, 100 rpm/s, 10s)<br><br>4000 rpm, 800 rpm/s, 30s<br><br>stop: (0 rpm, 500 rpm/s, 0s) | Large Pipette, NO BUBBLES<br><br>Or just Recipe 7: 4000 rpm, 800 rpm/s, 30s<br><br>The 10sec low-spin spreads PR |
| *Pre-Bake* | **115°C, 5m** | HotPlate w/ Lid Down |
| *Mount to Si carrier wafer* | get 4-inch Si from dicing room | |

| | | |
|---|---|---|
| Measure Thickness of Carrier wafer | Plumb Micrometer: Thickness @ 5 points:<br><br>------<br><br>------ | Can get any relatively clean wafer from the 'Wafer Disposal' bin in bay 2, or a new 'Reclaimed Wafer' from the Panasonic supplies drawer<br><br>Make sure thickness does not deviate more than 100um |
| Heat Carrier | 125C, 2m | |
| Apply wax<br>Mount Sample<br>Remove carrier & cool | apply wax as thinly as possible, to carrier directly<br>enough to contact most of sample in center and very edges<br>press sample edges to make sure sample is fairly level | Do this in a fume hood! PR will release neurotoxins when heated! |
| | | |
| | | |
| *Dice Wafer* | **Dicing Saw w/ Std. Resnoid Blades** | Separate samples by dicing through waveguides, creating facets in the process |
| Tool: ADT Dicing Saw | ˜1 hrs | |
| Prepare Carrier | Use standard UV-release tape and metal frame<br>Prepare the tape and frame by themselves | |

| | | |
|---|---|---|
| Mount Sample | Place sample in center of frame/tape carrier, and press on underside of tape to completely adhere tape to device backside | |
| Load Recipe | Blumenthal > Demis_APC_SiOnWaxOnTape <br> –Speed = 0.8 mm/sec, <br> –110mm cut length, <br> –Depth = 0.490 mm <br> –Cut No. = 1 for both Angles 1/0° and 1/90° | Standard Silicon dicing parameters |
| Change Blade | Setup saw for 9RU or 22RU Resnoid blade (stocked) <br> 49mm flange (maximum exposure, smallest flange) | 9µm grit preferable |
| Load Sample | 'Wafer Load' (foam chuck) | |
| Align Rotation + 1st cut | 'Manual Wafer Align' <br> Get correct angle with 'rotate for initial align' <br> Correct rotation to long dice lines. <br> Set 'Cut Position' to right-most point of 1st desired cut | |
| Align Blade | 'Manual Y Offset' <br> Choose Cut Pos. 2mm from edge of wafer <br> Align to the cut & 'Finish' | Make sure this cuts fully thru sample but not thru carrier! |
| 1st Cut | 'Partial Wafer Cut' <br> –'Next' if it shows correct Angle (eg. '1/0°') <br> – 'Next' to complete alignment (Cut Pos already chosen for this cut only) <br> – 'Next' to set current Pos. as First Index <br> – 'Next' to set current Pos. as Last Index (eg. Index #1 to #1) <br> – 'Finish' to Cut wafer & exit | |

| | | |
|---|---|---|
| Inspect | At Wafer Unload, hit 'Cancel' to prevent vacuum release | |
| | Click 'I' and up or down arrow, to bring sample to Scope | |
| | Click 'Auto Focus: At Wafer' | |
| | Make sure sample fully cut | |
| 2nd Cut | 'Partial Wafer Cut' | |
| | –'Next' if it shows correct Angle (eg. '1/0°') | |
| | – 'BACK' to Re-do alignment (Need new Cut Pos.) | |
| | – Find 2nd Dice Line, and set Cut Pos. @ Right & 'Finish' | |
| | – 'Next' to complete alignment | |
| | – 'Next' to set current Pos. as First Index | |
| | – 'Next' to set current Pos. as Last Index (eg. Index #1 to #1) | |
| | – 'Finish' to Cut wafer & exit | |
| Inspect | At Wafer Unload, hit 'Cancel' to prevent vacuum release | |
| | Click 'I' and up or down arrow, to bring sample to Scope | |
| | Click 'Auto Focus: At Wafer' | |
| | Make sure sample fully cut | |
| Unload Sample | 'Wafer Unload' | |
| | Water rinse/N2 dry | |
| | 'Finish' to release. | |
| | Place in UV exposer | |
| | Time = 60 sec, 'Start' | |
| | Remove Si carrier from tape | |
| | | |
| | | |

| | | |
|---|---|---|
| ***DicingProtect Removal*** | **Clean Samples for testing** | Edge pieces will be used for SEM Facet inspection |
| Tool: Fume Hood in Bowers Lab | ~1 hrs | |
| Remove from Carrier | Set Hotplate to 130°C<br>Place carrier, wait ~5m<br>Hold carrier with tweezers, Pull piece out sliding with other tweezers<br>Immediately place tilted facedown and let go with tweezers | If tweezers get stuck to sample, heat them up on the hotplate (with sample) and retry |
| Cool | 1m | |
| Solvent Clean | Holding sample aloft, ACE repeatedly until PR + Wax is gone, then MoL/ISO/N2 dry | Any cloudiness is dried ACE or wax residue - redo ACE/MoL/ISO |
| | | |
| | | |
| ***Facet Inspection*** | **SEM to measure core dimensions** | |
| Tool: JEOL 7600F FESEM | ~2hrs | |

| | | |
|---|---|---|
| Cleave edge piece | Side pieces with straight waveguides<br><br>Scribe repeatedly on backside, or shallow Dice<br><br>Cleave with glass slides to break<br>Piece should only be ˜7.5mm long (x orig width, ˜1cm) | Shallow dice on backside works extremely well:<br>–use program 'Demis_APC_SiOnTape'<br>– Place piece face-down on tape/frame carrier<br>– Depth = tape + 100μm - may cleave itself, but usually good facets<br>– break away from top-side (device side) |
| Mount to SEM holder | WG facets face-up, on x/y/z conductive tape, with clip | |
| Metal Coat | Hummer Au/Pd coat: (Volts = 0, DC Plate)<br>[Vac] until 0.060 Torr<br>[Gas] and adust until 0.100 Torr<br>[HV] increase Volts until 10 mA<br>[STOP] once coating @ 10mA for 60 sec | |
| Load + image in SEM | 5 kV, Current=9,<br>5mm distance<br>LABE det. inserted, SEI imaging<br>Locate widest guide (last in set)<br>Optimize Focus & Astigmatism (no skew when de-focused) | |
| Image Core | Once image optimized with SEI, snap image with LABE detector | removes charging artifacts, although using same excitation |

| Save thickness + width measurements | repeat for all 26 waveguides | best thickness meas. on widest cores |
|---|---|---|